Università di Napoli "Federico II"

Università di Camerino

PhD program in QUANTUM TECHNOLOGIES

XXXVI cycle

Transport and noise properties of Ferromagnetic Josephson junctions at the $0 - \pi$ transition.

PhD DISSERTATION by

Roberto CAPECELATRO

Settore Scientifico Disciplinare: FIS/03 (02/B2)

Tutors: Prof. Procolo Lucignano
Dr. Gabriele Campagnano

a.y. 2022/2023

Contents

List of Figures

List of Tables

Acronyms

AB Ambegaokar - Baratoff. 14, 20, 27, 67–69

ABS Andreev Bound States. 29, 41, 43, 48–50, 56, 94, 97, 99–106, 109, 111, 113–115, 128, 129

BCS Bardeen Cooper Schrieffer. 11–14, 44, 46, 83

BdG Bogoliubov de Gennes. 24, 39, 77, 78, 81, 82, 88, 89

CPR current-phase relation. 19, 26, 28–30, 37, 39, 42, 43, 66–69, 71–73, 78, 81, 82, 87, 89, 95, 98–103, 105, 107–115, 129

F Ferromagnet. 19–23, 34, 75

FFLO Fulde - Ferrel - Larkin - Ovchinnikov. 19, 33

FI Ferromagnetic Insulator. 18, 21, 23–25, 28, 35, 40, 62–65, 68, 69, 74–80, 83, 86, 90, 125

GF Green's Function. 23–26, 36, 44, 47, 48, 52, 54–60, 65, 66, 81, 94, 95, 105

JJ Josephson junction. 13–30, 32, 35, 38, 41, 43, 44, 48–50, 52, 55–57, 62, 63, 65–68, 70–75, 77–81, 85, 86, 89–92, 96–101, 103–112, 114, 125, 128

MQC Macroscopic Quantum Coherence. 17

MQT Macroscopic Quantum Tunneling. 16, 20

NS Normal Metal - Superconductor. 48, 49

QD Quantum Dot. 23, 24, 30, 50, 52, 55, 97, 103, 104, 108, 111

QPC Quantum Point Contact. 29, 30, 100

RCSJ Resistively and Capacitively Shunted Junction. 15, 22

RGF Recursive Green's Function. 24–26, 28, 39, 44, 52, 57, 59, 65, 82

SF Superconductor - Ferromagnetic. 18, 21, 23

SFIS Superconductor - Ferromagnetic Insulator - Superconductor. 18, 20, 22–24, 27, 28, 30, 35, 38, 44, 50, 53, 56, 62, 63, 65, 66, 68, 70, 71, 73, 75, 77–79, 81, 89, 90, 125

SFS Superconductor - Ferromagnet - Superconductor. 17–20, 22–24, 27, 30, 33, 81, 86

SIS Superconductor - Insulator - Superconductor. 13–18, 20, 27, 32

SN Superconductor - Normal Metal. 12

SNS Superconductor - Normal Metal - Superconductor. 49, 95, 96

SOC Spin - Orbit Coupling. 21, 24, 27, 35, 37, 38, 62–64, 67–78, 86, 89, 125

SQDS Superconductor - Quantum Dot - Superconductor. 19, 23, 24, 29, 30, 41, 44, 49, 50, 52, 56, 91, 92, 96–101, 104–108, 110, 112, 114, 128

SQUID Superconducting - Quantum - Interference - Device. 16, 17, 19, 30, 31

Introduction

Josephson Effect

Superconductivity is an ordered phase of matter characterizing materials that can host charge currents without heat dissipation, i.e. *supercurrents*, [1–6]. This is possible because in superconductors, according to Bardeen Cooper Schrieffer (BCS) theory [1], couples of electrons with opposite spin and momentum are paired together in the so-called *Cooper pairs* of charge $2e$ (e is the electron charge). Although a thorough discussion on the microscopic nature of superconductivity is far from the objectives of this thesis and we thus refer the interested reader to Refs.[1–6], it can be useful to recall the main findings of BCS theory.

Transition from normal metal to superconducting state can be only achieved at temperatures below a certain threshold, called critical temperature T_C, which depends on the specific material. For $T < T_C$, electrons near the Fermi surface, $k \sim k_F$ (k_F being the Fermi *quasi-momentum*), experience a weak phonon-mediated attractive potential that leads to the formation of Cooper pairs with a spatial extension of $\xi_0 = (\hbar v_F)/(2\pi k_B T_C)$ (v_F is the Fermi velocity and k_B is the Boltzmann constant), called superconducting coherence length [1–6]. In conventional BCS superconductors, Cooper pairs consist of time-reversed pairs of electrons, namely, with $k, \uparrow$ and $-k, \downarrow$. Their wave-function, which must be totally antisymmetric due to the Pauli exclusion principle, is the product of an antisymmetric spin-singlet state, e.g. $|S^2 = 0, S_z = 0\rangle \propto |\uparrow\downarrow\rangle - |\downarrow\uparrow\rangle$, and a symmetric wave-function in real space, often referred to have *s-wave* symmetry [1–6]. For this reason, they effectively behave like bosons, and, contrary to electrons in normal metals, they can be collectively arranged in a minimum energy state that is separated by an energy gap Δ from the superconductor fermionic excitations, called quasiparticles, Fig. 1.

Moreover, Cooper pair condensate can be described by a collective macroscopic wave-function

$$\Psi(\vec{r}) = |\Psi(\vec{r})| e^{i\varphi} = \sqrt{\rho(\vec{r})} e^{i\varphi},$$

where φ is the phase common to all Cooper pairs and ρ is their spatial density, that is found to be proportional to the gap Δ in BCS theory [1–6]. Note that $\Psi(\vec{r})$ has to fulfill the above mentioned prescriptions regarding spatial and spin symmetries.

In other words, superconductors can be seen as macroscopic quantum objects whose properties are encoded in their macroscopic state Ψ. Due to the phase coherence of all the Cooper pairs in the condensate state, in the presence of a current bias dissipationless currents arise inside the superconductor. Nevertheless, superconductivity can be suppressed if the current and, so the energy, supplied to the system exceeds the critical

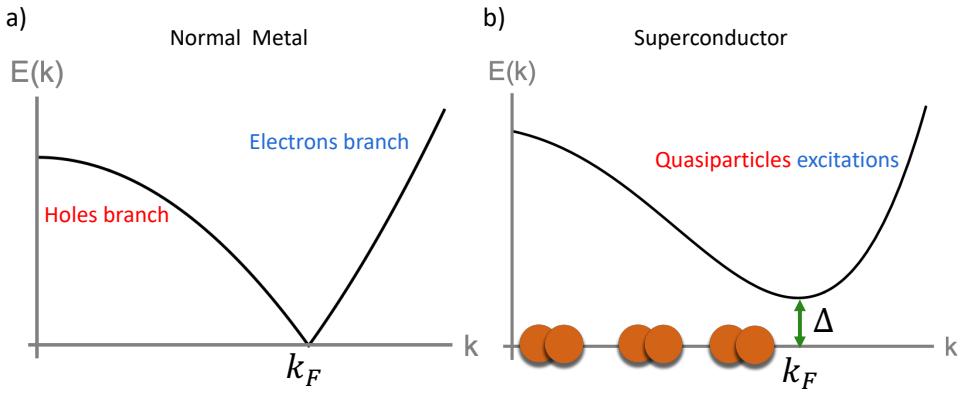

Figure 1: Comparison between the excitations spectrum in a normal metal in (a) and the one of a BCS superconductor in (b). In the superconductor energy spectrum, a gap Δ opens up between the Cooper pairs condensate and the quasiparticles excitations. While in normal metals below the Fermi surface $k < k_F$ only hole-like excitations are possible and the viceversa is valid for electronic ones, in the superconductor quasiparticles excitations have no definite charge and thus no more *hole-* and *electron-* branches exist.

value $I > I_C$ [1–6], analogously to the fact that at $T > T_C$ no superconducting phase is possible [1–6].

Interestingly, superconducting-like properties can be induced in normal materials when they are placed in contact with superconductors [6–8]. This effect known as *proximity effect* is observable in Superconductor - Normal Metal (SN) interfaces and consists in the penetration of superconducting correlations inside N, Fig. 2. Cooper pairs enter the normal layer over a distance from the interface of $\xi = \hbar v_F/(2\pi k_B T)$, that is called normal coherence length, and become available for superconducting transport in SN heterostructures [6–8].

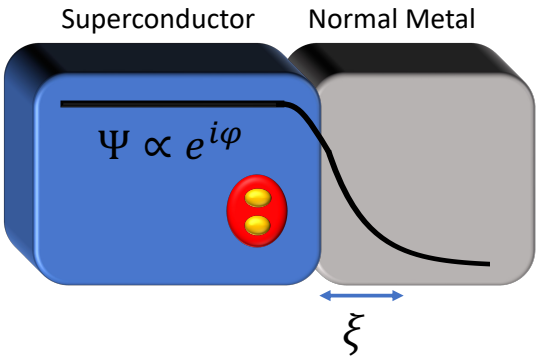

Figure 2: Proximity effect at a SN interface. Penetration of the superconducting wave-function in the normal layer over the normal coherence length $\xi = \hbar v_F/(2\pi k_B T)$ is shown. Simultaneously a leakage of Cooper pairs occurs in S near the interface, i.e. *inverse proximity effect*

Penetration of Cooper pairs wave-function in normal materials is at the bottom of the famous Josephson Effect [7–10] that describes the supercurrent flow in a weak

link between two superconducting leads, i.e. a Josephson junction (JJ), Fig. 3. The weak link often consists of a thin layer of non-superconducting material called *barrier* [7–10], that in most of the superconducting circuits applications is an insulator, i.e. Superconductor - Insulator - Superconductor (SIS) JJ [7–10].

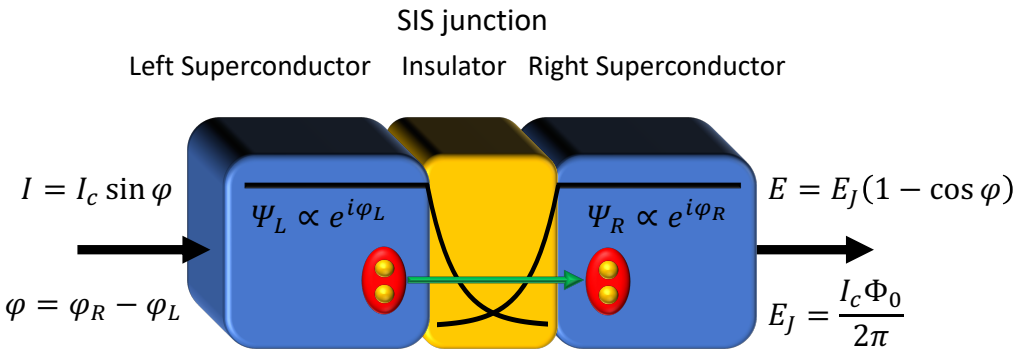

Figure 3: SIS JJ. The exponential decay of the wave-functions $\Psi_{L/R}$ of the superconducting leads inside the barrier is shown. The overlap between Ψ_L and Ψ_R, in the presence of a current bias I, makes the Cooper pairs tunneling possible, giving rise to the supercurrent $I = I_C \sin\varphi$ across the insulating layer. I_C is the JJ critical current and E is the energy stored in the junction.

Due to the overlap of the leads wave-functions, $\Psi_{L/R} \propto e^{i\varphi_{L/R}}$, inside the barrier, a current bias $I < I_C$ allows the Cooper pairs to tunnel across the junction thus giving rise to a supercurrent. Josephson current measurements in SIS JJs, also called *tunnel* JJs, represent an accessible way to experimentally observe a quantum effect at macroscopic scale.

Josephson Effect appeal for research on quantum phenomena primarily stems from the fact that it relates easily measurable macroscopic variables, as the current I and voltage V across barrier, to the phases of the superconducting electrodes wave-functions, $\varphi_{L/R}$, that have a pure quantum nature [6–10].

For conventional BCS superconductors [1] and insulating barrier, i.e. SIS JJ, the two Josephson relations for the junction supercurrent I and voltage V respectively read

$$I(\varphi) = I_C \sin\varphi, \quad V = \frac{\Phi_0}{2\pi}\frac{\partial\varphi}{\partial t},$$

where the critical current I_C is the maximum dissipationless current flowing through the barrier, $\varphi = \varphi_R - \varphi_L$ is the phase difference between left and right superconducting leads and $\Phi_0 = h/2e = (\hbar\pi/e)$ the superconducting flux quantum (h and $\hbar$ being the complete and reduced Planck constants, respectively), thus describing the coherent tunneling of Cooper pairs between the two electrodes. Josephson equations also allow us to derive the coupling energy $E(\varphi)$ stored in the JJ. Integration over time t of the electrical work necessary to change the JJ phase yields

$$E(\varphi) = \int IV dt = \int \frac{\Phi_0}{2\pi} I_C \sin\varphi d\varphi = E_J(1 - \cos\varphi),$$

where the Josephson energy is defined as $E_J = I_C(\Phi_0/2\pi) = I_C(\hbar/2e)$ and we choose to set $E(\varphi = 0) = 0$ for the sake of simplicity, Fig. 3. Critical current is hence a measure

of the coupling between the S leads phases across the weak link and it depends on the nature and geometry of the barrier [6–10].

Josephson effect thus represents a unique playground to both study some leads and barrier microscopic properties and test the BCS theory of superconductivity. Josephson relations characterize the junction current-voltage behavior, $I - V$, together with the constraint that for $I < I_C$ there is no voltage drop between the leads. The features of the $I - V$ diagram are signatures of the superconducting gap and the dissipation mechanisms occurring in the junction Fig. 4 (a). Measuring the voltage drop appearing across the JJ when the bias current is ramped up to I_C, we can infer the value of Δ, since the system switches from the 0 voltage to resistive state at $V = 2\Delta/e$, corresponding to the energy necessary to break a Cooper pair and create two quasiparticles excitations [6–10]. From the slope of the high voltage branch we can also calculate the normal state resistance of the barrier, $R_N = V/I$ [6–10]. In this context, the hysteretic $I - V$ curve in Fig. 4 (a) turns out to be typical of insulating SIS junctions and becomes the fingerprint of tunnel JJs with high resistance barriers, intrinsically characterized by low dissipation [6–10]. Analogously, the temperature dependence of the critical current, i.e.

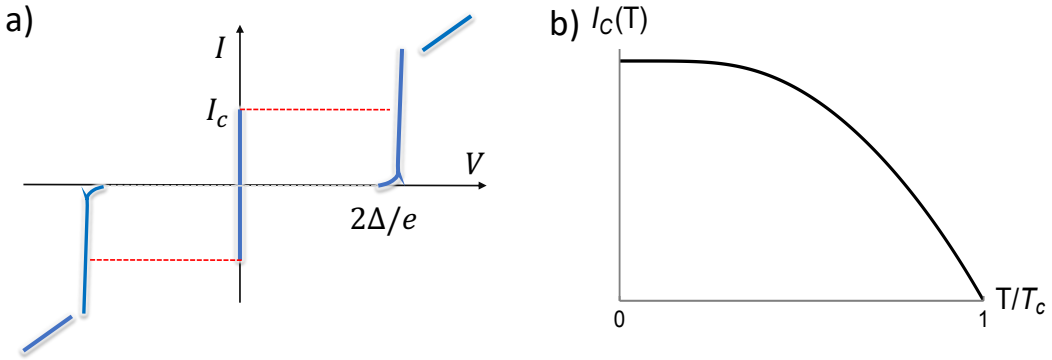

Figure 4: The experimental benchmarks assuring the insulating properties (e.g. high resistance) of the barrier are the hysterestic current-voltage $I(V)$ curve (a) and the monotonic AB trend in the $I_C(T)$, with I_C vanishing at the S leads critical temperature T_C (b). From their features it is possible to extract information about the superconducting gap Δ and about the normal state resistance of the barrier R_N.

$I_C(T)$, quantifies how much the Josephson current and thus the coupling between the electrodes is reduced when increasing T. $I_C(T)$ is, at the same time, a test for BCS predictions on the temperature behavior of the gap, $\Delta(T)$, and a source of information about the barrier properties. In the case of SIS junctions, for example, Ambegaokar and Baratoff [11, 12] worked out an analytic expression for $I_C(T)$ reading

$$I_C R_N = \left(\frac{\pi\Delta(T)}{2e}\right) \tanh\left(\frac{\Delta(T)}{2k_B T}\right),$$

from which R_N and/or $\Delta(T)$ can be derived. This relation for BCS superconductors yields the monotonic AB trend in Fig. 4 (b) identifying conventional tunnel SIS junctions.

On top of that, not only do JJs show quantum effects on macroscopic scale but, under proper conditions, the phase difference between the leads φ can effectively behave as a

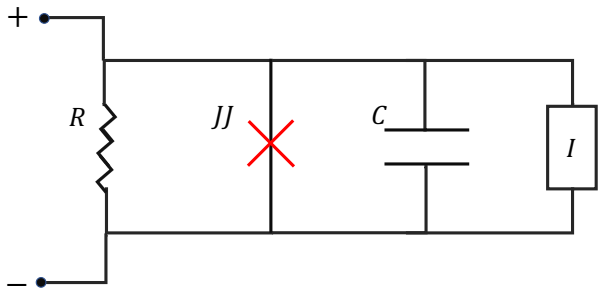

Figure 5: Current-biased JJ equivalent circuit, according to the RCSJ model. This involves a resistor R accounting for dissipative effects in the finite voltage state and the shunting capacitance C in parallel with the JJ.

macroscopic quantum variable. Macroscopic quantum effects are especially observable in current-biased SIS junctions.

From the circuital perspective, ideal Josephson junctions act as a non-linear inductors [6–8, 10]

$$V = \frac{\Phi_0}{(2\pi I_C \cos\varphi)} \frac{dI}{dt} = L_J \frac{dI}{dt} ,$$

with Josephson inductance $L_J = \Phi_0/(2\pi I_C \cos\varphi)$. However, when considering resistive and capacitive effects a more realistic picture of the JJ behavior is provided by the Resistively and Capacitively Shunted Junction (RCSJ) model [6–8, 10]. The equivalent circuit for the JJ consists in a parallel of a resistor R, a capacitor C and the junction itself, with the current-bias provided by I, Fig. 5. Here, R (often coinciding with R_N) and C account for dissipative effects in the finite voltage regime and geometric capacitance between the two S leads, respectively [6–8, 10]. Kirchoff law for this circuit, together with Josephson relations, yields an equation of motion for the phase φ [6–8, 10]

$$I = I_C \sin\varphi + V/R + \frac{dV}{dt} = I_C \sin\varphi + \frac{\hbar}{2eR}\frac{d\varphi}{dt} + \frac{\hbar C}{2e}\frac{d^2\varphi}{dt^2} .$$

This actually describes the dynamics of a *fictitious* phase particle of mass $M = (\hbar C)/2e$ subject to a drag force with coefficient $\gamma = \hbar/(2eR)$ moving in a tilted cosinusoidal potential $U(\varphi) \propto (1 - \cos(\varphi) - (I/I_c))$, called *washboard potential*, Fig. 6. When I becomes larger than I_C, $U(\varphi)$ has no more wells and thus no stable points for φ particle, that starts slipping downward the potential hills [6–8, 10]. This correspond to the junction jumping from the dissipationless to the finite voltage state, i.e. from the zero-voltage to the high voltage branch of the $I-V$ characteristic in Fig. 4(a) [6–8, 10]. Nevertheless, in SIS tunnel JJs with small capacitance and high resistance, the *phase-particle* can also escape from a given potential well by the means of quantum tunneling with the JJ switching to the running (finite voltage) state for $I < I_C$, Fig. 6 [13–22]. Although, this phenomenon, known as Macroscopic Quantum Tunneling (MQT), is only visible at very low temperatures, when other thermal escape processes are prevented [6, 7, 13–22], it indicates that φ is properly a macroscopic quantum variable, thus being described by a quantum operator $\hat{\varphi}$. Experimental evidences of MQT were of fundamental importance for research on quantum phenomena, since for the first time proved that SIS JJs can show genuine quantum mechanical effects, thus, paving the way

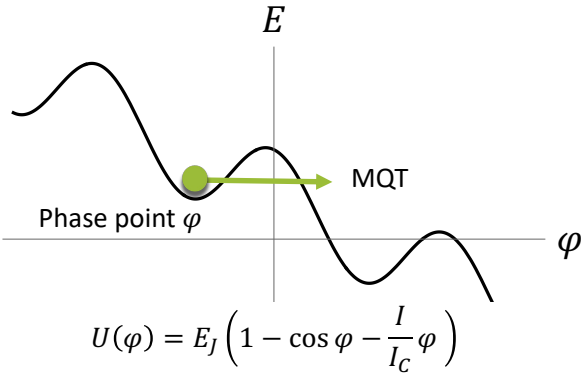

Figure 6: Washboard potential for the current-biased JJ $U(\varphi)$ is shown. Under proper conditions (very high junction resistance and/or very low capacitance) the phase of the JJ can behave like a macroscopic quantum degree of freedom that can experience tunnel effect between the wells of the potential (MQT).

to their application in superconducting quantum bits (qubits) [13–22]. Qubits are the building blocks for the emergent field of quantum computation and, roughly speaking, consist in two levels systems whose states play the role of logical 0 and 1 states [10, 23–32]. In this framework, quantum tunneling of φ is the key ingredient to build artificial two levels systems in all those superconducting qubits architectures exploiting the JJ phase as macroscopic quantum degree of freedom, as phase and flux qubits [10, 23–31].

Flux Qubits designs, for example, are based on the Superconducting - Quantum - Interference - Device (SQUID), i.e. a superconducting ring with two tunnel JJs as in Fig. 7 [27–31].

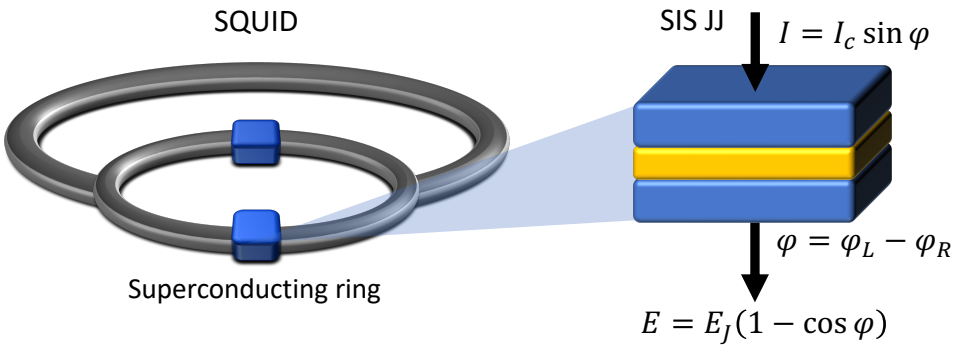

Figure 7: Basic scheme of the SQUID (Supercoducting-Quantum-Interference-Device) as a superconducting ring with two SIS Josephson junctions.

In order to make a SQUID behave like a qubit an external magnetic flux bias of $\Phi_{BIAS} = \Phi_0/2$ is needed, Fig. 8(a)-(b). For $\Phi_{BIAS} = \Phi_0/2$, the SQUID exhibits a bistable potential configuration, $U(\Phi)$ ($U(\varphi)$), with two degenerate minima at $\Phi = \pm\Phi_0/2$, corresponding to macroscopic quantum states with clockwise $|\downarrow\rangle$ and counter-clockwise $|\uparrow\rangle$ currents in the loop, Fig. 8 (a) and (c). In this case, the magnetic flux $\hat{\Phi} = \Phi_0\hat{\varphi}/(2\pi)$ piercing the loop plays the role of macroscopic quantum variable that can tunnel between the wells of the SQUID potential $U(\Phi)$ (here $\hat{\varphi}$ is the phase difference

between the two JJs of the ring).

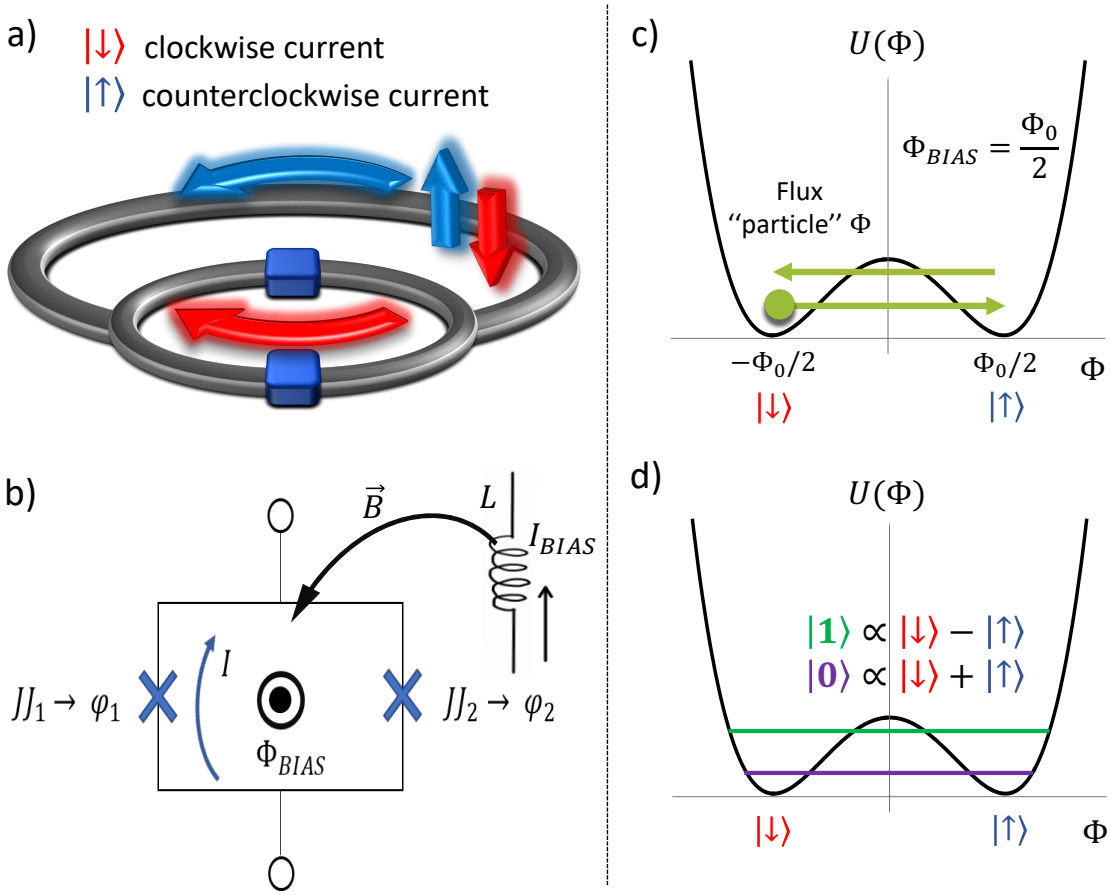

Figure 8: Basic scheme of the Flux Qubit as a SQUID with an external magnetic flux bias (a) and its circuital scheme involving an inductor L to bias the superconducting ring with the external magnetic flux (b). For $\Phi_{BIAS} = \Phi_0/2$, the system assumes a bistable potential configuration with two minima, in $\Phi = \pm\Phi_0/2$, corresponding to the macroscopic quantum states $|\downarrow\rangle$ and $|\uparrow\rangle$, i.e. supercurrent flowing clockwise and counter-clockwise around the loop, respectively (c). Coherent quantum tunneling of the flux "particle" between the two potential wells (c) leads to coherent superpositions of $|\downarrow\rangle$ and $|\uparrow\rangle$, resulting in the two qubit states, $|0\rangle$ and $|1\rangle$ (d). Figures adapted from https://www.dwavesys.com (a) and from Ref.[33] (c)

Coherent tunneling of the flux (phase) particle between the two minima generates coherent superpositions of $|\downarrow\rangle$ and $|\uparrow\rangle$ states, giving rise to the so-called *bonding* and *anti-bonding* states that act as the two qubit states $|0\rangle \propto |\downarrow\rangle + |\uparrow\rangle$ and $|1\rangle \propto |\downarrow\rangle - |\uparrow\rangle$, Fig. 8 [13, 14, 27–31, 33].

In JJs operating in the quantum "regime", the charge on one of the leads, called *island*, expressed in number of Cooper pairs, $\hat{Q} = e\hat{n}$, is the quantum mechanical conjugate of the phase $\hat{\varphi}$, fulfilling the commutation relation $[\hat{\varphi}, \hat{n}] = i$. For this reason, similar principles apply to qubits that use the charge Q degree of freedom. In particular, coherent superposition of macroscopic quantum states of charge Q observable in Cooper Pair Boxes [34–39], i.e. Macroscopic Quantum Coherence (MQC), led to the first charge qubits and transmons schemes [23–26].

Why ferromagnetic Josephson junctions?

In recent years, the growing complexity of the barriers employed in JJs in terms of layout and materials has significantly increased the "parameters space" for a full understanding and control of their properties [7, 10]. In particular, junctions with ferromagnetic barriers, i.e. Superconductor - Ferromagnet - Superconductor (SFS) JJs, provide unique platforms for observing intriguing phenomena resulting from the coexistence and competition of superconducting and magnetic ordering such as $0-\pi$ transitions [40–56], spin-triplet supercurrents [57–75] and hysteretic current vs. field, $I(H)$, behavior [76–79]. These effects, in turn, open up new scenarios for exploring different tuning mechanisms for JJs and incorporating smart functionalities in superconducting circuitry.

$0-\pi$ transitions consist in a change in the equilibrium phase difference from $\varphi = 0$ to $\varphi = \pi$ when a JJ is in the ground state [40–56]. π JJs, with a built-in phase difference of π, are currently subject to intense research activity due to their applicability as architectural elements for superconducting quantum computing devices, in view of the increased robustness against magnetic noise and a more compact design [80–86]. The advantage they carry especially to flux and phase qubits schemes lies in the fact that, due to the flux quantization inside the SQUID ($\Phi_{BIAS} = \Phi_0\varphi/(2\pi)$ with φ being the difference between the two junctions phases), an intrinsic π-shift is equivalent to an external flux bias $\Phi_{BIAS} = \Phi_0/2$. This provides the intriguing chance of building a self-biased qubit by simply using one SFS JJ in the π phase in place of a conventional SIS JJ inside the loop, Fig. 9 [80–88]. In this way not only are simpler and more compact qubits schemes possible, hopefully paving the way to scalable designs, but this solution could help in reducing the external flux lines needed for qubits control, thus, avoiding the dephasing due to noise in the external flux [80, 81, 89].

Ferromagnetic junctions including spin-mixing effects, such as magnetic impurities, non-homogeneous exchange field or spin-orbit interaction, have been also identified as promising platforms to host and engineer unconventional spin-triplet superconductivity [57–72]. Equal-spin triplet Cooper pairs are characterized by $S = 1$ and $S_z = \pm 1$ ($|1,1\rangle_{S,S_z} = |\uparrow\uparrow\rangle$ and $|1,-1\rangle_{S,S_z} = |\downarrow\downarrow\rangle$) and, being insensitive to exchange field of the ferromagnet (in principle detrimental for conventional spin-singlet Cooper pairs), give rise to long-range superconductivity in Superconductor - Ferromagnetic (SF) heterostructures. These devices, in which spin-polarized supercurrents can arise without dissipation, thus represent the possible building blocks for the emerging field of superconducting spintronics [57–72].

More recently, ferromagnetic tunnel JJs with hysteretic current vs. field, $I(H)$, behavior [76–79] have been proposed to realize a hybrid transmon qubit scheme. The hysteretic behavior of the ferromagnetic barrier indeed provides an alternative and intrinsically digital control of the JJ critical current I_C and Josephson energy E_J. In this way, the qubit frequency, proportional to E_J, can be properly tuned by means of magnetic field pulses [78, 79].

In this framework, our research activity involves both transport and current-noise properties of magnetic JJs, with a focus on JJs with Ferromagnetic Insulator (FI) barriers, i.e. Superconductor - Ferromagnetic Insulator - Superconductor (SFIS) JJs, that would be more suitable for applications in superconducting quantum circuits, due to their lower dissipation with respect to junctions with normal-metal ferromagnets.

We investigated both the $0-\pi$ transitions and realization of π states in SFIS JJs [90] and the presence of spin-triplet supercurrents when spin-mixing effects are also considered [91]. We explored the possibility of controlling and tuning temperature-induced $0-\pi$ transitions in SFIS JJs by external control knobs, in view of engineering temperature stable π JJs [90]. Indeed, having tunable $0-\pi$ devices that can be switched between the 0 and π phases, without being strongly affected by noise, would represent a further important step toward application of ferromagnetic junctions in qubits [90].

We theoretically modeled the transport in experimental NbN / GdN / NbN SFIS JJs displaying peculiar $I_C(T)$ curves with non-monotonic trend, Ref.[75], showing that this was due to an *incipient* $0-\pi$ transition possibly resulting from the interplay of spin-mixing mechanisms and disorder [91]. Moreover, the analysis we carried out on the spin pair correlations in FI, highlighted the possible link between this $I_C(T)$ behavior and the competition of the oscillating singlet supercurrents with long-range spin-polarized triplet currents [91].

Further, we studied the current fluctuations, $\delta I(\varphi)$, in a simple magnetic junction at the $0-\pi$ transitions with the aim of understanding whether these phase switchings are accompanied by enhanced current noise [92]. In other words, we investigated if the current-noise response to charge or magnetic fluctuations, at the $0-\pi$ transitions, is different from that of the JJ in the standard 0 phase. We considered a Superconductor - Quantum Dot - Superconductor (SQDS) junction in an external magnetic field that, due to its simplicity, represents an interesting playground to study the mechanisms underlying the $0-\pi$ current noise response to magnetic fluctuations [92]. Our results pointed out the presence of Josephson current jumps, i.e. strongly non-harmonic $I(\varphi)$ behavior, that in certain regimes can characterize the $0-\pi$ transitions, as a source of current noise amplification [92]. This kind of analysis could be relevant for future researches on the feasibility of employing tunable $0-\pi$ devices in superconducting circuits.

$0-\pi$ transitions and π junctions

The Josephson energy stored in the JJ indeed reads: $E=\Phi_0 I_C/(2\pi)(1-\cos\varphi)$ [6, 7], thus, the ground state energy, as well as the corresponding phase difference φ, depends on the sign of the critical current. In conventional JJs the ground state occurs at $\varphi=0$ ($I_C>0$), by contrast in the *so-called* π junctions the minimum energy corresponds to $\varphi=\pi$ ($I_C<0$) [45, 50, 51], this translating to a change in sign of the JJ current-phase relation (CPR), $I(\varphi)=I_C\sin(\varphi+\pi)=-I_C\sin\varphi$. Flux quantization inside a SQUID, reading $\Phi=\Phi_0\varphi/(2\pi)$ (Fig. 8(b)), implies that an intrinsic π-shift in the relative phase φ between the two JJs is equivalent to an external flux bias $\Phi_{BIAS}=\Phi_0/2$. In Refs.[80, 81], by exploiting this fact, alternative flux qubits architectures using SQUIDs with one SFS π junction, acting as static π phase shifter, have been proposed, in Fig. 9. These π qubits are naturally characterized by a bistable potential configuration without any external flux bias, thus being a simple example of self-biased flux qubit that might provide an efficient solution to the magnetic stability problem of the circuit [82, 85].

In this case only small magnetic fluxes for the qubit manipulation and readout are needed [80], as compared to $\Phi_0/2$ for conventional flux qubits [27, 28], that can be obtained for fields of few mT also in small size qubits (reduced area of the SQUID

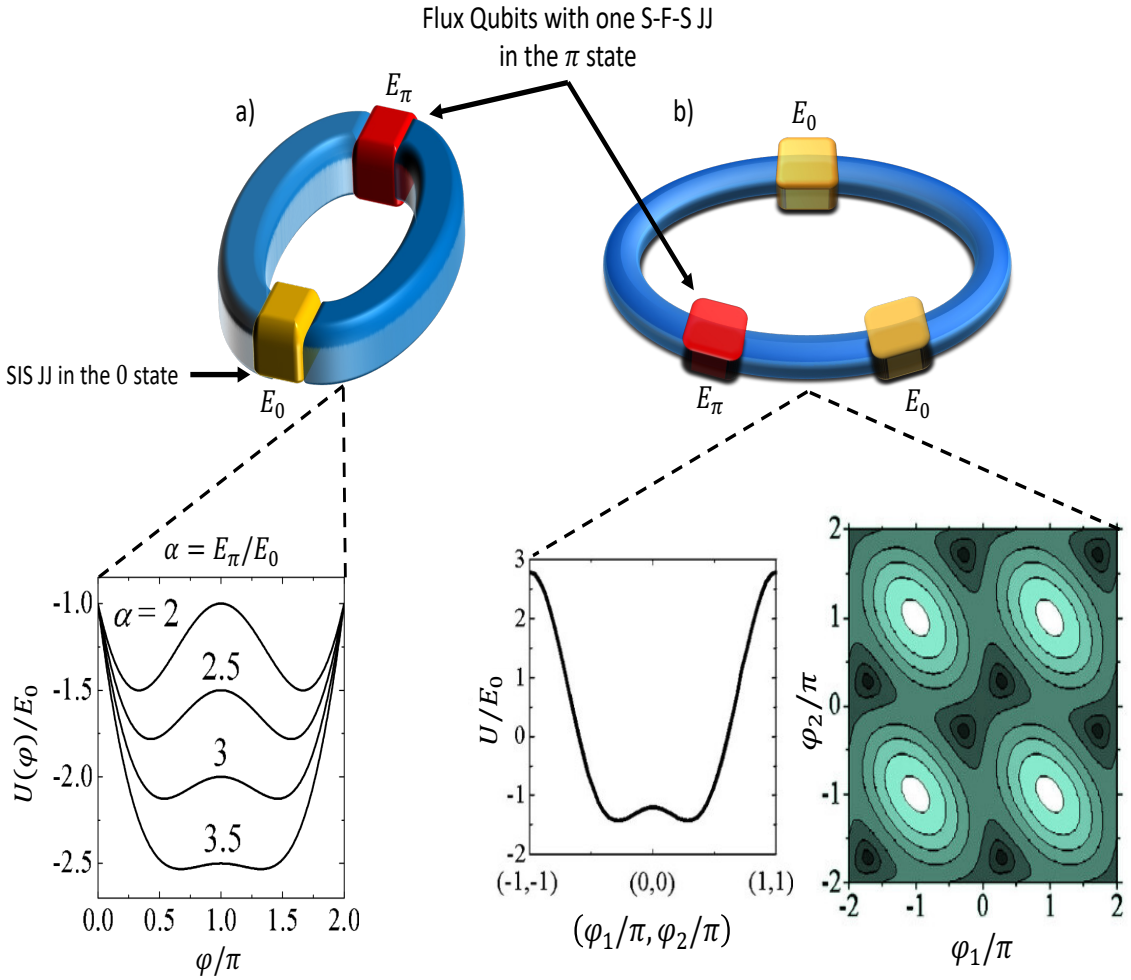

Figure 9: Scheme of the Flux Qubit proposed in Ref.[80] with one conventional SIS JJ in the 0 state and one ferromagnetic π JJ, together with its potential energy configuration $U(\varphi)$ with respect to the 0 JJ phase φ (or flux $\Phi = \Phi_0\varphi/(2\pi)$). By varying the ratio between the energies of π and 0 JJs the barrier between the two minima is modified (a). Scheme of the three JJs Flux Qubit proposed in Ref.[81] with one ferromagnetic π JJ, together with its potential energy U as a function of the two 0 JJs phases φ_1 and φ_2, in the whole phases space and along the φ_1 - φ_2 diagonal (b).

loop), with a considerable improvement for large-scale integration [80, 81].

The desired π-shift can be promisingly implemented in SFS JJs where $0 - \pi$ transitions take place as a consequence of the peculiar nature of proximity effect at the interface between *s-wave* superconductors and ferromagnetic materials [41–44, 48, 50, 51, 58]. Cooper pairs in the S leads are characterized by spin-singlet symmetry, while the exchange field favors the alignment of Cooper pairs spins, thus trying to suppress the superconductivity induced in Ferromagnet (F) [48, 50, 51, 58]. However, superconducting pairing correlations are still possible inside the F layer, since the system reaches a new equilibrium in the *so-called* Fulde - Ferrel - Larkin - Ovchinnikov (FFLO) state, where Cooper pairs with non-zero net momentum can survive [94, 95]. When spin-singlet Cooper pairs enter the ferromagnet the energies of their electrons are, in-

deed, splitted due to the Zeeman interaction with exchange field $h = g\mu_B B$ (where g is the Landé factor in F, μ_B is the Bohr magneton and B is the magnetic field), i.e. $E^{ex}_{\uparrow,\downarrow} = \mp h/2$. Hence, the Cooper pairs electrons acquire a relative momentum $|\vec{q}| = h/v_F$ (with $\hbar = 1$), Fig. 10.

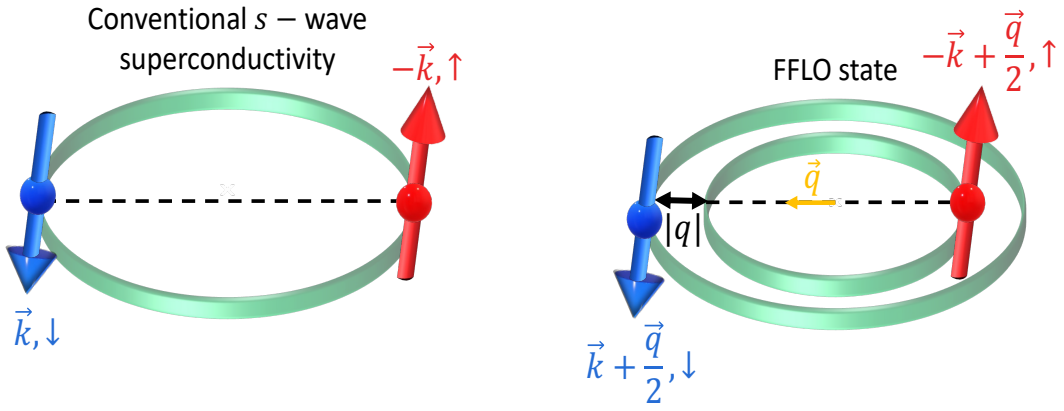

Figure 10: Pictorial representation of Cooper pairs in momentum space in conventional s-wave superconductors and in the FFLO state, figure adapted from Ref.[93].

This reflects in the spatial modulation of the Cooper pairs wave-function inside the F barrier along the direction normal to the SF interfaces [45, 46]. In this case, the pairing function oscillations are superimposed to its exponential decay inside the ferromagnet, yielding

$$\Psi(x) \propto e^{-\frac{x}{\xi_{F1}}} e^{-\frac{ix}{\xi_{F2}}}$$

with ξ_{F1}/ξ_{F2} being the characteristic decay/oscillation length in the ferromagnet, that, in clean limit (low impurities concentration), respectively, read $\xi_{F1} = v_F/(2\pi T)$ and $\xi_{F2} = v_F/(2\pi h)$ (here and in the following $\hbar = k_B = 1$) [45, 51, 59]. As a consequence, also the JJ equilibrium supercurrent (and thus its critical current I_C) is an oscillating function of the F layer thickness d_F, Fig. 11(a). A change in the supercurrent sign can, therefore, occur when d_F equals half-integer multiples of the oscillation period, ξ_{F2}, [45, 96], with the system ground states phase moving from $\varphi = 0$ to $\varphi = \pi$, as the experiment in Ref.[46] testified. The hallmark of a $0-\pi$ transition is a peculiar *cusp-like* trend of the JJ critical current with increasing its F barrier thickness, i.e. $I_C(d_F)$, Fig. 11 (b). Nevertheless, $I_C(d_F)$ measurements do not allow to observe $0-\pi$ transitions in a single JJ, that is bound to be either in the 0 or in π phase. On the other hand, by changing the temperature T and/or the exchange field h we can modify the superconducting coherence length, ξ_{F1}, and/or the spatial period of current oscillations, ξ_{F2}, thus inducing a 0 to π switch in a single Josephson device. The proof of temperature-induced $0-\pi$ transitions was first provided in Ref.[45]. Their results suggest the possibility to realize both the 0 and π phases in a single JJ, where the fingerprint of the $0-\pi$ transition is a *cusp-like* $I_C(T)$ behavior that strongly deviates from the well-known monotonic Ambegaokar-Baratoff (AB) trend for SIS JJs, Fig. 11 (c) [11, 12, 45].

Even though SFS JJs are suitable for achieving $0-\pi$ transitions and π states, these systems are affected by dissipative effects possibly due to the quasiparticles present in

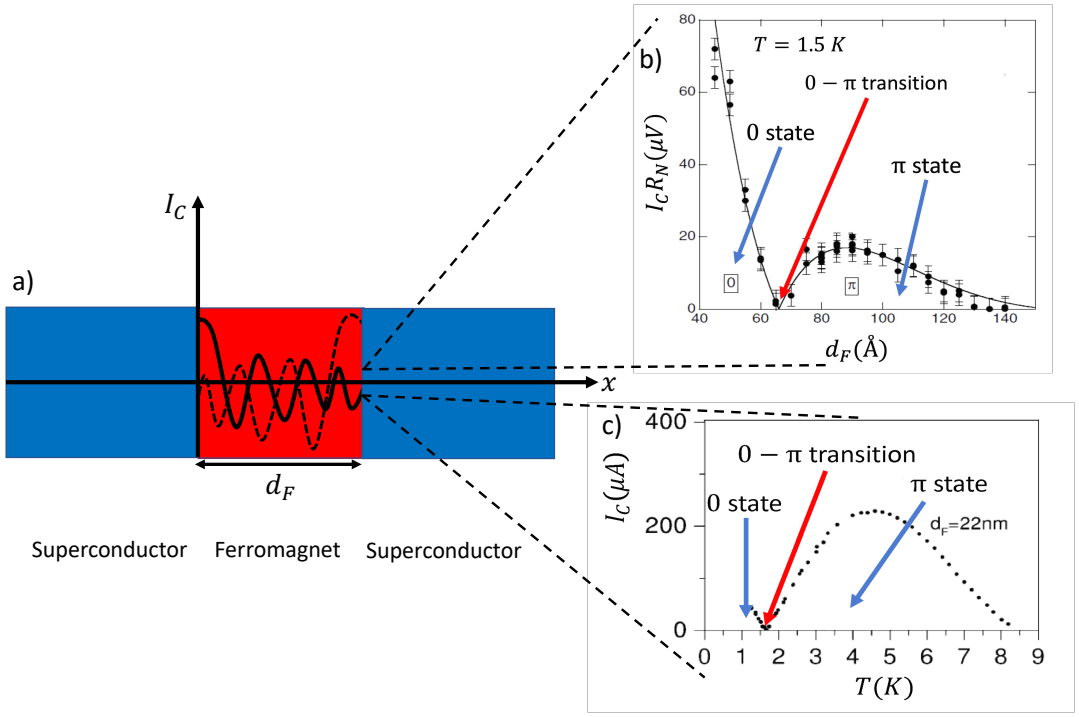

Figure 11: Supercurrent oscillations in SFS junctions (a) that induce a crossover from the 0 to the π state by changing the ferromagnetic layer thickness (b), pictures adapted from Ref.[51] and Ref.[46]. First experimental evidences of temperature induced $0-\pi$ transitions in singe SFS junction (c), picture adapted from Ref.[45].

junctions with normal metal ferromagnets [34, 89], leading to short decoherence times when they are employed in Josephson quantum devices. To overcome this issue, π-JJs with a nonmetallic barrier result to be more suitable for this kind of applications [89], since quasiparticles contribution is sizably reduced in SIS tunnel junctions, even though not negligible [97–102]. As matter of fact, $0-\pi$ transitions in SFIS JJs have been investigated both theoretically [73, 103–105] and experimentally [66, 75, 106–108], and the possibility to reach an equilibrium phase of π has been theoretically predicted also in this case [73, 103–105]. Moreover, experimental evidence of macroscopic quantum tunneling (MQT) phenomena in SFIS JJs [109, 110] has been provided, together with the proof of their hysteretic current-voltage $I(V)$, typical of insulating tunnel JJs [111–116], thus giving promise for their application in quantum hybrid circuits [117].

Spin-triplet supercurrents

If the appearance of opposite-spin triplet pair correlations, with total spin momentum $S = 1$ and spin z-component $S_z = 0$, is automatically predicted when modeling the proximity-induced superconductivity inside the ferromagnet, when considering non-homogeneous exchange field distributions also equal-spin Cooper pairs, characterized by $S = 1$ and $S_z = \pm 1$ ($|1,1\rangle_{S,S_z} = |\uparrow\uparrow\rangle$ and $|1,-1\rangle_{S,S_z} = |\downarrow\downarrow\rangle$), can be found [57–59, 61–72]. On the one hand, opposite-spin triplet pairing correlations, with $|1,0\rangle_{S,S_z} = 1/\sqrt{2}(|\uparrow\downarrow\rangle + |\downarrow\uparrow\rangle)$, are characterized by an oscillating behavior and a fast decay inside

the ferromagnet, as well as spin-singlet wave-function, $|0,0\rangle_{S,S_z} = 1/\sqrt{2}(|\uparrow\downarrow\rangle - |\downarrow\uparrow\rangle)$. Therefore, these cannot be distinguished from spin-singlet correlations by the means of critical current measurements, since they both lead to $0-\pi$ transitions and to the same $I_C(d_F)$ and $I_C(T)$ behaviors, Fig. 12. On the other hand, the spin-aligned triplet Cooper pairs are immune to the exchange field of the F layer, hence their wave-functions decay is slower with respect to to singlet and opposite-spin triplet components and do not show any spatial modulation, Fig. 12. While both equal-spin and opposite-spin components

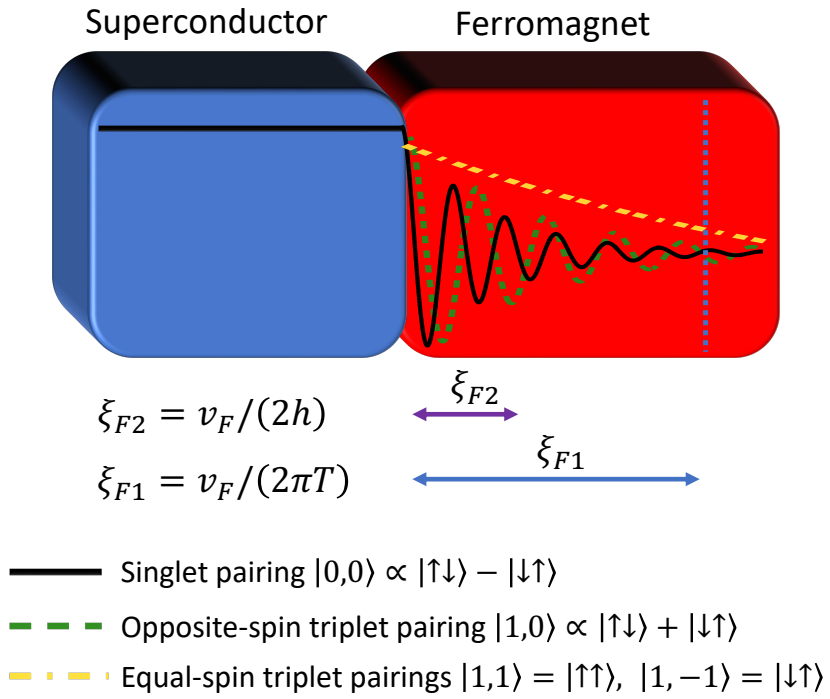

Figure 12: Cooper pairs wave-functions for different spin symmetries at the SF interface. For short F layer, $x < \xi_{F1}$, while spin-singlet and opposite-spin triplet pairing functions oscillate and strongly decay inside F, the equal-spin triplet pairings that are insensitive to the exchange field are only subject to a slow decay. When the F layer thickness increases, $x \gg \xi_{F1}$, both equal-spin and opposite-spin components decay over the thermal decay length, $\xi_{F1} = v_F/(2\pi T)$, as $e^{-x/\xi_{F1}}$. Picture adapted from Ref.[59].

present the same exponential decay on length scales given by $\xi_{F1} = v_F/(2\pi T)$ (in the limit of clean ferromagnets), they show different short-distance decay, respectively proportional to ξ_{F1}/x (i.e. $v_F/(2\pi T x)$) and ξ_{F2}/x (i.e. $v_F/(2hx)$) [59, 60, 65, 72]

$$\Psi_{|0,0\rangle,|1,0\rangle} \propto \left(\frac{v_F}{2hx}\right) \cos\left(\frac{2hx}{v_F}\right) e^{-(2\pi T x)/v_F},$$
$$\Psi_{|1,1\rangle,|1,-1\rangle} \propto \left(\frac{v_F}{2\pi T x}\right) e^{-(2\pi T x)/v_F}.$$

Therefore, for F barrier thickness within the characteristic oscillation length ξ_{F2} and the exponential decay length ξ_{F1}, i.e. $\xi_{F2} < x < \xi_{F1}$, opposite-spin correlations are rapidly reduced while equal-spin ones slowly decrease. On the contrary, for long barriers $x \gg \xi_{F1}$ both components decay as $e^{-x/\xi_{F1}}$, Fig. 12.

Spin-triplet Cooper pairing functions are thus longer-range than spin-singlet and can carry non-dissipative spin currents, thus constituting the essential element for the emerging field of superconducting spintronics [62, 63, 65, 70].

Equal-spin triplet currents can be artificially generated in SF heterostructures with multi-domain ferromagnets or with multiple F layers [58, 59, 65], where the orientation of the exchange field varies along the barrier. Indeed, the spatial change of the spin-quantization axis of the system introduces spin-flipping processes that promote the generation of triplet Cooper pairs. Evidences of spin-polarized supercurrents have been also reported in JJs with magnetically inhomogeneous SF interfaces [58, 65, 67, 70, 72] and in multi-layered ferromagnetic, S-F'-F-F"-S, JJs, where the F', F" spin-mixer layers mediate the conversion of singlet to triplet pair correlations [62–64, 68–71, 113]. Recently, theoretical and experimental studies investigated the role of spin-orbit coupling (Spin - Orbit Coupling (SOC)) [118–124] in combination with a magnetic exchange field in triplet pair generation [73, 125–127]. Other important building blocks of spintronic circuits, in view of maximizing the ratio between spin-polarized and zero-spin currents in JJs, are magnetic insulating barriers with spin-dependent transmission, so-called *spin-filters*, which often consist of multi-layered structures involving thin ferromagnetic films and insulating barriers [67].

Tunnel junctions with ferromagnetic insulator (FI) barriers, made of NbN / GdN / NbN sandwiches, have been proposed to implement spin-filter JJs in a single-layered barrier. In these devices, combining the domain-wall structure of the GdN ferromagnet with its insulating properties, not only are the spin-polarized Cooper pairs available for the transport but the unpolarized supercurrents should be reduced [66, 75, 108, 115, 128–131]. Moreover, macroscopic quantum tunneling has been observed in these SFIS JJs [109], making them especially well-suited for superconducting circuits in which a very low dissipation is required [56, 104, 110, 114, 117]. In particular, in Ref.[75] unconventional *incipient* $0-\pi$ transitions in NbN / GdN / NbN possibly related to the presence of spin-triplet currents have been detected. These peculiar $0-\pi$ transitions are characterized by the presence of a plateau or a non-zero local minimum in the $I_C(T)$, in place of the cusp-like curves typical of SFS $0-\pi$ JJs.

Noise in ferromagnetic junctions

We can consider the problem of noise in ferromagnetic JJs at different levels and thus imagine different analyses that we might carry out to accomplish their noise characterization. First, we may think of the noise contribution that a SFS π JJ would provide, in terms of decoherence, to a superconducting qubit architecture, by considering that noise comes from the coupling between the π JJ and the environment. The impact of π junctions as passive phase shifters in flux qubits architectures [30] in terms of noise and decoherence effects has been theoretically studied by means of Caldeira-Legget model. In Ref.[89], the damped dynamics of the π JJ has been studied within the context of RCSJ model by considering the JJ as coupled to a bosonic bath with a Ohmic dissipation through a shunting resistance R. Then the π JJ noise contribution when it is coupled to an ordinary flux qubit has been analyzed. Although the results indicated that for current density values as in Ref.[53] the qubit dephasing time would be very short, if insulating π JJs with large junction area and large critical current are employed, the

coherence time can be strongly increased [89]. Then, the role of a quasiparticles in SFS and SFIS JJs can be considered, since they constitute one of the most relevant noise sources in superconducting qubits [34, 97–100, 132, 133]. In this respect, ferromagnetic Josephson devices could in principle behave as standard junctions. Indeed, contrary to singlet Cooper pairs, quasiparticles currents are less sensitive to the exchange field of the ferromagnet [79]. As well as it happens for non-magnetic junctions, quasiparticles noise might be reduced even if not disregarded in insulating tunnel barriers [98–100, 133], e.g. SFIS JJs or multi-layered heterostructures with insulating and ferromagnetic materials. The effect of magnetic noise in qubits architectures involving ferromagnetic junctions can be also studied. Recently, a transmon design including one SFIS JJ has been proposed in Refs. [78, 79], where the influence of magnetic flux noise on the JJ and thus on the qubit coherence times has been analyzed. Flux noise due to external field and magnetization fluctuations in F has been taken into account in the case of Ohmic and of $1/f$ spectral density. First estimates of dephasing time due to magnetic noise have been compared with Purcell noise, dielectric losses and quasiparticles noise. Under appropriate conditions, magnetization noise does not constitute a practical limit to the application of SFIS JJs in qubits, if compared with standard quasiparticles dissipation in state-of-the-art architectures [79]. Conversely, an in depth study of the magnetization dynamics inside the F layer of JJs at microscopic scale and of how exchange field fluctuations in F affect the Josephson current is still lacking. Exchange field noise in FI can provide fluctuations of both the critical current I_C (and thus E_J) and current-phase relation $I(\varphi)$, thus leading to dephasing and relaxation processes when the JJ is embedded in qubits circuits [79]. Thus, studying the microscopic properties of magnetic noise sources in SFIS JJs would be a further step toward the noise characterization of ferromagnetic qubits schemes.

On the other hand, we can ask whether $0-\pi$ transitions are themselves a source of current noise amplification in SFS and SFIS junctions. A thorough research on $0-\pi$ current noise is missing. The main target of such investigation would be understanding if at $0-\pi$ transitions the JJ current-noise response to magnetic fluctuations is enhanced. This aspect needs to be clarified in view of the possible integration of tunable $0-\pi$ devices in the superconducting circuitry.

Content of this thesis

We address both the study of $0-\pi$ transitions and spin-triplet currents in SFIS junctions and the current noise characterization of magnetic JJs at the $0-\pi$ transitions. Specifically, by using lattice Green's Function (GF) techniques [73, 134–137], we theoretically investigated the transport properties of SFIS JJs with particular attention to the temperature dependence of the critical current $I_C(T)$, that might be used as a fingerprint of the JJ, and to the spin-resolved pairing correlations. We explored the possibility to tune and control the $0-\pi$ transitions by a direct action on $I_C(T)$. We predicted that combining spin-mixing and disorder effects a temperature stable π state may be achieved [90]. We applied the same techniques to model the $I_C(T)$ behavior of experimental SFIS JJs of Ref.[75], and studied the pairing correlations functions induced inside the FI barrier. We identified a connection between the appearance spin-polarized triplet supercurrents and unconventional *incipient* $0-\pi$ transitions characterized by

non-monotonic $I_C(T)$ curves [91]. In view of a future applicability of ferromagnetic JJs in superconducting circuits, the versatility of lattice GF techniques guarantees an efficient method of studying and possibly designing novel junctions. For example, more complex SF heterostructures might be used to engineer and control spin-triplet currents [91], as well as specific Josephson current features (e.g. in the case of anomalous Josephson Effect [74, 138–144]) or $I_C(T)$ behaviors [90].

Furthermore, we analyzed the static current noise in a magnetic SQDS junction, studying the mechanisms underlying the current noise response to magnetic fluctuations at the $0-\pi$ transitions. We pointed out a current-noise amplification phenomenon linked to the presence of jump-like discontinuities in the Josephson current, $I(\varphi)$, that accompany these phase switchings in short ballistic junctions [92]. On the one hand, our findings on Quantum Dot (QD) JJs could be useful to understand the way $0-\pi$ ferromagnetic JJs react to the presence of exchange field noise and analyze possible solutions to mitigate this effect. On the other hand, this increased sensitivity to magnetic fluctuations might be exploited to infer information about magnetization noise in ferromagnetic JJs and design novel kind of Josephson spin-noise detectors [92].

This thesis is, thus, organized as follows.

- In Chap. 1 we introduce the Nambu-Gor'kov Green's functions for a superconducting system and present the spin-resolved pair correlations. We report the Josephson current calculation in a SQDS JJ and extend it to a 2D JJ. Then, we show how to compute the QD Green's function in the SQDS JJ and illustrate the Recursive Green's Function (RGF) method used in the case of a 2D-lattice barrier.

- In Chap. 2 we use a tight-binding Bogoliubov de Gennes (BdG) approach with the RGF method to study the temperature dependent transport properties of a SFIS JJ. We investigate the possibility to tune and control the $0-\pi$ transitions through a direct action on the junction $I_C(T)$.

- In Chap. 3 we apply the lattice Green's function techniques to model the $I_C(T)$ behavior of experimental NbN/GdN/NbN JJs in Ref.[75] showing unconventional $0-\pi$ transitions. We investigate the symmetries of the pairing correlations induced in the FI GdN barriers.

- In Chap. 4 we study the static current noise in a magnetic SQDS JJ in the presence of magnetic field fluctuations at the $0-\pi$ transitions. Then we explore how to exploit this kind of devices as spin-noise detectors.

Transport in junctions with ferromagnetic insulator barrier (SFIS)

Tight-Binding model and Recursive Green's Function Method

We model the SFIS JJ as 2D tight-binding lattice, Fig. 13, and study the Josephson effect using the BdG approach [73, 90, 135, 136].

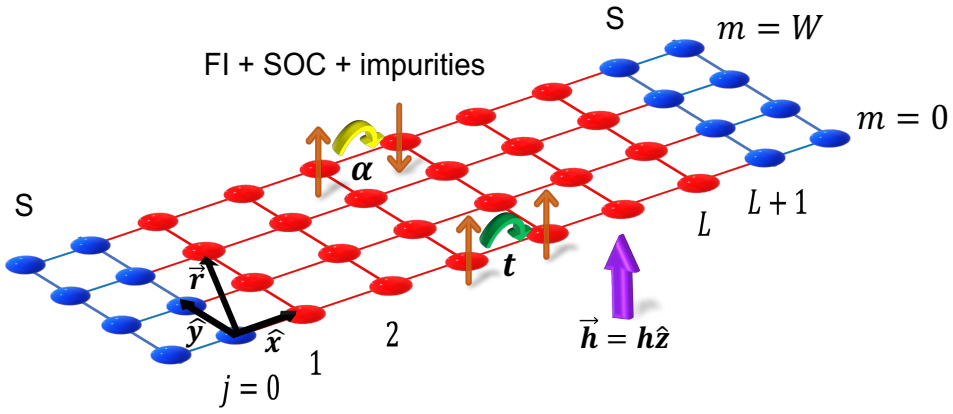

Figure 13: $2D$-lattice model of the SFIS JJ including exchange field, spin-orbit coupling (SOC) and impurities in the barrier. The junction lies in the $x-y$ plane and it is represented by a lattice with $(L+2)$ and W sites along x and y directions, respectively. The influence of the S leads (blue sites) is condensed in the border stripes at $j=0$ and $j=L+1$. The FI barrier (red sites) extends from $j=1$ to $j=L$ along the transport direction, i.e. along x. The exchange field h (violet arrow) is parallel to the z axis, thus perpendicular to the JJ plane. The hopping t between nearest-neighbor sites is here represented by green arrows. The SOC α is depicted by the spin-flipping process highlighted by the yellow arrow.

The proximity effect in SFS junctions has widely been investigated with quasi-classical approaches (i.e. Eilenberger equations, [50, 51, 58, 145–147]), however our approach results to be especially well-suited in the case of short tunnel junctions. Further, a tight-binding description of the junction turns out to be very convenient for modeling the desired interactions in the FI barrier Hamiltonian site by site. In this way, spin-mixing effects, like SOC or non-uniform exchange field patterns, as well as magnetic and non-magnetic impurities, very common in the experimental samples, can be straightforwardly included in the JJ model.

The transport properties, as well as the superconducting pairing correlations are encoded in the barrier GF, and, hence, can be studied by computing the FI layer GF [90]. The latter, in Matsubara representation, is given by $\check{G}_{\omega_n}(\vec{r},\vec{r}\,')$, where $\vec{r}=j\vec{x}+m\vec{y}$ and $\vec{r}\,'=j'\vec{x}+m'\vec{y}$ run over all the possible lattice site indices $j,j'=0,1,\ldots,L,L+1$ and $m,m'=1,\ldots,W$. The barrier GF is, thus, a $4WL\times 4WL$ matrix in the Nambu⊗spin space, whose blocks with fixed $(\vec{r},\ \vec{r}\,')$ can be numerically calculated by solving the Gor'kov equation [3, 4, 73] (its derivation is provided in Appendix A))

$$\left[i\omega_n\check{1}-\sum_{\vec{r}_1}\begin{pmatrix}\hat{H}(\vec{r},\vec{r}_1) & \hat{\Delta}(\vec{r},\vec{r}_1)\\ -\hat{\Delta}^*(\vec{r},\vec{r}_1) & -\hat{H}^*(\vec{r},\vec{r}_1)\end{pmatrix}\right]\times\check{G}_{\omega_n}(\vec{r}_1,\vec{r}\,')=\hat{\tau}_0\hat{\sigma}_0\delta(\vec{r}-\vec{r}\,'),$$

where $\omega_n = (2n+1)\pi T$ is the fermionic Matsubara frequency with T the temperature, while $\hat{H}$ and $\hat{\Delta}$ describe the normal state Hamiltonian and the superconducting interactions inside the barrier (in spin space). Here, $\check{1}$ is the unit matrix in Nambu⊗spin space.

In principle, calculating $\check{G}_{\omega_n}(\vec{r},\vec{r}\,')$ would consist in the inversion of the system Hamiltonian matrix $\check{H}(\vec{r},\vec{r}\,')$

$$\check{H}(\vec{r},\vec{r}\,') = \begin{pmatrix} \hat{H}(\vec{r},\vec{r}\,') & \hat{\Delta}(\vec{r},\vec{r}\,') \\ -\hat{\Delta}^*(\vec{r},\vec{r}\,') & -\hat{H}^*(\vec{r},\vec{r}\,') \end{pmatrix} .$$

For systems with $L \times W$ lattice sites the Hamiltonian ($\check{H}(\vec{r},\vec{r}\,')$) is a $4LW \times 4LW$ matrix. From a computational point of view, the number of operations needed for its inversion scales as $L^3 \times W^3$, thus, making the calculation hard for large size lattices.

We solve the Gor'kov equation for the barrier GF by applying the RGF technique [73, 134–137, 148, 149]. RGF is a numerical technique that allows calculating the Green's function (GF) of a central device when it is connected to two leads. This method is extremely useful if the device GF cannot be computed from the direct inversion of its Hamiltonian, e.g. for very large devices. The RGF is applicable to systems (devices and leads) which are described by lattice models. When dealing with a JJ, the two leads are the superconducting electrodes and the central device is the barrier. RGF method consists in dividing the 2D lattice of the junction along the transport direction in transverse stripes, Fig. 14(a), and recursively calculating the GFs at each stripe of the barrier, starting from the two superconducting leads, Fig. 14(b).

In other words, with this technique we manage to solve the Gor'kov equations for the barrier GF one transverse stripe at a time from one S lead to the other and viceversa. In practice, we divide the FI in L isolated stripes, Fig. 14(a), whose *bare* GF $\check{G}^0_{j,j}$ (for the isolated stripe, not connected to the leads and to adjacent stripes) can be easily computed by direct inversion of their Hamiltonian (tight-binding Hamiltonian of the single stripe) as follows:

$$\check{G}^0_{j,j} = \left[i\omega_n \check{1} - \check{H}^0_{j,j} \right]^{-1} , \tag{1}$$

where $\check{1}$ is the $4W \times 4W$ unit matrix for the stripe j, $\check{H}^0_{j,j}$ is the Hamiltonian of the stripe j, involving only interactions in $\check{H}(\vec{r},\vec{r}\,')$ between lattice sites at the positions $\vec{r} = j\vec{x} + m\vec{y}$ and $\vec{r}\,' = j\vec{x} + m'\vec{y}$, with same index j.

Then, we recursively attach the FI barrier stripes to the leads one after the other, by the means of the hopping matrices $\check{T}^{\pm}$ involving the couplings between lattice sites belonging to adjacent stripes. In this way, we are able to cast a *Dyson-like* equation to compute the *interacting* GF of the stripe j, $\check{G}_{j,j}$, when it is connected to the leads

$$\check{G}_{j,j} = \left[i\omega_n \check{1} - \check{H}^0_{j,j} - \check{T}^- \check{G}^R_{j+1,j+1} \check{T}^+ - \check{T}^+ \check{G}^L_{j-1,j-1} \check{T}^- \right]^{-1} ,$$

where $\check{G}^L_{j-1,j-1}$ and $\check{G}^R_{j+1,j+1}$ indicate the GF of stripes in $j-1$ and $j+1$ when they are connected only to the left and right lead, respectively (see Chap. 1 for more details). We repeat this procedure for all the barrier stripes, $1 < j < L$, until we get the GF of the connected system, Fig. 14(b). Green's function of the stripe j, $\check{G}_{j,j}$, can be visualized

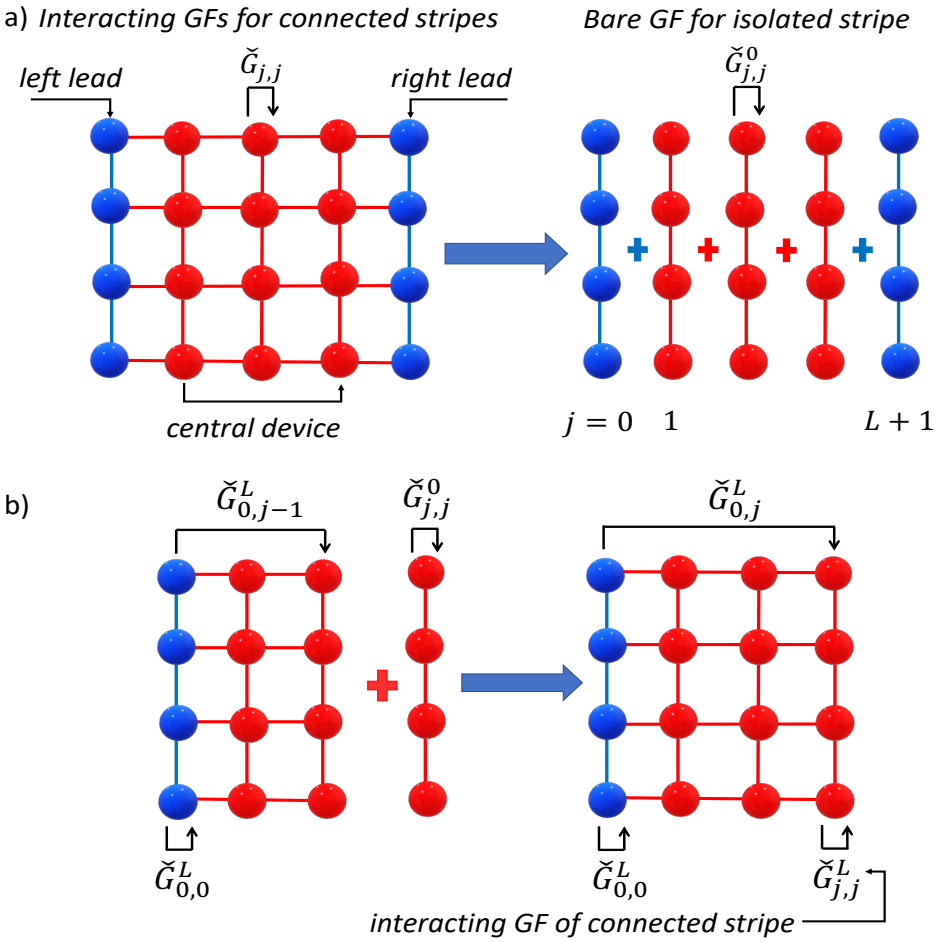

Figure 14: In (a) the schemes representing the system made up of two leads and one central device and its division in transverse stripes are shown. $\check{G}_{j,j}$ is the *interacting* GF of the j-th stripe when connected to the others. $\check{G}^0_{j,j}$ stands for the *bare* GF of the isolated j-th stripe. In (b) the scheme describing how to connect the stripe j to the left lead is presented. The first $j-1$ stripes are already connected. In order to add the stripe j, its interacting GF when it is connected to the previous stripes, $\check{G}^L_{j,j}$, and the one linking it with the left lead, $\check{G}^L_{0,j}$, need to be computed. The same procedure has to be carried out starting from the right lead. Figures adapted from Ref.[90].

as a 2×2 block matrix in the Nambu space, where each block consists in a $2W \times 2W$ sub-matrix:

$$\check{G}_{j,j} = \check{G}_{\omega_n}(\vec{r},\vec{r}') = \begin{bmatrix} \hat{G}_{\omega_n}(\vec{r},\vec{r}') & \hat{F}_{\omega_n}(\vec{r},\vec{r}') \\ -\hat{F}^*_{\omega_n}(\vec{r},\vec{r}') & -\hat{G}^*_{\omega_n}(\vec{r},\vec{r}') \end{bmatrix}, \tag{2}$$

where $\vec{r} = j\vec{x} + m\vec{y}$, $\vec{r}' = j\vec{x} + m'\vec{y}$ with j fixed.

The off-diagonal terms of the matrix in the right-hand side of Eq. 2 are the so-called *anomalous* Green's functions $\hat{F}_{\omega_n}$, that describe the superconducting pair correlations, from which we can derive the four pairing components with s-wave symmetry at each

stripe j:

$$\frac{1}{W}\sum_{\omega_n}\sum_{m=1}^{W}\hat{F}_{\omega_n}(\vec{r},\vec{r}) = \sum_{\nu=0}^{3} f_\nu(j)\hat{\sigma}_\nu \; i\;\hat{\sigma}_2 \;, \tag{3}$$

where f_0 is the spin-singlet component and f_ν with $\nu = 1,2,3$ are the spin-triplet correlations. Analogously, we can compute the GF connecting adjacent stripes $\check{G}_{j,j+1}$ and $\check{G}_{j+1,j}$ entering the Josephson current formula that can be written as

$$J(j,\phi) = -\frac{ie}{2}T\sum_{\omega_n} Tr\left[\hat{\tau}_3 \otimes \hat{\sigma}_0 \left(\check{T}^{+}\check{G}_{j,j+1} - \check{T}^{-}\check{G}_{j+1,j}\right)\right] \;, \tag{4}$$

where $\hat{\sigma}_0$ is the unit matrix in spin space and $\hat{\tau}_3$ is the analogous of Pauli matrix $\hat{\sigma}_3$ in the Nambu space. Further, from the knowledge of $\check{G}_{j,j+1}$ and $\check{G}_{j+1,j}$ we can derive the odd-parity pairs correlation functions in p-wave symmetry.

RGF approach allows us to obtain the junction transport properties, such as CPR and $I_C(T)$ and pairing correlations, from the only knowledge of the S leads GFs, that can be analytically calculated for semi-infinite leads [149, 150] (see Appendix B), and of the barrier Hamiltonian. Interestingly enough, the only assumption of this method is the hypothesis of rigid superconductors [73, 134, 136], hence, it returns the pair correlations in the barrier without the need of assuming specific boundary conditions on the barrier GF at the interfaces with the electrodes. From a computational point of view the RGF technique is much more efficient than calculating the GF of the barrier by direct inversion of its Hamiltonian matrix. With the RGF technique we have to do $2L$ steps in which we invert one $2W \times 2W$ matrix. Hence, the number of operations to do scales as $L \times W^3$, thus gaining a factor L^2 in efficiency with respect to the direct inversion of the Hamiltonian that scales as $L^3 \times W^3$. This makes the calculations simpler also for large size systems.

Tunable $0-\pi$ transitions in SFIS junctions

Tuning the exchange field of the barrier is an available technique to manipulate the JJ critical current, thus driving the switching between 0, $0-\pi$ and π regimes, since modifications in h lead to changes in the oscillation length of the singlet and opposite-spin triplet supercurrents [45, 50, 51]. However, this approach does not provide an easy engineering of ferromagnetic JJs based devices. Indeed, the exchange field is an intrinsic property of the magnetic barrier and, moreover, the current experimental procedures required for its manipulation may induce magnetic noise. For this reason, it would be extremely useful to find alternative and more accessible mechanisms that can be exploited to drive the $0-\pi$ transition in such devices. We recognize spin-mixing effects and lattice impurities as good candidates to approach this kind of task. Spin-orbit coupling has been investigated in previous works [73] to induce the $\pi-0$ transition in SFS JJs. However a thorough study of the SOC effect on the $I_C(T)$ with $0-\pi$ cusps is lacking. On the other hand, while previous works investigated the $0-\pi$ transition induced in SIS JJs by magnetic impurities [40, 151–153], the chance of controlling the $0-\pi$ transition by means of lattice non-magnetic impurities is not yet well explored. In particular, we extend the results in Ref.[73] to the temperature dependence of I_C, by identifying the SOC as a tool to drive the switching between the $0-\pi$ and 0 regime, i.e.

from a cusp-like to an AB $I_C(T)$ curve. On the other hand, we analyze the peculiar role that impurities may have for the $I_C(T)$ manipulation. We show that disorder effects

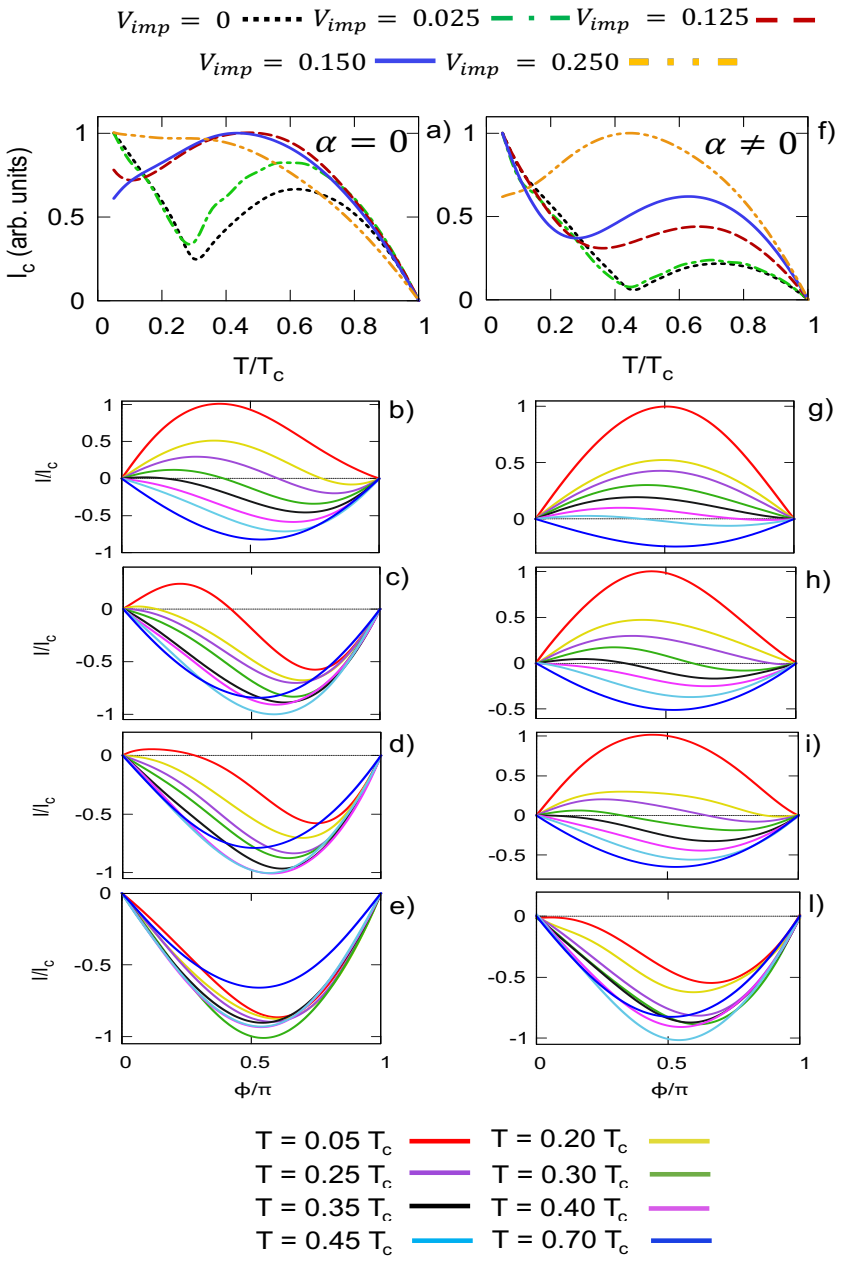

Figure 15: Effect of increasing V_{imp} on temperature-induced $0-\pi$ transitions in the cases without and with SOC (a, f). Corresponding calculated CPRs (b-e, g-l) and formation of π state.

could promote the system moving to the π state at lower temperatures, with respect to to the clean case. This reflects in a temperature broadening of the $0-\pi$ transition that changes the *cusp-like* trend in the $I_C(T)$ in a local minimum. In this respect, we find out the opportunity to reach a temperature stable π regime, starting from a $0-\pi$ JJ, by increasing the strength of the impurity potential. Therefore, a well-defined phase difference of π can be established between the two superconductors separated

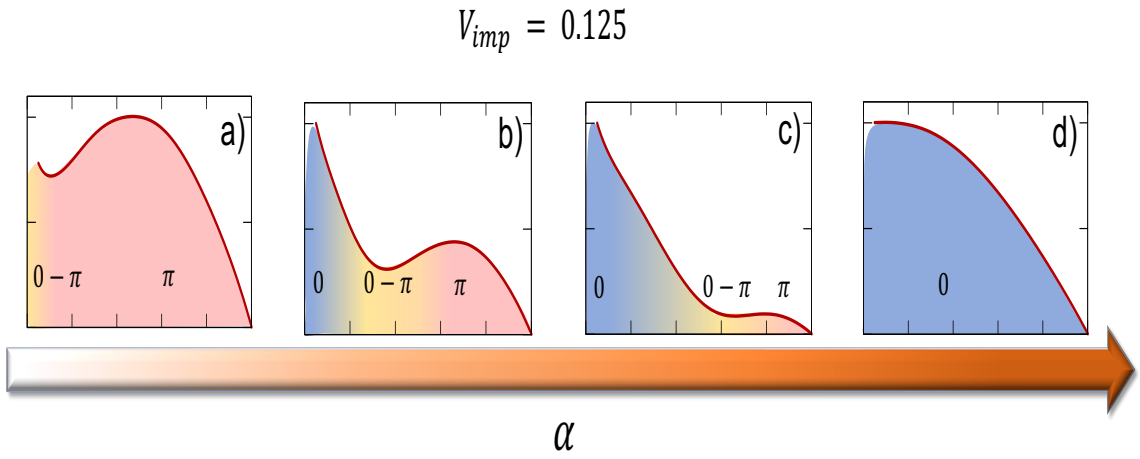

Figure 16: Effect of SOC strength (α) increasing on the $I_c(T)$ behavior, at fixed value of the impurity potential ($V_{imp} = 0.125$).

by a ferromagnetic insulator, which shows great stability over the whole temperature range, Fig. 15.

In addition we present how the interplay between SOC and non-magnetic disorder may be exploited for the engineering of fully tunable $0-\pi$ JJs which can be switched between the 0, $0-\pi$ and π regimes. In principle, by choosing the impurities concentration inside the barrier in order to have a stable π state over a wide range of temperatures, the SOC could be exploited as tuning mechanism, controllable by external means, to move the JJ toward $0-\pi$ and 0 states, Fig. 16. As supplementary analysis we also calculate the correlation functions in these SFIS JJs in the presence of SOC and impurities, both for s-wave and p-wave symmetry (respectively even and odd pairing functions in real space). Indeed, besides the short-range singlet and triplet pairings with total spin projection $S_z = 0$, in our system we also find the equal spin-triplet long-range correlation pairs with total spin projection $S_z = \pm 1$ on the direction of the exchange field, due to the presence of SOC which allows the spin symmetry breaking at S/FI interfaces. In particular, we show that intensifying the impurities strength results in an enhancement of the odd-frequency correlations (i.e. s-wave equal-spin triplet and p-wave singlet, respectively). Therefore, we identify SFIS JJs as sources of unconventional odd-frequency superconductivity and equal-spin triplet pairings when spin-mixing (SOC) and disorder effects are involved [58, 59, 61, 73, 154–160].

Spin-Triplet Transport in SFIS junctions

With the aim of probing the presence of spin-triplet supercurrents in the SFIS JJs and deeply investigating their influence on the JJ current, i.e. on the $I(\varphi)$ and $I_C(T)$, we apply the theoretical techniques of Refs.[73, 90, 135, 136] to analyze the spin pair correlations in NbN/GdN/NbN JJs of Ref.[75] and model their peculiar non-monotonic $I_C(T)$ behavior.

Indeed, although, spin-mixing phenomena generating equal-spin Cooper pairs are very likely to occur in the ferromagnetic-insulating GdN barriers, possibly due to its domain-wall structure, spin-orbit coupling or magnetic impurities, the capability of

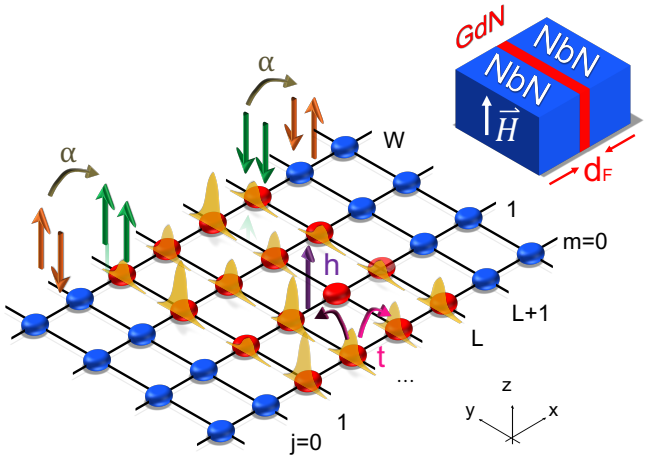

Figure 17: SFIS JJs $2D$-lattice model. The barrier (in red) has a total thickness L along x and width W along y. The spin-mixing mechanism due to SOC is depicted by the spin-flipping process highlighted at the interface between the S leads (blue sites) and the barrier. The impurities, with random strength, are depicted by the height of the yellow potential peaks. The exchange field h (violet arrow) is parallel to the z axis, while the hopping t between nearest-neighbor sites is represented by pink arrows. In the inset, sketch of NbN-GdN-NbN JJs of Ref.[91]. The external magnetic field H is parallel to the z axis, [91]

quantifying the amount of spin-polarized supercurrents remains a fundamental benchmark to prove triplet correlations [91]. In this context, solution of the Gor'kov equation for the real-space barrier Green's function with the RGF method offers a practical way to predict the spatial behavior of the Cooper pairs correlation functions inside the GdN.

Moreover, the tight-binding Bogoliubov de Gennes (BDG) description of the junction allows us to easily include the interactions we assume to generate spin-triplet pairs in the FI Hamiltonian. For the sake of simplicity, in Ref.[91] we assume that the interplay of spin-orbit field in the junction plane (thus perpendicular to the exchange field of the FI) and of non-magnetic impurities effectively mimics the spin-mixing effects occurring in the GdN, Fig. 17. In light of the results in Ref.[90], this choice is also suitable for reproducing the *incipient* $0-\pi$ transitions characterizing the $I_C(T)$ of the experimental samples, Fig. 18.

We successfully reproduce the critical current behavior for the analyzed JJs, where I_C is not completely suppressed at the transition temperature T_π. The simulated CPRs confirm that in all the cases a $0-\pi$ transition broadened in a range of temperatures of the order of some K occurs. The $I_C(T)$ curves show a region in which the I_C is constant in a wide range of temperatures, i.e. it shows a plateau, or alternatively a non-monotonic trend characterized by a non-zero local minimum, i.e. incipient $0-\pi$ transitions [75]. This behavior sets in due to the combined effects of impurities and spin-mixing mechanisms.

Such unconventional $I_C(T)$ behavior turns out to be the benchmark for the coexistence of spin-singlet and spin-triplet superconductivity in SFIS junctions, Fig. 19. When

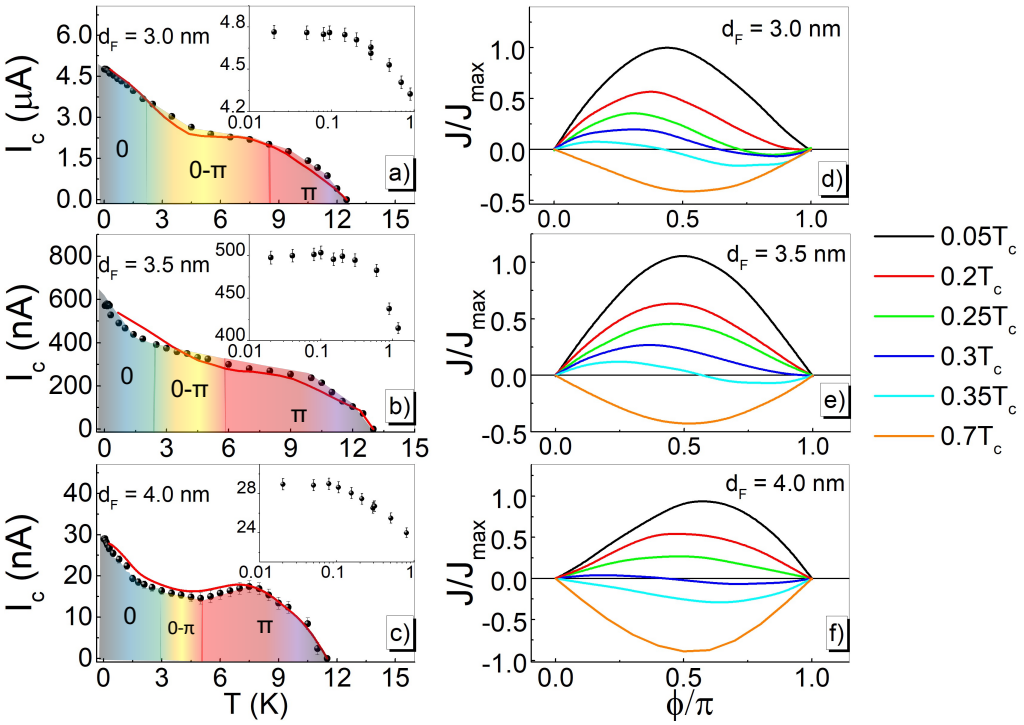

Figure 18: Comparison between the experimental $I_C(T)$ curves, tight-binding BdG simulations and corresponding CPRs. Critical current (black points) for spin-filter junctions with GdN barrier thickness $d_F = 3.0\,\text{nm}$ (a), $d_F = 3.5\,\text{nm}$ (b) and $d_F = 4.0\,\text{nm}$ (c). In the insets of figures (a), (b) and (c): measured saturation of the $I_c(T)$ down to 20 mK. The red lines are $I_c(T)$ curves obtained with the RGF method from the tight-binding BdG Hamiltonian of the barrier. In (d), (e) and (f): CPRs at selected temperatures near the $0-\pi$ transition to highlight the arising of higher order harmonics, compared with those in the 0 and π state, at 0.05 T_c and 0.7 T_c, respectively.

the $I_C(T)$ curve shows a plateau over a wide range of temperatures, the competition between the singlet and triplet pairing amplitudes becomes significant, in both s-wave and p-wave symmetries. When the $I_C(T)$ curve exhibits an incipient $0-\pi$ transition, the equal-spin triplet component is gradually suppressed, becoming irrelevant in the limit case of a more standard cusp-like $0-\pi$ transition. This last situation corresponds to relative low values of disorder and spin-mixing effects.

Magnetic noise in $0-\pi$ Josephson junctions

In the second part of this thesis, we investigate the current noise response of magnetic JJs when $0-\pi$ transitions occur [92]. The main goal of this research activity is to explore whether the $0-\pi$ transitions are accompanied by enhanced current fluctuations and if these are linked to an increased sensitivity to magnetic noise.

To focus our attention on the mechanisms underlying the current noise response to exchange field fluctuations, we consider a simple system consisting of a single-level quantum dot coupled to superconducting leads in the presence of an external magnetic field Fig. 20, i.e. SQDS JJ.

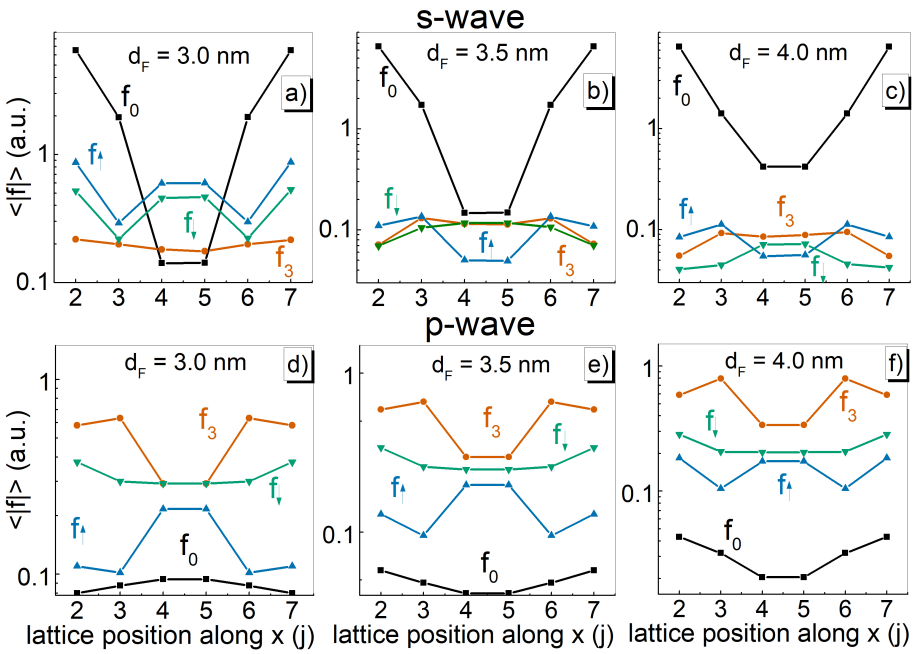

Figure 19: S- and p-wave spin-singlet and triplet pair-correlation amplitudes in the FI barrier. In (a), (b) and (c), the amplitudes of the ensamble average of the s-wave correlation functions $\langle|f|\rangle$, determined by numerical simulations at temperature $T = 0.025\ T_c$, being T_c the critical temperature, are shown as a function of the lattice position in the barrier along the x direction (with index j) for the junctions with GdN thickness $d_F = 3.0,\ 3.5$ and $4.0\,\mathrm{nm}$, respectively. f_0 is the spin-singlet (black line and square symbols), f_3 is the opposite-spin triplet (red line and circles) and $f_\uparrow$ ($f_\downarrow$) is the equal-spin triplet with up (down) S_z projection (respectively, blue line and up-triangle symbols, and green line and down-triangle symbols). In (d), (e) and (f), we show the same correlation functions components for the p-wave symmetry. Data are reported on a log-scale to highlight the gradual suppression of the equal-spin triplet pair-correlation amplitude when pointing towards a non-monotonic critical current vs. temperature $I_c(T)$ curve.

When superconducting pairings are induced on the dot, the supercurrent is carried by only two subgap Andreev Bound States (ABS), each split in two by the Zeeman interaction, and by the continuum quasiparticles spectrum. This makes it particularly straightforward to analyze and distinguish the bound states and quasiparticles contributions to the current noise in this device. Furthermore, by tuning the ratio between the superconducting gap Δ and the hybridization parameter between the dot and the superconducting leads Γ, we can control the quasiparticles current and thus achieve both short and long junction regimes. On top of that, this model allows us to easily visualize how the Andreev levels are modified when a $0-\pi$ transition, driven by the external field, sets in. This leads to a deep understanding of the difference between the JJ current noise close to and away from a $0-\pi$ switching.

In particular, when increasing the external magnetic field the Zeeman splitting between the two spin resolved ABS is enhanced, thus, leading to the appearance of zero-energy crossings of two particle-hole symmetric states in the ABS spectrum. These

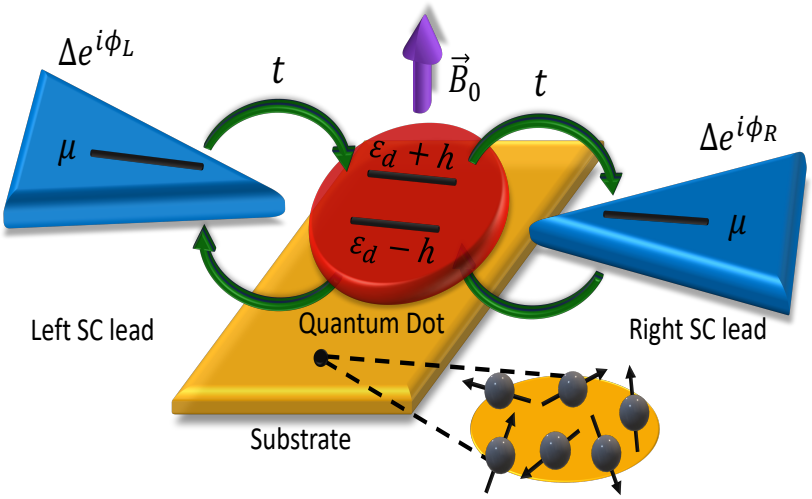

Figure 20: Scheme of the SQDS JJ in the presence of an external magnetic field $\vec{B}_0$. Here, ε_d is the dot energy and $h = g\mu_B|\vec{B}_0|$ is the Zeeman splitting between the two spin channels affecting the dot level when $\vec{B}_0$ is turned on. The two s-wave superconductors are chosen to have equal gap Δ and chemical potential μ. $\phi_{L/R}$ is the superconducting phase of the L/R lead, respectively. t is the amplitude of the hopping integral among the superconducting leads and the dot. A sketch of the fluctuations in the orientation of nuclear spins in the substrate beneath the dot is reported.

crossings accompany the exchange field driven transition of the system from the 0 to the π phase, that is accomplished when the two Andreev levels are completely swapped, Fig. 21. We show that the presence of ABS crossings between particle-hole symmetric levels in this kind of SQDS JJs reflects in the occurrence of sharp jumps in the CPR, from positive to negative currents, at the crossings phases along $0-\pi$ transitions, Fig. 22 [161–166]. Peculiar jump-discontinuities in CPR , well known in ballistic Quantum Point Contact (QPC)s in resonant regime and short ballistic JJs [50, 163, 167–169], have been already predicted in SQDS junctions along the $0-\pi$ switchings [50, 162, 170] and in topological parity transitions [166, 171, 172] also in the presence of Coulomb interaction on the dot [161–163, 165, 166, 170, 172–177], and correspond to a system state characterized by the contemporary presence of two minima in the total energy at $\phi = 0$ and π [50, 162, 163, 170]. We show that CPR jumps are the origin and the hallmarks of noise amplification at Zeeman field induced $0-\pi$ transitions, giving rise to strong current noise response. When analyzing the equilibrium current noise in the presence of magnetic static Gaussian fluctuations, in the small fluctuations regime, current fluctuations $\delta J(\phi)$ can be expanded in terms of the Zeeman field fluctuations δh [178–182]

$$\delta J(\phi, h) \approx \left.\frac{\partial J(\phi, h)}{\partial h}\right|_{\delta h=0} \delta h + \frac{1}{2}\left.\frac{\partial^2 J(\phi, h)}{\partial h^2}\right|_{\delta h=0} \delta h^2 ,$$

yielding the following expression for current variance σ_J^2

$$\sigma_J^2(\phi, h) = \langle \delta J^2(\phi, h) \rangle = \left(\left.\frac{\partial J(\phi, h)}{\partial h}\right|_{\delta h=0}\right)^2 \sigma_h^2 + \frac{1}{2}\left(\left.\frac{\partial^2 J(\phi, h)}{\partial h^2}\right|_{\delta h=0}\right)^2 \sigma_h^4 .$$

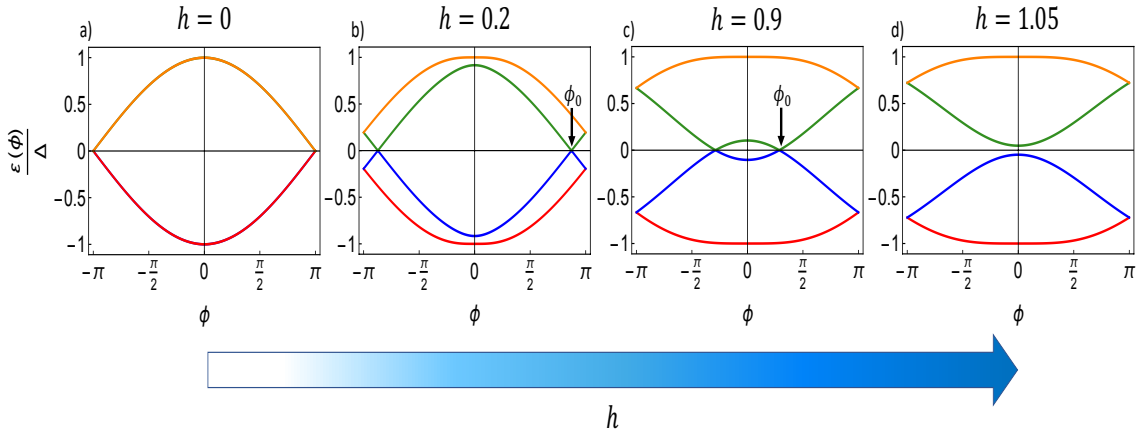

Figure 21: Andreev levels spectrum for the SQDS JJ along a Zeeman field induced $0-\pi$ transition. By increasing the Zeeman splitting between the different spin levels, Andreev Bound States (ABS) crossings at zero energy occur for $\phi = \pm\phi_0 \neq 0, \pm\pi$. Transition between the 0 and π phases is accomplished when the two near-zero ABS are switched.

CPR jumps reflect in δ-like divergences in $\partial_h J(\phi, h)$ and this translates to the appearance of $\sigma_J(\phi)$ peaks at ABS crossings $\phi = \pm\phi_0$.

We identify quasiparticles currents as a possible cause of current noise mitigation in $0-\pi$ JJ, since they do not show jump discontinuities, Fig. 23. This suggests that, in ballistic JJs, there might be a competition between quasiparticles poisoning and $0-\pi$ noise amplification.

Further, also the system temperature T plays a crucial role in smoothening the CPR jumps accompanying magnetic field driven $0-\pi$ transitions and washing out the σ_J peaks even at temperatures of the order of $T \approx 10^{-1} T_C$. In this context, temperature turns out to be a valuable resource as a control knob of sensitivity to magnetic noise in these devices, also in view of their application in superconducting quantum circuits.

On the other hand, although enhanced sensitivity of the current noise response to magnetic fluctuations along the $0-\pi$ transition may constitute a practical limit to employ these devices in quantum circuits, it also represents a unique opportunity to probe the magnetic fluctuations, accessing information about the microscopic noise sources from the junction equilibrium transport properties, thus, inspiring novel kind of Josephson spin-noise detectors.

Indeed, spin-noise spectroscopy exploiting *spin-fluctuations* to extract information about the system spin dynamics represents a promising investigation technique [183]. Specifically, probing the electron spin dynamics we can gain information about the underlying microscopic interactions such as spin-orbit coupling and magnetic disorder [183, 184]. Among the several methods to probe magnetization fluctuations, Faraday rotation spectroscopy, whose working principle consists in measuring spin fluctuations from the Faraday polarization rotation of a linearly polarized light impinging on the sample, deserves to be mentioned [185]. In particular, this method has been successfully applied to study electron-spin dynamics for conduction electrons in bulk GaAs [186] and to extract spin relaxation time and Landé g factor from the spin-noise signal.

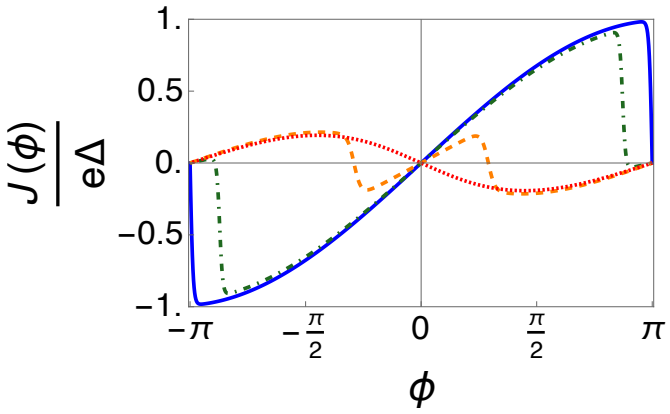

Figure 22: CPR behavior of the SQDS JJ in the resonant tunneling regime (at $\varepsilon_d = 0$, $\Delta = 0.01$, $\Gamma = 1$ and $T = 0.02\, T_C$) computed along the Zeeman induced $0-\pi$ switching at $h = 0$ (blue solid curve), $h = 0.2$ (green dot-dashed curve), $h = 0.9$ (orange dashed curve) and $h = 1.05$ (red dotted curve), respectively. Along the $0-\pi$ transition the JJ shows peculiar CPR jump discontinuities at the ABS crossings.

In Ref.[187], electrons and holes g factors have been derived for localized states in semiconductor (In, Ga)As/GaAs QDs from the measured magnetic fluctuations. Similarly, in view of having more compact experimental on-chip setups, SQUID-based magnetometry [6, 7] has been recognized as a valuable tool to measure magnetic field fluctuations in spin glasses [188, 189] and superconductors [190] with the sample being placed close to a dc-SQUID circuit [183].

Our proposal consists in exploiting the magnetic field dependence of Andreev tunneling characterizing Josephson effect in ballistic QPCs [161–165, 167, 168, 170, 172–177, 191–197] to detect spin fluctuations. Indeed, when the dot is tuned in resonance with the superconducting leads, the SQDS JJ appears to be much more sensitive to spin rather than charge noise (i.e. dot energy fluctuations), thus implying that, under appropriate conditions, the supercurrent noise fluctuations can be directly related to spin noise. In this scenario, the enhanced current noise sensitivity to magnetic field fluctuations of SQDS JJs, along the $0-\pi$ transitions, might be used to probe microscopic spin-noise sources and magnetization fluctuations in the ferromagnets employed as barriers in SFS and SFIS junctions for superconducting qubits [73, 75, 78–81, 86, 90, 91, 109]. Furthermore, the investigation of noise in these systems underlies the possibility to simultaneously highlight material specific features, such as the decay time of spin-spin correlations. Interestingly enough, our work might be relevant also to model noise in a Josephson junction through a Yu-Shiba-Rusinov state, recently realized by Karan et al. [198], and the oscillations of Gilbert damping, recently revealed by Yao et al. in ferromagnetic Josephson junctions [199].

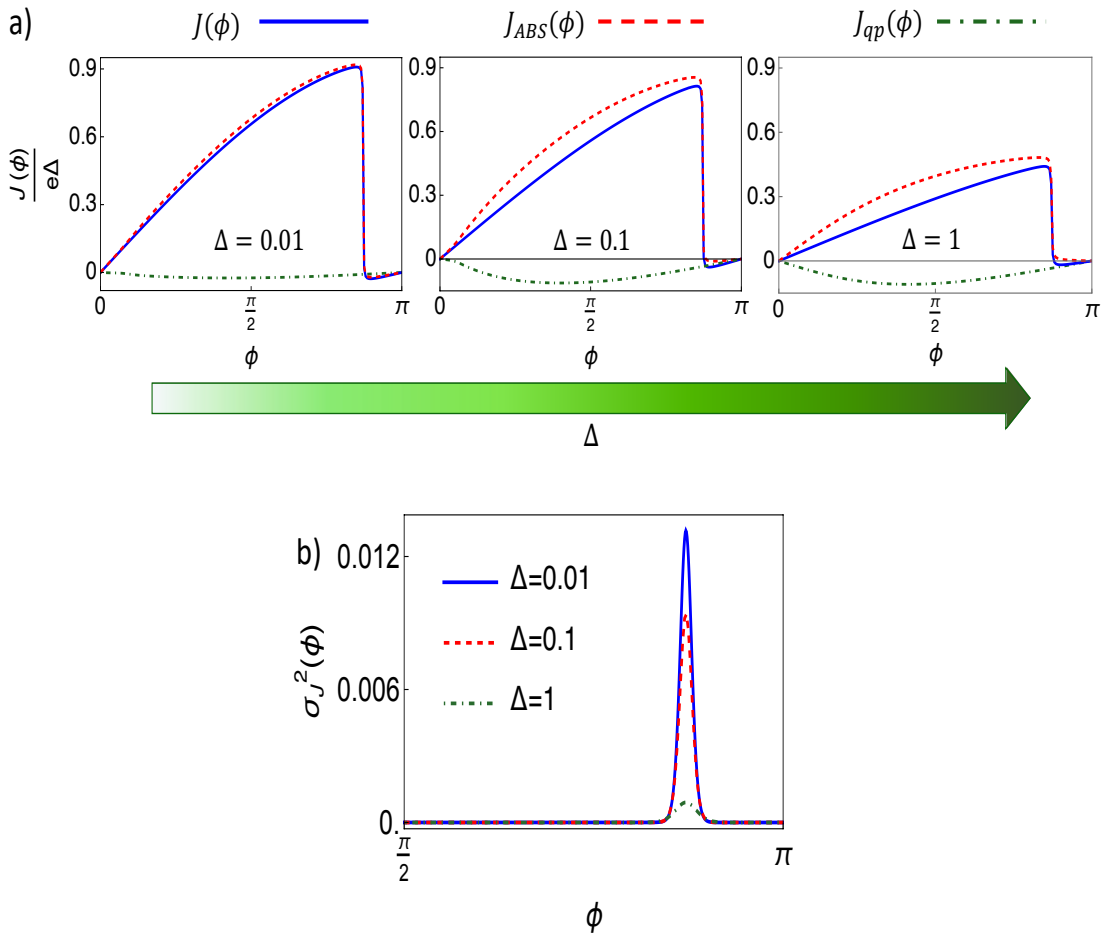

Figure 23: In the upper panel (a) the current-phase relation (blue solid lines) together with the relative current contributions of ABS (red dashed lines) and quasiparticles (green dot-dashed lines), computed at different values of the superconducting gap Δ, expressed in unity of Γ ($\Gamma = 1$ and $T = 0.02\,T_C$), are respectively shown. In the lower panel (b) the corresponding current variance curves $\sigma_J(\phi)$ are reported. As long as the system is in the short junction limit, i.e. $\Delta \ll \Gamma$, quasiparticles current remains negligible, while it reaches the same order of magnitude of the current carried by Andreev levels when Δ approaches Γ. Reduction of CPR jumps due to quasiparticles current leads to strong attenuation of the current noise peaks at the ABS crossings, when the JJ exits the short-junction regime

Chapter 1

Transport Properties of Josephson junctions

In this chapter, we discuss how to investigate the transport properties of Josephson junctions within the Green's functions formalism. First, we introduce the Nambu-Gor'kov Green's function formalism to describe superconductivity. We show that the Nambu-Gor'kov Green's function of the barrier encodes important information about the junction transport properties such as the subgap bound states (Andreev levels) [92] and spin-resolved pairs correlations [90, 91]. We provide the derivation of the Josephson current formula in the case of the SQDS junction and extend it to the case of 2D lattice models for JJs with finite size barriers. We show that the knowledge of the *interacting* barrier Green's function, when it is connected to the S leads, is necessary to calculate the current flowing through the junction ($J(\phi)$). Therefore, we specify our discussion to the calculation of the barrier GF in both the SQDS and in SFIS junctions. In the first case we derive the *interacting* dot GF in the Matsubara formalism by the means of perturbation theory. In the second case, we introduce the Recursive Green's function (RGF) method that allows us to calculate the barrier GF even for large-size systems.

1.1 Nambu-Gor'kov formalism

In the framework of the BCS theory, Hamiltonian for a conventional superconductor has the following form (in momentum space, $\vec{k}$) [1–7]:

$$H_{BCS} = \sum_{\vec{k}\sigma} \varepsilon_{\vec{k}} c^{\dagger}_{\vec{k}\sigma} c_{\vec{k}\sigma} + \sum_{\vec{k}} \left[\Delta^* c_{-\vec{k}\downarrow} c_{\vec{k}\uparrow} + c^{\dagger}_{\vec{k}\uparrow} c^{\dagger}_{-\vec{k}\downarrow} \Delta \right] + \frac{V}{g} \Delta^* \Delta. \tag{1.1}$$

Here V is the volume of the system, g electron-electron attractive potential due to the electron-phonon scattering and Δ is the superconducting gap, i.e. the complex order parameter, which has to be determined self-consistently [1–7].

The Hamiltonian in Eq. 1.1 can be diagonalized using the *Bogoliubov* transformations

$$\begin{aligned} \gamma^{\dagger}_{\vec{k}0} &= u_{\vec{k}} c^{\dagger}_{\vec{k}\uparrow} - v_{\vec{k}} c_{-\vec{k}\downarrow} \\ \gamma^{\dagger}_{\vec{k}1} &= u_{\vec{k}} c_{\vec{k}\uparrow} + v_{\vec{k}} c^{\dagger}_{-\vec{k}\downarrow}, \end{aligned} \tag{1.2}$$

where by conventional choice

$$u_{\vec{k}}^2 = \frac{1}{2}\left(1 + \frac{\varepsilon_{\vec{k}}}{E_{\vec{k}}}\right), \quad v_{\vec{k}}^2 = \frac{1}{2}\left(1 - \frac{\varepsilon_{\vec{k}}}{E_{\vec{k}}}\right), \tag{1.3}$$

with $E_{\vec{k}} = \varepsilon_{\vec{k}} + \Delta$. Using this change of basis in Eq. 1.1 yields the diagonal Bogoliubov Hamiltonian [3–5]:

$$H_B = \sum_{\vec{k}} \sqrt{\varepsilon_{\vec{k}}^2 + \Delta^2}\left[\gamma_{\vec{k}0}^\dagger \gamma_{\vec{k}0} + \gamma_{\vec{k}1}^\dagger \gamma_{\vec{k}1}\right] + \mu\,, \tag{1.4}$$

where μ is the ground state energy of the Bogoliubov superconductor, that is often chosen equal to its chemical potential in the normal state. Note that Bogoliubov annihilation γ and creation $\gamma^\dagger$ operators, respectively, annihilate and create quasiparticles without definite charge, thus they coherently mix quasielectron and quasihole excitations.

Hence, to describe the Bogoliubov quasiparticle excitations is very useful to introduce the charge analogue of the electron spinors, the *Nambu* spinors [3–5]:

$$\Psi_{\vec{k}} = \begin{pmatrix} c_{\vec{k}\uparrow} \\ c_{-\vec{k}\downarrow}^\dagger \end{pmatrix}, \qquad \Psi_{\vec{k}}^\dagger = \left(c_{\vec{k}\uparrow}^\dagger,\ c_{-\vec{k}\downarrow}\right). \tag{1.5}$$

In this formalism, the first and the second components of the Nambu destruction operator ($\Psi_{\vec{k}}$) respectively destroy an electron in the state ($\vec{k}\uparrow$) and a hole in the state ($-\vec{k}\downarrow$).

We can introduce the field operators in real space, thus obtaining the Nambu field operators [4, 73, 136]

$$\Psi(\vec{r}) = \begin{pmatrix} \psi_\uparrow(\vec{r}) \\ \psi_\downarrow^\dagger(\vec{r}) \end{pmatrix}, \ \Psi^\dagger(\vec{r}) = \left(\psi_\uparrow^\dagger(\vec{r}),\ \psi_\downarrow(\vec{r})\right) \tag{1.6}$$

From the Nambu operators we can define the *Nambu-Gor'kov Green's function* as follows:

$$\check{G}(\vec{r}, t, \vec{r}', t') = -i\big\langle T(\Psi(\vec{r}, t)\,\Psi^\dagger(\vec{r}', t'))\big\rangle \tag{1.7}$$

where T is the time-ordering operator and the brackets $\langle\ \rangle$ denote the thermal average $\langle O\rangle = Tr\left(e^{-H/(k_B T)}O\right)$ (where H is the Hamiltonian of the system). This Green's function takes the form of a 2×2 matrix in the particle-hole space (Nambu space):

$$\check{G}(\vec{r}, t, \vec{r}', t') = \begin{bmatrix} G_1 & F_1 \\ F_2 & G_2 \end{bmatrix} \tag{1.8}$$

where its elements are respectively

$$G_1 = G_{\uparrow\uparrow}(\vec{r}, t, \vec{r}', t') = -i\big\langle T\left(\psi_\uparrow(\vec{r}, t)\,\psi_\uparrow^\dagger(\vec{r}', t')\right)\big\rangle, \tag{1.9}$$

$$G_2 = G_{\downarrow\downarrow}^\dagger(\vec{r}, t, \vec{r}', t') = -i\big\langle T\left(\psi_\downarrow^\dagger(\vec{r}, t)\,\psi_\downarrow(\vec{r}', t')\right)\big\rangle, \tag{1.10}$$

$$F_1 = F_{\uparrow\downarrow}(\vec{r}, t, \vec{r}', t') = -i\big\langle T\left(\psi_\uparrow(\vec{r}, t)\,\psi_\downarrow(\vec{r}', t')\right)\big\rangle, \tag{1.11}$$

$$F_2 = F_{\downarrow\uparrow}^\dagger(\vec{r}, t, \vec{r}', t') = -i\big\langle T\left(\psi_\downarrow^\dagger(\vec{r}, t)\,\psi_\uparrow^\dagger(\vec{r}', t')\right)\big\rangle. \tag{1.12}$$

The diagonal elements of $\check{G}$ matrix represent respectively the particle-particle and the hole-hole propagator and they are called *normal Green's functions* $G(G^{\dagger})$. The off-diagonal elements of $\check{G}$ matrix represent respectively the particle-hole and the hole-particle propagators and they are called *anomalous Green's functions* F $(F^{\dagger})$. Hence, the anomalous Green's functions can be regarded as the Cooper pairs' correlations (condensate Green's function).

Pair correlations and their symmetries

In the case of a BCS superconductor, the only Cooper pairs' correlations allowed are the zero-spin singlet correlations.
In the presence of exchange field or other interactions that provide spin mixing effects, e.g. spin-orbit coupling, the Green's functions G and F in the Nambu-Gor'kov $\check{G}$ matrix become non trivial 2×2 matrices in the spin space ($\hat{G}$ and $\hat{F}$) that read [73, 136]

$$\check{G}\left(\vec{r}, t, \vec{r}', t'\right) = \begin{bmatrix} \hat{G} & \hat{F} \\ -\hat{F}^{*} & -\hat{G}^{*} \end{bmatrix} \tag{1.13}$$

For example, if the exchange field h is homogeneous, the $\hat{F}$ matrix (also called Pair Correlations' matrix) is an off-diagonal matrix and can be represented in the form [73]:

$$\hat{F} = f_0 \hat{\sigma}_0 i\hat{\sigma}_2 + f_3 \hat{\sigma}_3 i\hat{\sigma}_2. \tag{1.14}$$

Here, f_0 is the amplitude of the singlet component of the Cooper pairs' correlations matrix while f_3 is the zero-spin triplet component, $\hat{\sigma}_i$ are the Pauli matrices in the spin space.
In the real time representation the singlet and zero-spin triplet correlations have the following form:

$$\begin{aligned} f_0 \sim & \left\langle T\left(\psi_{\uparrow}\left(\vec{r}, t\right) \psi_{\downarrow}\left(\vec{r}', 0\right)\right)\right\rangle - \left\langle T\left(\psi_{\downarrow}\left(\vec{r}, t\right) \psi_{\uparrow}\left(\vec{r}', 0\right)\right)\right\rangle \\ f_3 \sim & \left\langle T\left(\psi_{\uparrow}\left(\vec{r}, t\right) \psi_{\downarrow}\left(\vec{r}', 0\right)\right)\right\rangle + \left\langle T\left(\psi_{\downarrow}\left(\vec{r}, t\right) \psi_{\uparrow}\left(\vec{r}', 0\right)\right)\right\rangle. \end{aligned} \tag{1.15}$$

When also spin-mixing interactions are present, also the spin-aligned triplet components appear in the Pair Correlations' matrix $\hat{F}$

$$\begin{aligned} f_{\uparrow\uparrow} \sim & \left\langle T\left(\psi_{\uparrow}\left(\vec{r}', t\right) \psi_{\uparrow}\left(\vec{r}', 0\right)\right)\right\rangle \\ f_{\downarrow\downarrow} \sim & \left\langle T\left(\psi_{\downarrow}\left(\vec{r}, t\right) \psi_{\downarrow}\left(\vec{r}', 0\right)\right)\right\rangle. \end{aligned} \tag{1.16}$$

In the Matsubara representation, the $\hat{F}$ matrix can be expressed in terms of the Cooper pairs' correlation functions as [73]

$$\hat{F}_{\omega_n}\left(\vec{r}, \vec{r}'\right) = \sum_{\nu=0}^{3} f_{\nu}(\vec{r}, \vec{r}') \hat{\sigma}_{\nu} i\hat{\sigma}_2 \tag{1.17}$$

where $\omega_n = \pi T(2n+1)$ (with T as the temperature) is the Matsubara frequency, $f_1$and f_2 are the spin-aligned triplet components of the anomalous Green's function $\hat{F}$. In the

matrix form of the Eq. 1.17, the spin aligned components appears as diagonal elements while the opposite spin components are the off-diagonal elements.

$$\hat{F} = \begin{pmatrix} f_{\uparrow\uparrow} & f_{\uparrow\downarrow} \\ f_{\downarrow\uparrow} & f_{\downarrow\downarrow} \end{pmatrix} = \begin{bmatrix} if_2 - f_1 & f_3 + f_0 \\ f_3 - f_0 & if_2 + f_1 \end{bmatrix} \tag{1.18}$$

Pauli exclusion principle requires the Cooper pairs wave-function to be totally anti-symmetric. This constraint reflects also on the symmetry properties of pair correlations in Matsubara formalism. Indeed, among all the combinations of momentum (space), spin and frequency (time) symmetries only those which yield pairing correlations with an overall odd symmetry are allowed. Some insights about the symmetries in momentum and frequency can be gained by considering, for example, spin-triplet correlations, e.g. f_3 or $f_{\uparrow\uparrow/\downarrow\downarrow}$. These are even symmetry in spin domain, therefore they can be either odd in momentum and even in frequency or even in momentum and odd in frequency. If we consider spin-triplet correlations with odd orbital (momentum) symmetry, e.g. p-wave, they must have even-frequency symmetry. On the contrary if these are even orbital symmetry, e.g. s-wave symmetry, they must be odd-frequency functions. From a more physical point of view, we can say that, when the orbital part is odd the Cooper pairs electrons avoid each other in space, while an odd frequency symmetry implies that electrons avoid each other in time. Similar considerations can be applied to spin-singlet correlations. We summarize these results in Tab. 1.1 [59].

Spin	Momentum	Frequency	Overall symmetry
Singlet (odd)	Even	Even	Odd
Singlet (odd)	Odd	Odd	Odd
Triplet (even)	Odd	Even	Odd
Triplet (even)	Even	Odd	Odd

Table 1.1: Spin, momentum and frequency symmetries in Cooper pairs. Requirement of Pauli exclusion principle on the overall odd symmetry of pairing correlations has to be fulfilled. Table adapted from [59].

Andreev levels from Nambu-Gor'kov Green's function

Dynamics of Nambu-Gor'kov GF is governed by the Gor'kov equation of motion for $\check{G}$, whose derivation is provided in Appendix A, that in the Matsubara representation reads

$$\left[i\omega_n \hat{\tau}_0 \hat{\sigma}_0 - \int d\vec{r}_1 \begin{pmatrix} \hat{H}(\vec{r},\vec{r}_1) & \hat{\Delta}(\vec{r},\vec{r}_1) \\ -\hat{\Delta}^*(\vec{r},\vec{r}_1) & -\hat{H}^*(\vec{r},\vec{r}_1) \end{pmatrix} \right] \times \check{G}(\vec{r}_1,\vec{r}') = \hat{\tau}_0\hat{\sigma}_0\delta(\vec{r}-\vec{r}'), \tag{1.19}$$

where $\hat{H}$ is the normal state Hamiltonian of the system and $\hat{\tau}_j$ with $j = 0-3$ are the unit and Pauli matrices in the particle-hole space, respectively. Solution of Gor'kov GF allows, in principle, to study the superconducting properties of every material starting from the knowledge of the pairing mechanisms involved, i.e. of $\hat{\Delta}(\vec{r},\vec{r}')$, regardless of the origin of superconductivity. It is thus extremely useful to study proximity effect in normal materials in contact with superconductors and, more generally, JJs. We have

already shown how symmetry properties of the pair correlations can be derived inside the barrier of a JJ from its anomalous GF, as in Eq. 1.17-1.18.

However, Nambu Gor'kov GF of the barrier encodes other important information about the system transport properties, such as the Andreev bound states ABS of the junction. Andreev levels constitute the discrete part of the energy spectrum of a JJ and lie within the superconducting gap of the leads, i.e. $\varepsilon < \Delta$, while above-gap quasiparticles excitations represent the continuum part (here we assume leads with equal order parameter Δ). Andreev levels can be calculated from the poles of the barrier GF, that is by solving the following secular equation

$$\det\left[z\hat{\tau}_0\hat{\sigma}_0 - \int d\vec{r}_1 \begin{pmatrix} \hat{H}\left(\vec{r},\vec{r}_1\right) & \hat{\Delta}\left(\vec{r},\vec{r}_1\right) \\ -\hat{\Delta}^*\left(\vec{r},\vec{r}_1\right) & -\hat{H}^*\left(\vec{r},\vec{r}_1\right) \end{pmatrix}\right] = 0\,, \tag{1.20}$$

where we perform the analytic continuation of Matsubara frequency ω_n to the complex plane, i.e. $i\omega_n \to z$. Through ABS supercurrent can flow across the junction by the means of *Andreev reflection* processes at the interfaces between the S leads and the barrier. Andreev reflection is a process involving electrons impinging on a Normal Metal - Superconductor (NS) interface, Fig. 1.1. It consists in the back reflection of a electron of charge $-e$ coming from the N side as a hole of charge $+e$ while a Cooper pair of charge $-2e$ is generated in the superconductor. In the case the energy of the

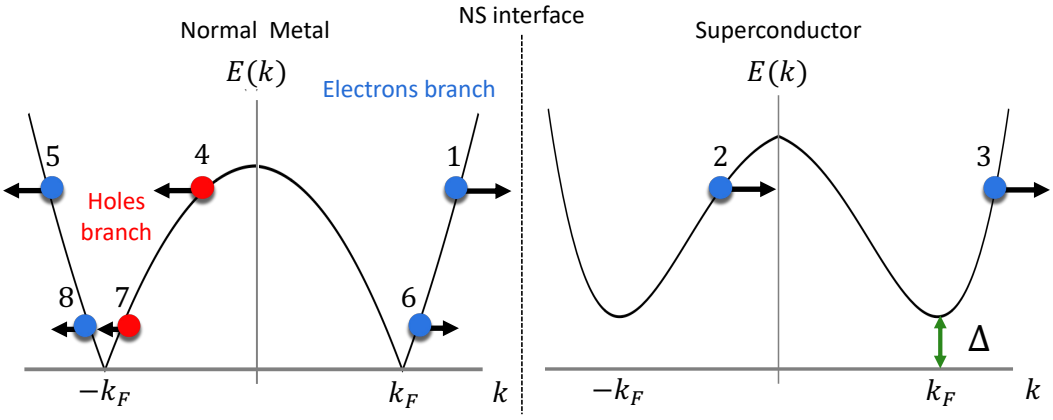

Figure 1.1: Schematic diagram of excitation spectra E_k at NS interface. An incident electron at (1), with energy $E > \Delta$, can be transmitted in the superconductor at (2,3) or be reflected back as a hole at (4) or as an electron at (5). In particular, the reflection from (1) state to (4) state is an Andreev reflection of the electron as a hole of opposite momentum. An electron impinging on NS at (6), with energy $E < \Delta$, can only be reflected in (8) or undergo Andreev reflection at (7), since there are no subgap states available for transmission in S. Adapted from Ref.[200].

electron exceeds the energy gap Δ, the probability of having an Andreev reflection is rather small. Nevertheless, incident electrons with energy lower than the Δ can only be reflected back at NS either as an electron or as a hole, hence, the probability of Andreev reflection becomes sizable.

In Superconductor - Normal Metal - Superconductor (SNS) JJs, by the means of two Andreev reflections, a supercurrent can be carried through the junctions. Let us

consider, for the sake of simplicity, only the current flowing from the left superconductor to the right lead Fig. 1.2. When a Cooper pair in the left superconductor reach the left

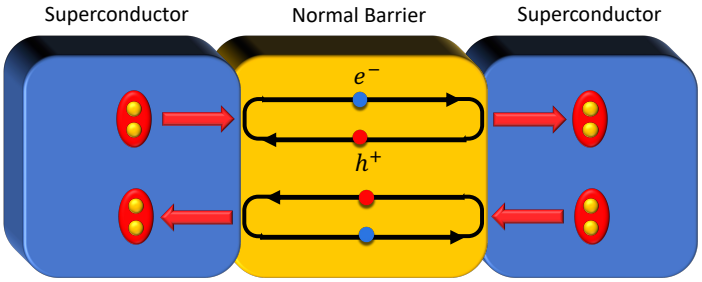

Figure 1.2: Scheme of the Andreev reflection in a SNS JJ. The blue points are the electrons, the red points are the holes and the Cooper pair are in red and yellow.

interface a hole, coming from N "annihilates" one of the two electrons of the pair, this resulting in a transmitted electron $e-$ in the barrier. This electron is then reflected back as a hole $h+$ at the other interface while at the same time a Cooper pair is transmitted in the right superconductor. In this way supercurrent can be sustained in SNS JJs. This effect can be also seen as a constructive interference between the electron like and

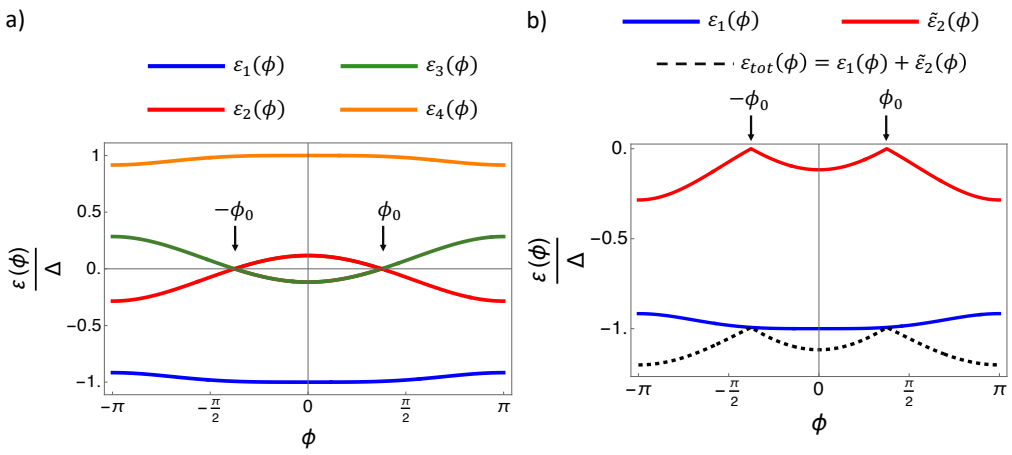

Figure 1.3: Example of Andreev levels crossings for the SQDS JJ in an external magnetic field analyzed in Chap. 4 (a). Andreev levels that effectively carry the supercurrent through the SQDS JJ and its total energy state (b).

the hole like excitations, in the normal region, giving rise to subgap Andreev bound states [6, 46, 200]. By the means of the SNS the supercurrents propagates from one superconducting lead to the other. For the sake of clarity we report, in Fig. 1.3 (a), an example of ABS spectrum for the single level quantum dot junction analyzed in Chap. 4, SQDS JJ.

The ABS that effectively carry current through the junction are the ones with negative energy, i.e. below the chemical potential of the leads μ, Fig. 1.3(b). Under specific conditions only the Andreev levels contribute to the Josephson current with the quasiparticles currents that, at low temperature, can be disregarded. This is the case of short junctions in the ballistic transport regime, characterized by the fact that the

superconducting coherence length ξ is much larger then the barrier thickness L, i.e. $\xi \gg L$, which has to be much shorter than the mean free path of electrons l, i.e. $l \gg L$. For short ballistic junctions, the current flowing through the JJ, $J(\phi)$, can be simply written as the derivative of the total junction energy, defined as the sum of the negative energy Andreev levels, Fig. 1.3(b), with respect to the JJ phase ϕ [167, 168, 192, 201, 202]

$$J_{ABS}(\phi) = \sum_{j,\,\varepsilon \leq 0} \frac{\partial \varepsilon_j(\phi)}{\partial \phi}. \tag{1.21}$$

1.2 Josephson current formula

In this section, we report the calculation methods to compute the equilibrium Josephson current of the systems analyzed in the next chapters, i.e. in the SFIS JJ and in the magnetic SQDS JJ. For the sake of simplicity, we firstly derive the current formula for the case of the SQDS junction, as in Ref.[92], and then extend it to the 2D tight-binding lattice model of the SFIS JJ employed in Refs.[90, 91].

$J(\phi)$ in a Quantum Dot Josephson junction (SQDS JJ)

The current flowing through a system composed by two leads and a quantum dot, as in Fig. 20, can be derived by the means of the tunneling Hamiltonian method [4]. In the case of Josephson junctions, the current is, in principle, driven by both the voltage bias V and the superconducting phase difference $\phi = \phi_L - \phi_R$ between the S leads. Since we are interested in the equilibrium transport properties of the JJ, in the following we assume no bias voltage is considered, i.e. $V = 0$, but the calculation can be easily generalized to the finite voltage case [4].

We start the discussion, introducing the field operator formalism in particle-hole $\otimes$ spin space (i.e. Nambu$\otimes$spin space), hence defining ψ_D and $\psi_{i,\vec{k}}$ as the field operators annihilating an electron on the QD and on the lead i ($i = L, R$) in the state $\vec{k}$, respectively, as:

$$\psi_D = \left(d_\uparrow, d_\downarrow, d_\uparrow^\dagger, d_\downarrow^\dagger\right)^{\mathrm{T}}, \psi_{i,\vec{k}} = \left(c_{i,\vec{k},\uparrow}, c_{i,\vec{k},\downarrow}, c_{i,-\vec{k},\uparrow}^\dagger c_{i,-\vec{k},\downarrow}^\dagger\right)^{\mathrm{T}}. \tag{1.22}$$

In this framework, the system Hamiltonian H made up of leads, dot and tunneling Hamiltonians, $H = H_{leads} + H_D + H_T$, can be written as follows

$$\begin{aligned} H_{\text{leads}} &= \sum_{i=L,R} \sum_{\vec{k}} \psi_{i,\vec{k}}^\dagger \check{H}_{i,\vec{k}} \psi_{i,\vec{k}}, \quad H_D = \psi_D^\dagger \check{H}_D \psi_D, \\ H_T &= \sum_{i=L,R} \sum_{\vec{k}} \psi_D^\dagger \check{H}_T \psi_{i,\vec{k}} + \text{H.c.}, \end{aligned} \tag{1.23}$$

where $\check{H}_D$, $\check{H}_{i,\vec{k}}$ and $\check{H}_T$ are the QD, the lead i and the hopping Hamiltonian matrices in Nambu$\otimes$spin space, respectively. Here and in the following, the symbol $\hat{\cdot}$ stands for 2×2 matrices in spin or Nambu space while $\check{\cdot}$ indicates the 4×4 matrices in Nambu$\otimes$spin space. In particular, we indicate with $\hat{\sigma}_0$ and $\hat{\sigma}_\nu$ ($\nu = 1, 2, 3$) the identity and the Pauli

matrices in the spin space, respectively, while $\hat{\tau}_0$ and $\hat{\tau}_\nu$ ($\nu = 1, 2, 3$) play the same role in the Nambu space.

Without any loss of generality, we compute the current flowing from the dot to the right lead, since it is equal to the current from the dot to the left bank apart for the sign [4, 203]. Henceforth, we adopt units with $\hbar = c = k_B = 1$, where c is the speed of light and k_B is the Boltzmann constant.

The junction current in the Heisenberg picture reads as [4]

$$J(t) = -|e| \left\langle \frac{dN_R(s)}{ds} \right\rangle \tag{1.24}$$

where e is the electron charge, $N_R(s) = \sum_{\vec{k},\sigma} c^\dagger_{R,\vec{k},\sigma}(s) c_{R,\vec{k},\sigma}(s)$ is the electron number operator in the R electrode at time s and the summation over $\vec{k}$ and spin σ states has to be performed. In the case no bias voltage is applied to the banks, the Heisenberg equation for N_R yields

$$\frac{dN_R(s)}{ds} = i\left[H, N_R(s)\right]. \tag{1.25}$$

If we assume the tunneling Hamiltonian $\hat{H}_T$ has the simple form

$$\hat{H}_T = t\hat{\sigma_0}, \tag{1.26}$$

with t being the $\vec{k}$-independent hopping amplitude between the leads and the dot, we can derive with straightforward calculations the following expression for the current [4]:

$$J(s) = -i|e|t \sum_{\vec{k},\sigma} \left(\left\langle c^\dagger_{R,\vec{k},\sigma}(s) d_\sigma(s) \right\rangle - \left\langle d^\dagger_\sigma(s) c_{R,\vec{k},\sigma}(s) \right\rangle \right). \tag{1.27}$$

Notice that, here, in the hypothesis of time-translational invariance the equal time correlators $\langle c^\dagger_{R,\vec{k},\sigma}(s) d_\sigma(s)\rangle$ and $\langle d^\dagger_\sigma(s) c_{R,\vec{k},\sigma}(s)\rangle$ can be computed at time $s = 0$. Moreover, if no bias voltage is applied to the leads J simply coincides with the Josephson current $J(\phi)$.

By taking the approximation of flat-band superconducting electrodes [176], the current formula can be further simplified substituting the $c_{R,\vec{k},\sigma}$ operators with their $\vec{k}$-independent analog $c^\dagger_{R,\sigma}$:

$$J(\phi) = -i|e|t \sum_{\sigma} \left(\left\langle c^\dagger_{R,\sigma} d_\sigma \right\rangle - \left\langle d^\dagger_\sigma c_{R,\sigma} \right\rangle \right). \tag{1.28}$$

The correlation functions $\left\langle c^\dagger_{R,\sigma} d_\sigma \right\rangle$ and $\left\langle d^\dagger_\sigma c_{R,\sigma} \right\rangle$ are the so-called *lesser Green's functions* in Non-equilibrium Green's function formalism [4]. These correlators mix the dot states with the ones in the right lead, describing the propagation of electrons between from the dot to the lead and vice versa. In equilibrium conditions, e.g. when no bias voltage is applied to the junction, $\langle c^\dagger_{R,\sigma} d_\sigma\rangle$ and $\langle d^\dagger_\sigma c_{R,\sigma}\rangle$ can be directly related to the diagonal elements of the so-called dot-lead and lead-dot Green's functions (i.e.

$\check{G}_{c_R,d}$, $\check{G}_{d,c_R}$) in the Nambu⊗spin space, thus leading to the following current formula in the thermal Matsubara representation [73, 90, 91, 134–136]

$$J(\phi) = -\frac{ie}{2} T \sum_{\omega_n} Tr\left[\hat{\tau}_3 \otimes \hat{\sigma}_0 \left(\check{H}_T \check{G}_{c_R,d}(\omega_n) - \check{H}_T \check{G}_{d,c_R}(\omega_n)\right)\right] , \tag{1.29}$$

where Tr stands for the trace over the Nambu⊗spin space and T is the temperature. In the above equation, the summation over the fermionic Matsubara frequencies $\omega_n = (2n+1)\pi T$ is performed.

$J(\phi)$ in a 2D lattice model JJ

Results in Eq. 1.29 can be easily extended to the case in which the barrier is a 2D tight binding lattice with L sites in the transport direction and W sites in the transverse direction, Fig. 1.4. Indeed, when dividing the barrier in L transverse stripes, in the

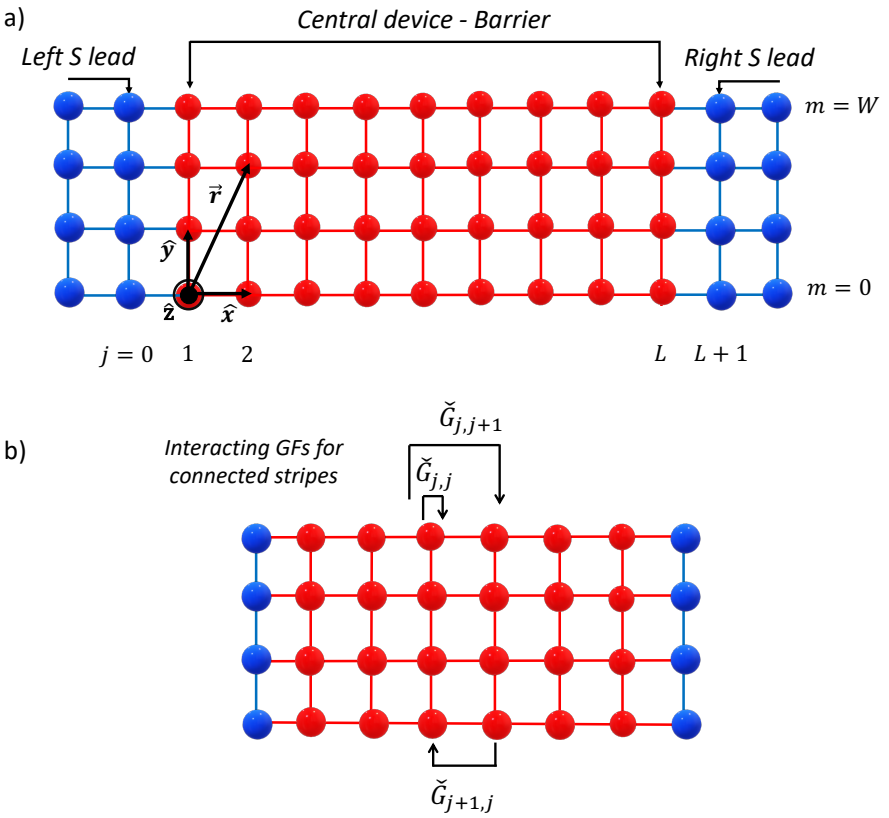

Figure 1.4: In (a) a representation of the 2D tight-binding lattice model of the SFIS junction with $L+2$ sites along the transport direction ($\hat{x}$ axis) and W transverse sites (along $\hat{y}$ axis) is shown. The S electrodes are treated as semi-infinite leads and their influence on the system transport properties is described by the two edge stripes in $j = 0, L+1$, while the barrier extends from the stripe in $j = 1$ to the one in $j = L$. In (b) the Green's functions entering the Josephson current formula, Eq. 1.30, are depicted.

hypothesis of nearest-neighbors hopping, only adjacent stripes can be connected (i.e.

the j-th stripe is linked to the $j-1$-th and $j+1$-th) by the means of the hopping matrices $\check{T}^{\pm}_{j,j+1}$ (that here play the role of the tunneling Hamiltonian H_T in Eq. 1.29).

Therefore, the Josephson current $J(\phi)$ at the position j in the barrier can be written in terms of the GFs connecting the stripes in j and $j+1$, i.e. $\check{G}_{j,j+1}$ and $\check{G}_{j+1,j}$, as follows

$$J(j,\phi) = -\frac{ie}{2} T \sum_{\omega_n} Tr\left[\hat{\tau}_3 \otimes \hat{\sigma}_0 \left(\check{T}^{+}_{j,j+1}\check{G}_{j,j+1} - \check{T}^{-}_{j,j+1}\check{G}_{j+1,j}\right)\right] , \tag{1.30}$$

where, in the case of the 2D lattice model, $\hat{.}$ stands for $2W \times 2W$ stripe matrices in the spin space while $\check{.}$ indicates $4W \times 4W$ stripe matrices in the Nambu$\otimes$spin space. Note that in equilibrium conditions, the Josephson current $J(\phi)$ is uniform inside the barrier and does not depend on the position along the transport direction j.

In this context, both in the case of the SQDS junction (SQDS JJ) and in that of the 2D lattice model junction the knowledge of the *interacting* GFs connecting the central device to the leads reveals to be necessary to compute the Josephson current. In the next section, we present the procedure to calculate the dot-lead/lead-dot GFs, $\hat{G}_{c_R,d}$, $\hat{G}_{d,c_R}$, by the means of the perturbation theory. Then, we illustrate the Recursive Green's function (RGF) method to compute the barrier GF in the case of 2D lattice model JJ.

1.3 Green's function of a Quantum Dot junction

In this section, we show the procedure to connect the QD to the superconducting leads by calculating its *interacting* GF $\check{G}_{dd}$ in the Matsubara representation. The dot GF indeed encodes important information about the junction transport properties such as the Andreev Bound States forming inside the superconducting gap and through which supercurrent flows. Moreover, we show that the knowledge of $\check{G}_{dd}$ is necessary to obtain the lead-Dot/Dot-lead GFs, $\check{G}_{c_R,d}$, $\check{G}_{d,c_R}$, needed in the Josephson current calculation.

In order to compute $G_{dd}(\omega_n)$, we consider the coupling between the leads and the Dot as a small perturbation and we calculate the interaction effect on the Dot within the perturbation theory framework. Starting from the *bare* leads and Dot GFs, i.e. $\check{G}^0_{i=L/R}$ and $\check{G}^0_{dd}$, we can express $\check{G}_{dd}$ in terms of the following Dyson series :

$$\begin{aligned}\check{G}_{dd}(\omega_n) = \check{G}^0_{dd}(\omega_n) + \sum_{i=L,R} \check{G}^0_{dd}(\omega_n)\check{H}_T\check{G}^0_i(\omega_n)\check{H}_T\check{G}^0_{dd}(\omega_n) + \\ + \sum_{i=L,R} \check{G}^0_{dd}(\omega_n)\check{H}_T\check{G}^0_i(\omega_n)\check{H}_T\check{G}^0_{dd}(\omega_n)\check{H}_T\check{G}^0_i(\omega_n)\check{H}_T\check{G}^0_{dd}(\omega_n) + ... \quad ,\end{aligned} \tag{1.31}$$

that is easily obtained by the means of Feynman diagrams approach (Fig. 1.5).

Each diagram of the expansion contributing to the Dot GF ($\check{G}_{dd}(\omega_n)$) consists of a sequence of Dot/lead *bare* propagators ($\check{G}^0_{dd}(\omega_n)/\check{G}^0_i(\omega_n)$) separated by the scattering processes between the lead and Dot. The Dyson perturbative expansion for the Dot GF can be re-written in a more compact way by exploiting the defintion of Dot self-energy $\check{\Sigma}(\omega_n)$,

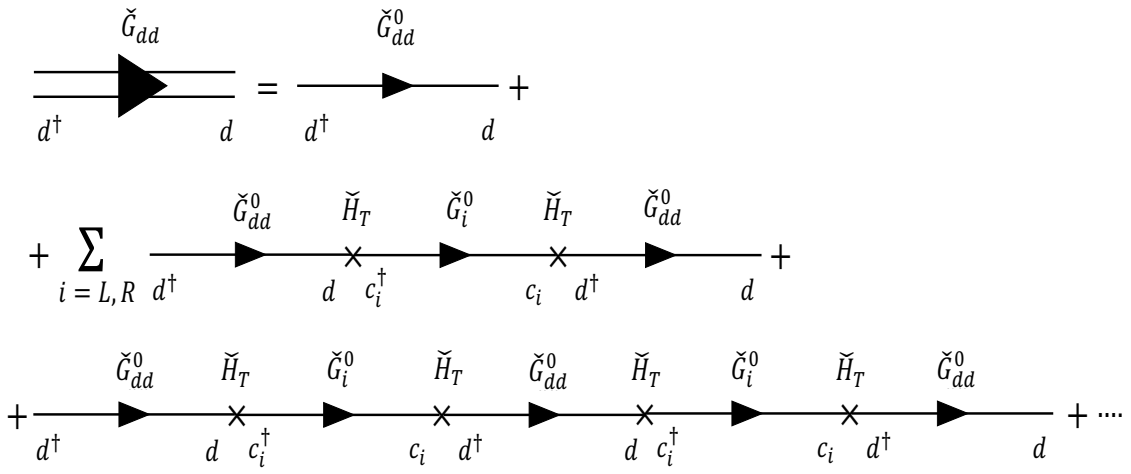

Figure 1.5: Feynman diagram representation of the perturbative expansion for $\hat{G}_{dd}$.

$$\check{G}_{dd}(\omega_n) = \check{G}^0_{dd}(\omega_n) + \check{G}^0_{dd}(\omega_n)\check{\Sigma}(\omega_n)\check{G}^0_{dd}(\omega_n) +$$

$$+\check{G}^0_{dd}(\omega_n)\check{\Sigma}(\omega_n)\check{G}^0_{dd}(\omega_n)\check{\Sigma}(\omega_n)\check{G}^0_{dd}(\omega_n) + \ldots \quad , \tag{1.32}$$

where the expression for $\check{\Sigma}(\omega_n)$ follows straightforwardly from the Feynman diagrams in Fig. 1.6 :

$$\check{\Sigma}(\omega_n) = \sum_{i=L,R} \check{H}_T \check{G}^0_i(\omega_n) \check{H}_T \, . \tag{1.33}$$

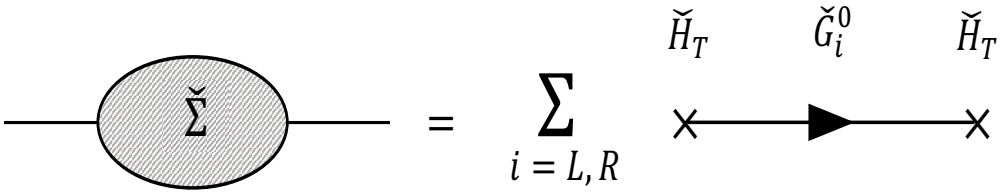

Figure 1.6: Self-energy of the Quantum Dot due to the coupling with the leads.

We can perform the re-summation of the QD Dyson series in Eq. 1.32, thus, reaching the Dyson equation for $\check{G}_{dd}(\omega_n)$ (Fig. 1.7):

$$\check{G}_{dd}(\omega_n) = (\check{G}^0_{dd}(\omega_n)^{-1} - \check{\Sigma}(\omega_n))^{-1} \quad , \tag{1.34}$$

that, recalling the definition of the dot GF in Matsubara representation, i.e. $\check{G}^0_{dd}(\omega_n) = \left(\check{1}\omega_n - \check{H}_D\right)^{-1}$, and the result in Eq. 1.33, yields

$$\check{G}_{dd}(\omega_n) = (i\omega_n\check{1} - \check{H}_D - \sum_{i=L,R} \check{H}_T \check{G}^0_i(\omega_n)\check{H}_T)^{-1} \quad , \tag{1.35}$$

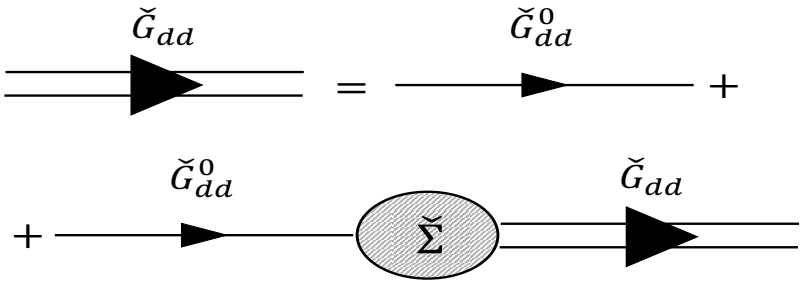

Figure 1.7: Feynman diagram representation of the Dyson equation for the Quantum Dot Green's function.

with $\check{1}$ being the identity matrix in Nambu⊗spin space.

We highlight that the dot and superconducting leads Green's functions, $\check{G}_{dd}$ and $\check{G}^0_i$, have the structure of 4×4 matrices in Nambu⊗spin space, organized as follows

$$\check{G}_{dd} = \begin{pmatrix} \hat{G}_{dd} & \hat{F}_{dd} \\ -\hat{F}^*_{dd} & -\hat{G}^*_{dd} \end{pmatrix}, \quad \check{G}^0_i = \begin{pmatrix} \hat{G}^0_i & \hat{F}^0_i \\ -\hat{F}^{0,*}_i & -\hat{G}^{0,*}_i \end{pmatrix}. \tag{1.36}$$

The off-diagonal terms of the GFs in Eq. 1.36 are the so-called *anomalous* GFs $\check{F}_{dd}$ and $\check{F}^0_i$, describing the superconducting pair correlations in the dot and leads, respectively.

By calculating the dot GF poles we access the knowledge about the junction spectrum of subgap Andreev levels that carry the supercurrent through the JJ [4, 5]. Starting from the Eq. 1.35, and performing its analytic continuation, i.e. $i\omega_n \to z$, we obtain the ABS by solving in z the following secular equation:

$$\det\left(z\check{1} - \check{H}_D - \sum_{i=L,R} \check{H}_{\mathrm{T}} \check{G}^0_i(z) \check{H}_{\mathrm{T}} \right) = 0\,. \tag{1.37}$$

Analogously to $\check{G}_{dd}$ in Eq. 1.35, also the GFs connecting leads and Dot, $\check{G}_{c_i d}/\check{G}_{d c_i}$ (involved in the calculation of Josephson current [4, 73, 90–92, 135, 136]), can be calculated by the means of the perturbation theory. Their expression in terms of $\check{G}^0_i$ and $\check{G}_{dd}$ at the first non-vanishing order in the interaction ($\hat{H}_T$) are, respectively:

$$\begin{aligned} \check{G}_{c_i d} &\simeq \check{G}_{dd} \check{H}_T \check{G}^0_i, \\ \check{G}_{d c_i} &\simeq \check{G}^0_i \check{H}_T \check{G}_{dd}\,. \end{aligned} \tag{1.38}$$

1.4 Green's function of the SFIS JJ: Recursive Green's Function Method

Green's function for a finite size barrier

In principle, the barrier GF for the SFIS JJ described with the 2D lattice in Fig. 1.4, can be computed similarly to the SQDS JJ case. In other words, we can include the influence of the leads on the barrier by the means of a self-energy term. More generally,

this technique could be applied to any system composed by two leads and one central device regardless its size. If the Hamiltonian of the system is written as

$$H = H_{cd} + \sum_{i=L,R} H^i_{lead} + H^i_T \,, \tag{1.39}$$

where H_{cd}, H^i_{lead} and H^i_T are the Hamiltonians of the central device, of the lead i and of the interaction between the lead i and the device, respectively, then the device self-energy Σ_{cd} reads as

$$\Sigma_{cd} = H^i_T G^{0,i}_{lead} H^i_T \,, \tag{1.40}$$

with $G^{0,i}_{lead}$ being the *bare* GF of the isolated lead i. For this reason, computing the central-device GF G_{cd} translates to the inversion of the effective Hamiltonian $H^{eff}_{cd} = H_{cd} + \Sigma_{cd}$,

$$G_{cd} = \left[E + i\eta^+ - H^{eff}_{cd}\right]^{-1} \,, \tag{1.41}$$

where the parameter $\eta^+ \to 0^+$ is necessary to preserve causality. Note that, according to this convention, taking $\eta > 0$ allows us to compute the retarded GF while choosing $\eta < 0$ we can calculate the advanced GF [3].

In the case of a tight-binding lattice H^{eff}_{cd} at least consists of a $LW \times LW$ matrix (with L and W number of longitudinal and transverse lattice sites, respectively), when neglecting both spin-dependent and superconducting interactions. For this reason, the number of operations needed for its inversion scales as $O((LW)^3)$, thus making the calculation of G_{cd} very expensive from a computational point of view and constituting a limitation for studying the transport properties of large size systems.

In this context, the RGF method represents a sophisticate numerical technique that allows calculating the Green's function (GF) of a central device described by lattice model when it is connected to two leads. This method is extremely useful if the device GF cannot be computed from the direct inversion of its Hamiltonian. Indeed, as we show in next section, number of operations need to compute the barrier GF in this way scales as $O(LW^3)$, thus gaining factor of L^2 in the algorithm efficiency.

Recursive Green's Function Method

RGF was first introduced in the study of electronic transport in mesoscopic systems [134, 137, 148, 149]. Moreover, in the last twenty years this has been widely employed to investigate the transport properties of superconducting JJs [73, 135, 136]. In this section, we briefly illustrate the main features of the RGF technique applied to our case, without the purpose of providing a thorough explanation of the method, that can be found in Refs.[73, 134–137, 148, 149].

Let us specify the discussion to the case of the Josephson junction in Fig. 1.4. Here and in the following, we assume that the system is described by a tight-binding Hamiltonian including only nearest neighbors interactions. The RGF method consists in dividing the barrier Fig. 1.8, along the transport direction, in transverse stripes, whose GFs have to be computed by recursively connecting them to the leads. In particular, we suppose that the *bare* Matsubara GF of each stripe j can be calculated from the definition as follows:

$$\check{G}^0_{j,j} = \left[i\omega_n \check{1} - \check{H}^0_{j,j}\right]^{-1} \,, \tag{1.42}$$

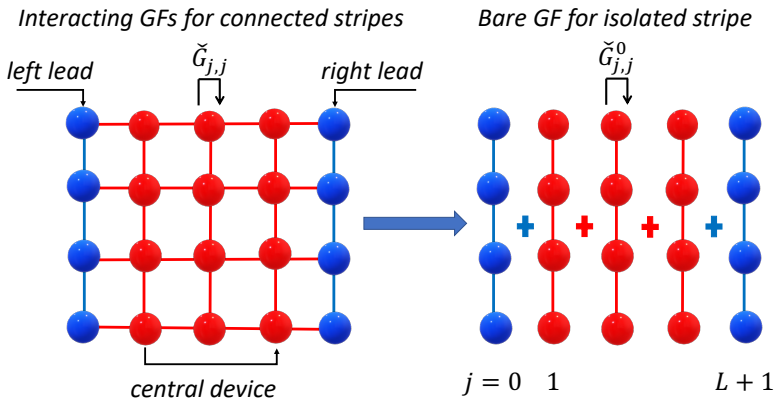

Figure 1.8: Scheme of the system made up of two leads and one central device, on the left. On the right, the system divided in stripes. $\check{G}_{j,j}$ is the *interacting* GF of the j-th stripe when connected to the others. $\check{G}^0_{j,j}$ stands for the *bare* GF of the isolated j-th stripe.

where $\check{H}^0_{j,j}$ is the Hamiltonian of the stripe, involving only couplings between lattice sites within the same stripe (i.e. lattice sites at the positions $\vec{r} = j\vec{x} + m\vec{y}$ and $\vec{r}\,' = j\vec{x} + m'\vec{y}$, with same index j, whose interaction is included in $\hat{H}(\vec{r}, \vec{r}\,')$).

In order to derive the full barrier GF, we have to compute the *interacting* GF of each stripe j, $\check{G}_{j,j}$, that corresponds to the stripe GF when it is connected to the two leads and to its nearest neighbors (i.e. $(j-1)$-th and $(j+1)$-th stripes).

As a starting point, the knowledge of the two leads GFs is necessary. In practice, we consider semi-infinite leads and encode their influence in their surface GFs for the two edges (respectively with $j = 0$ and $j = L + 1$ in Fig. 1.8). These latter can be evaluated by applying the calculation method used in Refs.[135, 150], that we report in Appendix B. Then the GF for each stripe j, i.e. $\check{G}_{j,j}$, can be recursively computed by the means of a *Dyson-like* equation [73, 135, 149], thus attaching the stripes to the superconductors one at a time. In other words, this method consists in "propagating" the surface GFs of the S leads inside the barrier. Leads surface GFs are defined as $\check{G}^L_{0,0}(\omega_n)$ and $\check{G}^R_{L+1,L+1}(\omega_n)$ for the left and right S leads.

Here and in the following we indicate with $\check{G}_{j,j}$ the GF of the j-th barrier stripe when it is linked to both the left and right leads, whereas $\check{G}^L_{j,j}$ ($\check{G}^R_{j,j}$) stands for the GF of the stripe j when it is only connected to the left (right) lead.

For the sake of clarity, we show how to calculate the *interacting* GF for the first stripe of the barrier (with $j = 1$, Fig. 1.8) when it is attached to the left S lead (with $j = 0$, Fig. 1.8), i.e. $\check{G}^L_{1,1}$. Two adjacent stripes can be attached by using the hopping matrices $\check{T}^{\pm}$, including the interactions between sites belonging to nearest neighbor transverse stripes.

Therefore, we can easily find a *Dyson-like* equation for the first barrier stripe, $\check{G}^L_{1,1}$, starting from its *bare* GF, $\check{G}^0_{1,1}$:

$$\check{G}^L_{1,1} = \check{G}^0_{1,1} + \check{G}^0_{1,1}\check{T}^-_{1,0}\check{G}^L_{0,1}\,, \tag{1.43}$$

where we exploit the fact that $\check{T}^-_{1,0}$ is the interaction term between the 0-th (left lead) and the first stripe (barrier).

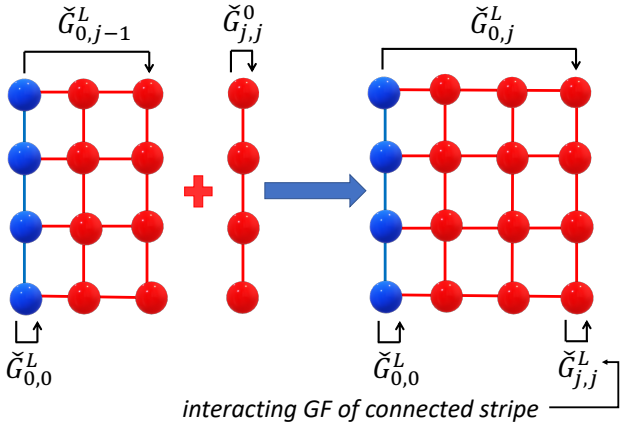

Figure 1.9: Scheme describing how to connect the stripe j to the left lead. The first $j-1$ stripes are already connected. In order to add the stripe j, $\check{G}^L_{j,j}$ and $\check{G}^L_{0,j}$ need to be computed.

We observe that this expression for $\check{G}^L_{1,1}$ in Eq. 1.43 depends on the knowledge of the GF connecting the stripes 0 and 1 (namely $\check{G}^L_{0,1}$), which needs to be evaluated. Analogously to $\check{G}^L_{1,1}$, we can derive $\check{G}^L_{0,1}$ as follows :

$$\check{G}^L_{0,1} = \check{G}^L_{0,0}\check{T}^+_{0,1}\check{G}^L_{1,1}\,, \tag{1.44}$$

where we exploit the fact that $\check{G}^0_{0,1}$ vanishes, because the *bare* GFs, $\check{G}^0$, cannot connect together different stripes. Hence, we obtain two coupled equations for the $\check{G}^L_{1,1}$, Eqs. 1.43-1.44, that depend only on the *bare* GF of the stripe 1, the surface GF of the left S lead and the matrices $\check{T}^{\pm}$.

If we assume the hopping matrices between nearest neighbor stripes (i.e. $\check{T}^+_{j,j+1}$ and $\check{T}^-_{j+1,j}$) are equal for every value of the index j, we can simply indicate with $\check{T}^{\pm}$ the stripes interactions.

With straightforward calculations, we manage to find a more compact expression for $\check{G}^L_{1,1}$:

$$\check{G}^L_{1,1} = \left[i\omega_n\check{1} - \check{H}^0_{1,1} - \check{T}^+\check{G}^L_{0,0}\check{T}^-\right]^{-1}, \tag{1.45}$$

where we explicitly use the Eq. 1.42. This equation can be easily generalized to the j-th stripe as follows

$$\check{G}^L_{j,j} = \left[i\omega_n\check{1} - \check{H}^0_{j,j} - \check{T}^+\check{G}^L_{j-1,j-1}\check{T}^-\right]^{-1},\ 0 \le j \le L\,, \tag{1.46}$$

thus, allowing the calculation of the j-th stripe GF from the one of the $j-1$-th, Fig. 1.9.

By repeating the procedure, starting from the right (R) side (i.e. starting from the stripe with $j = L+1$ in Fig. 1.8), we can connect the stripe j to the right lead in the following way:

$$\check{G}^R_{j,j} = \left[i\omega_n\check{1} - \check{H}^0_{j,j} - \check{T}^-\check{G}^R_{j+1,j+1}\check{T}^+\right]^{-1}\ L+1 \le j \le 1\,. \tag{1.47}$$

Then, the GF $\check{G}_{j,j}$ inside the barrier ($1 \le j \le L$) is computed by using the formula

$$\check{G}_{j,j} = \left[i\omega_n\check{1} - \check{H}^0_{j,j} - \check{T}^-\check{G}^R_{j+1,j+1}\check{T}^+ - \check{T}^+\check{G}^L_{j-1,j-1}\check{T}^-\right]^{-1}. \tag{1.48}$$

At last, we obtain GFs connecting adjacent stripes (namely the stripe j with the ones at $j-1$ and $j+1$) by the relations

$$\begin{aligned}
\check{G}_{j+1,j} &= \check{G}^R_{j+1,j+1}\,\check{T}^+_{j+1,j}\,\check{G}_{j,j},\\
\check{G}_{j,j+1} &= \check{G}_{j,j}\,\check{T}^-_{j,j+1}\,\check{G}^R_{j+1,j+1},\\
\check{G}_{j-1,j} &= \check{G}^L_{j-1,j-1}\,\check{T}^-_{j-1,j}\,\check{G}_{j,j},\\
\check{G}_{j,j-1} &= \check{G}_{j,j}\,\check{T}^+_{j,j-1}\,\check{G}^L_{j-1,j-1}\,,
\end{aligned} \tag{1.49}$$

that we use in the calculation of the Josephson current, Eq. 1.30.

From the computational point of view, this method requires attaching the L stripes to both left and right leads, by inverting the $4W \times 4W$ matrices in the Eqs. 1.46-1.47 for the left and right Green's functions. The RGF algorithm thus involves $2L$ matrix inversions of $4W \times 4W$ GF matrices and, for this reason, scales as $O(LW^3)$, thus gaining factor of L^2 with respect to the direct inversion of the whole barrier Hamiltonian.

From the barrier Green's Function to the Pair Correlations

Green's function of the stripe j, $\check{G}_{j,j}$, is a $4W \times 4W$ matrix in Nambu⊗spin space, where W is the number of lattice sites in each stripe. It can be visualized as a 2×2 block matrix in the Nambu space, where each block consists in a $2W \times 2W$ sub-matrix:

$$\check{G}_{j,j} = \check{G}_{\omega_n}(\vec{r},\vec{r}\,') = \begin{bmatrix} \hat{G}_{\omega_n}(\vec{r},\vec{r}\,') & \hat{F}_{\omega_n}(\vec{r},\vec{r}\,') \\ -\hat{F}^*_{\omega_n}(\vec{r},\vec{r}\,') & -\hat{G}^*_{\omega_n}(\vec{r},\vec{r}\,') \end{bmatrix}, \tag{1.50}$$

where $\vec{r} = j\vec{x} + m\vec{y}$, $\vec{r}\,' = j\vec{x} + m'\vec{y}$ with j fixed. In Fig. 1.10 we provide an example of the GF of a single stripe with 2 sites along the transverse direction, i.e. along y.

The off-diagonal terms of the matrix in the right-hand side of Eq. 1.50 are the so-called *anomalous Green's functions* $\hat{F}_{\omega_n}$, that describe the superconducting pair correlations. Furthermore, by taking the off-diagonal elements of the stripes GFs ($\check{G}_{j,j}$) in the right-hand side of Eq. 1.50, $\hat{F}_{\omega_n}(\vec{r},\vec{r}\,')$ with $\vec{r} = \vec{r}\,' = j\vec{x} + m\vec{y}$ (with j fixed), we can derive the four pairing components with s-wave symmetry at each stripe j along the $\vec{x}$-direction:

$$\frac{1}{W}\sum_{\omega_n}\sum_{m=1}^{W}\hat{F}_{\omega_n}(\vec{r},\vec{r}) = \sum_{\nu=0}^{3} f_\nu(j)\hat{\sigma}_\nu\, i\,\hat{\sigma}_2\,, \tag{1.51}$$

where f_0 is the spin-singlet component and f_ν with $\nu = 1,2,3$ are the spin-triplet components.

Similar considerations can be applied to the GFs connecting the j-th stripe with its neighbors $j \pm 1$ (i.e. $\check{G}_{j,j+1}$, $\check{G}_{j+1,j}$, $\check{G}_{j,j-1}$, $\check{G}_{j-1,j}$), from which we can calculate the odd-parity pairing functions:

$$\begin{aligned}
&\frac{1}{4W}\sum_{\omega_n}\sum_{m=1}^{W}\left(\hat{F}_{\omega_n}(\vec{r}+\hat{x},\vec{r}) + \hat{F}_{\omega_n}(\vec{r},\vec{r}-\hat{x}) - \hat{F}_{\omega_n}(\vec{r},\vec{r}+\hat{x}) - \hat{F}_{\omega_n}(\vec{r}-\hat{x},\vec{r})\right)\\
&\qquad = \sum_{\nu=0}^{3} f_\nu(j)\,\hat{\sigma}_\nu\, i\,\hat{\sigma}_2\,,
\end{aligned} \tag{1.52}$$

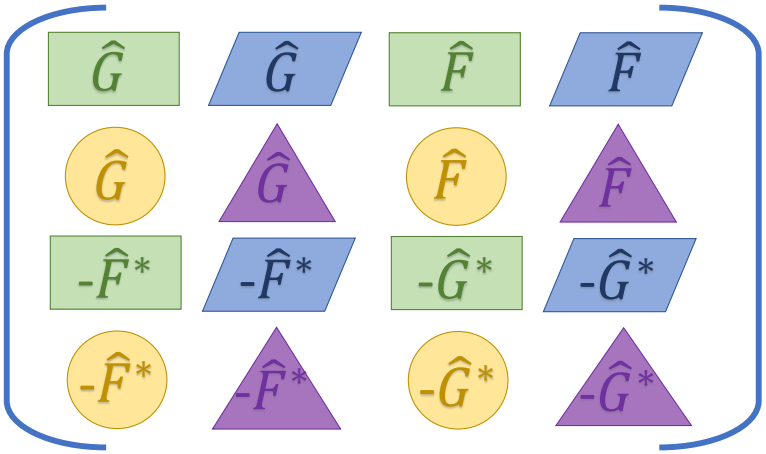

Figure 1.10: Schematic representation of the stripe GF matrix structure, in the case of only 2 sites along the transverse direction. Different colors stand for different propagators $\check{G}(j\hat{x}+\hat{y}, j\hat{x}+\hat{y})$, $\check{G}(j\hat{x}+\hat{y}, j\hat{x}+2\hat{y})$, $\check{G}(j\hat{x}+2\hat{y}, j\hat{x}+\hat{y})$, $\check{G}(j\hat{x}+2\hat{y}, j\hat{x}+2\hat{y})$, with this being 4×4 matrices in Nambu$\otimes$spin space. The blocks of the same colors indicate the 2×2 blocks of a given GF in spin space. For example, in green we have the blocks of $\check{G}(j\hat{x}+\hat{y}, j\hat{x}+\hat{y})$, i.e. $\hat{G}(j\hat{x}+\hat{y}, j\hat{x}+\hat{y})$, $\hat{F}(j\hat{x}+\hat{y}, j\hat{x}+\hat{y})$, $-\check{F}^*(j\hat{x}+\hat{y}, j\hat{x}+\hat{y})$, $-\check{G}^*(j\hat{x}+\hat{y}, j\hat{x}+\hat{y})$.

that give rise to p-wave superconductivity.

Making explicit the term in right hand side of Eqs. 1.51 (Eq. 1.52), we can rewrite the s-wave (p-wave) pairing components as

$$\begin{cases} f_0 = \dfrac{f_{\uparrow\downarrow} - f_{\downarrow\uparrow}}{2} \\ f_3 = \dfrac{f_{\uparrow\downarrow} + f_{\downarrow\uparrow}}{2} \\ f_1 = \dfrac{f_{\downarrow\downarrow} - f_{\uparrow\uparrow}}{2} \\ f_2 = \dfrac{f_{\uparrow\uparrow} + f_{\downarrow\downarrow}}{2\,i}, \end{cases} \tag{1.53}$$

from which we extract the standard spin correlation functions, f_0, f_3, $f_\uparrow$ (that is $f_{\uparrow\uparrow}$) and $f_\downarrow$ (that is $f_{\downarrow\downarrow}$).

Chapter 2

Tuning the $0-\pi$ transitions in SFIS JJs

In this chapter, we investigate the transport properties of Josephson junctions with a ferromagnetic insulator barrier with a focus on the temperature behavior of the Josephson current (i.e. current-phase relation) and of the critical current I_C [90]. Since the capability of engineering a temperature stable π JJ would be of vital importance in view of the possible implementation of π qubits with ferromagnetic JJs in superconducting quantum circuits, we explore the opportunity to tune and control the $0-\pi$ transitions through a direct action on the JJ $I_C(T)$, that may be used as a fingerprint of the junction. We investigate the specific role of impurities as well as of possible spin mixing mechanisms, due to the spin orbit coupling (SOC).

First, we present the 2D tight-binding lattice model of the SFIS junction. Then, we recall and extend previous theoretical results [73, 104] on $0-\pi$ transitions in ferromagnetic insulator barriers induced by exchange field variations to the junction $I_C(T)$. Then, we study influence of SOC and disorder effects on the peculiar $I_C(T)$ cusp present in $0-\pi$ JJs. We show that transition between the 0 and the π phases can be properly tuned, thus achieving stable π junctions over the whole temperature range [90]. At the end, we present first analysis of Cooper pairs correlation functions when the system switches from a cusp-like $0-\pi$ to a π regime [90].

2.1 SFIS Junction Model

Tight-Binding Hamiltonian

In this section, we describe the SFIS JJ using a two dimensional lattice model, shown in Fig. 2.1. We, thus, introduce the tight-binding Hamiltonian of the system including both the FI barrier and the superconducting electrodes Hamiltonians. Then, we report our choice of the system energy parameters we used for the simulations. In Fig. 2.1, L is the length of the ferromagnetic insulator barrier, W is the width of the junction, expressed in units of lattice sites, and $\vec{x}$ ($\vec{y}$) is the unit vector along the longitudinal (transverse) direction. Here, the vector $\vec{r} = j\vec{x} + m\vec{y}$ points a lattice site with $j = 0, 1, \ldots, L, L+1$ and $m = 1, \ldots, W$. The Hamiltonian of the junction in the Nambu $\otimes$

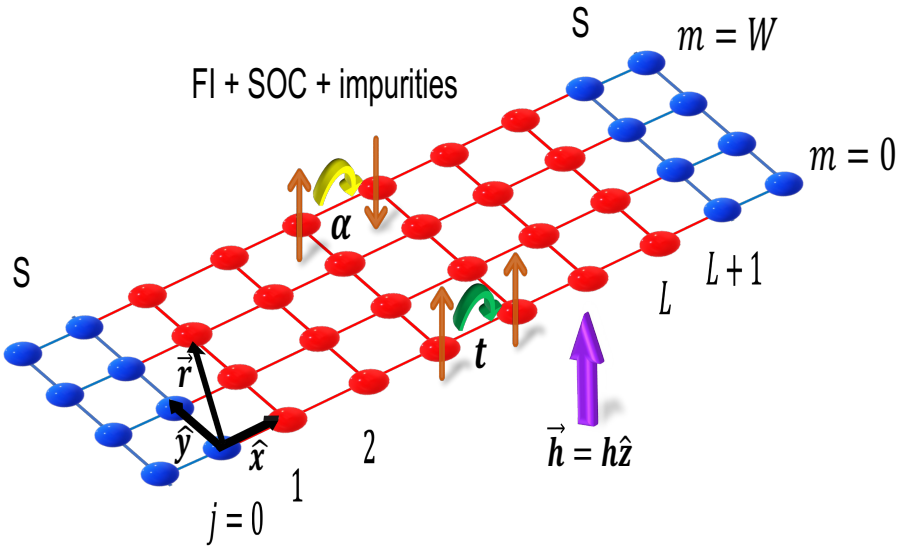

Figure 2.1: Schematic representation of the SFIS junction geometry with a ferromagnetic insulator barrier in the presence of spin-orbit coupling (SOC) and impurities. The junction lies in the $x-y$ plane and it is represented by a lattice with $(L+2)$ and W sites along x and y directions, respectively. The influence of the S leads (blue sites) is condensed in the border stripes at $j=0$ and $j=L+1$. The FI barrier (red sites) extends from $j=1$ to $j=L$ along the transport direction, i.e. along x. The exchange field h (violet arrow) is parallel to the z axis, thus perpendicular to the JJ plane. The hopping t between nearest-neighbor sites is here represented by green arrows. The SOC α is depicted by the spin-flipping process highlighted by the yellow arrow.

spin space is given by

$$\check{\mathcal{H}} = \sum_{\vec{r},\vec{r}'} \Psi^{\dagger}(\vec{r}) \begin{bmatrix} \hat{H}(\vec{r},\vec{r}') & \hat{\Delta}(\vec{r},\vec{r}') \\ -\hat{\Delta}^{*}(\vec{r},\vec{r}') & -\hat{H}^{*}(\vec{r},\vec{r}') \end{bmatrix} \Psi(\vec{r}') \tag{2.1}$$

with

$$\Psi(\vec{r}) = \left[\psi_{\uparrow}(\vec{r}), \psi_{\downarrow}(\vec{r}), \psi^{\dagger}_{\uparrow}(\vec{r}), \psi^{\dagger}_{\downarrow}(\vec{r})\right]^{T} . \tag{2.2}$$

$\psi^{\dagger}_{\alpha}(\vec{r})$ and $\psi_{\alpha}(\vec{r})$ are the field operators creating/annihilating an electron with spin α at lattice point $\vec{r}$. Here, we recall that the symbols $\hat{.}$ and $\check{.}$ describe the 2×2 and 4×4 matrices in spin and Nambu$\otimes$spin spaces respectively.

In Eq. 2.1, $\hat{H}$ is the normal-state hamiltonian of the junction while $\hat{\Delta}$ describes the superconducting pairing potential. The former can be written as $\hat{H} = \hat{H}_s + \hat{H}_{FI}$, with $\hat{H}_s$ and $\hat{H}_{FI}$ referring to the S leads and FI barrier, respectively.

In Fig. 2.1, the S regions extend for $j<1$ and $j>L$. $\hat{H}_s$ consists in a kinetic term (i.e. $\hat{H}_s = \hat{H}_s^K$) that reads:

$$\begin{aligned} \hat{H}_s^K(\vec{r},\vec{r}') = &\{-t_s\left(\delta_{\vec{r},\vec{r}'+\vec{x}} + \delta_{\vec{r}+\vec{x},\vec{r}'}\right)\hat{\sigma}_0 - t_s\left(\delta_{\vec{r},\vec{r}'+\vec{y}} + \delta_{\vec{r}+\vec{y},\vec{r}'}\right)\hat{\sigma}_0 \\ &- \left(4t_s - \mu_s\right)\delta_{\vec{r},\vec{r}'}\hat{\sigma}_0\} \times \left[\Theta\left(-j+1\right) + \Theta\left(j-L\right)\right] \end{aligned} \tag{2.3}$$

where t_s and μ_s are the hopping parameter and the chemical potential, respectively, and Θ is the Heaviside step-function. Here and in the following, we indicate with $\hat{\sigma}_0$ and $\hat{\sigma}_\nu$ ($\nu = 1, 2, 3$) the unit and the Pauli matrices in the spin space, respectively.

We take the pairing potential $\hat{\Delta}$ different from zero only in the S leads, which, thus, vanishes inside the FI barrier. $\hat{\Delta}$ is of spin-singlet s-wave symmetry and is expressed as

$$\hat{\Delta}(\vec{r}, \vec{r}\,') = \Delta \delta_{\vec{r},\vec{r}\,'}\, i\,\hat{\sigma}_2 \times \left[\Theta\left(-j+1\right) e^{i\phi_L} + \Theta\left(j-L\right) e^{i\phi_R}\right], \tag{2.4}$$

where $\phi = \phi_L - \phi_R$ defines the phase difference across the junction and ϕ_L (ϕ_R) is the phase in the left (right)-hand side superconductor. In our model, the order parameter Δ is constant in the leads and it is not derived from self-consistent calculations. Further, we assume that there is no disorder in the superconductors.

The FI barrier extends from $j = 1$ to $j = L$ and its hamiltonian consists of four terms

$$\hat{H}_{FI} = \hat{H}^K_{FI} + \hat{H}^{SOC}_{FI} + \hat{H}^{ex}_{FI} + \hat{H}^{i}_{FI}\,. \tag{2.5}$$

$\hat{H}^K_{FI}$ is the kinetic energy,

$$\begin{aligned}\hat{H}^K_{FI}(\vec{r}, \vec{r}\,') =& \{-t_{FI}\left(\delta_{\vec{r},\vec{r}\,'+\vec{x}} + \delta_{\vec{r}+\vec{x},\vec{r}\,'}\right)\hat{\sigma}_0 - t_{FI}\left(\delta_{\vec{r},\vec{r}\,'+\vec{y}} + \delta_{\vec{r}+\vec{y},\vec{r}\,'}\right)\hat{\sigma}_0 \\ & - \left(4t_{FI} - \mu_{FI}\right)\delta_{\vec{r},\vec{r}\,'}\hat{\sigma}_0\} \times \Theta\left(j\right)\Theta\left(L+1-j\right)\,.\end{aligned} \tag{2.6}$$

The spin-orbit coupling (SOC) is Rashba-like [118] and reads

$$\begin{aligned}\hat{H}^{SOC}_{FI}(\vec{r}, \vec{r}\,') =& i\alpha\left[\{\delta_{\vec{r},\vec{r}\,'+\vec{x}} - \delta_{\vec{r}+\vec{x},\vec{r}\,'}\}\,\hat{\sigma}_2\right. \\ & \left. - \{\delta_{\vec{r},\vec{r}\,'+\vec{y}} - \delta_{\vec{r}+\vec{y},\vec{r}\,'}\}\,\hat{\sigma}_1\right]\Theta\left(j\right)\Theta\left(L+1-j\right)\,.\end{aligned} \tag{2.7}$$

The exchange potential is

$$\hat{H}^{ex}_{FI}(\vec{r}, \vec{r}\,') = -\vec{h}\,' \cdot \boldsymbol{\sigma}\,\delta_{\vec{r},\vec{r}\,'}\Theta\left(j\right)\Theta\left(L+1-j\right)\,, \tag{2.8}$$

where $\boldsymbol{\sigma}$ is the vector of the Pauli matrices $(\hat{\sigma}_1, \hat{\sigma}_2, \hat{\sigma}_3)$. The on-site random impurity potential is

$$\hat{H}^{i}_{FI}(\vec{r}, \vec{r}\,') = v_{\vec{r}}\,\hat{\sigma}_0\,\delta_{\vec{r},\vec{r}\,'}\Theta\left(j\right)\Theta\left(L+1-j\right)\,. \tag{2.9}$$

In the above equations, t_{FI} is the hopping integral among nearest-neighbor lattice sites (in the following we omit the subscript FI for simplicity, i.e. we take $t_{FI} = t$), μ_{FI} the Fermi energy, α the amplitude of the spin-orbit interaction, $v_{\vec{r}}$ the on-site random impurity potential strength, uniformly distributed in the range $-V_{imp} \leq v_{\vec{r}} \leq V_{imp}$. Finally, so as to introduce a spin-dependent disorder, the exchange field is assumed to be affected by small on-site fluctuations $\vec{\delta_h}$ and is modeled as $\vec{h}\,' = \vec{h} + \vec{\delta_h}$. The strength of the $\vec{\delta_h}\left(\vec{r}\right)$ is extracted randomly from a uniform distribution in the range $-h/10 \leq \delta_h \leq h/10$. For the sake of simplicity, we choose δ_h to lie along the $\vec{h}$-direction. Since the junction plane, where the spin-orbit interaction is active, coincides with the xy-plane, the exchange field $\vec{h}\,'$ is always taken in the perpendicular direction, $\vec{h}\,' = h'\vec{z}$ (along the z-direction). In this way we are able to introduce the spin-mixing mechanisms generating equal-spin triplet correlations in FI, that are very likely to occur in ferromagnetic junctions [59, 60, 65, 75]. We note that in the presence of SOC field in the xy-plane, choosing $\vec{\delta_h}\left(\vec{r}\right) \parallel \vec{z}$ is sufficient to mimic a slight magnetic disorder.

In the following we report the choice of the model parameters used for these calculations. Henceforth, we adopt units with $\hbar = c = k_B = 1$, where c is the speed of light and k_B is the Boltzmann constant. All the energies are, thus, scaled by t and the magnitude of the spin-orbit coupling α is scaled by ta, where the lattice constant is set $a = 1$. The Josephson current in Eq. 1.30, here indicated as $I(\phi)$, is calculated in units of $I_0 = e\Delta$. Further, we fix several parameters as $t_s = t = 1$, $\mu_{FI} = 0$, $\mu_s = 3$, $\Delta = 0.005$. The chosen chemical potential mismatch at FI and S interfaces allows to describe the insulating regime in our model. In order to focus our attention on the short-junction regime, typical of tunnel junctions employed in superconducting circuits, we fix the number of lattice sites along the transport direction to be $L = 8$ in all the simulations, unless otherwise indicated. For lattice spacings of fractions of nm, this barrier length corresponds to few lattices. In particular, this thickness is consistent with GdN films of $3 \div 4$ nm employed in SFIS JJs of Ref.[75, 116], for which $a \approx 5 \times 10^{-1}$ nm [208]. Moreover, since typical experimental SFIS JJs are characterized by barriers with transverse dimensions larger than their length [75, 116], we choose $W = 32$.

Transport properties of the SFIS JJ

Barrier GF is given by $\check{G}_{\omega_n}(\vec{r}, \vec{r}')$, where $\vec{r} = j\vec{x} + m\vec{y}$ and $\vec{r}' = j'\vec{x} + m'\vec{y}$ run over all the possible lattice site indices $j, j' = 0, 1, \ldots, L, L+1$ and $m, m' = 1, \ldots, W$. The barrier Matsubara GF is, thus, a $4WL \times 4WL$ matrix in the Nambu$\otimes$spin space, whose blocks with fixed $(\vec{r}, \vec{r}')$ can be numerically calculated by solving the Gor'kov equation

$$\left[i\omega_n \hat{\tau}_0 \hat{\sigma}_0 - \sum_{\vec{r}_1} \begin{pmatrix} \hat{H}(\vec{r}, \vec{r}_1) & \hat{\Delta}(\vec{r}, \vec{r}_1) \\ -\hat{\Delta}^*(\vec{r}, \vec{r}_1) & -\hat{H}^*(\vec{r}, \vec{r}_1) \end{pmatrix} \right] \times \check{G}_{\omega_n}(\vec{r}_1, \vec{r}') = \hat{\tau}_0 \hat{\sigma}_0 \delta(\vec{r} - \vec{r}'), \tag{2.10}$$

where $\omega_n = (2n+1)\pi T$ is the fermionic Matsubara frequency and T is the temperature. Here and in the following, $\hat{\tau}_0$ and $\hat{\tau}_\nu$ ($\nu = 1, 2, 3$) are the analogous of the unit and Pauli's matrices in the Nambu space, respectively.

Starting from the surface GFs of the two S leads, as they are reported in Ref.[135] (see Appendix B), solve the Gor'kov Eq. 2.10 recursively calculating the GF at each stripe transverse j inside the FI barrier. $\check{G}_{j,j}$ with RGF technique $\check{G}_{j,j}$ structure in Nambu$\otimes$spin space, in Eq. 1.50, is here reported for the sake of clarity:

$$\check{G}_{j,j} = \check{G}_{\omega_n}(\vec{r}, \vec{r}') = \begin{bmatrix} \hat{G}_{\omega_n}(\vec{r}, \vec{r}') & \hat{F}_{\omega_n}(\vec{r}, \vec{r}') \\ -\hat{F}^*_{\omega_n}(\vec{r}, \vec{r}') & -\hat{G}^*_{\omega_n}(\vec{r}, \vec{r}') \end{bmatrix}, \tag{2.11}$$

where $\vec{r} = j\vec{x} + m\vec{y}$, $\vec{r}' = j\vec{x} + m'\vec{y}$ with j fixed.

The barrier stripes can be connected (to the leads and to each other) by using the hopping matrices $\check{T}^{\pm}$, given by

$$\check{T}^{\pm} = \begin{pmatrix} -t & \mp\alpha & 0 & 0 & \ldots \\ \pm\alpha & -t & 0 & 0 & \ldots \\ \ldots & \ldots & \ldots & \ldots & \ldots \\ 0 & 0 & \ldots & t & \pm\alpha \\ 0 & 0 & \ldots & \mp\alpha & t \end{pmatrix}, \tag{2.12}$$

involving the hopping and spin-orbit coupling along the x-direction. Since we consider nearest-neighbors hopping, only adjacent stripes can be connected by the $\check{T}^{\pm}$ matrices (i.e. the j-th stripe is linked to the $j-1$-th and $j+1$-th).

From the anomalous Green's functions in Eq. 2.11, i.e. $\hat{F}_{\omega_n}(\vec{r},\vec{r}')$, we access the information about pair correlation functions in *s-wave* symmetry inside the FI, as in Eq. 1.51.

Once we have connected each barrier stripe j to the superconducting banks, i.e. $\check{G}_{j,j}$ has been computed for each $1<j<L$, we use Eqs. 1.49 to calculate the GFs connecting adjacent stripes that enter the Josephson current formula Eq. 1.30. In the clean case, when no impurities are supposed to be present in the barrier, i.e. $V_{imp}=0$ in Eq. 2.9, we manage to reconstruct the whole JJ current-phase relation (CPR , i.e. $I(\phi)$) at fixed temperature T by varying the phase bias ϕ between the two S leads in Eq. 1.30. We notice that here the ferromagnet exchange fields and the spin-orbit are assumed to be perpendicular, with the first one pointing along the z-axis and the second one lying in the xy-plane. In this way no *anomalous* Josephson Effect [138–144] is induced on the JJ CPR , that remains an antisymmetric function of ϕ, $I(\phi)=-I(\phi)$. For this reason, computing $I(\phi)$ for ϕ values in the interval $[0,\pi]$ is sufficient to describe the junction transport properties. Finally, the critical current $I_c(T)$ is estimated from the CPR at different temperatures between 0 and T_c, by taking its maximum in absolute value ($I_c(T)=\max_{\phi}[|I(\phi,T)|]$).

When the presence of impurities in the barrier is accounted, i.e. when $V_{imp}\neq 0$, both the temperature dependence of the critical Josephson current (i.e. $I_c(T)$) and correlations functions are averaged over N_s samples with different random impurity configurations. We choose $N_s=200$ for both the $I_c(T)$ curves and the pairing correlation functions. In particular, the ensemble average of the Josephson current (Eq. 1.30) over a number of different samples is obtained as: $<I>=\frac{1}{N_s}\sum_{n=1}^{N_s} I_n$, where I_n is the Josephson current in the n-th sample. Then, evaluating the average Josephson current by varying ϕ in the range from 0 to π we obtain the average CPR at fixed T (i.e. $I(\phi,T)$) and the averaged critical current $I_c(T)$.

2.2 Tuning of 0, $0-\pi$ and π regimes with the exchange field h

In this section, we extend the results in Refs.[73, 104], that theoretically predict $0-\pi$ transitions in SFIS JJs driven by magnetic fields, to the temperature dependence of the critical current $I_C(T)$. In particular, we illustrate how the $I_C(T)$ behavior is affected by varying the exchange field h, showing that our model recovers the possibility to switch between the 0, $0-\pi$ and π regimes in SFIS JJs, as reported in the literature for normal-metal ferromagnetic barriers [45–47, 49, 52, 204]. As the exchange field enters the formula for the supercurrent oscillation length inside a ferromagnet, modifications in h lead to changes in the I spatial period and, thus, in the equilibrium state of the system. In this way, the transition temperature $T_{0-\pi}$ between the 0 and π phases, at which a cusp is visible in the $I_C(T)$, can be tuned so as to obtain 0 or π states that are stable over the whole temperature range from 0 to T_C. In Fig. 2.2 (a) we show the temperature dependence of the critical current, obtained for increasing values of h in

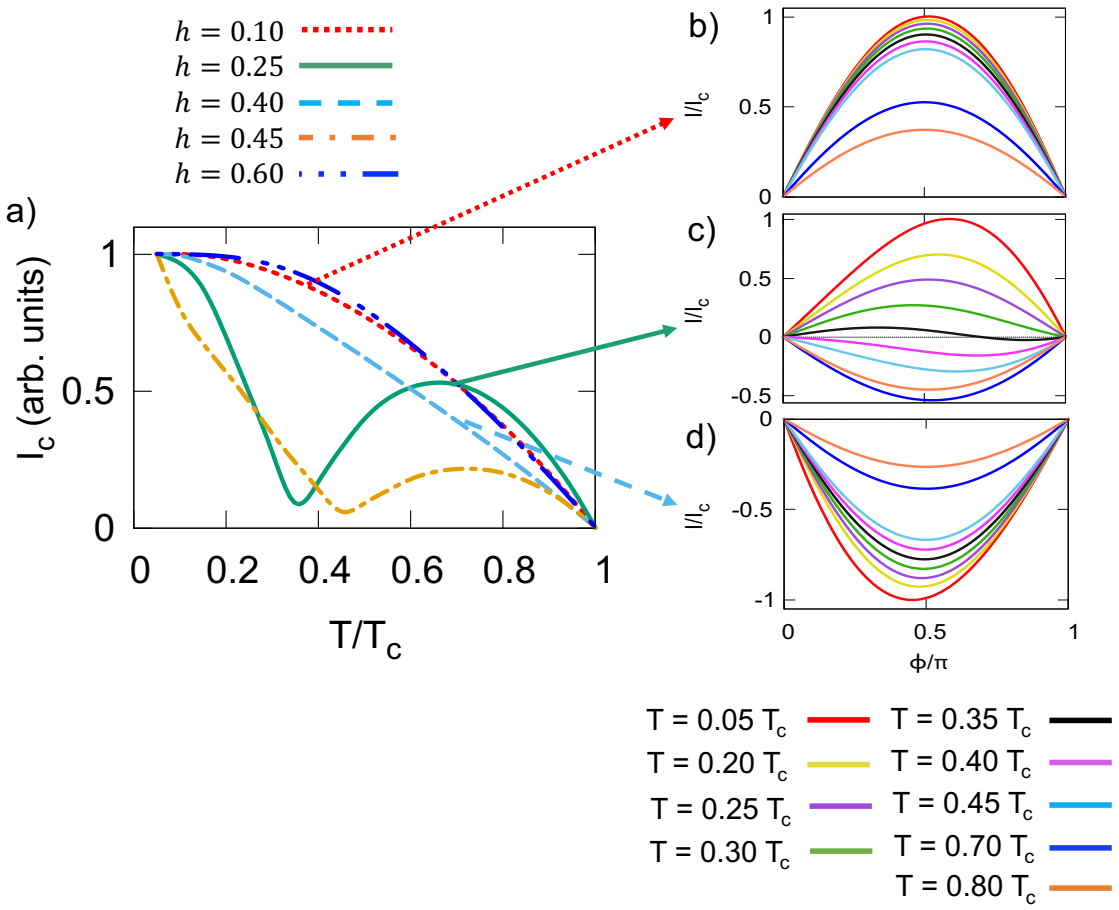

Figure 2.2: (a): $I_c(T)$ for different values of h. For these simulations we used $\alpha = 0.04$, $L = 8$ and $W = 32$ sites in the x and y direction. CPR of a 0 (b), $0-\pi$ (c) and π (d) JJ, obtained for $h = 0.10$, 0.25, 0.40, respectively. In (e) the Josephson current (at $T = 0.1T_C$ and $\phi = \pi/2$) as a function of the exchange field h and SOC strength α is shown.

the clean limit (i.e. $V_{imp} = 0$ and $\delta_h = 0$) at fixed spin-orbit field strength $\alpha = 0.04$.

We can notice that, starting from the Ambegaokar-Baratoff (AB) [11] behavior ($h = 0.10$, red dotted curve), I_C is strongly modified with increasing the exchange field h in the ferromagnetic layer, causing the system to move towards $0-\pi$ regime ($h = 0.25$, green curve), where a non-monotonic dependence of $I_C(T)$ is visible, and temperature stable π state ($h = 0.40$, dashed light-blue curve). Then, undergoing some oscillations, the AB trend is established again when h increases ($h = 0.60$, dot-dot-dashed blue curve). Moreover, the cusp-minimum of the $0-\pi$ transition appears to be shifted in temperature as h varies. We also report in Figs. 2.2 (b-d) the CPR corresponding to the $I_C(T)$ curves obtained for $h = 0.10$, 0.25, 0.40, respectively. As can be seen, the AB-type curves shown in (a) correspond to pure 0 (b) and π (d) JJs, stable over the whole range of temperatures.

However, it is worth noting that varying the exchange field of the FI in a such wide range of values, would require strong external fields, that are detrimental for superconductivity. This effect would be even more considerable in the short junction

regime, namely the situation we are considering.

In the following sections, we explore the possibility to manipulate the junction $I_C(T)$ by the means of spin-orbit and non-magnetic impurities, thus proposing new mechanisms to engineer tunable $0-\pi$ Josephson devices. Indeed, we show how 0, $0-\pi$ and π phases can be more easily attained acting on the SOC and non-magnetic impurities.

2.3 The role of spin-orbit coupling (SOC). Switching between 0 and π state.

In order to investigate efficient tools for controlling the transition between 0, $0-\pi$ and π regimes, we focus on how spin mixing and disorder effects can be exploited for this task. In this section, we consider the case of a clean ($V_{imp}=0$ and $\delta_h=0$) $0-\pi$ SFIS JJ which presents temperature induced $0-\pi$ transitions and analyze the effect of SOC on its $I_C(T)$ behavior. For the following numerical simulations, we fix the exchange field inside the FI to the value $h=0.45$ such that for zero SOC, i.e. $\alpha=0$, the JJ exhibit $0-\pi$ cusp in the $I_C(T)$, dashed purple curve in Fig. 2.3.

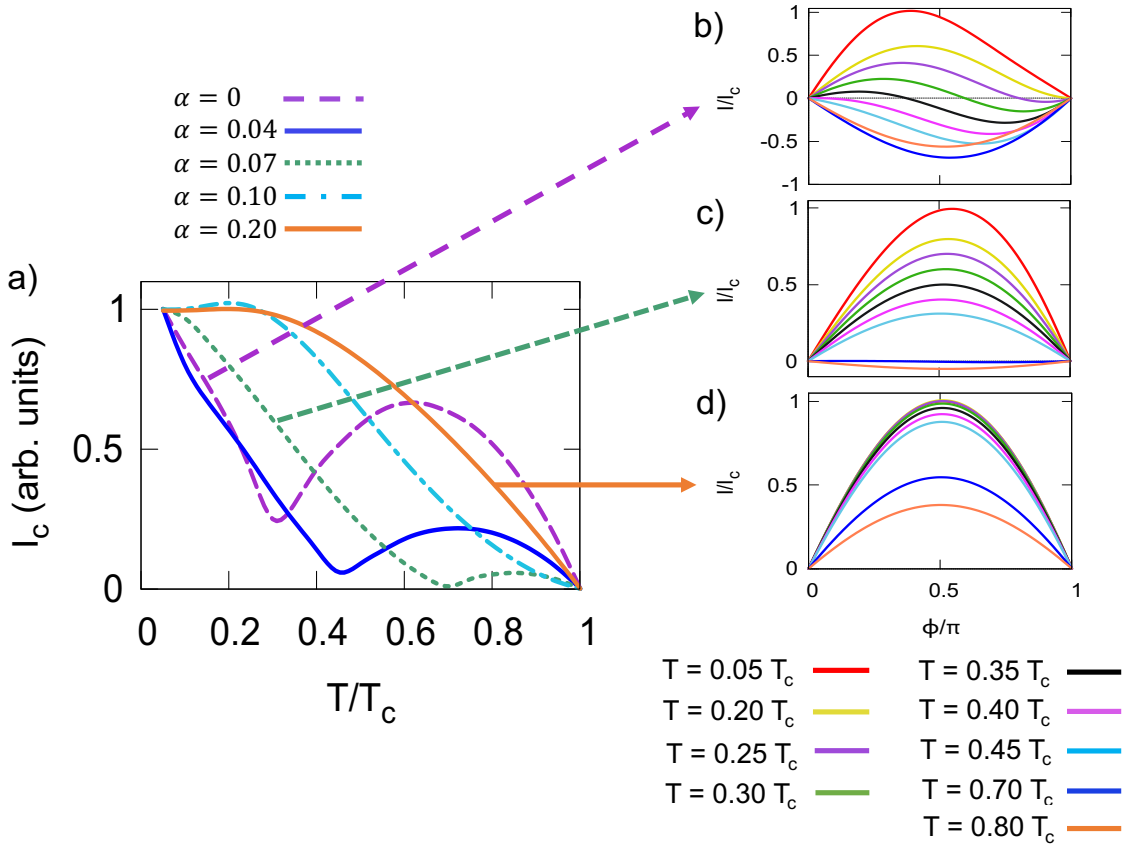

Figure 2.3: Effect of SOC increasing on the $I_C(T)$ (a) and current-length relation (CLR) (e). We set the exchange field $h=0.45$ in (a-d). In (b-d), the CPR s relative to the simulations in (a) for $\alpha=0, 0.07, 0.2$ are shown.

In Fig. 2.3 (a) we can see that, starting from a $0-\pi$ transition corresponding to

$\alpha = 0$, we recover the Ambegaokar-Baratoff behavior [11] for $\alpha = 0.20$. For larger α the critical current is always of AB type. We can also notice that the second lobe of the $I_C(T)$ curve is reduced in height and its (cusp-like) minimum is shifted toward higher temperatures when α increases, until the non-monotonic $I_c(T)$ behavior visibly changes and it completely disappears in the AB regime. In Figs. 2.3 (b-d), the characteristic CPR corresponding to $I_c(T)$ curves for $\alpha = 0$, 0.07, 0.20 are shown. We can notice that the $0-\pi$ transition is well evident for $\alpha = 0$ and only slightly appreciable for $\alpha = 0.07$, while it is completely washed out for $\alpha = 0.20$. Hence, by increasing α, we induce a shift in the transition temperature $T_{0-\pi}$ towards higher values, until the $0-\pi$ transition cancels out. Further, we observe visible contributions due to the second and higher order harmonics in the CPR at $T_{0-\pi}$, when the first order harmonic appears strongly weakened [54, 55]. Our results confirm the fact that SOC stabilizes the 0 state rather than the π state [73] in these devices.

To better illustrate this mechanism, in Fig. 2.4 we show the critical Josephson current as a function of the length of the ferromagnetic-insulator layer (with L from $L = 3$ to $L = 50$), i.e. current-length relation (CLR). In these simulations we used $T = 0.1T_c$ and $\phi = \pi/2$ respectively. Furthermore, we set $h = 0.45$, $\alpha = 0, 0.07, 0.20$ and a uniform distribution of the exchange field in the 2D lattice is assumed ($\delta_h = 0$). The change in sign of Josephson current, indicating the corresponding $0-\pi$ transitions

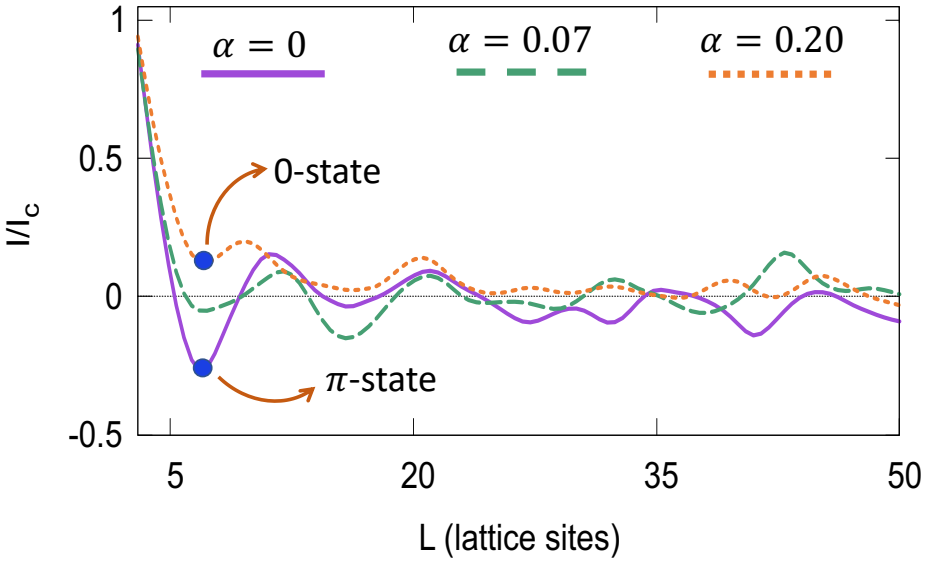

Figure 2.4: Effect of SOC increasing on the CLR $I(L)$ is shown. CLR is computed by varying the length of the junction from $L = 3$ to $L = 50$, with $\phi = \pi/2$, $T = 0.1T_c$ and $W = 32$, for $\alpha = 0, 0.07, 0.2$. The CLR curves are normalized to the value of their current at $L = 3$.

at fixed lengths of the FI layer due to the presence of the exchange potential, is more frequent in the cases with $\alpha = 0$ and $\alpha = 0.07$. The effect of SOC increasing is the suppression of the above-mentioned $0-\pi$ transitions and consequently a mostly always positive Josephson current for $\alpha = 0.20$. Indeed, the SOC produces a shift of the CLR curve from lower to higher current values; negative critical currents are representative

of π states while, when I_c becomes positive (at fixed length L), the $\pi - 0$ transition occurred and the system reaches the 0 final-state under the SOC growth. Taking h and L fixed, there is no possibility that, by further increasing α, the system will return to the π state experiencing another $0 - \pi$ transition.

A qualitative explanation of this effect follows. The short-range spin-triplet component $S_z = 0$ appears in S/FI systems due to exchange field breaking time-reversal symmetry in F. In the presence of spin-orbit interaction, the spin-mixing effect at S/FI interfaces allows for long-range equal spin-triplet components $S_z = \pm 1$ inside the ferromagnetic region. The $S_z = 0$ components (singlet and zero-spin triplet) show an oscillating behavior due to the different phase shifts acquired by the up and down-spin electrons of the Cooper pair, as they propagate in F, while the $S_z = \pm 1$ pairing components show a long-range decay, since the exchange field h has the same effect on the two equal spin electrons [58, 67, 94, 95]. In the long junction limit all the pairing functions decay exponentially over the thermal coherence length $\xi_T = \frac{v_F}{2\pi T}$, whereas the oscillation period of the zero-spin pairing components is given by $\xi_h = \frac{v_F}{2h}$ [51, 59, 60, 73]. Therefore, for $x \gg \xi_T$, heuristically, the Josephson current can be considered as consisting of two contributions:

$$I \sim I_{S_{z=\pm 1}} e^{-x/\xi_T} + I_{S_{z=0}} e^{-x/\xi_T} \cos\left(\frac{x}{\xi_h}\right), \tag{2.13}$$

where $I_{S_{z=0}}$ and $I_{S_{z=\pm 1}}$ are the amplitudes of the opposite spin and parallel spin components, respectively. Increasing the SOC results in an enhancement of the non-oscillating part of the Josephson current, whose superposition with the oscillating term produces, in turn, an enlarged total current and, thus, may prevent that I_c vanishes in the $0 - \pi$ transition.

In this context, while raising the exchange field drives promotes the system switching between 0, $0 - \pi$ and π regimes, since it changes the spatial period of the current oscillations, spin-orbit progressively leads the system toward a stable 0 state.

To better illustrate what we explain in terms of the $I_C(T)$ behavior, in Fig. 2.5 we additionally report the density plot of Josephson current (at $T = 0.1T_c$ and $\phi = \pi/2$) as a function of the exchange field h and SOC strength, α, for a wider range of these latter parameters. The black/dark-violet regions indicate negative values of the current, where the JJ is π. For low values of spin-orbit coupling varying the h drives the system toward a sequel of $0 - \pi$ transitions. In particular, we can notice a well-defined π-*island* that in our simulations appear stable in temperature. The white/light-yellow regions, where $I > 0$, indicate conventional 0-JJs, with a mostly constant occurrence at low values of the exchange field ($h < 0.05$) for any value of α. More generally, when α increases the 0 state is favored. Intermediate orange-red areas represent JJs which show a good probability to undergo a $0 - \pi$ transition, since the critical current is very low. Our results, obtained for SFIS JJs, are in accordance and extend those previously demonstrated in [73, 136].

Ultimately, our results identify SOC as a useful tool for driving the evolution of the $I_c(T)$ of SFIS JJs from $0 - \pi$ to 0 regime.

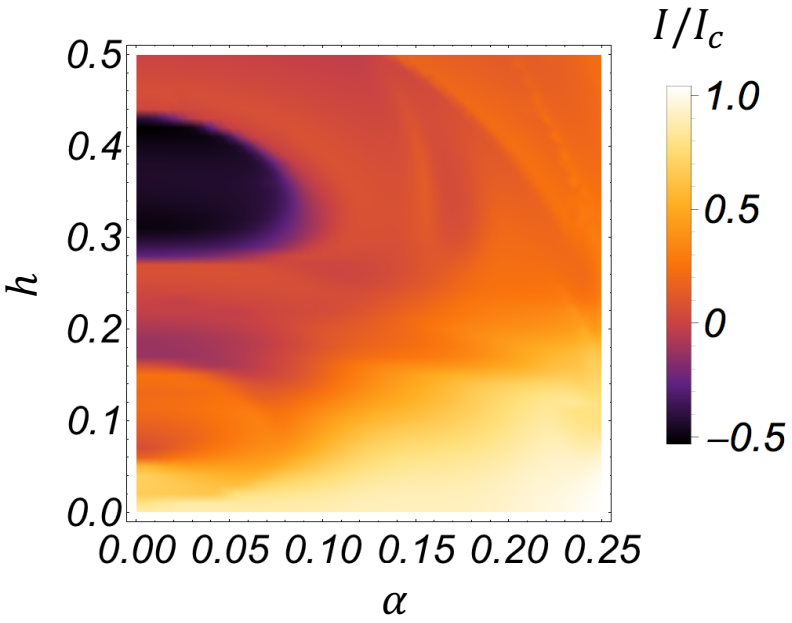

Figure 2.5: An example density plot of the Josephson current (at $T = 0.1T_C$ and $\phi = \pi/2$) as a function of the exchange field h and SOC strength α is shown. Yellow/white zones correspond to the system being in the 0 state while in violet zones it is in the π phase.

2.4 The dirty regime: the role of impurities in the formation of π-JJs

It is legitimate to ask under which conditions the junction displays a stable π state over the whole temperature range, similar to what happens in the case of the 0 state with strong SOC. Real systems are affected by the unavoidable presence of impurities and in this section, we show that interesting features for the existence of π states in SFIS JJs can be detected in the presence of non-magnetic impurities, modeled as scalar on-site potentials.

In what follows we focus on the effect of disorder on the $I_c(T)$ curves exhibiting a $0-\pi$ transition and on the corresponding CPR. In particular, firstly we consider the case of a SFIS JJ in the presence of disorder, secondly we analyze the combined effect of impurities and SOC on the $I_c(T)$ of these devices. As a matter of fact, the influence of increasing V_{imp} results in different scenarios.

In the following simulations, we use $\alpha = 0.04$ (for the case with SOC) and four different values of $V_{imp} = 0.025, 0.125, 0.150, 0.250$. Moreover, here, small on-site exchange field fluctuations are considered ($\delta_h \neq 0$) to model a more realistic scenario in which the exchange field may be non-uniform in the whole barrier. In Fig. 2.6 (a) the $I_c(T)$ curve at $\alpha = 0$ is calculated as the impurity potential increases. We notice that for high values of V_{imp} the system changes its $I_c(T)$ behavior leaving the $0-\pi$ regime and reaching a stable π state almost over the whole temperature range, as it is evident in the corresponding CPR s (Figs. 2.6 (c-e)). Precisely, for $V_{imp} = 0.025$ (green curve) both the maximum of the second lobe and the dip of the $0-\pi$ transition settle at

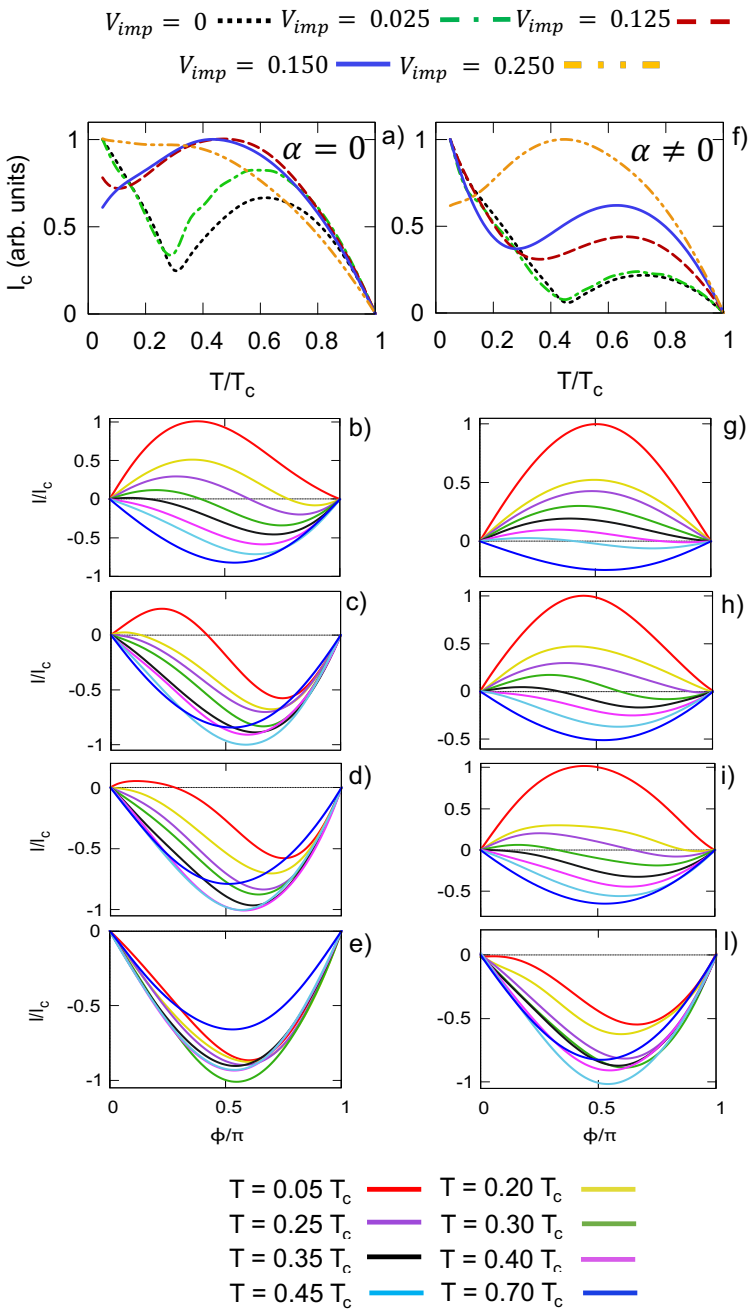

Figure 2.6: Effect of increasing V_{imp} on the JJ critical current $I_C(T)$ in the cases without and with SOC (a, f). Corresponding calculated CPR s (b-e, g-l) and formation of temperature stable π state.

higher values of current with respect to the clean regime (black line in Fig. 2.6 (a)). Consequently, the clear effect of increasing V_{imp} is the filling of the minimum of the $0-\pi$ transition and its shifting toward very low temperatures (red and blue curves), leading to the AB-like behavior for the highest disorder configuration (orange curve), corresponding to a pure π regime (Fig. 2.6 (e)). The presence of impurities seems to be a driving force for the conversion of a $0-\pi$ JJ into a pure π one. As it is shown, in the absence of SOC the realization of an almost pure π-JJ is feasible even for small

values of the impurity potential (Fig. 2.6 (c, d)).

In the presence of SOC (Fig. 2.6 (f)) the clean $I_c(T)$ curve (black line) exhibits a $0-\pi$ transition occurring at $T \sim 0.45T_c$, characterized by a lower value of the current in the π state. In this case, we can notice that enhancing the impurity strength produces a more gradual filling of the $0-\pi$ dip together with its broadening (Fig. 2.6 (f), red and blue curves), shifting it toward higher critical current values and lower temperatures. When passing from the $0-\pi$ regime to the π one, with $\alpha \neq 0$, the system also shows a peculiar plateau region in the $I_c(T)$ extended over a wide range of temperatures, for intermediate values of V_{imp} (Fig. 2.6 (f), red curve).

The combined effect of SOC and impurities allows to stabilize the $0-\pi$ transition over a wide range of temperatures. However, for $V_{imp} = 0.250$, we observe a sharp change in the $I_c(T)$ behavior, where neither the plateau nor the $0-\pi$ dip are no longer visible, suggesting that the $0-\pi$ transition may occur at very low temperatures and that the pure π regime may be reached at larger values of V_{imp}.

We may further analyze the system response to the presence of disorder by looking at the CPR (Figs. 2.6 (b-e), (g-l)), corresponding to the $I_c(T)$ curves in Figs. 2.6 (a) and (b), respectively. For the first scenario (Fig. 2.6 (a, b-e)), the increase of V_{imp} produces strong modifications in the CPR, characterized by an enhanced contribution of higher order harmonics at low temperatures, reflecting the lowering of the $0-\pi$ transition temperature ($T_{0-\pi}$). Further, for $V_{imp} = 0.250$ the CPRs are opposite in sign with respect to the typical $\sin\phi$ behavior, indicating that a phase difference of π is established across the junction.

In Fig. 2.6 (f, g-l), the CPRs in the case of $\alpha \neq 0$ are presented. Here, the $0-\pi$ transition gradually moves to lower temperatures as V_{imp} increases, until the junction is totally π for the highest value of V_{imp} (Fig. 2.6 (l)).

In Fig. 2.6 (f) we observe that the influence of the SOC on the dirty SFIS JJs consists in stabilizing the $0-\pi$ regime even for moderately high values of the impurity potential. Here, the result of the coexistence of two competing effects, namely the spin-orbit and the disorder, is noticeable. Indeed, as for the clean regime, also in the dirty case the SOC tends to bring the system toward the 0 state; whereas the non-magnetic on-site impurities encourage it to turn toward the π state. This results in the slowdown of the switching from $0-\pi$ to π $I_c(T)$ behavior, which, thus, takes place more gradually as V_{imp} is enlarged. For this reason, the system goes through an intermediate regime involving a widened $0-\pi$ transition characterized by the plateau in the critical current, before reaching the π regime. In this situation, we can better visualize how the impurities drive the transformation of the $I_c(T)$ from that of a $0-\pi$ JJ to the one of a π-JJ. Indeed, this mechanism is only slightly perceivable when $\alpha = 0$ and the entire process happens almost suddenly.

We can provide a qualitative picture of this phenomenon in Fig. 2.7 In the clean case, for temperatures lower than the $0-\pi$ transition one ($T < T_{0-\pi}$) the lower energy level is the 0 state. When $T = T_{0-\pi}$ the 0 and π energy levels are coinciding; finally, for $T > T_{0-\pi}$ the $0-\pi$ transition has occurred and the Josephson energy minimum is reached at $\phi = \pi$ (Fig. 2.7 (a)). On the other hand, the presence of on-site non-magnetic impurities produces a broadening in energy (and, therefore, in temperature) of the 0 and π energy levels (Fig. 2.7 (b)). The latter, becoming wider, give rise to an overlap region in which the JJ comes to be in a "hybrid $0-\pi$ state" over a more or less extended range

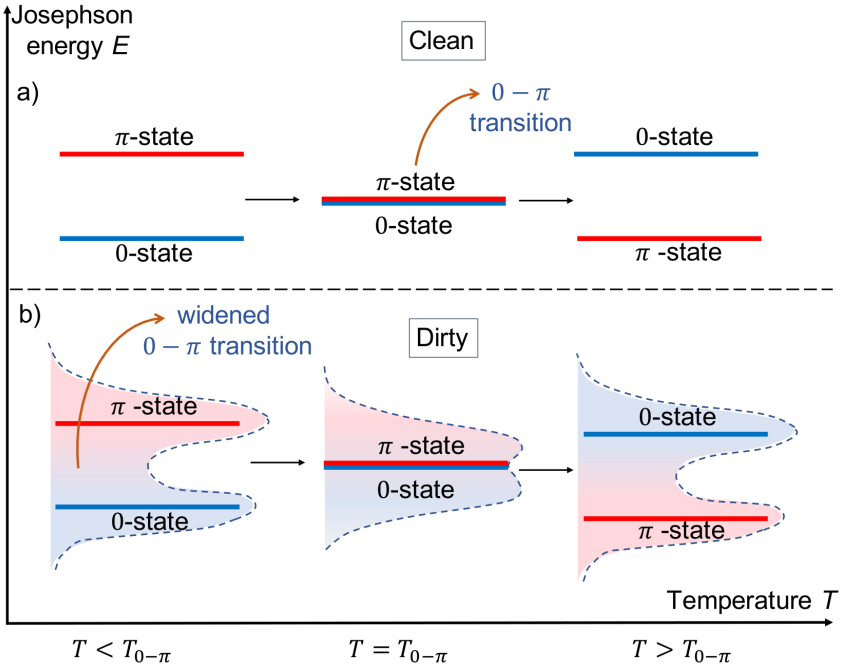

Figure 2.7: Schematic representation of 0 and π energy levels in the clean (a) and dirty (b) regime. In the latter case, the broadening in energy, due to the presence of on-site non-magnetic impurities, is shown.

of temperatures. When the impurities strength is enhanced, the overlapping between the levels grows together with the probability that, for $T > T_{0-\pi}$, the system prefers to stabilize in the lower π energy state. Finally, we illustrate, in Fig. 2.8, the possibility to build up a controllable device that can host all the $I_c(T)$ regimes, in view of possible applications in superconducting quantum circuits. Here, we show that, once we have fixed the impurity potential strength in such a way to have an almost pure π-JJ in the $\alpha = 0$ configuration (Fig. 2.8 (a)), by adding the spin-orbit interaction and modifying its coupling strength, we manage to drive the junction toward $0 - \pi$ (Figs. 2.8 (b-c)) and 0 (Fig. 2.8 (d)) regimes. This happens in a reversible manner, in the sense that decreasing the SOC would bring back the system in the initial π state.

2.5 Pairing functions in the presence of spin-mixing and disorder effects

In this section, as a further investigation, we analyze the pair correlations induced in the FI barrier in the presence of both SOC and impurities. In particular, we study how spin-resolved pairs correlations are modified when increasing the impurity potential strength V_{imp} in both s-wave and p-wave symmetries. Our goal is to understand if the transition to a temperature stable π state is accompanied by the appearance of unconventional pairing mechanisms in the ferromagnetic insulator.

In SFIS JJs, the exchange field breaks the time-reversal symmetry, giving rise to the zero-spin triplet pairing correlations. However, when we consider systems with impuri-

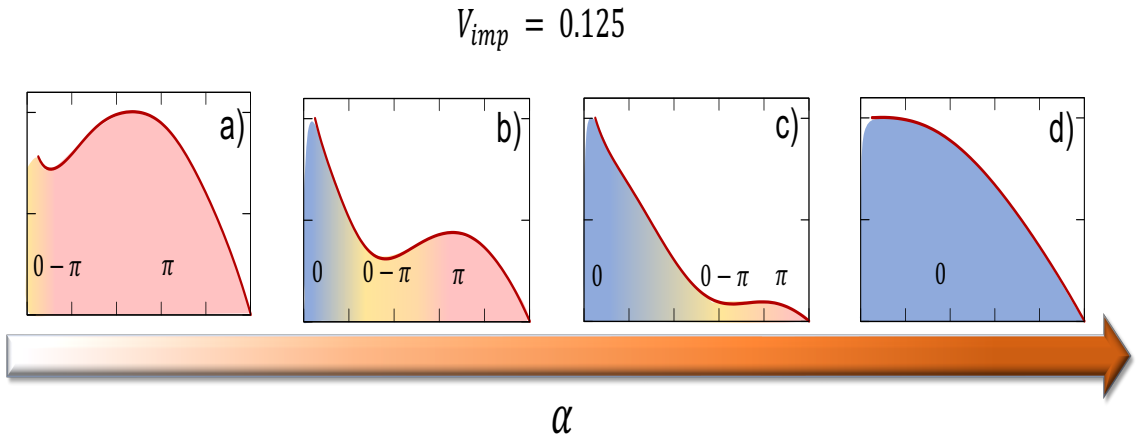

Figure 2.8: Effect of SOC strength (α) increasing on the $I_C(T)$ behavior, at fixed value of the impurity potential ($V_{imp} = 0.125$). The $I_C(T)$ curves are calculated for the following values of $\alpha = 0$, 0.04, 0.07, 0.20. The $I_c(T)$ curves in (a) and (b) correspond to the ones in Fig. 2.6 (a) and (f), respectively, for $V_{imp} = 0.125$.

ties and SOC the chance to have more exotic pairing components becomes relevant. In particular, in the presence of SOC, triplet pairings with parallel spins (with $S_z = \pm 1$ projection) emerge. Indeed, the generation of equal-spin triplet correlations via SOC is provided by the fact that, at interfaces, this latter breaks the spin symmetry, leading to a mixing of spin up and spin down channels in such a way that the total spin **S** is no longer a good quantum number. As a result, the proximity amplitudes in the ferromagnet will intrinsically be a mixture of singlet and triplet pair correlations.

Moreover, we notice that SOC breaks also the inversion symmetry at the S/FI interfaces, thus, all four types of pair amplitudes (i.e. s-wave singlet, s-wave triplets, p-wave singlet, p-wave triplets) can be found in the F region [59–61]. Since the Pauli's principle requires the pairing correlations to be totally anti-symmetric, the possible types of pairing functions have to fulfill specific symmetry properties with respect to spin, momentum and frequency [59–61, 154, 156, 158, 160]. For this reason, the s-wave singlet as well as the p-wave triplets are even functions of the Matsubara frequencies ω_n (even-frequency), while s-wave triplets and p-wave singlet are odd-frequency.

In Figs. 2.9 we show the amplitude of spatial profile of the calculated s and p-wave correlation functions (Eqs. 1.51, 1.52 and 1.53) as a function of the position inside the FI barrier (expressed in terms of the number # of sites), corresponding to the system configurations analyzed in the previous section in the presence of SOC and disorder, Figs. 2.6 (f, g-l).

In the following calculations we set $T = 0.025\,T_c$ and $\phi = 0$. As well as for the systems in Figs. 2.6 (f, g-l), we choose the following values of the on-site impurity potential: $V_{imp} = 0.025$ (Figs. 2.9 (a, b, f)), $V_{imp} = 0.125$ (Figs. 2.9 (c)), $V_{imp} = 0.150$ (Figs. 2.9 (d)) and $V_{imp} = 0.250$ (Figs. 2.9 (e, g)). The plots in (b-e) represent a zoomed view of the s-wave spin-triplet components, while in (f, g) we show a zoomed view of the p-wave correlations for the configurations with the lowest and highest value of V_{imp}.

In the s-wave symmetry, the majority component is the spin-singlet one f_0 (for

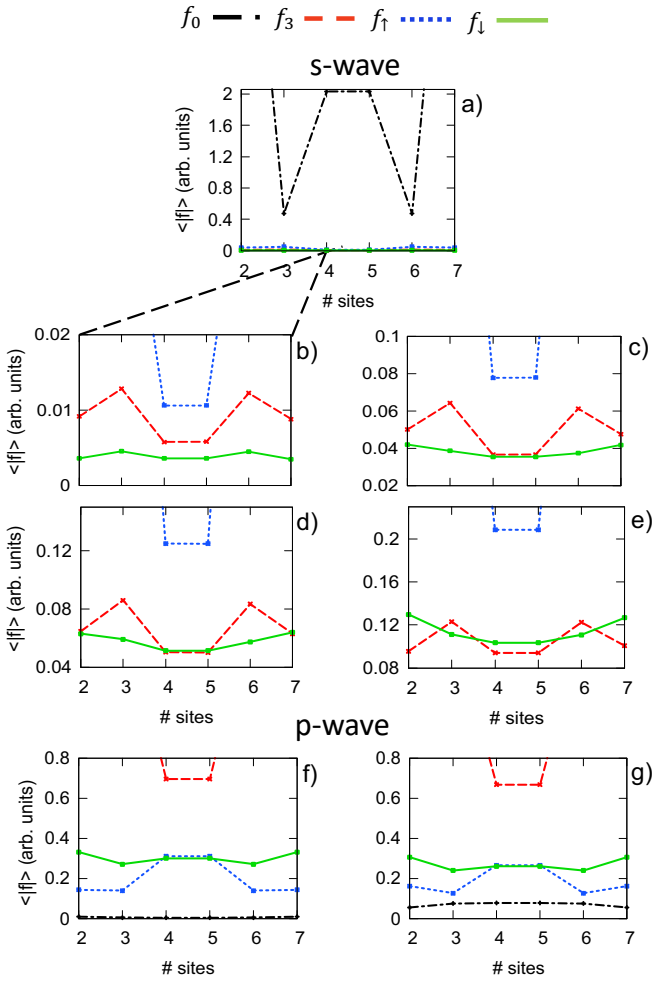

Figure 2.9: Module of spatial profile of s and p-wave pairing components, calculated at $h = 0.45$, $\alpha = 0.04$, $T = 0.025T_c$ and $\phi = 0$, for $V_{imp} = 0.025$ (a, b, f), $V_{imp} = 0.125$ (c), $V_{imp} = 0.150$ (d) and $V_{imp} = 0.250$ (e, g).

simplicity only shown in Fig. 2.9 (a)); nevertheless, this is to be expected since we are considering a short-FI barrier directly coupled to conventional s-wave singlet SCs. Furthermore, f_0 is an even-frequency function and in the Matsubara summation it is reinforced. We observe that the s-wave spin-triplet pairings, initially generated by SOC at interfaces, survive throughout the FI region and intriguingly appear remarkably enhanced by the effect of increasing the impurity potential V_{imp}.

In the middle of the FI barrier (site # 4) we obtain that, passing from $V_{imp} = 0.025$ to $V_{imp} = 0.250$ (Figs. 2.9 (b, e)), the s-wave singlet f_0 (even-frequency) remains almost unchanged, while the s-wave spin-triplets (odd-frequency) f_3, $f_\uparrow$ and $f_\downarrow$ result increased by a factor ~ 15, ~ 21, ~ 33, respectively.

Further, in Figs. 2.9 (f, g), it is shown that a sizeable p-wave pairing is already induced in the FI layer in the nearly-clean situation ($V_{imp} = 0.025$). In this case, the majority contribution is provided by the zero-spin triplet (f_3). However, this latter results enlarged by the influence of non-magnetic disorder, while the triplet correlations (even frequency), contrary to s-wave ones, appear rather stable with respect to the

increment of lattice impurities. Finally, at site # 4 comparing the p-wave pairings with the s-wave ones corresponding to the highest value of impurities strength, we find that the equal-spin components $f_\uparrow$ and $f_\downarrow$ are almost of the same order of magnitude in both s and p-wave cases.

Our results highlight the importance of SFIS JJs with SOC and tuned impurities as promising platforms hosting unconventional odd-frequency superconductivity and showing sizeable equal-spin triplet pairings.

Moreover, we recognize a possible link between the presence of unconventional pairing mechanisms in the FI barrier and $I_C(T)$ behaviors characterized by broadened $0-\pi$ transitions, with both phenomena turning out to be consequence of the interplay of spin-mixing and disorder effects.

2.6 Summary

We focused our attention on the problem of the tunability of $0-\pi$ transitions in SFIS JJs. The possibility to realize controllable devices that can be switched between different working regimes (namely 0, $0-\pi$ and π) might be a further step toward the application of JJs with ferromagnetic links in superconducting circuitry [91]. We extended the analysis carried out in Ref.[73] to the case of $0-\pi$ junctions with FI barriers. Using a tight-binding BdG model we manage to study the temperature dependent transport properties of these devices. In particular, we studied the influence of spin-mixing and disorder effects on SFIS JJs, focusing on the $I_c(T)$ behavior and on the correlation functions. We pointed out the role of SOC in driving the switching between $0-\pi$ and 0 regimes and the capability to induce $0-\pi$ to π conversions by adding disorder to the system. In particular, the engineering of the impurity concentration (that is strongly linked with the model parameter V_{imp}) could lead to the realization of stable π junctions, highly desired for superconducting circuits.

Moreover, we figure out the opportunity to obtain a fully tunable system, starting from a π-JJ and tuning the spin-orbit field by external means. Tuning the SO-interaction in semiconducting quantum wells [118, 205, 206] can be achieved by gating the structure. In the devices studied here, this procedure is yet unexplored, but, as we have shown, could produce potentially interesting effects and it worths further investigation. In this context, the SFIS JJs analyzed here could represent an intriguing and unexplored platform which can be switched among the three different regimes.

As a further analysis, we studied the correlation functions in the presence of SOC and impurities. In particular, we observe an enhanced contribution of the odd-frequency pairings, i.e. s-wave triplets and p-wave singlet, due to the increasing of non-magnetic disorder. Therefore, we recognize these tunable SFIS JJ s as good candidates to host unconventional superconducting pairing mechanisms and source of sizeable spin-triplet superconductivity, confirming the results of Refs. [73, 91].

Chapter 3

Coexistence of spin-singlet and triplet currents in SFIS JJs

Our theoretical investigation on temperature-induced $0-\pi$ transitions in SFIS junctions, points out the role that spin-mixing, provided by spin-orbit coupling (SOC), and disorder effects may have in inducing unconventional $I_C(T)$ behaviors [90]. In particular, we observe how the presence of impurities promotes higher harmonics contributions in the CPR. These do not vanish at the transition temperature $T_{0-\pi}$, where the first harmonic is negligible, thus preventing the junction $I_C(T)$ going to 0 at the $0-\pi$ switching. When increasing the impurity potential strength, the typical cusp-like $I_C(T)$ behavior is transformed into a non-monotonic trend characterized by a local minimum, while, at the same time $T_{0-\pi}$ is progressively shifted toward lower values. Under proper conditions, this allows the system to reach a stable π regime all over the whole temperature range between $T = 0$ and $T = T_C$. On the other hand, the interplay between impurities and SOC tends to stabilize an intermediate $0-\pi$ regime characterized by a widened $0-\pi$ transition and a plateau region in the $I_C(T)$. Furthermore, we predict that these peculiar $I_C(T)$ characteristics are accompanied by the presence of unconventional odd-frequency pairing correlations of which a sizable fraction is of spin-triplet symmetry. These results suggest that the combined action of spin-mixing mechanisms and disorder might be also invoked to explain the *incipient* $0-\pi$ transitions observed in spin-filter JJs in Ref.[75].

For this reason, in this chapter, we apply our tight-binding BdG approach, reported in Chap. 1-2, to model the critical current characteristics, i.e. the $I_C(T)$ curves, of the NbN/GdN/NbN junctions analyzed in Refs.[75, 91]. We use the same 2D tight-binding Hamiltonian in Eqs. 2.5-2.9 to describe the SFIS JJs and we adjust accordingly the energy parameters to properly describe the samples under study.

By combining Rashba-like spin-orbit coupling, on-site non-magnetic impurities and on-site scalar fluctuations of the ferromagnet exchange field in the JJ Hamiltonian, we mimic the spin-mixing effects, that are very likely to occur in large ferromagnetic barriers due to magnetic impurities, domain wall structure or spin-active interfaces [75, 91].

Moreover, by computing the barrier Green's function in real space as shown in Chap. 1 we are able to analyze the spatial configuration of pair correlations inside the FI, in view of a better understanding of the link between *incipient* $0-\pi$ transitions

and spin-triplet supercurrents.

3.1 Modeling experimental junctions

In this section, we report the choice of the system parameters used to model the experimental JJs. Henceforth, we adopt units with $\hbar = c = k_B = 1$, where c is the speed of light, k_B is the Boltzmann constant and $\hbar$ is the reduced Planck constant. The junction plane coincides with the xy-plane whereas the exchange field $\mathbf{h}'$ is always in the perpendicular direction $\mathbf{h}' = h'\mathbf{z}$ (along the $\mathbf{z}$-direction), Fig. 3.1. All the energy

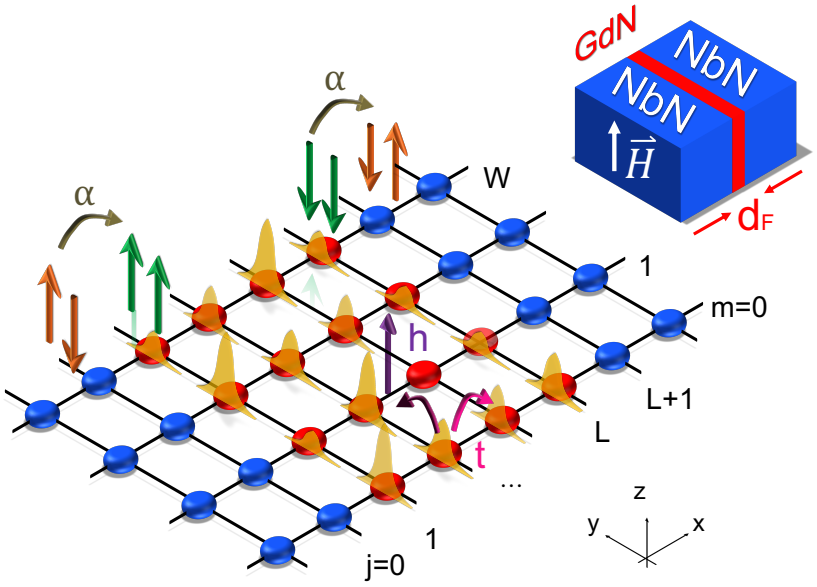

Figure 3.1: Picture of the Superconductor/Insulating ferromagnet/Superconductor (SFIS) junction $2D$-lattice model. The barrier (highlighted in red) has a total thickness L along x. The junction width is W along y. The spin-mixing mechanism due to the spin-orbit coupling is depicted by the spin-flipping process highlighted at the interface between the superconducting boundaries (blue sites) and the barrier. The impurities, with random strength depicted by the height of the yellow potential peaks, are represented on each site of the lattice. The exchange field h (violet arrow) is parallel to the z axis, while the hopping t between nearest-neighbor sites is here represented by pink arrows. In the inset, sketch of the experimental NbN-GdN-NbN Josephson junctions. The external magnetic field H is parallel to the z axis, [91]

parameters are expressed in dimensionless units where the energy scale is the hopping t in the FI. The α is scaled by ta (with a lattice constant), while the Josephson current is calculated in units of $J_0 = \mathrm{e}\Delta$.

In our simulations, we fix several parameters as $t = 1$, $\mu_{FI} = 0$, $\mu_s = 3$, $\Delta = 0.005$, $h = 0.25$. Further, we note that NbN (S leads) and GdN (FI barrier) are characterized by almost equal hopping parameters [207–209], which are, thus, set equal $t_s = t$ for the sake of simplicity. As a matter of fact, in order to have a good agreement with

experimental data, we model these devices as tunnel junctions with GdN barrier in the ferromagnetic half metal regime [210–212]. Thus, we choose to assume different chemical potentials for the S and FI regions. The estimate for the exchange energy $h = \left|\vec{h}\right|$ is chosen in agreement to the exchange field measured in several works for the bulk GdN [130, 208, 209, 213, 214], given that $t \approx 3\,\text{eV}$ [207–209] and the experimental constant lattice of GdN is $a_{GdN} = 4.974\,\text{Å}$.

When modeling the experiments, we use α as a measure of the spin-mixing and it is chosen to be $\alpha = 0.04$, unless otherwise indicated. Although we choose a small spin-orbit field so that $\alpha \ll h$, it breaks the spin symmetry at interfaces and is sufficient to cause the generation of long-range equal-spin triplet correlations with total spin projection $S_z = \pm 1$.

Finally, the strength of on-site impurities is randomly extracted from a uniform distribution in the range $-V_{imp}/2 < v_{\vec{r}} < V_{imp}/2$. Here, we take V_{imp} in the range $0.05 - 0.50$. The chosen values of V_{imp} will be reported below where we will specify our considerations to the different analyses carried out in the main text. Due to the presence of disorder, we perform ensemble averages over several samples to obtain the final $I_c(T)$ curves and correlations. In particular, we use $N_S = 50 - 100$ samples to compute the average $I_c(T)$ and $N_S = 200 - 300$ samples for the average correlation functions, depending on the strength of V_{imp}.

To model the $I_c(T)$ curves of the experimental JJs with barrier thickness $d_F = 3.0, 3.5, 4.0\,\text{nm}$, we choose systems with dimensions in the $\mathbf{x}$ and $\mathbf{y}$ directions, respectively: $(L = 8,\ W = 24)$, $(L = 8,\ W = 28)$, $(L = 8, W = 32)$, expressed in units of lattice sites.

Tunnel junctions experience an exponential suppression of the critical current when increasing the barrier thickness. In our model, this implies dealing with systems of few lattice sites, hence, we choose $L = 8$ and keep it fixed in all the numerical simulations, in agreement with the short-junction limit. However, the main effect of increasing the experimental sample thickness (and so the magnetic area of the FI) consists in enhancing the magnetic activity of the junction [75].

In our model, we manage to mimic this effect by changing the flux of the exchange field $\Phi(h) = LWh$ through the JJ (by the means of the width of the barrier W) and by tuning the impurity potential strength V_{imp} (thus, changing the influence of disorder effects in the system). In particular, by varying the width of the barrier W, we change the JJ effective area. In this way, we are able to control the exchange field flux $\Phi(h) = LWh$, without modifying the value of h, which is kept fixed to that of the bulk GdN [130, 208, 209, 213, 214]. Therefore, we use $\Phi(h)$ and V_{imp} as effective control parameters to model the peculiar $I_c(T)$ behavior of different junctions.

We notice that the Hamiltonian parameters, as well as the lattice size, have no microscopic origin and are chosen to describe the main mechanisms that are expected to occur in the experimental devices. Even though the lattice size is scaled down compared to the experimental system, we think that our theoretical model should give qualitatively an accordance with the experimental results as long as the model parameters are adjusted accordingly.

3.2 Unconventional incipient $0-\pi$ transitions

In this section, we focus on the peculiar behavior of the $I_c(T)$ in tunnel ferromagnetic spin-filter JJs studied in Ref.[75]. These samples, in Fig. 3.2, show unconventional incipient $0-\pi$ transitions for which the I_c is not suppressed at transition temperature,$T_{0-\pi}$. In practice, these devices are characterized by $I_c(T)$ curves showing a region in which the I_c is constant in a wide range of temperatures, i.e. a plateau, or shows a non-monotonic trend characterized by a non-zero local minimum.

In Fig. 3.2 (a), (b) and (c), we show the comparison between the $I_c(T)$ curves measured down to 20 mK at zero field for the junctions with GdN barriers $d_F = 3.0$ nm, 3.5 nm and 4.0 nm (black points), respectively, and the simulations obtained with the tight-binding BdG lattice model (red straight lines). In the insets, we report the measured $I_c(T)$ values down to dilution temperatures.

The experimental data evolve from a plateau over a wide range of temperatures (a few Kelvins) observed for the junctions with GdN thickness $d_F = 3.0$ and 3.5 nm into a non-monotonic $I_c(T)$ curve for the junction with $d_F = 4.0$ nm. The agreement between numerical outcomes and experimental data is certified by the capability to reproduce the unconventional plateau (Fig. 3.2 (a) and (b)) and the non-monotonic behavior (Fig. 3.2 (c)). We can relate the plateau in the $I_c(T)$ curve to an overall broadening of a $0-\pi$ transition in temperature. The calculated CPRs in Figs. 3.2 (d), (e) and (f) indicate that at low temperatures the JJs are in the 0-state (light blue gradient region in Figs. 3.2 (a), (b) and (c)), while at temperatures above $T = 0.7\ T_c$ the JJs are in the π state (red gradient region). Compared to what has been theoretically and experimentally observed in $0-\pi$ SFS and SFIS JJs [45, 56, 88, 106, 107], when the plateau is measured in the JJs with $d_F = 3.0$ nm and 3.5 nm in Figs. 3.2 (a) and (b), the CPRs exhibit the presence of higher order harmonics in the Josephson current J for a wide range of temperatures (yellow gradient region). The transition region is reduced when the $I_c(T)$ curve gradually points towards a non monotonic behavior, as shown in Fig. 3.2 (c). In all the cases reported in Fig. 3.2, the $0-\pi$ transition extends over a few Kelvins in temperature around 4.2 K, in agreement with previous findings reported in Ref. [108].

3.3 Spin triplet supercurrents and $0-\pi$ transitions

In order to investigate the symmetries of proximity induced superconducting pairings in the GdN layer, we derive the pair correlations from the computed barrier GF, Eq. 1.48, by exploiting the results in Eqs. 1.51-1.53

In Fig.3.3, we show the amplitude of the correlation functions $\langle|f|\rangle$ ($\langle\cdot\rangle$ indicates the ensemble average, due to the presence of random on-site impurities) determined from numerical simulations for the three devices at $T = 0.025\ T_c$ (corresponding to 0.3 K) and $\phi = 0$, where ϕ is the phase-difference across the device. The correlation functions are determined for the spin-singlet (f_0), spin-triplet with opposite spins (f_3) and equal-spin triplet functions ($f_\uparrow$ and $f_\downarrow$), both in s-wave (Figs. 3.3 (a), (b) and (c)) and p-wave symmetries (Figs. 3.3 (d), (e) and (f)), as a function of the position in the lattice along the x direction, with index $j = 1, \ldots, L$. In order to assure the total antisymmetry of the fermionic wave-function, triplet superconductivity for even-

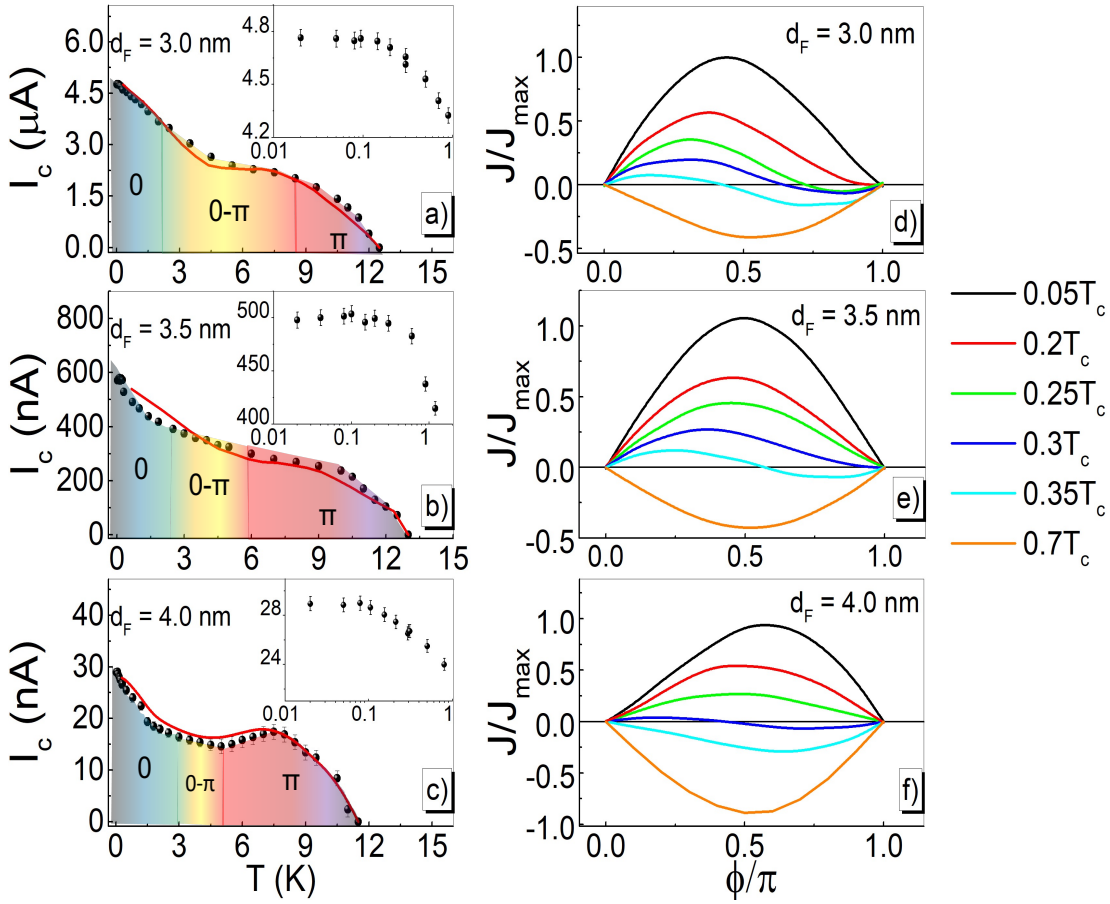

Figure 3.2: Comparison between the experimental $I_c(T)$ curves, tight-binding BdG simulations and corresponding CPRs. Critical current I_c as a function of the temperature T curves (black points) for spin-filter junctions with GdN barrier thickness $d_F = 3.0\,\text{nm}$ (a), $d_F = 3.5\,\text{nm}$ (b) and $d_F = 4.0\,\text{nm}$ (c). In the insets of figures (a), (b) and (c): measured saturation of the $I_c(T)$ down to 20 mK. The error bars on the measured I_c are of the order of 1% and represent the statistical error due to intrinsic critical current fluctuations [109]. The red lines are $I_c(T)$ curves obtained from the maximum of the CPR calculated with the RGF method from the tight-binding BdG Hamiltonian of the barrier. The amplitude of the simulated critical current has been multiplied by the experimental I_c measured at 20 mK. In (d), (e) and (f): CPRs at selected temperatures near the $0-\pi$ transition to highlight the arising of higher order harmonics, compared with those in the 0 and π state, at 0.05 T_c and 0.7 T_c, respectively, being T_c the critical temperature. The CPRs have been normalized to the maximum value of the current at 0.05 T_c. The color-gradient in (a), (b) and (c) represents the temperature range for the 0-state (light blue), the π state (light red), and the width of the $0-\pi$ transition region (yellow region), obtained from the CPRs in (d), (e) and (f).

frequency pairing is conventionally of p-wave type [215]. As shown in the following, for symmetry reasons here the dominant orbital part in the triplet pairing channel happens to be of s-wave type. All the cases show a dominant s-wave singlet component f_0 at the superconductor/barrier interface that strongly decays toward the middle of the barrier thickness. This is reasonable because the sides of the FI-layer are attached

to the superconducting leads with a usual BCS s-wave symmetry [11] and, due to the proximity effect, the singlet pair wavefunction enters the barrier. In the middle of the barrier (lattice position $j = 4$), where the spin mixing and the exchange field effects take place, a competition between the s-wave triplet and singlet pair amplitudes arises. On the contrary, for the p-wave case, the singlet component f_0 turns out to be much lower than the corresponding s-wave one. At the same time, we may observe a prevalence of the zero-spin p-wave triplet component f_3 at the superconductor/barrier interface, while in the middle of the barrier thickness the spin-aligned triplet correlations become relevant. These results are justified by symmetry considerations [58, 65, 72]. Indeed, for the s-wave symmetry, the singlet is an even-frequency function, while the triplets are odd-frequency. The viceversa is valid for the p-wave case. The 3.0 nm-thick barrier

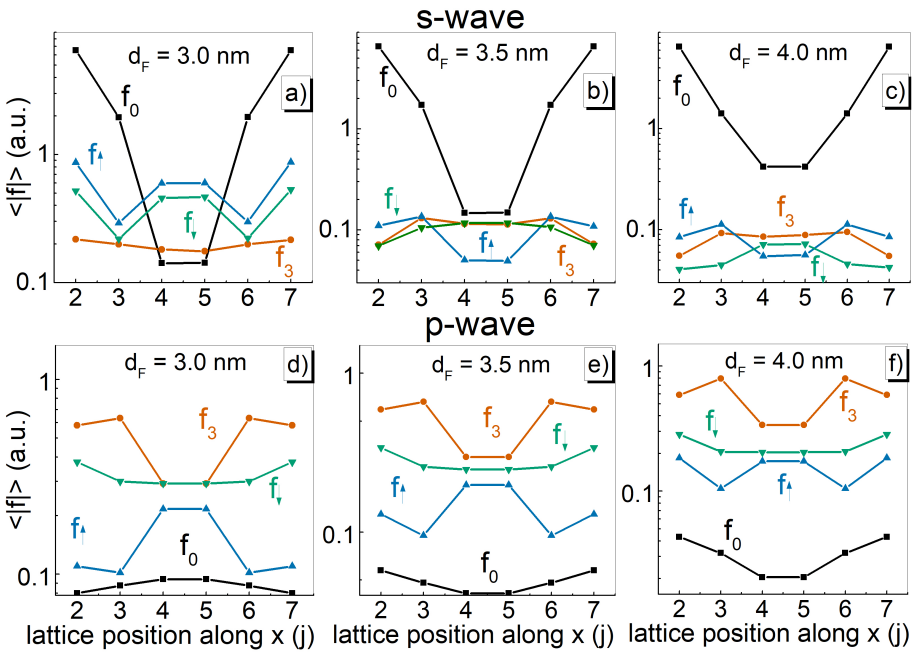

Figure 3.3: S- and p-wave spin-singlet and triplet pair-correlation amplitudes in the FI barrier. In (a), (b) and (c), the amplitudes of the ensamble average of the s-wave correlation functions $\langle|f|\rangle$, determined by numerical simulations at temperature $T = 0.025\ T_c$, being T_c the critical temperature, are shown as a function of the lattice position in the barrier along the x direction (with index j) for the junctions with GdN thickness $d_F = 3.0$, 3.5 and 4.0 nm, respectively. f_0 is the spin-singlet (black line and square symbols), f_3 is the opposite-spin triplet (red line and circles) and $f_\uparrow$ ($f_\downarrow$) is the equal-spin triplet with up (down) S_z projection (respectively, blue line and up-triangle symbols, and green line and down-triangle symbols). In (d), (e) and (f), we show the same correlation functions components for the p-wave symmetry. Data are reported on a log-scale to highlight the gradual suppression of the equal-spin triplet pair-correlation amplitude when pointing towards a non-monotonic critical current vs. temperature $I_c(T)$ curve.

junction exhibits s-wave triplet correlations functions larger than the singlet one, with a major contribution provided by the equal-spin triplet component with $S_z = +1$, $f_\uparrow$ (Fig. 3.3 (a)). For what concerns the p-wave spin-correlation functions for this device,

f_3 provides the main contribution at the borders, while $f_\downarrow$ competes with f_3 in the middle of the barrier (lattice position $j = 4$), as shown in Fig. 3.3 (d). Moreover, the opposite- and equal-spin p-wave triplet components are nearly a factor 2 larger than the corresponding s-wave singlet component. By increasing the thickness of the barrier, thus gradually pointing towards an incipient $0-\pi$ transition with a non-monotonic behavior in the $I_c(T)$ curve, in the s-wave cases we can observe a progressive suppression of the equal-spin triplet components and a dominant spin-singlet channel. At the same time, in the p-wave case, we observe a slight reduction of the ratio between the equal-spin triplets ($f_\uparrow$, $f_\downarrow$) and the major zero-spin component (f_3). Thus, the p-wave opposite spin-triplet components are of the same order of magnitude compared to the corresponding s-wave spin-singlet component, while the equal-spin triplet components are instead reduced.

Our theoretical results in Figs. 3.2-3.3 show that the characteristic behavior of the $I_c(T)$ is related to the amplitude of the different s-wave spin-correlation functions. In Tab. 3.1, we summarize the values of the pair-correlations in the middle of the barrier thickness (lattice position $j = 4$), in units of the majority zero-spin component, i. e. f_0 for the s-wave (Tab. 3.1 A) and f_3 for the p-wave cases (Tab. 3.1 B), respectively. Indeed, we observe a general decrease in the relative weight of the s-wave equal-spin triplet components ($f_\uparrow$ and $f_\downarrow$) in the junctions that show an increasing non-monotonicity of the $I_c(T)$ curves. Hence, the more $I_c(T)$ exhibits a behavior approaching the $0-\pi$ regime, the lower is the weight of the s-wave equal-spin correlations. This is in agreement with the fact that spin-aligned supercurrents are insensitive to exchange field and, thus, cannot give rise to $0-\pi$ transitions.

(A)		s-wave		(B)	p-wave	
d_F (nm)	$f_\uparrow/f_0$	$f_\downarrow/f_0$	f_3/f_0	$f_\uparrow/f_3$	$f_\downarrow/f_3$	f_0/f_3
3.0	4.21	3.23	1.28	0.74	1.00	0.32
3.5	0.34	0.80	0.78	0.67	0.84	0.14
4.0	0.11	0.15	0.20	0.51	0.60	0.06

Table 3.1: **S- and p-wave symmetry spin-correlations.** Ensamble average of the pair-correlation amplitudes $\langle\|f\|\rangle$, here represented as f, in the middle of the barrier (lattice position along x $j = 4$) for Josephson junctions with GdN thickness d_F: $f_\uparrow$ and $f_\downarrow$ for up- and down spin triplet correlation functions, respectively, f_3 for opposite-spin triplet, f_0 for spin-singlet. In (A) and (B), f is reported for both s- and p-wave symmetry in units of the major zero-spin component: spin-singlet f_0 for the s-wave correlations and the zero-spin triplet f_3 for the p-wave correlations, respectively

3.4 Tuning the $0-\pi$ transitions (and spin-triplet supercurrents) via external magnetic fields

As a further investigation on the spin-symmetries of Josephson current at the incipient $0-\pi$ transitions, the $I_c(T)$ response to an external magnetic field applied in the plane of the JJs has been measured [91]. In Fig. 3.4 we show the evolution of the normalized critical current $I_c(T, H/H_0)/I_c(0.3\,\mathrm{K}, H/H_0)$ as a function of a weak magnetic field H/H_0, where H_0 is the amplitude of the first lobe of the Fraunhofer pattern curve,

acquired by applying the magnetic field from $+2.4\,\mathrm{mT}$ to $-2.4\,\mathrm{mT}$. H_0 is estimated at each investigated temperature T (from $T = 0.3\,\mathrm{K}$ to $T = 8\,\mathrm{K}$). The results are reported

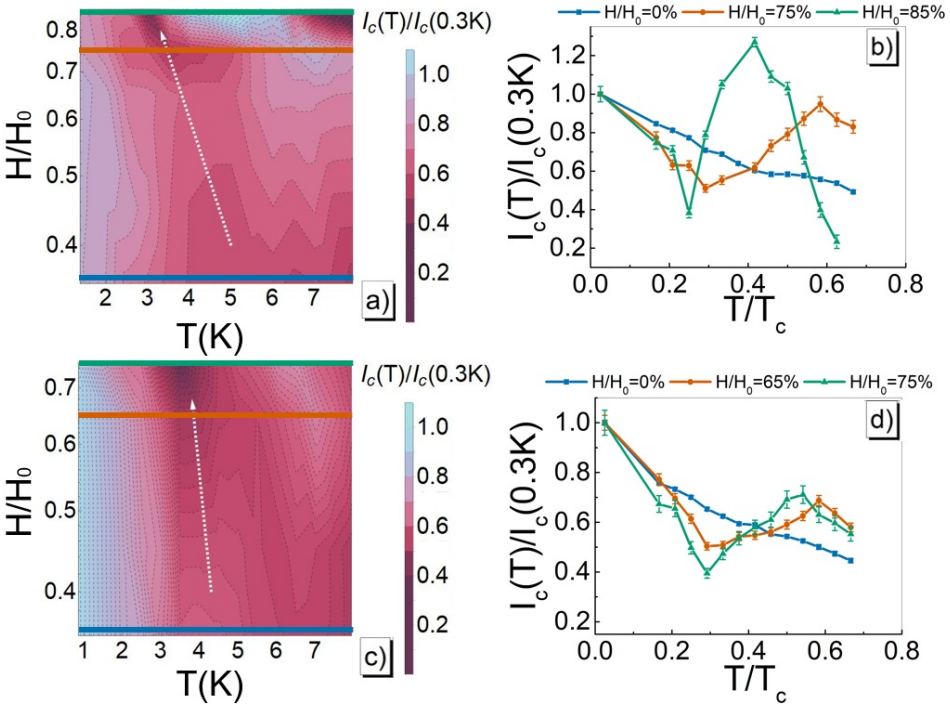

Figure 3.4: **Tuning of the $I_c(T)$ curves in the presence of an external magnetic field.** Normalized critical current $I_c(T, H/H_0)/I_c(0.3\,\mathrm{K}, H/H_0)$ density plots as a function of the percentage of magnetic field periodicity H/H_0 and the temperature T, for the Josephson junctions with GdN thickness (a) $d_F = 3.0\,\mathrm{nm}$ and (c) $d_F = 3.5\,\mathrm{nm}$. The critical current I_c values at each temperature T are measured by fixing the external magnetic field to H/H_0, where H_0 is the amplitude of the first-lobe of the Fraunhofer pattern measured at the same temperature T. Blue, red and green lines refer to the cross sections reported in (b) and (d): blue squares for $H/H_0 = 0\%$, red circles for $H/H_0 = 75\%$ in (b) and $H/H_0 = 65\%$ for (d), green triangles for $H/H_0 = 85\%$ for (b) and $H/H_0 = 75\%$ for (d). Straight lines in plots (b) and (d) are only a guide for the eye. The error bar on each measured point is of the order of few percents and it is due to intrinsic I_c fluctuations[109]. The white dashed arrows in (a) and (c) are a guide for the eye and highlights the shift of the minimum in the $I_c(T, H/H_0)/I_c(0.3\,\mathrm{K}, H/H_0)$ by increasing H/H_0.

in Fig. 3.4 in the two density-plots (a) and (c) for the junctions with $d_F = 3.0\,\mathrm{nm}$ and $3.5\,\mathrm{nm}$, respectively. Increasing the field H/H_0, the plateau structure at zero field evolves into a non-monotonic behavior with a minimum (dark region around $70-80\%H_0$ and between 2 and 4 K) and a maximum (bright region around $70-80\%H_0$ and between 4 and 6 K). The effect is more pronounced for the JJ with $d_F = 3.0\,\mathrm{nm}$. The blue, green and red dashed line cuts are related to the cross-section curves reported in Fig. 3.4 (b) and (d), where the gradual appearance of an enhanced dip and a non-monotonic behavior in the normalized $I_c(T)$ curves can be observed by increasing H/H_0.

These samples hence turn out to be sensitive to weak magnetic fields [75, 108, 109]. Even if the strength of the external magnetic field is not enough to generate a

complete magnetic ordering, slight modifications in the microscopic structure of the barrier arise [216], which has been already predicted to occurr in systems with tunable domain walls [217], intrinsic SOC [218] and magnetic impurities [151]. At zero field, the magnetic disorder is maximum and likely introduces electronic defect states in the barrier [219]. As the field increases, the system evolves towards a more ordered phase, and hence defect states density reduces. Therefore, the tunability of the $I_c(T)$ shape from the plateau towards a non-monotonic curve by applying an external magnetic field can be related to a reduction of the disorder in the barrier.

This picture is supported by numerical simulations obtained when changing the strength of the impurity potential in the $2D$-lattice model while keeping fixed all the other parameters. As a matter of fact, in order to have a good agreement with experimental data, we model the GdN as a ferromagnetic half metal [210–212]. Hence, local impurity potentials in the FI barrier are assumed to induce small site-dependent fluctuations of the chemical potential. In our approach, the coexistence of spin mixing mechanisms, promoted by SOC-like interactions, and on-site impurities model the magnetic disorder. In Fig. 3.5 (a), in fact, we can notice that the characteristic $0-\pi$ behavior is modified by increasing the impurity potential V_{imp}. The enhancement of the impurity strength produces a shift of the minimum of the curve towards lower temperatures and higher critical current values, with a consequent broadening of the typical $0-\pi$ cusp that progressively gives rise to the plateau. Viceversa, decreasing V_{imp}, one can recover the $0-\pi$ transition. In Figs. 3.5 (b)-(g) we finally report the s- and p-wave correlation functions corresponding to simulated $I_c(T)$ curves for different impurity potentials V_{imp} in (a): $V_{imp}=0.3$, $V_{imp}=0.23$ and $V_{imp}=0.05$. We here take as a reference the JJ with $d_F=4.0\,\mathrm{nm}$, i.e. the simulations for lattice dimensions $L=8$, $W=32$. While the p-wave components appear to be approximately unaffected by disorder (Figs. 3.5 (e)-(g)), for the s-wave symmetry the effect of increasing the impurity strength V_{imp} results in a pronounced enhancement of the equal-spin triplet pairing correlations, $f_\uparrow$ and $f_\downarrow$ (e.g. Figs. 3.5 (b)-(d)).

In Fig. 3.6, we show how the impurities and the SOC affect the $I_c(T)$ shape. Lattice dimensions are $L=8, W=32$, i. e. they refer to the JJ with $d_F=4.0\,\mathrm{nm}$. To accomplish the $I_c(T)$ diagram, we select the following values for α and V_{imp}: from panels (a) to (d), (e) to (h), (i) to (l) and (m) to (p), $V_{imp}=0.05$, 0.23, 0.3, respectively, and from panels (a) to (m), (b) to (n), (c) to (o) and (d) to (p), $\alpha=0.2$, 0.1, 0.07, 0.04. For small values of α and V_{imp} (bright red- and blue-scales), the simulated $I_c(T)$ curve shows a cusp-like $0-\pi$ transition, provided that the exchange field h in the junction is non-zero, as it occurs in SFS JJs tipically reported in literature [45, 56, 88, 106, 107]. By increasing α (dark red-scale), the main effect is to reduce the height of the second maximum in the $I_c(T)$ curve, without recovering the plateau structure observed in SFIS JJs. At very large α (see panel (a) in Fig. 3.6), the $0-\pi$ transition is washed out and an AB-like shape sets in, stabilizing a "0"-phase. In this case the main contribution is expected from the spin-singlet, though the spin-triplet correlations are increased compared to the cases with smaller α.

At the same time, by keeping the spin-orbit field weak and by increasing V_{imp} (dark blue-scale), the minimum of the $0-\pi$ transition occurs at higher critical current values and it is broadened in temperature, but always showing a non-monotonic trend for the $I_c(T)$. The characteristic plateau structure is observed only when considering a

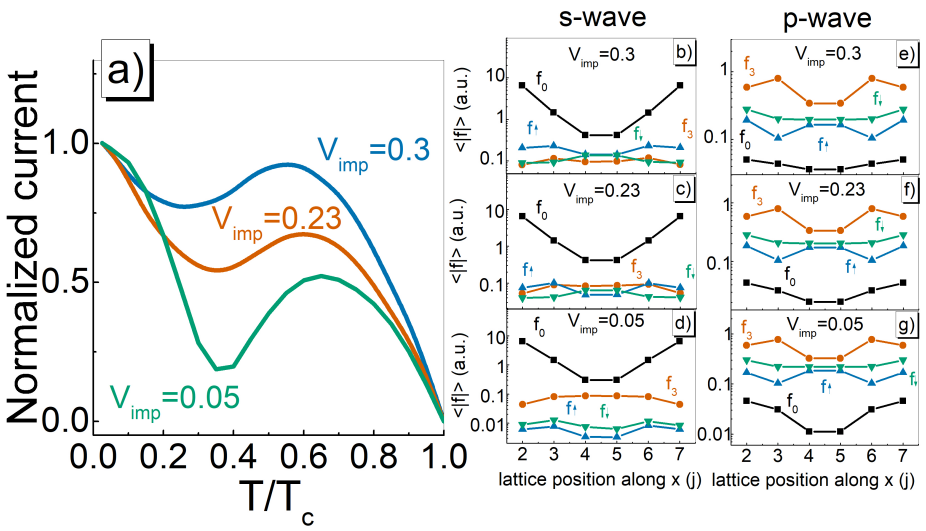

Figure 3.5: **Simulated $I_c(T)$ curves and calculated pair-correlation amplitudes as a function of the impurity potential.** In (a), normalized critical current I_c vs. temperature T curves simulated with the 2D-lattice model at fixed dimensions for three different impurity potential V_{imp} values: $V_{imp} = 0.05$ (green curve), $V_{imp} = 0.23$ (red curve) and $V_{imp} = 0.3$ (blue curve). The current is normalized to the maximum of the CPR at the lowest investigated temperature T, while T is normalized to the critical temperature T_c. In (b), (c) and (d), calculated s-wave ensamble average of the pair amplitude $\langle \|f\| \rangle$ in arbitrary units for different impurity potential values V_{imp} in (a). In (e), (f) and (g), calculated p-wave ensamble average of the pair amplitude $\langle \|f\| \rangle$ in arbitrary units for different impurity potential values V_{imp} in (a). f_0 is the spin-singlet component (black line and square symbols), f_3 is the opposite-spin triplet component (red line and circle symbols), $f_{\uparrow(\downarrow)}$ is the up (down) equal-spin triplet component (blue lines and up-triangle symbols, and green lines and down-triangle symbols, respectively). Both s- and p-wave data are reported on a log-scale.

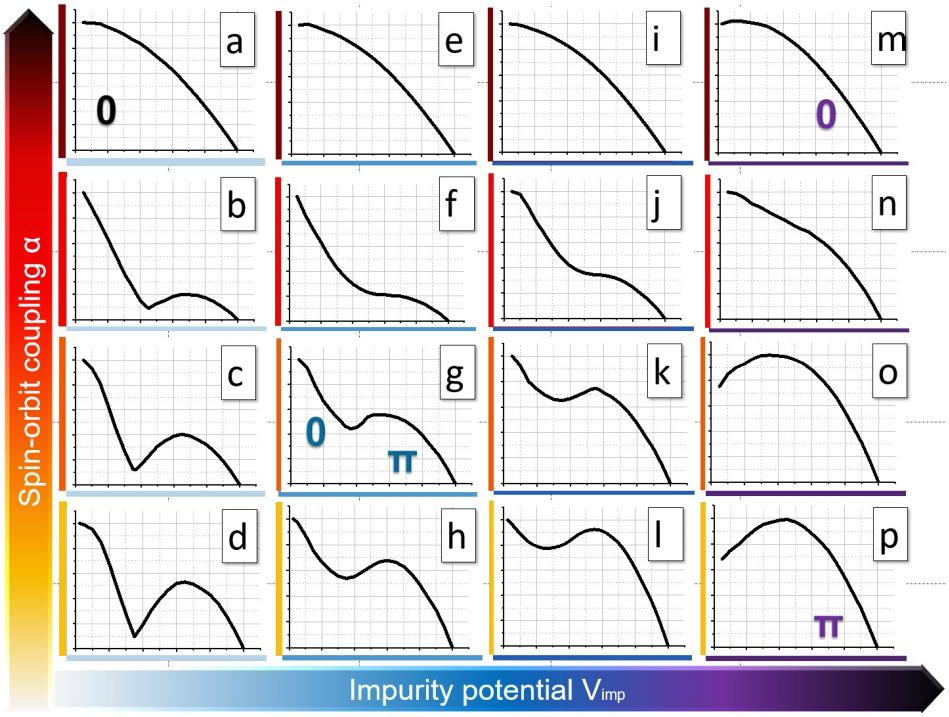

Figure 3.6: **Competition between the spin-orbit coupling and the impurity potential and their effect on the $I_c(T)$.** Normalized critical current I_c vs. T curves simulated with the tight-binding BdG 2D-lattice model as a function of the spin-orbit coupling α and the on-site impurity potential V_{imp}. In all the panels, the I_c (y-axis) is normalized to its value at the lowest temperature investigated, i.e. $T = 300\,\text{mK}$, while the T (x-axis) is normalized to the critical temperature of the device T_c. Red-color scale refers to increasing values of α, while blue-color scale refers to increasing V_{imp} values, with parameters reported in the main text. The scale on the y-axis on each plot ranges from 0 to 1.1, as on the x-axis. Minor thicks represent an increment of 0.1. We also highlight for sample curves in panel (a), (g), (m) and (p) the state of the Josephson junction: 0, $0-\pi$ or π.

combined effect of SOC and impurities, once fixed the dimensions of the system. As it is shown for the SFIS JJ with $d_F = 3.0\,\text{nm}$ in Fig. 18 (a) and Fig. 19 (a), the formation of the plateau goes along with the coexistence of comparable spin-singlet and triplet superconductivity. In the limit of large V_{imp} (see panel (p) in Fig. 3.6), the $0-\pi$ transition is shifted towards very low T values, stabilizing a "π"-phase almost over the whole temperature range. This evidence is given by the sharp decrease of I_c when the temperature drops. In this regime, in agreement with Fig. 3.5, we predict an enhanced contribution of the s-wave spin-triplet components due to the interplay of spin-orbit and disorder. In the limit of large V_{imp} and α (see panel (m) in Fig. 3.6), an AB-like behavior is recovered. This latter corresponds to a stable "0"-phase, reflecting the fact that, in the competition between SOC and impurity scattering, the equilibrium state is dominated by α. This also confirms the presence of a threshold value of α (at fixed value of h), above which the JJ is always in the "0"-phase [73, 90].

A transition between the peculiar plateau-shape of the $I_c(T)$ curve towards an incipient $0-\pi$-curve is experimentally observed increasing the strength of an external weak magnetic field (Fig. 3.4). The position in temperature of the $I_c(T)$ dip is an important benchmark relating the $0-\pi$ transition induced by the weak magnetic field to the combined effect of impurities, exchange field fluctuations and spin-orbit coupling in the simulations. For weak on-site impurity potential, by increasing α, the minimum of the $I_c(T)$ curve occurs at the same temperature. Instead, as shown in Fig. 3.5, when increasing V_{imp}, the minimum is shifted in temperature, as it occurs in the experimental $I_c(T)$ curves at a finite external magnetic field. We highlight the evolution of the $0-\pi$ transition and the dip shift in the experimental data in Fig. 3.4 (a) and (c) by using the dashed white arrow in figure.

3.5 Summary

We built on a previous study of the critical current $I_C(T)$ as a function of the temperature T in SFIS NbN-GdN-NbN JJs [75], to investigate the coexistence and tunability of singlet and triplet pairings. By using a tight-binding BdG approach and lattice Green's function techniques [73, 90, 135, 136], we modeled the $I_C(T)$ curves in the whole temperature range, along with the corresponding CPR as a function of the temperature T. We found correspondence between neat experimental benchmarks in the temperature behavior of the critical current, showing unconventional non-monotonicity and theoretical modeling. Lattice Green's function techniques allowed us to study the spin-singlet and triplet correlation functions in the FI barrier. Our results showed that such unconventional $I_c(T)$ behavior turns out to be the benchmark for the coexistence of spin-singlet and spin-triplet superconductivity in SFIS junctions [73, 135, 136]. These phenomena set in due to the combined effects of impurities and spin-mixing mechanisms. When the $I_C(T)$ curve shows a plateau over a wide range of temperatures, the competition between the singlet and triplet pairing amplitudes becomes significant, in both s-wave and p-wave symmetries. When the $I_C(T)$ curve exhibits an incipient $0-\pi$ transition, the equal-spin triplet component is gradually suppressed, becoming irrelevant in the limit case of a more standard cusp-like $0-\pi$ transition. This last situation corresponds to relative low values of disorder and spin-mixing effects. Our approach highlighted the role played by the disorder in the barrier in generating broadened $0-\pi$ transitions.

At the same time, the presence of a spin-mixing effect, in this context provided by the spin-orbit interaction, is crucial to reproduce the characteristic plateau in the $I_C(T)$ curves. Furthermore, the obtained results confirmed that the reinstatement of an overall ordering in the system by the means of an external magnetic field points towards the recovery of more standard $0 - \pi$ transition. Within this picture, the application of a weak magnetic field might represent a tool for controlling the relative weight of equal-spin-triplet transport in SFIS JJs.

Chapter 4

Current noise in magnetic $0-\pi$ Josephson junctions

In this chapter we investigate the current noise at $0-\pi$ transitions in magnetic Josephson junctions, in particular, whether these phases changes are accompanied by an increased sensitivity to magnetic noise. We consider a superconductor - quantum dot - superconductor (SQDS) JJ as a simple prototype of magnetic junction [92]. We study the equilibrium current noise in SQDS JJs in an external magnetic field in the presence of magnetic and dot energy fluctuations. We consider the case of static Gaussian noise, which is justified if the magnetic noise can be described in the "central spin model" within the "frozen spin approximation" [183, 184, 220]. We analyze the microscopic mechanisms underlying the current noise response to magnetic field fluctuations in these devices. Further, we investigate how to extract information about magnetic noise sources from current fluctuations, thus, paving the way to a novel spin-noise spectroscopy technique.

In the first section of this chapter, we introduce the SQDS JJ model and the different transport regimes that can be explored in these devices, i.e. short and long junction limits and resonant and non-resonant tunneling regimes. In second section, we recall how magnetic field driven $0-\pi$ transitions take place in SQDS JJs. Then, we study the link between the presence of Andreev bound states crossings in the JJ energy spectrum along $0-\pi$ switchings and the amplification of current noise sensitivity to magnetic fluctuations, in the case of non-resonant tunneling (i.e. when quantum dot is off-resonance with respect to the superconducting leads). At the end, we explore the possibility to exploit the enhanced current noise in these devices to probe magnetic fluctuations, thus, proposing a novel kind of spin-noise detector based on the Andreev levels sensitivity to magnetic fluctuations [92].

4.1 Quantum Dot Junction Model

SQDS junction Hamiltonian

We model the device as a Josephson junction with a single level quantum dot (QD) barrier of energy ε_d in an external magnetic field $\vec{B}_0$, that we here chose to lie along the z-axis, thus perpendicular to the transport plane, i.e. $x-y$ plane, Fig. 4.1.

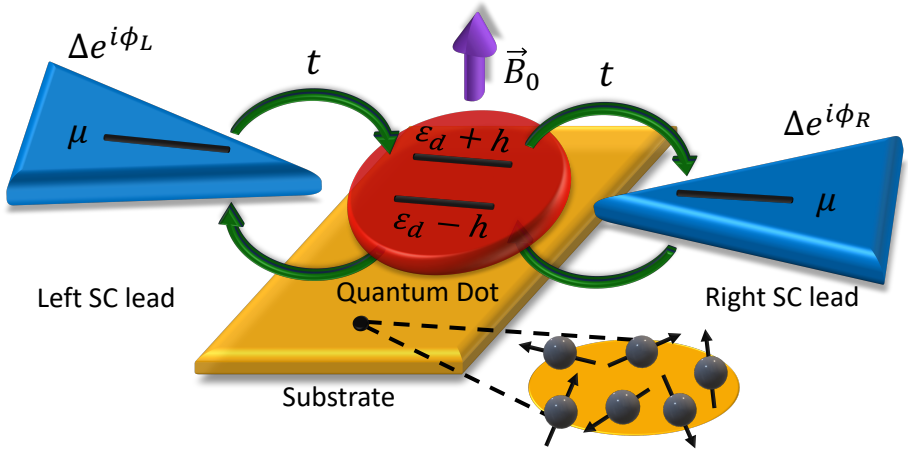

Figure 4.1: Scheme of the Superconductor - Quantum Dot -Superconductor Josephson junction (SQDS JJ) in the presence of an external magnetic field $\vec{B}_0$. Here, ε_d is the dot energy and $h = g\mu_B|\vec{B}_0|$ is the Zeeman splitting between the two spin channels affecting the dot level when $\vec{B}_0$ is turned on. The two s-wave superconductors are chosen to have equal gap Δ and chemical potential μ. $\phi_{L/R}$ is the superconducting phase of the L/R lead, respectively. t is the amplitude of the hopping integral among the superconducting leads and the dot. Finally, a sketch of the fluctuations in the orientation of nuclear spins in the substrate beneath the dot is reported.

In the presence of noise the Hamiltonian can be written as

$$H = H_{\rm S} + H_{\rm noise} \tag{4.1}$$

where $H_{\rm S}$ denotes the system Hamiltonian in the absence of fluctuations while $H_{\rm noise}$ accounts for noise fluctuations. The system Hamiltonian is:

$$H_{\rm S} = H_{\rm leads} + H_{\rm D} + H_{\rm T}\,, \tag{4.2}$$

where $H_{\rm D}$, $H_{\rm leads}$ and $H_{\rm T}$ are the dot, the leads and the tunneling Hamiltonian, respectively. The dot Hamiltonian, depends on the dot energy, ε_d, and the Zeeman splitting provided by the magnetic field, $\vec{h} = h\vec{z} = g\mu_B|\vec{B}_0|\vec{z}$, with μ_B and g denoting the Bohr magneton and the electronic gyromagnetic ratio:

$$H_{\rm D} = \varepsilon_d \sum_{\sigma=\uparrow,\downarrow} d_\sigma^\dagger d_\sigma + h\left(d_\uparrow^\dagger d_\uparrow - d_\downarrow^\dagger d_\downarrow\right)\,, \tag{4.3}$$

where d_σ indicates the annihilation operator for electrons of spin $\sigma =\uparrow,\downarrow$ on the dot. Following Ref.[162], we neglect Coulomb interaction on the dot. This assumption is justified in the limit of large coupling between the leads and the dot, namely the situation considered in the following sections. Indeed, if the transparency from the dot to the leads is close to unity, the lifetime of electrons on the dot is too short to observe Coulomb blockade effects [162, 176]. For the sake of simplicity, the superconducting electrodes are supposed to be s-wave with equal chemical potential μ, normal-state dispersion $\varepsilon_{\vec{k},\sigma}$

and superconducting gap Δ, thus yielding the following leads Hamiltonian

$$H_{\text{leads}} = \sum_{i=L,R} \sum_{\vec{k}} \sum_{\sigma=\uparrow,\downarrow} (\varepsilon_{\vec{k},\sigma} - \mu) c^{\dagger}_{i,\vec{k},\sigma} c_{i,\vec{k},\sigma} + \\ + \sum_{i=L,R} \sum_{\vec{k}} \Delta e^{i\phi_i} c^{\dagger}_{i,\vec{k},\uparrow} c^{\dagger}_{i,-\vec{k},\downarrow} + \text{H.c.}, \tag{4.4}$$

where $c_{i,\vec{k},\sigma}$ represents the annihilation operator for electrons in the state $\vec{k}$ with spin σ on the lead i ($i = L, R$). Here, ϕ_i is the superconducting phase in the lead i. We set $\phi_L = -\phi/2$, $\phi_R = \phi/2$ and $\mu = 0$.

The tunneling Hamiltonian H_{T} reads

$$H_{\text{T}} = t \sum_{i=L,R} \sum_{\vec{k}} \sum_{\sigma} c^{\dagger}_{i,\vec{k},\sigma} d_{\sigma} + \text{H.c.}, \tag{4.5}$$

where the hopping amplitudes between the leads and the dot are chosen to be equal and $\vec{k}$-independent for both leads.

We assume rigid superconductors and constant hopping amplitude. The noise Hamiltonian H_{noise} only involves fluctuations of the dot energy and Zeeman field, i.e. $\delta\varepsilon_d$ and $\delta\vec{h}$, where the latter, in principle, can be non-collinear to the equilibrium Zeeman field $h\vec{z}$

$$H_{\text{noise}} = \delta\varepsilon_d \sum_{\sigma=\uparrow,\downarrow} d^{\dagger}_{\sigma} d_{\sigma} + \sum_{\sigma,\sigma'=\uparrow,\downarrow} d^{\dagger}_{\sigma} (\hat{\boldsymbol{\sigma}} \cdot \delta\vec{h}) d_{\sigma'} \,. \tag{4.6}$$

Here, $\hat{\boldsymbol{\sigma}} = (\hat{\sigma}_1, \hat{\sigma}_2, \hat{\sigma}_3)$ is the vector of the Pauli matrices in the spin space.

Fluctuations in dot energy, $\delta\varepsilon_d$, can originate from statistical retrapping processes of charge carriers in the substrate beneath the QD, possibly inducing fluctuations in the control gate voltage [180–182, 221, 222]. Fluctuations of the Zeeman field may arise, in this geometry, due to the interactions between the dot electrons and spins of the nuclei in the substrate that, for weak external fields, can be described within the so-called "central spin model" [183, 184, 220]. In this framework, the intrinsic dynamics of the spin-bath happens on time-scales $\tau_i \simeq 100\mu$s [183] and thus can be neglected. The noise Hamiltonian only involves the hyperfine coupling between electrons and nuclei of the substrate,

$$H^{\text{hf}}_{\text{noise}} \simeq \sum_{n} \sum_{\sigma,\sigma'=\uparrow,\downarrow} d^{\dagger}_{\sigma} A_n (\hat{\boldsymbol{\sigma}} \cdot \vec{I}_n) d_{\sigma'} \tag{4.7}$$

where $\vec{I}_n$ denotes the spin of the nucleus n and A_n quantifies the interaction between the n-th nucleus and the electron on the dot.

The effects of the hyperfine coupling between electrons and substrate nuclei, within the "frozen spin approximation" [184], yields, for an ensemble of N nuclei, an effective Overhauser field given by $\vec{B}_{\text{N}} = \sum_i A_i \vec{I}_i$ [183, 184]. Thus, Zeeman field fluctuations would simply read as $\delta\vec{h} = \mu_B g \delta\vec{B}_{\text{N}}$. It can be shown [183, 184] that, within this approximation, due to the rotational symmetry of the system, the direction of the total Zeeman coupling, i.e. $h\vec{z}+\delta\vec{h}$, does not affect the transport. Hence, later on we consider $\delta\vec{h}$ parallel to the equilibrium Zeeman field, i.e. $\delta\vec{h} = \delta h\vec{z}$.

Dot Green's function and Josephson current

Starting from the transport formalism described in Chap. 1, here, we define the QD, the lead i and the hopping Hamiltonian matrices in Nambu⊗spin space, $\check{H}_{\rm D}$, $\check{H}_{i,\vec{k}}$ and $\check{H}_T$, respectively, reading

$$\begin{aligned} &\check{H}_{i,\vec{k}} = (\varepsilon_{\vec{k}_i} - \mu_s)\hat{\tau}_3 \otimes \hat{\sigma}_0 + i\Delta e^{i\phi_i}\left(\frac{\hat{\tau}_1 + i\hat{\tau}_2}{2}\right) \otimes \hat{\sigma}_2 + \text{H.c.}, \\ &\check{H}_{\rm D} = \hat{\tau}_3 \otimes (\varepsilon_d \hat{\sigma}_0 + h\hat{\sigma}_3), \qquad \check{H}_T = t\hat{\tau}_3 \otimes \hat{\sigma}_0 \,. \end{aligned} \tag{4.8}$$

Then, we recall the Dyson equation for the dot GF, Eq. 4.9,

$$\check{G}_{dd}(\omega_n) = \left(i\omega_n \check{1} - \check{H}_D - \sum_{i=L,R} \check{H}_T \check{G}_i^0(\omega_n) \check{H}_T \right)^{-1} \quad , \tag{4.9}$$

where $\check{1}$ is the identity matrix in Nambu⊗spin space, $\check{G}_i^0(\omega_n)$ is *bare* GF of the lead i ($i = L, R$) and we set $\hbar = k_B = 1$.

For the sake of completeness, we recall that from the dot GF poles we access the knowledge about the junction ABS spectrum [4, 5, 162]. Performing the analytic continuation of Eq. 4.9, i.e. $i\omega_n \to z$, we obtain the ABS by solving in z the following secular equation:

$$\det\left(z\check{1} - \check{H}_D - \sum_{i=L,R} \check{H}_T \check{G}_i^0(z) \check{H}_T \right) = 0. \tag{4.10}$$

Here, we approximate normal-state dispersion $\varepsilon_{\vec{k},\sigma}$ of the two leads, assuming that they are described by a flat band with a constant density of state ρ_0 (i.e. the leads density of states at the Fermi level) [162, 176, 203]. Under this assumptions, $\check{G}_i^0(\omega_n)$ reads [92, 162, 176, 203]

$$\check{G}_i^0(\omega_n) = \frac{-i\omega_n \pi\rho_0}{\sqrt{\Delta^2 + \omega_n^2}}\check{1} + \frac{i\Delta\pi\rho_0}{\sqrt{\Delta^2 + \omega_n^2}} \left(e^{i\phi_i}\left(\frac{\hat{\tau}_1 + i\hat{\tau}_2}{2}\right) - e^{-i\phi_i}\left(\frac{\hat{\tau}_1 - i\hat{\tau}_2}{2}\right)\right) \otimes \hat{\sigma}_2 \,. \tag{4.11}$$

Then, using the results of Eqs. 4.9 and 4.11, it easy to derive the $\hat{G}_{dd}(\omega_n)$ for the Hamiltonian in Eq. 4.8.

Defining the auxiliary matrix $\hat{P}(\omega_n)$ as

$$\check{P}(\omega_n) = \left(i\omega_n \check{1} - \check{H}_D - \sum_{i=L,R} \check{H}_T \check{G}_i^0(\omega_n) \check{H}_T \right) \quad , \tag{4.12}$$

and introducing $\Gamma = 2\pi\rho_0 t^2$ [162, 176, 203, 204], describing the dot-lead hybridization,

we can explicitly write $\check{G}_{dd}(\omega_n)$ as follows :

$$\check{G}_{dd}(\omega_n) = \frac{1}{\det\left(\check{P}(\omega_n)\right)}\times \tag{4.13}$$

$$\begin{pmatrix} \frac{i\Gamma\omega_n}{\sqrt{\Delta^2+\omega_n^2}}-h+i\omega_n-\varepsilon_d & 0 & 0 & \frac{\Gamma\Delta}{2}\frac{\left(e^{-\frac{i\phi}{2}}+e^{\frac{i\phi}{2}}\right)}{\sqrt{\Delta^2+\omega_n^2}} \\ 0 & \frac{i\Gamma\omega_n}{\sqrt{\Delta^2+\omega_n^2}}+h+i\omega_n-\varepsilon_d & -\frac{\Gamma\Delta}{2}\frac{\left(e^{-\frac{i\phi}{2}}+e^{\frac{i\phi}{2}}\right)}{\sqrt{\Delta^2+\omega_n^2}} & 0 \\ 0 & -\frac{\Gamma\Delta}{2}\frac{\left(e^{-\frac{i\phi}{2}}+e^{\frac{i\phi}{2}}\right)}{\sqrt{\Delta^2+\omega_n^2}} & \frac{i\Gamma\omega_n}{\sqrt{\Delta^2+\omega_n^2}}+h+i\omega_n+\varepsilon_d & 0 \\ \frac{\Gamma\Delta}{2}\frac{\left(e^{-\frac{i\phi}{2}}+e^{\frac{i\phi}{2}}\right)}{\sqrt{\Delta^2+\omega_n^2}} & 0 & 0 & \frac{i\Gamma\omega_n}{\sqrt{\Delta^2+\omega_n^2}}-h+i\omega_n+\varepsilon_d \end{pmatrix},$$

where $\det\left(\check{P}(\omega_n)\right)$ reads

$$\begin{aligned}\det\left(\check{P}(\omega_n)\right) = &\left(\left(i\omega_n+\frac{i\omega_n\Gamma}{\sqrt{\Delta^2-(i\omega_n)^2}}-h\right)^2-\varepsilon_d^2-\frac{\Gamma^2\Delta^2\cos\left(\phi/2\right)^2}{\Delta^2-(i\omega_n)^2}\right)\times \\ &\left(\left(i\omega_n+\frac{i\omega_n\Gamma}{\sqrt{\Delta^2-(i\omega_n)^2}}+h\right)^2-\varepsilon_d^2-\frac{\Gamma^2\Delta^2\cos\left(\phi/2\right)^2}{\Delta^2-(i\omega_n)^2}\right).\end{aligned} \tag{4.14}$$

Once the *interacting* dot GF $\check{G}_{dd}$ is obtained, also the GFs connecting leads and dot, entering the Josephson current in Eq. 1.29, can be calculated by the means of perturbation theory. Their expression at the first non-vanishing order in the interaction ($\check{H}_T$) are, respectively:

$$\begin{aligned}\check{G}_{c_Rd} &\simeq \check{G}_{dd}\check{H}_T\check{G}^0_R, \\ \check{G}_{dc_R} &\simeq \check{G}^0_R\check{H}_T\check{G}_{dd}.\end{aligned} \tag{4.15}$$

By recalling that $\check{G}_{dd}$ and $\check{G}^0_i$ structure in Nambu$\otimes$spin space is given by

$$\check{G}_{dd} = \begin{pmatrix} \hat{G}_{dd} & \hat{F}_{dd} \\ -\hat{F}^*_{dd} & -\hat{G}^*_{dd}\end{pmatrix}, \quad \check{G}^0_i = \begin{pmatrix} \hat{G}^0_i & \hat{F}^0_i \\ -\hat{F}^{0,*}_i & -\hat{G}^{0,*}_i\end{pmatrix}. \tag{4.16}$$

and exploiting Eqs. 4.5 and 4.15, the CPR formula, Eq. 1.29, can be further simplified

$$J\left(\phi\right) = \frac{iet^2}{2}T\sum_{\omega_n} Tr_\sigma\left[\hat{F}_{dd}(\omega_n)\hat{F}^{0,*}_R(\omega_n) - \hat{F}^0_R(\omega_n)\hat{F}^*_{dd}(\omega_n)\right], \tag{4.17}$$

where the trace over the Nambu space has been performed and the remaining trace Tr_σ is over the spin space. Here, $\hat{F}_{dd}$ and $\hat{F}^0_R$ are the anomalous blocks (in spin space) of the dot and bare R lead GFs, respectively. It is worth noticing that only the superconducting correlation functions of the dot and bare R lead contribute to the charge transfer across the junction [203].

Finally, we can write the more clear-cut Josephson current equation by expliciting the dot and right lead GFs, i.e. $\hat{F}_{dd}$ and $\hat{F}^0_R$, and performing the trace over spin space [92, 162, 168, 176, 203]

$$J(\phi) = eT\Delta\Gamma \sin\left(\frac{\phi}{2}\right) \sum_{\omega_n} \frac{\Re\left(F_{dd,\downarrow\uparrow}(\omega_n)\right)}{\sqrt{\Delta^2+\omega_n^2}}\,, \tag{4.18}$$

with $F_{dd,\downarrow\uparrow}(\omega_n)$ being the $\downarrow\uparrow$ element of the anomalous dot GF. By analytic continuation of $F_{dd,\downarrow\uparrow}(\omega_n)$, i.e. $i\omega_n \to z = \omega + i\eta^+$ (with $\eta^+ \to 0^+$), we can get the retarded dot GF $F^R_{dd,\downarrow\uparrow}(\omega)$ from which the expressions of Andreev levels and quasiparticles (continuum spectrum) current contributions can be derived. These, in the zero temperature limit, respectively read [176, 203, 204, 223]

$$J_{ABS}(\phi) = 2e\Gamma\Delta \sin\left(\frac{\phi}{2}\right) \int_{-\Delta}^{0} \frac{d\omega}{2\pi} \frac{\Im\left(F^R_{dd,\downarrow\uparrow}(\omega)\right)}{\sqrt{\Delta^2-\omega^2}}\,, \tag{4.19}$$

$$J_{QP}(\phi) = 2e\Gamma\Delta \sin\left(\frac{\phi}{2}\right) \int_{-\infty}^{-\Delta} \frac{d\omega}{2\pi} \frac{\Re\left(F^R_{dd,\downarrow\uparrow}(\omega)\right)}{\sqrt{\omega^2-\Delta^2}}\,. \tag{4.20}$$

In the following, the Josephson current J is scaled by $e\Delta$.

Choosing the transport regime

In SNS junctions ballistic and diffusive regimes differ from the fact that the electron mean free path l in N is, respectively, much longer and much shorter then the barrier length L. In ballistic regime the short junction condition, i.e. $\xi \gg L$, can be rewritten in terms of the superconducting gap Δ and the Thouless energy, defined as $E_{\mathrm{Th}} = v_F/L$ [167, 168, 192, 201, 202]. Since in the zero temperature limit $\xi = \xi_0 = v_F/\pi\Delta$, we have that

$$\xi \gg L \implies \Delta \ll E_{\mathrm{Th}}\,. \tag{4.21}$$

Similar considerations can be applied to the diffusive limit, i.e. $l \ll L$, where coherence length and Thouless energy read $\xi = \sqrt{D/(\pi\Delta)}$ and $E_{\mathrm{Th}} = D/L^2$ (D being the electron diffusion constant in N) [51, 167, 168, 192, 201, 202]. We collect these considerations in Tab.4.1.

	ξ	E_{Th}	Short junction	Long junction
ballistic	$v_F/(\pi\Delta)$	v_F/L	$\xi \gg L$ or $\Delta \ll E_{\mathrm{Th}}$	$\xi \ll L$ or $\Delta \gg E_{\mathrm{Th}}$
diffusive	$\sqrt{D/(\pi\Delta)}$	D/L^2	$\xi \gg L$ or $\Delta \ll E_{\mathrm{Th}}$	$\xi \ll L$ or $\Delta \gg E_{\mathrm{Th}}$

Table 4.1: Short and Long junction limits in ballistic and diffusive regimes in SNS JJs. Table adapted from [168].

In the SQDS JJ, where the ballistic transport condition is naturally satisfied, the line-width of the dot level Γ plays the same role of Thouless energy E_{Th} in diffusive SNS

JJs [167, 168, 192, 201, 202]. Thus, the small and long junction conditions reading, respectively, $\Delta \ll E_{\mathrm{Th}}$ and $\Delta \gg E_{\mathrm{Th}}$, simply become $\Delta \ll \Gamma$ and $\Delta \gg \Gamma$ [167, 168, 192]. For this reason, moving the JJ in short and long junction regimes, here, simply translates to tuning the value of Δ or Γ. Short junction limit is characterized by negligible quasiparticles contribution to Josephson current [167, 168, 192], thus representing the proper regime to simulate transport properties of novel tunnel ferromagnetic Josephson junctions with insulating barrier [73, 75, 78, 90, 91], more suitable for quantum circuits applications in view of the low quasiparticles current. For this reason, all along this work we analyze SQDS JJs characterized by $\Delta \ll \Gamma$ and all the energy parameters are scaled by Γ, that is chosen to be $\Gamma = 1$. Furthermore, in the framework of short junction regime, the dot energy ε_d, possibly controlled by external gate voltage, plays the role of further tuning parameter for the transport through the quantum dot junction. By tuning dot on and off resonance with the superconducting leads chemical potential, Fig. 4.2, we control the current flowing through the JJ, reaching two different regimes, respectively called "resonant" and "non-resonant" tunneling, the former being characterized by the maximum supercurrent achievable in these devices [167, 168, 192, 201, 202]. We summarize the transport regimes of the SQDS JJ that can be tuned by the

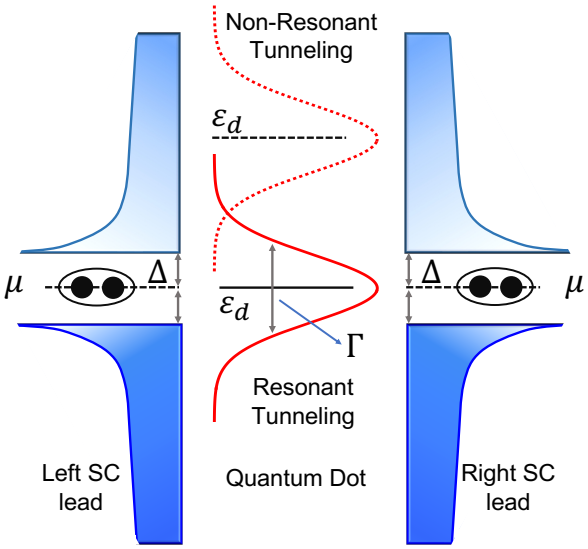

Figure 4.2: SQDS JJ level scheme in the absence of magnetic field. Dot level finite linewidth Γ is the result of hybridization with the leads. By controlling ε_d one can reach both "resonant" and "non-resonant" tunneling regime.

means of Δ/Γ and ε_d in Tab.4.2.

Regime	Tunneling	Δ/Γ	ε_d	quasiparticles current
Short	non-resonant	$\Delta \ll \Gamma$	$\varepsilon_d \neq \mu$	negligible
Short	resonant	$\Delta \ll \Gamma$	$\varepsilon_d = \mu$	negligible
Long	non-resonant	$\Delta \gg \Gamma$	$\varepsilon_d \neq \mu$	comparable with ABS
Long	resonant	$\Delta \gg \Gamma$	$\varepsilon_d = \mu$	comparable with ABS

Table 4.2: Short and Long junction regimes in resonant and non-resonant tunneling for SQDS JJs. Table adapted from [168].

4.2 Current noise in the static limit

We aim to exploit the junction current noise response as a probe of the magnetic noise source. Thus, we focus our attention on the intrinsic link between J and h fluctuations. In the following, we assume the two noise sources to be uncorrelated.

To keep the discussion simple, we further specify our analysis to the case of static Gaussian noise, where the QD degrees of freedom are characterized by time-independent zero-mean fluctuations, $\langle \delta h \rangle = \langle \delta \varepsilon_d \rangle = 0$, described by Gaussian probability distribution, $P(\delta\varepsilon_d)$ and $P(\delta h)$, with variance given by $\sigma^2_{\varepsilon_d} = \langle (\delta\varepsilon_d)^2 \rangle$ and $\sigma^2_h = \langle (\delta h)^2 \rangle$, respectively reading

$$P(\delta\varepsilon_d) = \frac{1}{\sqrt{2\pi}\sigma_{\varepsilon_d}} \exp\left(-\frac{(\delta\varepsilon_d)^2}{2\sigma^2_{\varepsilon_d}}\right), \quad P(\delta h) = \frac{1}{\sqrt{2\pi}\sigma_h} \exp\left(-\frac{(\delta h)^2}{2\sigma^2_h}\right) \tag{4.22}$$

The assumption of Gaussian static noise can be justified for magnetic fluctuations considering that, in the central spin model and "frozen spin approximation" [184], the Overhauser field $\vec{B}_{\mathrm{N}}$ yields classical static fluctuations, that in the limit of a large N are Gaussianly distributed with a standard deviation $\sigma_{B_{\mathrm{N}}} = B_{\mathrm{N\,max}}/\sqrt{N}$, $B_{\mathrm{N\,max}}$ indicating the maximum Overhauser field which is typically of the order of a few mT [129, 220, 224]. For an electron confined in a GaAs quantum dot and interacting with a typical number 100 spin-3/2 nuclei, this results in $\sigma_{B_{\mathrm{N}}} \sim 4$ mT [224] and, consequently, in an overall magnetic field with probability distribution given by $P(B_0) = \exp(-B_0^2/(2\sigma^2_{B_{\mathrm{N}}}))/(\sqrt{2\pi}\sigma_{B_{\mathrm{N}}})$. A careful discussion of the limits of validity of the frozen spin approximation in external magnetic fields can be found in Ref.[220]. In the context of Gaussian static noise, the SQDS JJ current-noise characterization reduces calculate the Josephson current variance as a function of the superconducting phase difference between the leads can be expressed as [178, 179, 225]:

$$\sigma^2_J(\phi) = \left\langle (\delta J(\phi))^2 \right\rangle = \left\langle J^2(\phi) \right\rangle - \left\langle J(\phi) \right\rangle^2 , \tag{4.23}$$

where $\langle \cdot \rangle$ is intended as the average over dot energy and Zeeman field fluctuations

distributions, $P(\delta\varepsilon_d)$ and $P(\delta h)$, thus yielding

$$\sigma_J^2(\phi) = \int_{-\infty}^{\infty} J^2(\phi, \varepsilon_d + \delta\varepsilon_d, h + \delta h)\, P(\delta\varepsilon_d) P(\delta h) d(\delta\varepsilon_d) d(\delta h) \\ - \left(\int_{-\infty}^{\infty} J(\phi, \varepsilon_d + \delta\varepsilon_d, h + \delta h)\, P(\delta\varepsilon_d) P(\delta h) d(\delta\varepsilon_d) d(\delta h) \right)^2 . \tag{4.24}$$

Small fluctuations

By assuming that the two noise channels, $\delta\varepsilon_d$ and δh, are uncorrelated, i.e. $\langle \delta\varepsilon_d \delta h \rangle = 0$, in the case of small fluctuations, i.e. for $\delta\varepsilon_d \approx \delta h \approx 0$, the CPR $J(\phi)$ can be expanded up to the second order as follows

$$J(\phi, \varepsilon_d, h) \approx J(\phi, \varepsilon_d, h)\Big|_{\substack{\delta\varepsilon_d=0 \\ \delta h=0}} + \frac{\partial J(\phi, \varepsilon_d, h)}{\partial h}\Big|_{\substack{\delta\varepsilon_d=0 \\ \delta h=0}} \delta h + \frac{\partial J(\phi, \varepsilon_d, h)}{\partial \varepsilon_d}\Big|_{\substack{\delta\varepsilon_d=0 \\ \delta h=0}} \delta\varepsilon_d \\ + \frac{1}{2}\frac{\partial^2 J(\phi, \varepsilon_d, h)}{\partial h^2}\Big|_{\substack{\delta\varepsilon_d=0 \\ \delta h=0}} \delta h^2 + \frac{1}{2}\frac{\partial^2 J(\phi, \varepsilon_d, h)}{\partial \varepsilon_d^2}\Big|_{\substack{\delta\varepsilon_d=0 \\ \delta h=0}} \delta\varepsilon_d^2, \tag{4.25}$$

yielding the following expression for the current fluctuations $\delta J = J - \langle J \rangle$

$$\delta J(\phi, \varepsilon_d, h) \approx \frac{\partial J(\phi, \varepsilon_d, h)}{\partial h}\Big|_{\substack{\delta\varepsilon_d=0 \\ \delta h=0}} \delta h + \frac{\partial J(\phi, \varepsilon_d, h)}{\partial \varepsilon_d}\Big|_{\substack{\delta\varepsilon_d=0 \\ \delta h=0}} \delta\varepsilon_d \\ + \frac{1}{2}\frac{\partial^2 J(\phi, \varepsilon_d, h)}{\partial h^2}\Big|_{\substack{\delta\varepsilon_d=0 \\ \delta h=0}} \left(\delta h^2 - \langle \delta h^2 \rangle\right) + \frac{1}{2}\frac{\partial^2 J(\phi, \varepsilon_d, h)}{\partial \varepsilon_d^2}\Big|_{\substack{\delta\varepsilon_d=0 \\ \delta h=0}} \left(\delta\varepsilon_d^2 - \langle \delta\varepsilon_d^2 \rangle\right), \tag{4.26}$$

where we use that $\langle \delta\varepsilon_d \rangle = 0$ and $\langle \delta h \rangle = 0$. Therefore, for uncorrelated noise sources small fluctuations expansion for $\sigma_J^2(\phi) = \langle \delta J^2(\phi) \rangle$ reads

$$\sigma_J^2(\phi, \varepsilon_d, h) = \left\langle \delta J^2(\phi, \varepsilon_d, h) \right\rangle = \left(\frac{\partial J(\varepsilon_d, h)}{\partial h}\Big|_{\substack{\delta\varepsilon_d=0 \\ \delta h=0}} \right)^2 \sigma_h^2 + \left(\frac{\partial J(\varepsilon_d, h)}{\partial h}\Big|_{\substack{\delta\varepsilon_d=0 \\ \delta h=0}} \right)^2 \sigma_{\varepsilon_d}^2 \\ + \frac{1}{2}\left(\frac{\partial^2 J(\varepsilon_d, h)}{\partial \varepsilon_d^2}\Big|_{\substack{\delta\varepsilon_d=0 \\ \delta h=0}} \right)^2 \sigma_{\varepsilon_d}^4 + \frac{1}{2}\left(\frac{\partial^2 J(\varepsilon_d, h)}{\partial h^2}\Big|_{\substack{\delta\varepsilon_d=0 \\ \delta h=0}} \right)^2 \sigma_h^4 \\ - \frac{1}{2}\left(\frac{\partial^2 J(\varepsilon_d, h)}{\partial \varepsilon_d^2}\Big|_{\substack{\delta\varepsilon_d=0 \\ \delta h=0}} \frac{\partial^2 J(\varepsilon_d, h)}{\partial h^2}\Big|_{\substack{\delta\varepsilon_d=0 \\ \delta h=0}} \right) \sigma_{\varepsilon_d}^2 \sigma_h^2, \tag{4.27}$$

Here, we use the fact that, for Gaussian distributions, all odd-order correlators vanish, i.e. $\left\langle (\delta\varepsilon_d)^{2n+1} \right\rangle = 0$ and $\left\langle (\delta h)^{2n+1} \right\rangle = 0$ with $n \in N$, and that the fourth

order moment of $\delta\varepsilon_d$ and δh can be expressed as $\left\langle(\delta\varepsilon_d)^4\right\rangle = 3\sigma^4_{\varepsilon_d}$ and $\left\langle(\delta h)^4\right\rangle = 3\sigma^4_h$, respectively [178, 179, 225].

Eq. 4.27, hence, relates the CPR variance to the width of ε_d and h statistical distributions, i.e. σ_{ε_d} and σ_h.

4.3 Zeeman field driven $0-\pi$ transitions in SQDS JJs

In this section, we analyze how Zeeman field driven $0-\pi$ transitions take place in a SQDS JJ [161–164]. In the following, we focus on the more general case in which the dot is off-resonance with respect to S leads chemical potential, i.e. $\varepsilon_d \neq 0$ in our case.

In Fig. 4.3, we show the ABS spectrum computed for increasing h along a Zeeman interaction driven $0-\pi$, transition. The Dot energy ε_d and Zeeman field amplitude h

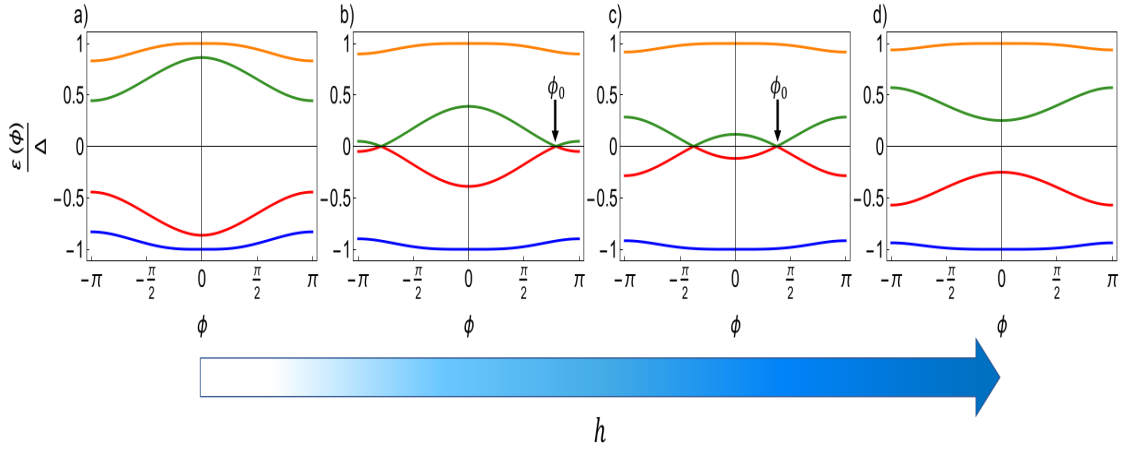

Figure 4.3: Andreev levels spectrum for the SQDS JJ ($\varepsilon_d = 1$, $\Gamma = 1$, $\Delta = 0.01$) along an exchange field induced $0-\pi$ transition, computed, from left to right, at $h = 0.5$ (a), $h = 1.05$ (b), $h = 1.3$ (c) and $h = 1.7$ (d), respectively. By increasing the Zeeman splitting between the different spin levels, Andreev Bound States (ABS) crossings at zero energy occur for $\phi = \pm\phi_0 \neq 0, \pm\pi$. Transition between the 0 and π phases is accomplished when the two near-zero ABS are switched.

affect the levels structure in different ways. The former opens up a gap in the Andreev spectrum, thus, moving apart the particle-hole symmetric levels. The latter introduces a Zeeman splitting between different spin channels [163, 164], Fig. 4.3(a), enhancing the exchange field strength leads to levels crossings at zero-energy when h effect on the ABS equals and overcomes the one of Dot energy ε_d, Fig. 4.3(b). At fixed Γ, crossings phase points $\pm\phi_0$ turn out to be only a function of h and ε_d. By further increasing the Dot Zeeman field the ABS crossing points are pushed toward $\phi_0 = 0$, Fig. 4.3 (c)., thus, driving the system to the π phase, where two particle-hole symmetric Andreev levels are switched, Fig. 4.3 (d).

In Appendix C, we demonstrate that the ABS crossings between particle-hole symmetric levels reflects in the occurrence of sharp jumps in the CPR, from positive to negative currents, at the crossings phases along $0-\pi$ transitions [161–166].

Indeed, the Andreev levels contributing to the junction supercurrent are those at negative energies, $\varepsilon(\phi) < 0$, i.e. those below the superconducting leads chemical potential. When ABS crossings appear, the near-zero state that actually carries current is a mix of the particle-like and hole-like levels and presents cusps at the ABS crossing phases $\pm\phi_0$, e.g. the level in red in Fig. 4.3 (b) and (c). Since, ABS contribution to Josephson current, $J_{ABS}(\phi)$, in the zero-temperature limit, can be simply computed by deriving the current-carrying levels with respect to ϕ [167, 168, 192, 201, 202]

$$J_{ABS}(\phi) = \sum_{j,\,\varepsilon\leq 0} \frac{\partial \varepsilon_j(\phi)}{\partial \phi}, \tag{4.28}$$

we can heuristically understand why the cusps lead to jump-like discontinuities in the CPR.

This effect is clearly visible in Fig. 4.4 where the junction CPRs $J(\phi)$ corresponding to the ABS spectra in Fig. 4.3, computed at temperature $T = 0.02\,T_C$, are reported. Peculiar jump-discontinuities in CPR are well known in ballistic quantum point contacts

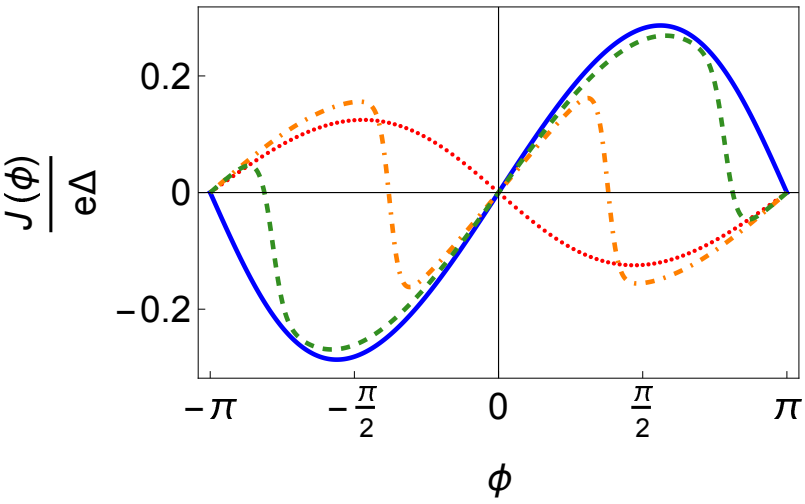

Figure 4.4: CPR behavior of the SQDS JJ (at $T = 0.02\,T_C$) corresponding to the ABS spectra in Fig. 4.3. $J(\phi)$ is computed at $h = 0.5$ (blue solid curve), $h = 1.05$ (green dashed curve), $h = 1.3$ (orange dotted-dashed curve) and $h = 1.7$ (red dotted curve), respectively. Along the $0-\pi$ transition the JJ shows peculiar CPR jump discontinuities at the ABS crossings.

(QPC) in resonant regime and short ballistic JJs [50, 163, 167–169, 171, 192, 202]. They have been already predicted in SQDS junctions along the $0-\pi$ switchings [50, 162, 170] also in the presence of Coulomb interaction on the Dot [161, 163, 165, 166, 173, 175–177, 191, 223], as well as in ferromagnetic Josephson devices with QPCs, e.g. SFcFS [50], and correspond to a state characterized by the presence of two minima in the total energy at $\phi = 0$ and π [50, 162, 163, 170].

This peculiar CPR behavior goes along with an enhanced contribution of higher harmonics, that is a well established signature of the transition from 0 (blue solid curve for $h = 0.5$) to π state (red dotted curve for $h = 1.7$) in JJs with ferromagnetic barriers [51, 58, 73, 90, 91]. We can better appreciate and summarize the transport

properties of the SQDS junction by looking at Fig. 4.5, where the density plot of the Josephson current as a function of the phase and exchange field, i.e. $J(\phi, h)$, (computed for $\varepsilon_d = 1$, $\Delta = 0.01$ and $T = 0.02\, T_C$) is presented. Josephson current

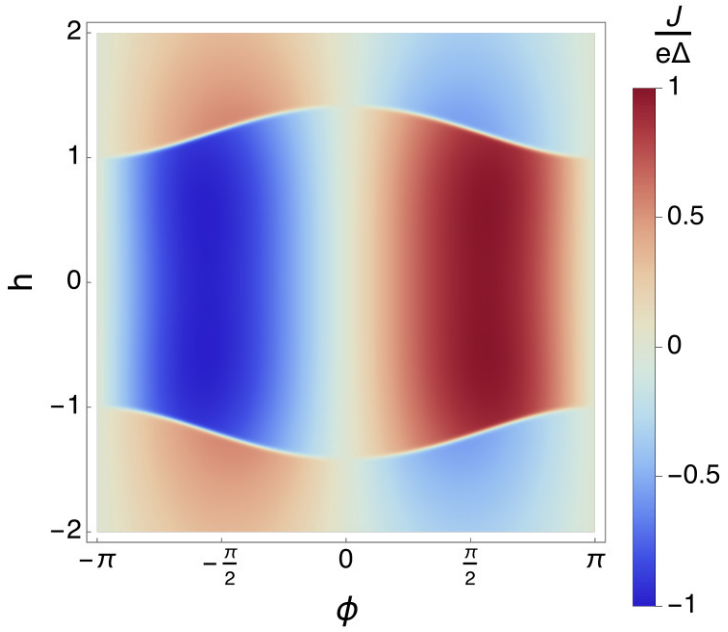

Figure 4.5: Density plot of Josephson current as a function of the phase and exchange field $J(\phi,h)$, computed at $\varepsilon_d = 1$, $\Gamma = 1$, $\Delta = 0.01$ and $T = 0.02\, T_C$. Transition between 0 and π phases is characterized by an intermediate transport regime in which the junction CPR shows peculiar jump-like discontinuities, abrupt change in the plot color when moving along the ϕ axis at fixed exchange field h value.

$J(\phi)$ is shown along the lines at fixed h value on the y-axis. In order to accomplish the $0-\pi$ transition, the system has to move across an intermediate regime in which the $J(\phi)$ shows sharp jump discontinuities, corresponding to sudden changes of color in the graphic. Furthermore, the junction starts its transitions toward the π state at $h = \pm 1$ lines when the Zeeman coupling equals the Dot energy, and ABS crossings appear at $\phi = \pm\pi$ in the energy spectrum. This corresponds to the situations in which one of the two Zeeman splitted Dot levels, with energy $\varepsilon = \varepsilon_d \pm h$ (Fig. 4.1), returns in resonance with the superconducting leads chemical potential, $\mu = 0$, thus entering the resonant tunneling regime [167, 168].

Current noise at $0-\pi$ transitions in non-resonant tunneling regime

The presence of CPR jumps at the ABS crossing phases, $\phi = \pm\phi_0$, gains relevance when the Hamiltonian parameters are affected by noise. In our case, CPR discontinuities may lead to an increased sensitivity of the current noise along the $0-\pi$ transition to ε_d and h fluctuations (Γ and Δ are kept fixed).

In particular, the abrupt change in sign of $J(\phi)$ leads to δ-like peaks in the current derivatives with respect to the dot energy and Zeeman field (see Appendix C). This effect can be observed in the $\partial_{\varepsilon_d} J(\phi)$ and $\partial_h J(\phi)$ density plots with respect to ϕ and h, in Figs.4.6 (a) and (b).

Here, $\partial_{\varepsilon_d} J(\phi)$ and $\partial_h J(\phi)$ amplitudes along the $0-\pi$ switching are increased by two orders of magnitude at the ABS crossings with respect to the background. In

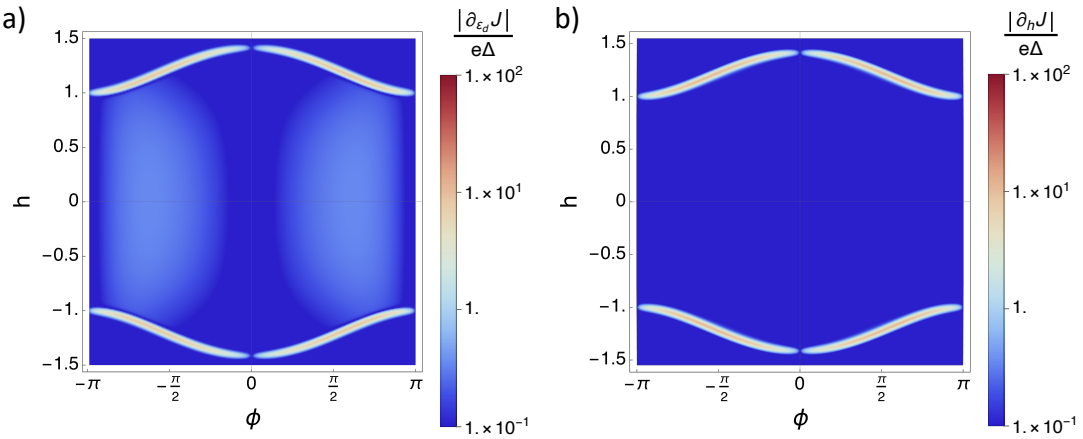

Figure 4.6: Density plots of the current derivatives along ε_d (a) and h (b) as a function of the phase and exchange field, $\partial_{\varepsilon_d} J(\phi,h)$ and $\partial_h J(\phi,h)$ ($\varepsilon_d = 1$, $\Gamma = 1$, $\Delta = 0.01$ and $T = 0.02\, T_C$). Along the $0-\pi$ transition $\partial_h J$ divergences at the CPR jumps appear, Fig. 4.5.

the presence of small fluctuations in the Zeeman field and/or dot energy, for which the expansion in Eq. 4.27 is valid, $\partial_{\varepsilon_d} J(\phi)/\partial_h J(\phi)$ divergences at ABS crossing phases suggest an enhanced current noise response to ε_d/h fluctuations. Amplified current noise response can be indeed found in Fig. 4.7 where we show the current variance σ_J^2 obtained with Eqs. 4.23-4.24 in the presence of both ε_d and h fluctuations taken with the same standard deviation $\sigma_{\varepsilon_d} = \sigma_h = 0.005$ for simplicity. In this density plot, we observe pronounced σ_J^2 peaks at the ABS crossing phases.

These results indicate that $0-\pi$ transitions in QD junctions and, in general, in short ballistic JJs, can be accompanied by enhanced current fluctuations, pointing out the CPR jumps to be a fingerprint of this noise amplification phenomenon. This might lead to decoherence effects when these are employed in superconducting qubits.

Mitigation of $0-\pi$ current noise via quasiparticles

The device sensitivity, whose fingerprint are the CPR jumps, is tightly connected to the Andreev spectrum dependence on the microscopic parameters, and it may be reduced in the presence of strong quasiparticles currents, that lower the current variance peaks. Indeed continuum levels live above the superconducting gap, $\varepsilon > \Delta$ and do not undergo to zero-energy crossings, thus, not contributing to the CPR jumps [92, 176, 203, 204, 223].

In Fig. 4.8, we analyze Andreev levels and quasiparticles current contributions for the CPR curve in Fig. 4.4 at $h = 1.05$ by varying the superconducting gap. We start from a deeply short junction limit, $\Delta = 0.01\Gamma$ to the case where $\Delta = \Gamma$.

The short junction regime is characterized by a negligible quasiparticles contribution to $J(\phi)$, Fig. 4.8 (a-b), when increasing the Δ/Γ ratio quasiparticles current gradually grows until reaching the same order of magnitude of ABS supercurrent when $\Delta \approx \Gamma$, as

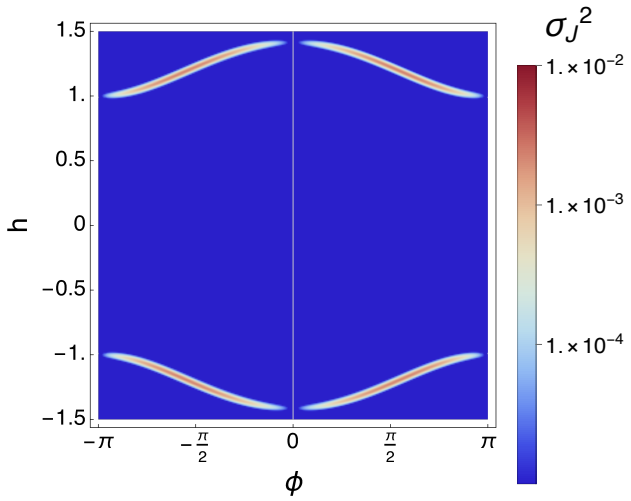

Figure 4.7: Density plot of current variance $\sigma_J^2(\phi, h)$, as a function of the superconducting phase difference and the exchange field, along the $0-\pi$ transition of Fig. 4.5, computed from the definition $\sigma_J^2(\phi, h) = \langle J^2(\phi)\rangle - \langle J(\phi)\rangle^2$ at $\varepsilon_d = 1$, $\Gamma = 1$, $\Delta = 0.01$, $T = 0.02\, T_C$ and $\sigma_{\varepsilon_d} = \sigma_h = 0.005$.

it is evident in Fig. 4.8 (c) . Moreover, here, we can appreciate that when quasiparticles contribution becomes sizable it is opposite in sign with respect to ABS current [162, 226], hence, leading to a reduction of the CPR jump. Hence, also the maximum of $\partial_{\varepsilon_d} J$ and $\partial_h J$ divergent peaks results decreased, since their height is proportional to the jump discontinuity in $J(\phi)$. This indicates a strong attenuation of the current noise sensitivity when the superconducting gap approaches the dot linewidth, as it is observable in Fig. 4.9. Interestingly, these findings suggest that a mitigation effect of the JJ sensitivity to magnetic fluctuations at the $0-\pi$ transitions sets in when quasiparticles current becomes sizable. In this framework, a sort of competition between quasiparticles and magnetic noise might establish in long junctions.

4.4 Resonant tunneling regime

Amplification of current noise response to magnetic fluctuations is also observable and results even more pronounced when the dot is tuned in resonance with the two S leads, i.e. $\varepsilon_d = 0$.

In resonant tunneling, the supercurrent carried through the QD reaches values up to $e\Delta$, being the maximum current sustainable in this kind of devices, as we can observe in Fig. 4.10, where the $J(\phi, h)$ density plot for $\varepsilon_d = 0$ is shown. Here, we can appreciate that the system transition toward the π state starts as soon as the exchange field interaction is switched on since the CPR exhibits jumps even for $h = 0$ at $\phi = \pm\pi$, as it is shown in Fig. 4.10, as a consequence of the gapless ABS spectrum at zero magnetic field, Fig. 4.11

Also in this case, CPR discontinuities lead to δ-like peaks in $\partial_h J(\phi)$ at ABS crossing phases, visible in the $\partial_h J(\phi)$ density plot in Fig. 4.12(a). This provides an enhanced cur-

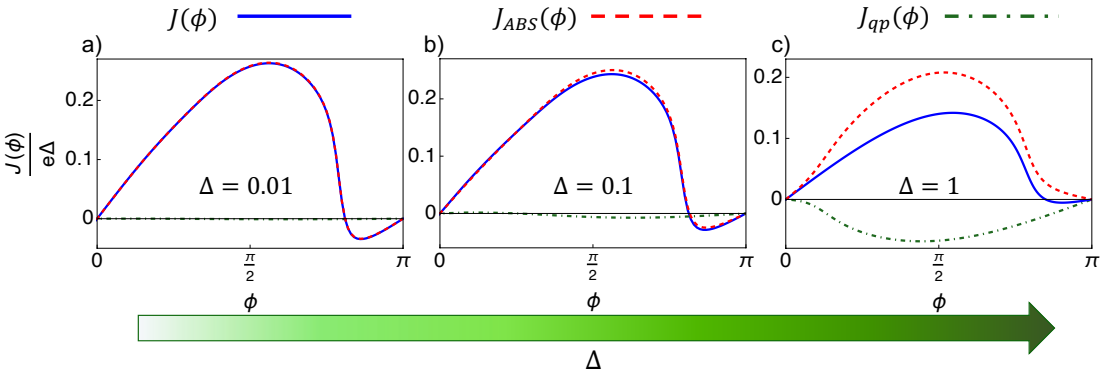

Figure 4.8: Current-phase relation (blue solid lines) together with the relative current contributions of ABS (red dashed lines) and quasiparticles (green dot-dashed lines), computed at different values of the superconducting gap Δ ($\varepsilon_d = 1$, $h = 1.05$, $\Gamma = 1$). As long as the system is in the short junction limit, i.e. $\Delta \ll \Gamma$, quasiparticle current remains negligible, while it reaches the same order of magnitude of the current carried by Andreev levels when Δ approaches Γ.

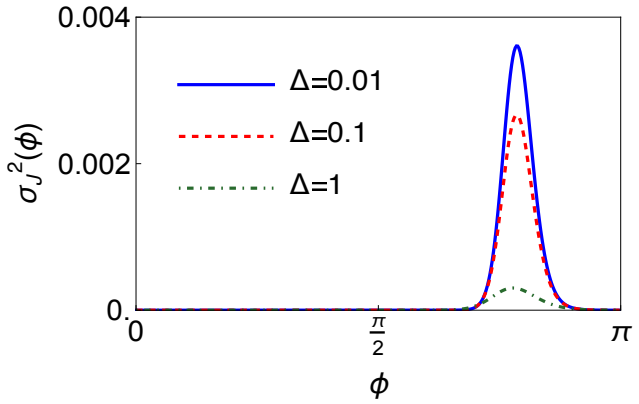

Figure 4.9: Current variance, computed at $\varepsilon_d = 1$, $\Gamma = 1$, $h = 1.05$, $\sigma_{\varepsilon_d} = \sigma_h = 0.005$ and $T = 0.02\, T_C$, for different values of the superconducting gap Δ. Strong attenuation of the current noise peaks at the ABS crossings, Fig. 4.3, is evident when Δ approaches Γ, with the SQDS JJ exiting the short-junction regime, Fig. 4.8.

rent noise response to h fluctuations whose hallmarks are the $\sigma_J(\phi)$ peaks, Fig. 4.12(b). Further, the height of $\partial_h J(\phi)$ and $\sigma_J(\phi)$ peaks is larger than in non-resonant limit by approximately one order of magnitude. On the other hand, the resonant tunneling limit strongly differs from the off-resonance case.

Specifically, when we tune the dot in resonance with the two superconducting electrodes (see Fig. 4.2) [167, 168], i.e. $\varepsilon_d = 0$, $\partial_{\varepsilon_d} J$ goes identically to 0, actually predicting a vanishing first order contribution in σ_{ε_d} to σ_J.

To demonstrate that $\partial_{\varepsilon_d} J$ vanishes at $\varepsilon_d = 0$ we recall the current formula in Eq. 4.18 yielding $\partial_{\varepsilon_d} J \propto \partial_{\varepsilon_d} F_{dd,\downarrow\uparrow}$. $F_{dd,\downarrow\uparrow}(\omega_n)$ has in general a cumbersome expression (the $\downarrow\uparrow$ element of the off-diagonal GF in Eq. 4.13) that in the limit of zero Zeeman field $h = 0$

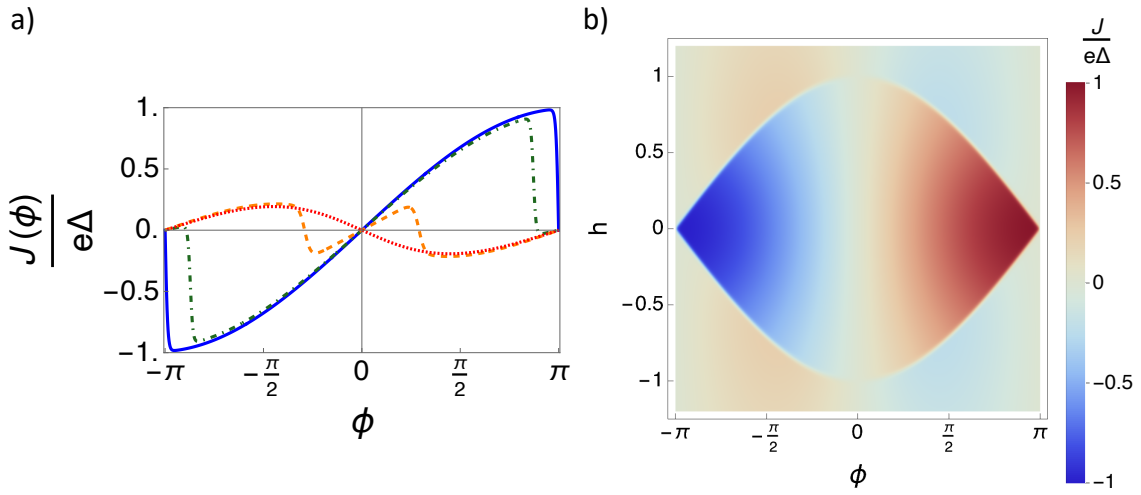

Figure 4.10: In (a) CPR of the SQDS JJ in the resonant tunneling regime (at $\varepsilon_d = 0$, $\Delta = 0.01$, $\Gamma = 1$ and $T = 0.02\,T_C$) computed along the Zeeman induced $0-\pi$ switching are reported, at $h = 0$ (blue solid curve), $h = 0.2$ (green dot-dashed curve), $h = 0.9$ (orange dashed curve) and $h = 1.05$ (red dotted curve), respectively. Along the $0-\pi$ transition the JJ shows peculiar CPR jump discontinuities at the ABS crossings. In (b) the density plot of Josephson current as a function of the phase and Zeeman field $J(\phi,h)$, computed at $\varepsilon_d = 0$, $\Gamma = 1$, $\Delta = 0.01$ and $T = 0.02\,T_C$, is shown. Transition between 0 and π phases is characterized by an intermediate transport regime in which the junction CPR shows peculiar jump-like discontinuities, e.g. abrupt change in the plot color when moving along the ϕ axis at fixed Zeeman field h value.

[176, 203] simplifies to

$$F_{dd,\downarrow\uparrow}(\omega_n) = \frac{\Gamma\Delta\cos\left(\frac{\phi}{2}\right)}{\sqrt{\Delta^2+\omega_n^2}}\times \left(-\omega_n^2-\varepsilon_d^2-\frac{\Gamma^2\left(\Delta^2\cos\left(\phi/2\right)^2+\omega_n^2\right)}{\left(\Delta^2+\omega_n^2\right)}-\frac{2\Gamma\omega_n^2}{\sqrt{\Delta^2+\omega_n^2}}\right)^{-1} \tag{4.29}$$

Starting from the above equation the current derivative along ε_d can be easily calculated in the resonant tunneling where it identically vanishes

$$\partial_{\varepsilon_d} F_{dd,\downarrow\uparrow}\Big|_{\varepsilon_d=0} = \partial_{\varepsilon_d} J\Big|_{\varepsilon_d=0} = 0\,, \tag{4.30}$$

thus yielding a zero first order contribution to the small fluctuations expansion of $\sigma_J^2(\phi)$

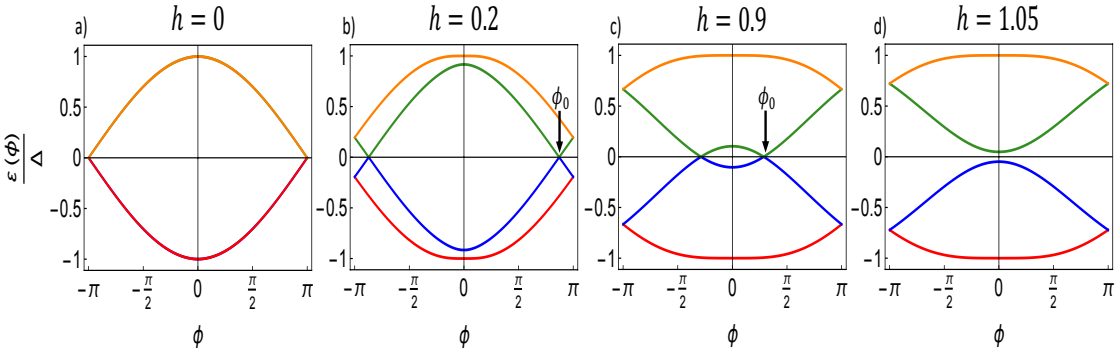

Figure 4.11: Andreev levels spectrum for the SQDS JJ ($\varepsilon_d = 0$, $\Gamma = 1$, $\Delta = 0.01$) along an Zeeman field induced $0-\pi$ transition, computed, from left to right, at $h = 0$ (a), $h = 0.2$ (b), $h = 0.9$ (c) and $h = 1.05$ (d), respectively. By increasing the Zeeman splitting between the different spin levels, Andreev Bound States (ABS) crossings at zero energy occur for $\phi = \pm\phi_0 \neq 0, \pm\pi$. Transition between the 0 and π phases is accomplished when the two near-zero ABS are switched.

in Eq. 4.27. The latter, for $\varepsilon_d = 0$, hence, reads

$$\sigma_J^2(\phi, \varepsilon_d = 0) = \left(\frac{\partial J(\varepsilon_d = 0)}{\partial h}\bigg|_{\substack{\delta\varepsilon_d=0 \\ \delta h=0}} \right)^2 \sigma_h^2$$

$$+ \frac{1}{2}\left(\frac{\partial^2 J(\varepsilon_d = 0)}{\partial \varepsilon_d^2}\bigg|_{\substack{\delta\varepsilon_d=0 \\ \delta h=0}} \right)^2 \sigma_{\varepsilon_d}^4 + \frac{1}{2}\left(\frac{\partial^2 J(\varepsilon_d = 0)}{\partial h^2}\bigg|_{\substack{\delta\varepsilon_d=0 \\ \delta h=0}} \right)^2 \sigma_h^4 \tag{4.31}$$

$$- \frac{1}{2}\left(\frac{\partial^2 J(\varepsilon_d = 0)}{\partial \varepsilon_d^2}\bigg|_{\substack{\delta\varepsilon_d=0 \\ \delta h=0}} \frac{\partial^2 J(\varepsilon_d = 0)}{\partial h^2}\bigg|_{\substack{\delta\varepsilon_d=0 \\ \delta h=0}} \right) \sigma_{\varepsilon_d}^2 \sigma_h^2,$$

Moreover, in case of negligible contribution from high order terms in σ_{ε_d} and σ_h, the current variance $\sigma_J^2(\phi)$ in Eq. 4.27 simply reduces to

$$\sigma_J^2(\phi, \varepsilon_d = 0) = \left(\frac{\partial J(\phi, \varepsilon_d = 0)}{\partial h}\bigg|_{\substack{\delta\varepsilon_d=0 \\ \delta h=0}} \right)^2 \sigma_h^2, \tag{4.32}$$

From now on we call, without any loss of generality, *small fluctuations regime* the limit, in terms of σ_{ε_d} and σ_h, in which Eq. 4.32 successfully reproduces the $\sigma_J(\phi)$ behavior predicted by its definition $\sigma_J^2(\phi) = \langle J^2(\phi)\rangle - \langle J(\phi)\rangle^2$.

For the sake of completeness, we show, for example, that the case reported in Fig. 4.12 (b), where the current variance was computed for $\sigma_{\varepsilon_d} = \sigma_h = 0.005$, falls within the above-mentioned limit, where $\sigma_J^2(\phi)$ peaks are directly proportional to Zeeman field variance σ_h^2.

For this purpose, first, we report in Fig. 4.13 the different σ_J^2 series terms corresponding to the current variance in Fig. 4.12(b) at $h = 0.2$, where we observe that

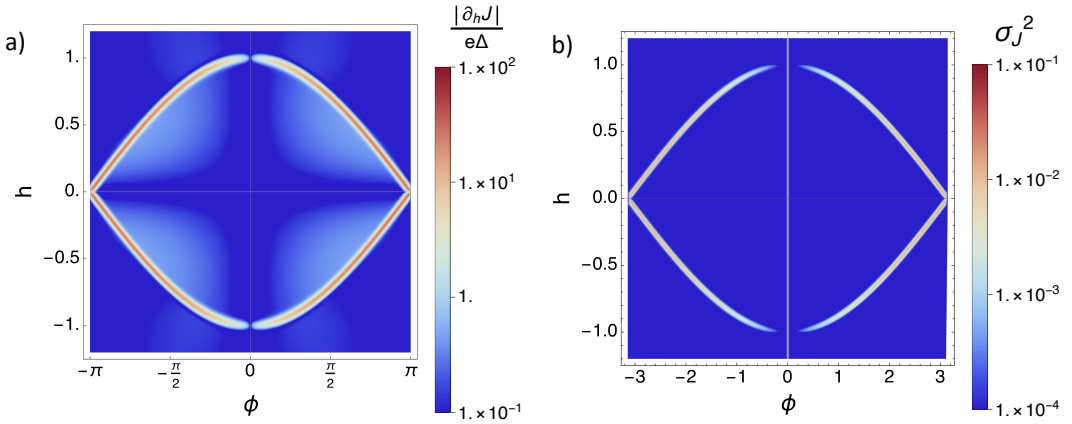

Figure 4.12: Density plots of the current derivative along h (left panel, (a)) and of the current variance $\sigma_J^2(\phi, h)$ (right panel (b)) as a function of the superconducting phase difference and the Zeeman field ($\varepsilon_d = 0$, $\Delta = 0.01$, $\Gamma = 1$ and $T = 0.02\, T_C$). $\sigma_J^2(\phi, h) = \langle J^2(\phi)\rangle - \langle J(\phi)\rangle^2$ is computed in the presence of dot energy and Zeeman field fluctuations with equal standard deviation $\sigma_{\varepsilon_d} = \sigma_h = 0.005$. Along $0 - \pi$ transition $\partial_h J$ divergences at the CPR jumps appear and the SQDS JJ exhibits current noise peaks.

the second order term in σ_h is two order of magnitude lower than the first order one, while the latter exceeds terms involving σ_{ε_d} by at least three order of magnitude, thus, testifying that dot energy contribution to current noise can be considered negligible in the resonant tunneling limit. Then, in Fig. 4.13 (b), we compare the results of the first order σ_J expansion in Eq. 4.32 with the $\sigma_J^2(\phi)$ curve computed by the means of its definition in Eq. 4.23, thus proving that small fluctuations approach succeeds in providing a good description of current noise.

Nevertheless, it is worth noticing that the larger is ε_d standard deviation with respect to σ_h the more significant higher order terms in σ_{ε_d} are for CPR noise.

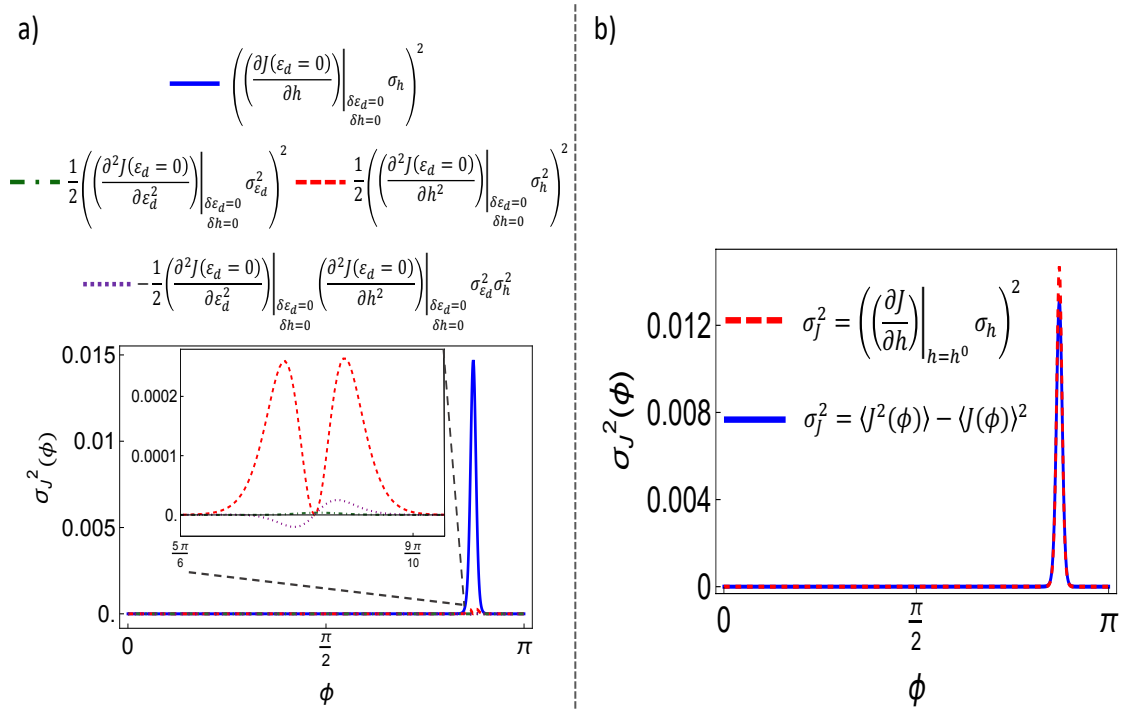

Figure 4.13: Different contributions to the small fluctuations expansion formula for the current variance σ_J^2, in Eq. 4.31 computed for the CPR curve at $h = 0.2$ in Fig. 4.10 ($\varepsilon_d = 0$, $\Gamma = 1$, $\Delta = 0.01$, $T = 0.02T_C$), for $\sigma_{\varepsilon_d} = \sigma_h = 0.005$, testifying that when the QD is in resonance with the S leads the dot energy noise contribution to current noise is negligible.

4.5 Andreev spin-noise detector

Although current noise amplification in magnetic JJs at $0-\pi$ transitions might represent a limitation to their applicability in superconducting quantum circuits, it also provides us with a novel tool for probing magnetic noise in these kind of devices and, in general, in ferromagnetic junctions. Indeed, the enhanced sensitivity of these systems to magnetic fluctuations that can be further maximized by choosing the proper transport regime, i.e. short-junction limit and resonant tunneling, would be a key ingredient for magnetic noise detection. Nevertheless, in view of a possible application of SQDS JJs as magnetic noise detectors, we should be able to isolate and analyze the magnetic field fluctuations contribution to current noise response σ_J. In this respect, the existence of "sweet spots" in the Hamiltonian parameters space where σ_{ε_d} contribution to σ_J can be disregarded, i.e. resonant tunneling $\varepsilon_d = 0$, and the junction is much more sensitive to magnetic rather than charge fluctuations, suggests a strategy to isolate the magnetic noise contribution. In addition, we observe in Fig. 4.12 that, in resonant tunneling, the current noise amplification accompanying the $0-\pi$ transition starts as soon as the magnetic field is switched on, and the largest current noise response is achieved at very low Zeeman coupling values. This suggests the possibility to have a high detection sensitivity without employing strong external magnetic fields that could in principle have detrimental effects on the superconducting leads. Moreover, the simple proportionality relation between current and magnetic noises, characterizing the small fluctuations

regime, guarantees an easy and efficient way to investigate the physical properties of magnetic noise sources in the barrier, starting from the only knowledge of the junction equilibrium transport properties.

In the case of resonant tunneling, quasiparticles current may have detrimental effects on the σ_J peaks and, thus, on the device sensitivity to magnetic fluctuations. In Fig. 4.14(a-c) we analyze Andreev levels and quasiparticles current contributions for the CPR computed at $h = 0.2$ in Fig. 4.10(a) (green-dashed curve) by varying the superconducting gap from a deeply short junction limit, $\Delta = 0.01\Gamma$, to the case where $\Delta = \Gamma$. These results highlight a strong attenuation of the current noise sensitivity

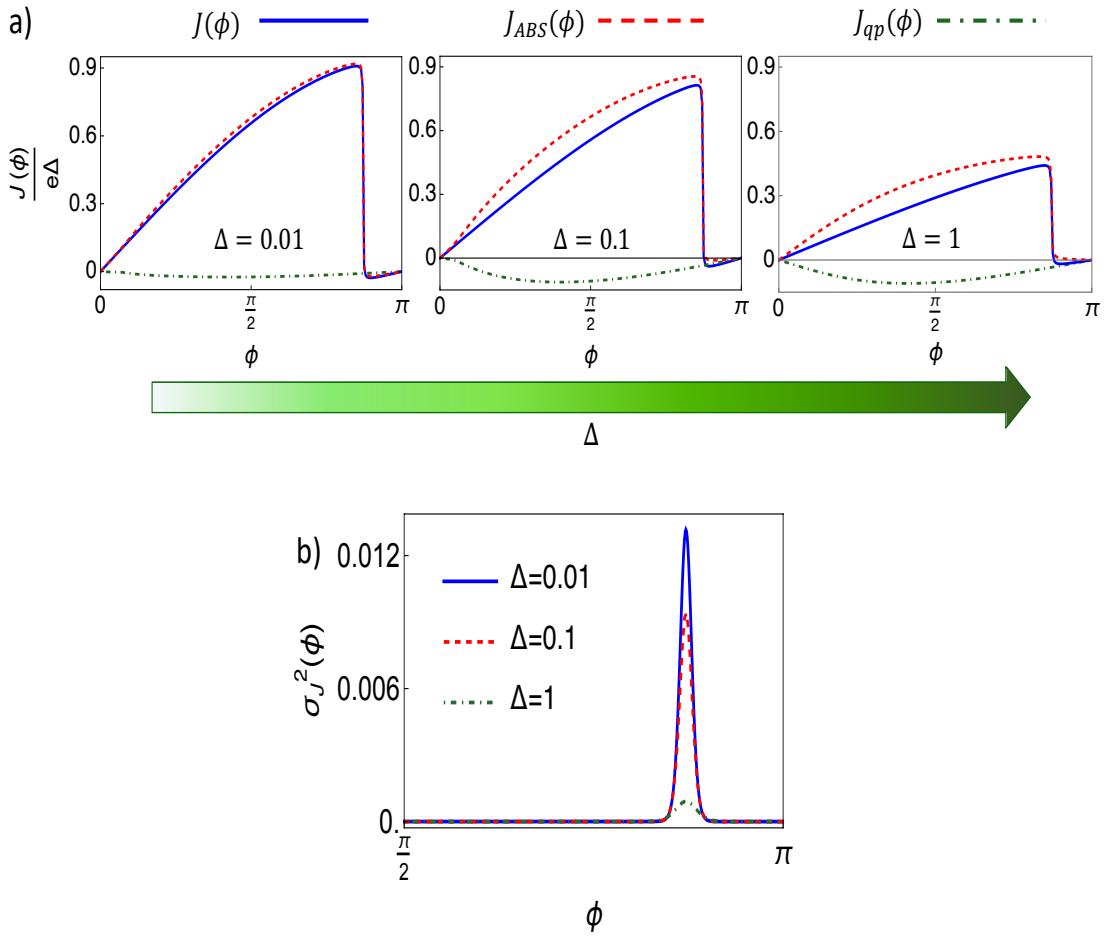

Figure 4.14: In the upper panel (a) the current-phase relation (blue solid lines) together with the relative current contributions of ABS (red dashed lines) and quasiparticles (green dot-dashed lines), computed at different values of the superconducting gap Δ, expressed in unity of Γ ($\Gamma = 1$ and $T = 0.02\,T_C$), are respectively shown. In the lower panel (b) the corresponding current variance curves $\sigma_J(\phi)$ are reported. As long as the system is in the short junction limit, i.e. $\Delta \ll \Gamma$, quasiparticles current remains negligible, while it reaches the same order of magnitude of the current carried by Andreev levels when Δ approaches Γ. Reduction of CPR jumps due to quasiparticles current leads to strong attenuation of the current noise peaks at the ABS crossings, when the JJ exits the short-junction regime

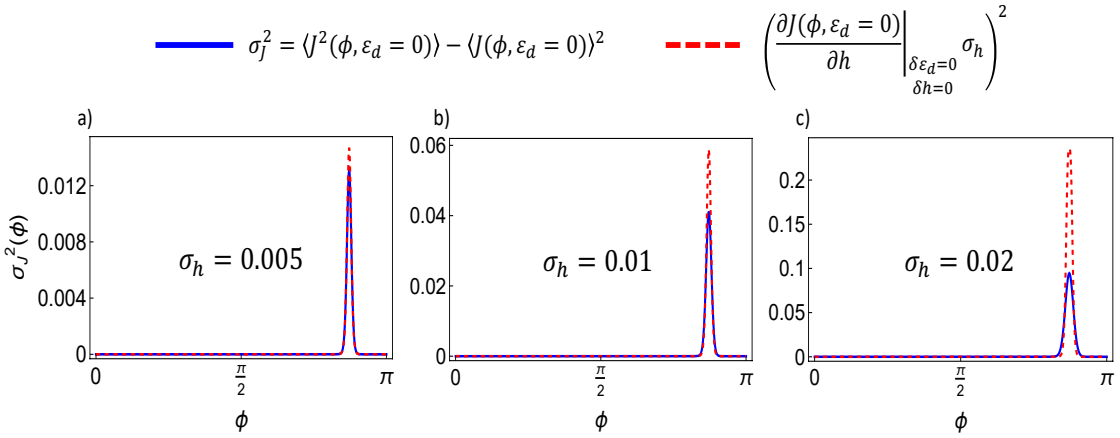

Figure 4.15: Comparison between $\sigma_J^2(\phi)$ calculated by the means of Eq. 4.23 and Eq. 4.32 for the CPR curve at $h = 0.2$ in Fig. 4.10 (a) ($\varepsilon_d = 0$, $\Gamma = 1$, $\Delta = 0.01$), at different values of the dot energy and Zeeman field standard deviations, $\sigma_{\varepsilon_d} = \sigma_h = 0.005$ (a), $\sigma_{\varepsilon_d} = \sigma_h = 0.01$ (b) and $\sigma_{\varepsilon_d} = \sigma_h = 0.02$ (c), respectively.

when $\Delta = \Gamma$, Fig. 4.14 (c), further justifying the choice of working in the short junction limit in order to have also the current noise response maximized. In the followings, we fix $\Delta = 0.01$, thus quenching the quasiparticles contribution to supercurrent that is detrimental for noise amplification.

Once the most favorable transport regime for magnetic noise detection has been determined, the success in using the SQDS JJ magnetic noise detector relies on the accuracy of Eq. 4.32. The latter, in resonant tunneling case, not only allows us to access information about magnetic noise sources but it assures that dot energy noise does not contributes to σ_J. It is thus important to identify the regime of validity of the small fluctuations approximation. For this purpose, in Fig. 4.15 we show the current variance σ_J^2 computed at different widths of the dot energy and Zeeman field distributions, i.e. σ_{ε_d} and σ_h, by comparing the outcomes of Eq. 4.23 and of Eq. 4.32. We note that the smaller is σ_h, i.e. the narrower is the Zeeman field noise distribution, the higher is the precision of Eq. 4.32 in reproducing the correct results both for σ_J^2 peaks height and width. These results are still better visualized when comparing the maximum of the $\sigma_J(\phi)$ peaks computed with the two approaches, in Fig. 4.16, where we observe that for $\sigma_h \leq 5 \times 10^{-3}$ Eq. 4.32 succeeds in providing an accurate description for the current variance that hence turns out to be proportional to σ_h. Not only these results validate the small fluctuations expansion approach but they also demonstrates that dot energy noise can be disregarded for σ_J^2 calculation in the resonant tunneling. In this scenario, these findings points out the possibility to extract information about the magnetic noise directly from the knowledge of the Josephson current variance and the junction equilibrium transport properties. Following Refs. [183, 184], we highlight that the small fluctuations condition does not limit the practical use of these systems as magnetic noise detectors. Indeed, we find that the expected Zeeman coupling distribution width σ_h^{exp} corresponding to magnetic field standard deviation $\sigma_{B_N} \sim 4\text{mT}$, as mentioned in Refs.[183, 184], is of the order of $\sigma_h^{\text{exp}} \sim 10^{-7}\text{eV}$, where we consider the electronic gyromagnetic factor in such heterostructures being $g \sim 0.3 \div 0.4$ [227–231], while in our

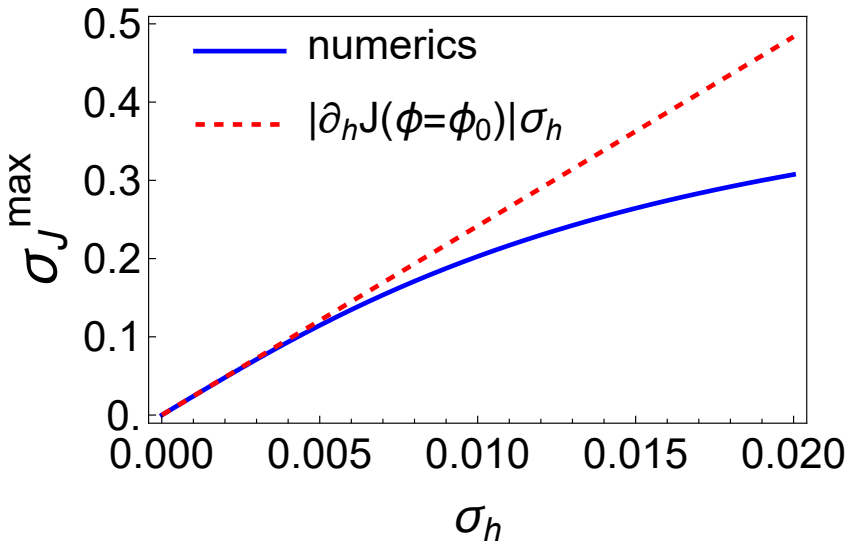

Figure 4.16: Maximum of the σ_J peaks at the ABS crossings for the CPR curve at $h = 0.2$ (green dot-dashed curve in Fig. 4.10) (a) computed by varying the Zeeman field standard deviation σ_h in comparison with the results predicted from first order σ_J expansion in Eq. 4.32.

case, when dealing with systems such that $\Gamma \sim 100\Delta$ and $\sigma_h = 5 \times 10^{-3}\Gamma$, we predict Zeeman field standard deviation $\sigma_h = 5 \times 10^{-5}$eV for $\Delta = 10^{-1}$meV.

4.6 Temperature induced Noise Damping

Starting from Eqs. 4.18-4.23 we calculate the current and its noise by varying the system temperature in the range $[0.02\,T_C,\ 0.5\,T_C]$. The results for the QD JJ at $h = 0.2$ (green-dashed curve in Fig. 4.10(a)) are shown in Figs.4.17 (a) and (b), respectively. We find that the sharp jumps, strongly evident when the temperature approaches zero, are significantly smoothed by the temperature.

CPR jump discontinuities in such systems represent a fingerprint of the enhanced sensitivity to magnetic noise. These findings suggest a strong damping of the current noise peaks, as confirmed by Fig. 4.17 (b), where the amplitude of σ_J peaks is reduced by one order of magnitude at $T = 0.1\,T_C$ and by more than two order of magnitude at $T = 0.3\,T_C$.

We can understand this effect by recalling the ABS current formula at finite temperature [167, 168, 192, 201, 202]

$$J_{ABS}(\phi) = \sum_{j,\varepsilon\leq 0} \frac{\partial \varepsilon_j(\phi)}{\partial \phi} \tanh\left(\frac{\varepsilon_j(\phi)}{2T}\right). \tag{4.33}$$

and looking at the current carrying Andreev levels, i.e. at $\varepsilon < 0$, in Fig. 4.18 (a). When we compute the Boltzmann thermal factor for the Andreev state exhibiting zero energy crossings at $\phi = \pm\phi_0$, by varying the system temperature, Fig. 4.18 (b), we notice that it exhibits a visible dip at the crossings, whose width grows with the temperature. This leads to the lowering and widening of the CPR jumps, together with a strong reduction

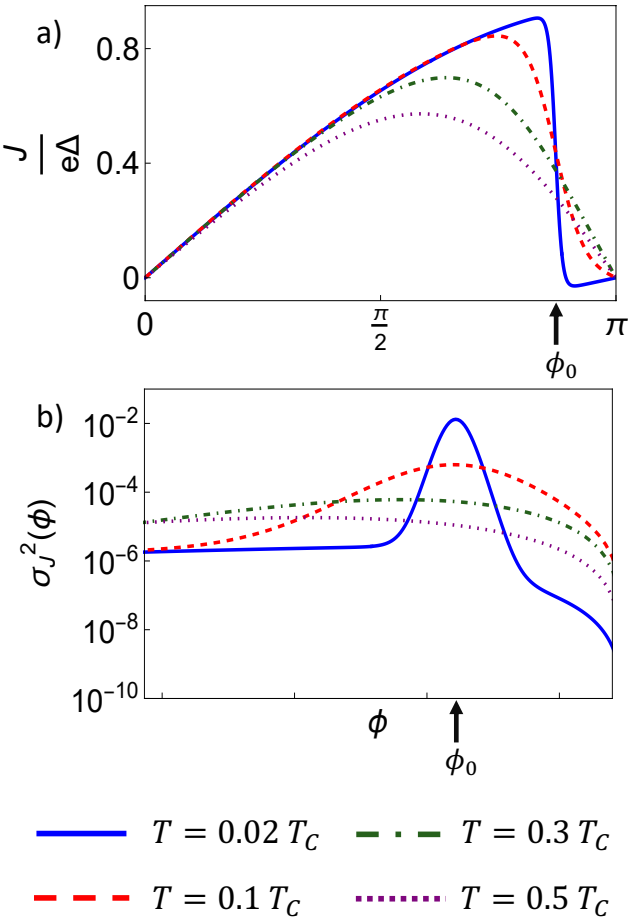

Figure 4.17: CPR and current variance $\sigma_J^2(\phi)$ modifications with the system temperature increasing. Results for the JJ with $h = 0.2$ in Fig. 4.10 computed at $T = 0.02T_C$ (blue solid curve), $T = 0.1T_C$ (red dashed curve), $T = 0.3T_C$ (green dot-dashed curve), $T = 0.5T_C$ (purple dotted curve), respectively, are reported. The temperature induced smoothing of CPR jumps and damping of the σ_J noise peaks are remarkable.

of σ_J peaks. In this scenario, the SQDS detector sensitivity is intrinsically related to the quantum mechanical nature of Andreev current governing the $0-\pi$ transition and thus is maximized at low working temperature, promising even improved performances when T is further reduced.

Zero temperature limit: Andreev bound states model for noise

Interestingly enough, as long as the junction is in the small fluctuations regime, its sensitivity to magnetic noise in the zero temperature limit seems to be approximately independent on the Zeeman coupling variance σ_h.

For $T = 0$, semi-analytical results for the Andreev levels current are indeed obtainable for a short-junction (i.e. $\Delta \ll \Gamma$) under the hypothesis of resonant tunneling, i.e. $\varepsilon_d = 0$, [162].

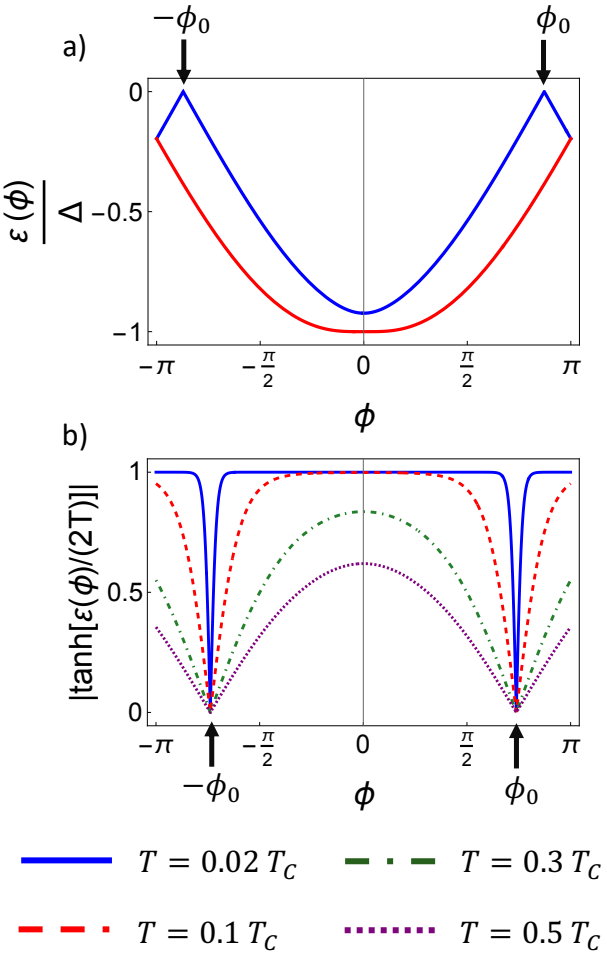

Figure 4.18: Negative energy states of the junction ABS spectrum (at $\varepsilon_d = 0$, $h = 0.2$, $\Delta = 0.01$ and $\Gamma = 1$) lying below the superconducting leads chemical potential, through which supercurrent flows across the junction, (a). In (b) the thermal damping factor computed for the Andreev level exhibiting zero energy crossings at $T = 0.02\,T_C$ (blue solid line), $T = 0.1\,T_C$ (red dashed line), $T = 0.3\,T_C$ (green dot-dashed line) and $T = 0.5\,T_C$ (purple dotted line), respectively, is shown. A dip is present at the ABS crossing phases, whose width is enhanced by the temperature increasing, thus, providing the CPR jumps smoothing.

It is easy to show that, for $\varepsilon_d = 0$, Eq. 1.37 reduces to

$$\det\left(z\check{1}\left(1+\frac{\Gamma}{\sqrt{\Delta^2-z^2}}\right)-h\hat{\sigma}_3\otimes\hat{\tau}_3-\frac{\Gamma}{\sqrt{\Delta^2-z^2}}\left(\Delta\cos\left(\frac{\phi}{2}\right)i\hat{\sigma}_2\otimes\hat{\tau}_2\right)\right)=0\,, \tag{4.34}$$

whose eigenvalues are the Andreev levels through which the supercurrent flow read [162]

$$\varepsilon_{1,2}(\phi)=\pm\Delta\cos\left(\arccos\left(\frac{\pm\cos(\phi/2)}{\sqrt{1+\frac{h^2}{\Gamma^2}}}\right)+\arctan\left(\frac{h}{\Gamma}\right)\right), \tag{4.35}$$

yielding the following expression for the ABS current across the junction

$$J(\phi) = \partial_\phi \varepsilon_1 + \partial_\phi \varepsilon_2 \left(1 - 2\Theta(\phi - \phi_0) - 2\Theta(-\phi - \phi_0)\right), \tag{4.36}$$

that shows by definition jumps at the ABS crossing points $\phi = \pm\phi_0 = \pm 2\arccos(\frac{h}{\Gamma})$. In the presence of exchange field static Gaussian fluctuations, with distribution $P(\delta h)$ given by Eq. 4.22, the current variance $\sigma_J^2 = \langle J^2 \rangle - \langle J \rangle^2$ reads

$$\sigma_J^2 = \int_{-\infty}^{\infty} J^2(h + \delta h, \phi)\, P(\delta h)\, d(\delta h) - \left(\int_{-\infty}^{\infty} J(h + \delta h, \phi)\, P(\delta h)\, d(\delta h) \right)^2, \tag{4.37}$$

that, in general, can only be numerically evaluated.

In order to obtain a simple analytic approximation for σ_J^2, in the low exchange field limit we can Taylor-expand J and J^2 around the mean Zeeman coupling h. We can thus express both the phase crossing points $\pm\phi_0$ and the Andreev levels derivatives $\partial_\phi \epsilon_{1,2}$ in terms of their first order approximation in h. In addition, when considering the small fluctuations limit we can disregard the higher order terms in the exchange field noise σ_h, obtaining the following approximate equation for σ_J^2 (at positive phases and exchange field values):

$$\begin{aligned} \sigma_J^2 \approx (\partial_\phi \varepsilon_2)^2 & \left[1 - \mathrm{erf}\left(\frac{\sqrt{1 - (\frac{h}{\Gamma})^2}\left(\phi - 2\arccos\left(\frac{h}{\Gamma}\right)\right)}{2\sqrt{2}\sigma_h} \right) \right]^2 \\ & + \; 2\sqrt{\frac{2}{\pi}}\sigma_h \exp\left(\frac{\left(1 - (\frac{h}{\Gamma})^2\right)\left(\phi - 2\arccos\left(\frac{h}{\Gamma}\right)\right)^2}{8\sigma_h^2} \right) \times \\ & \times \left((\partial_\phi \varepsilon_2)\,(\partial_h \partial_\phi \varepsilon_1) + (\partial_\phi \varepsilon_1)\,(\partial_h \partial_\phi \varepsilon_2) \right). \end{aligned} \tag{4.38}$$

The first term in the above current variance expression is dominant at the ABS crossings, since it is proportional to $(\partial_\phi \varepsilon_2)^2$, while the second one for $\sigma_h \to 0$ is small. This cause the σ_J Gaussian-like peaks to be roughly independent on σ_h at $T = 0$. On the other hand, the peaks width is proportional to that of the exchange field gaussian distribution, i.e. σ_h is noticeable. In Fig. 4.19, we compare the phase dependence of σ_J^2 for the Andreev levels current, Eq. 4.38, with the current variance computed in the Matsubara formalism in the low temperature limit, for $h = 0.2$, $\Gamma = 1$, $\Delta = 0.01$ and $\sigma_h = 0.1$. We can notice a good agreement between the two approaches, where the small difference in the noise peaks height is possibly related to the small but non-negligible quasiparticles current contribution accounted in the Matsubara calculation.

4.7 Summary

In conclusion we studied the equilibrium current noise in a SQDS JJ in an external magnetic field in the presence of magnetic and dot energy fluctuations. We investigated the microscopic mechanisms underlying the current noise response to magnetic field fluctuations in these devices and how to extract information about magnetic noise sources from current fluctuations, possibly, paving the way to a novel spin-noise spectroscopy technique. We considered the case of static Gaussian noise, which is justified

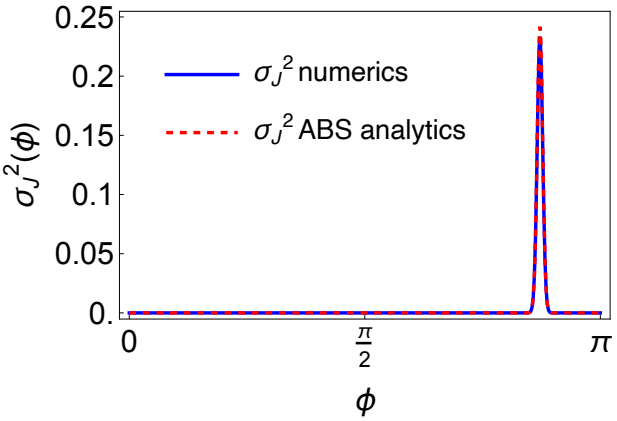

Figure 4.19: Current variance, $\sigma_J^2(\phi)$, computed with the semi-analytical ABS model (red dashed line) and with Matsubara numerical calculations (blue line) at $\varepsilon_d = 0$, $\Delta = 0.01$, $h = 0.2$, $\Gamma = 1$, and exchange field standard deviation $\sigma_h = 0.01$. The system temperature for σ_J Matsubara calculations has been set $T = 10^{-4}\, T_C$.

if the magnetic noise can be described in the "central spin model" within the "frozen spin approximation" [183, 184, 220]. Zeeman field induced $0-\pi$ transitions in SQDS JJ turn out to amplify current noise response to magnetic fluctuations. In these systems, along $0-\pi$ switchings the occurrence of peculiar CPR jump discontinuities, intrinsically linked to the presence of Andreev levels crossings, is visible at low temperatures [161, 162, 164]. CPR jumps are the origin of noise amplification, giving rise to strong current noise response, i.e. $\sigma_J(\phi)$, whose hallmarks are σ_J peaks at ABS crossings. Although enhanced sensitivity of the current noise response to magnetic fluctuations along the $0-\pi$ transition may constitute a practical limit to employ these devices in quantum circuits, it also represents a unique opportunity to probe the magnetic fluctuations, accessing information about the microscopic noise sources from the junction equilibrium transport properties, thus, inspiring novel kind of Josephson spin-noise detectors. We identified the short junction regime and the resonant tunneling as the most favorable conditions for magnetic noise detection from the current noise response. Indeed, we demonstrated that, when the dot is tuned in resonance with the leads, dot energy noise contribution to current fluctuations can be disregarded, thus leading to a simple proportionality relation between current variance σ_J and the standard deviation of the dot Zeeman splitting σ_h, in the small fluctuations regime. In addition, we investigated the quasiparticles destructive influence on CPR jumps and on the detection sensitivity, pointing out the best working regime for maximizing the amplification of current response to magnetic noise. In this scenario, system temperature T plays a crucial role in smoothening the CPR jumps accompanying the $0-\pi$ transitions and washing out the σ_J peaks, thus limiting the detectors sensitivity for $T \approx 10^{-1} T_C$ but suggesting even improved performances when T is further reduced. For this reason, temperature turns out to be a valuable resource as a control knob of sensitivity to magnetic noise in these devices, also in view of their application in superconducting quantum circuits.

Outline

Ferromagnetic Josephson junctions are object of intense research activity. Due to the competition between superconducting and ferromagnetic ordering, these platforms host many intriguing phenomena such as $0-\pi$ transitions and spin-triplet superconducting correlations. The former consist in a shift of π in the equilibrium junction phase, whose typical experimental signature is a cusp-like critical current vs. temperature behavior, i.e. $I_C(T)$ [45, 50, 51]. $0-\pi$ transitions are necessary for the realization of so-called π junctions, that may possibly employed in novel designs for self-biased flux and phase qubits [80, 86, 87, 89]. On the other hand, the capability to generate and control spin-triplet supercurrents paves the way to novel spin-filter junctions as building blocks for the emerging field of superconducting spintronics. More recently, junctions where the ferromagnetic layer is insulating, which are more suitable for quantum circuits applications in view of their low dissipation, have been theoretically and experimentally studied [66, 75, 104, 105, 108–110, 114, 116, 117, 130]. Possibility to induce peculiar temperature induced $0-\pi$ transitions has been predicted and investigated, while experimental signatures of spin-triplet transport have been provided. Our contribution to the characterization of ferromagnetic Josephson junctions concerns the study of both their transport and noise properties at the $0-\pi$ transition.

In the first part of the thesis, that summarizes the results of Refs.[90, 91], we investigated the transport properties of SFIS junctions by using a tight-binding Bogoliubov de Gennes model and well established lattice Green's function techniques. On the one hand, a tight-binding description of the junction is very convenient for modeling the desired interactions in the FI barrier Hamiltonian site by site such that spin-mixing effects, SOC or non-uniform exchange field patterns, as well as magnetic and non-magnetic impurities, very common in the experimental samples, can be straightforwardly included in the model. On the other hand, from the knowledge of the barrier Green's function GF we can easily access information about the symmetries of the superconducting correlations induced inside the FI [73, 90]. Moreover, the Recursive Green's Function method (RGF) provides an efficient way to compute the barrier GF also for large size systems [73, 90, 134, 135]

First, we focused our attention on the temperature dependence of the SFIS junctions critical current. $I_C(T)$, indeed, represents an easily accessible experimental measure encoding information about the barrier, and, thus, might be used as a fingerprint of the junction. In particular, we explored the possibility to tune and control the $0-\pi$ transitions through a direct action on the $I_C(T)$ behavior of the junction.

We studied how the presence of spin-mixing and disorder affects the typical cusp-like $I_C(T)$ curve of a $0-\pi$ junction, showing that the interplay between spin-orbit coupling and impurities leads to the occurrence of temperature broadened $0-\pi$ transitions and

to peculiar $I_C(T)$ plateaus. Further, we predicted that, while enhancing the spin-orbit coupling favors the 0 over π state, increasing the disorder the junction can be driven from a $0-\pi$ $I_C(T)$ behavior to a π state that is stable over the whole temperature range from 0 to T_C. In this context, we propose the combination of impurities engineering and SOC external tuning to build tunable $0-\pi$ Josephson devices that can be properly switched between 0, $0-\pi$ and π regimes [90]. These results might suggest new strategies to switch the junction between the 0 and π phases, without introducing strong noise and decoherence effects, possibly representing a further important step toward application of ferromagnetic junctions in qubits [90].

Then, we applied the same techniques to model the $I_C(T)$ behavior of experimental NbN / GdN / NbN SFIS JJs of Ref.[75] displaying peculiar $I_C(T)$ curves with non-monotonic trend, that we recognized as temperature broadened $0-\pi$ transitions, possibly resulting from the interplay of spin-mixing mechanisms and disorder [91]. Moreover, the analysis we carried out on the spin pair correlations in GdN pointed out the presence of spin-triplet components in both *s-wave* and *p-wave* symmetries, including unconventional odd-frequency s-wave correlations that appear to be enhanced when increasing the disorder. Our results highlight the possible link between this $I_C(T)$ behavior and the competition of the oscillating singlet supercurrents with long-range spin-polarized triplet currents [91], identifying weak external magnetic fields as an in situ control knob to tune the $0-\pi$ transition and, thus, the relative weight of spin-triplet correlations.

In view of a future applicability of ferromagnetic JJs in superconducting circuits, the versatility of lattice GF techniques guarantees an efficient method of studying and possibly designing novel junctions. For example, more complex SF heterostructures might be used to engineer and control spin-triplet currents [91], as well as specific Josephson current features (e.g. in the case of Anomalous Josephson Effect and Josephson Diode Effect [74, 138–144]) or $I_C(T)$ behaviors [90].

In the second part of this thesis, we studied the static current fluctuations, $\delta I(\varphi)$, in a simple magnetic junction at the $0-\pi$ transitions with the aim of understanding whether these phase switchings are accompanied by enhanced current noise [92]. We considered a SQDS junction in an external magnetic field that, due to its simplicity, represents an interesting playground to study the mechanisms underlying the $0-\pi$ current noise response to magnetic fluctuations [92]. Our results pointed out the presence of Josephson current jumps, i.e. strongly non-harmonic $I(\varphi)$ behavior, that in certain regimes can characterize the $0-\pi$ transitions, as a source of current noise amplification [92]. This translates to a high sensitivity of the system to magnetic and charge fluctuations along the $0-\pi$ in short ballistic junctions, that might be in principle detrimental for their circuital applications. However, we showed that this can be controlled by choosing the proper transport regime and, thus, tuning the quasiparticles current contribution, that has a destructive influence on CPR jumps. Moreover, temperature T, that smooths the CPR discontinuities, helps in lowering the junction current noise even at temperatures of the order of $T \approx 10^{-1}T_C$. On the one hand, our findings could be useful to understand the way $0-\pi$ ferromagnetic JJs react to the presence of exchange field noise and analyze possible solutions to mitigate this effect. On the other hand, this increased sensitivity to magnetic fluctuations in SQDS JJs represents a valuable opportunity to infer information about magnetization noise in ferromagnetic JJs, accessing knowledge of the microscopic noise sources from the junction equilibrium

transport properties and, thus, inspiring novel kind of Josephson spin-noise detectors. [92]. This kind of analysis could be relevant for future researches on the feasibility of employing tunable $0 - \pi$ devices in superconducting circuits.

Appendix A

Gor'kov equations

In this section we will derive the Gor'kov equations for the Green's function $\hat{\mathcal{G}}$ for a conventional BCS superconductor . In our treatment we will follow the Ref.[3]. We will apply the Equation-of-Motion technique [3] to obtain the Gor'kov equation for the Green's function. Let us consider an Hamiltonian of the following form

$$H = \sum_{\vec{p}\sigma} \xi_{\vec{p}} C_{\vec{p}\sigma} C^{\dagger}_{\vec{p}\sigma} + \frac{1}{2} \sum_{\vec{q}\vec{p}\vec{p}'\,\sigma\,\overline{\sigma}} V(\vec{q}) C^{\dagger}_{\vec{p}+\vec{q}\sigma} C^{\dagger}_{\vec{p}'-\vec{q}\overline{\sigma}} C_{\vec{p}'\overline{\sigma}} C_{\vec{p}\sigma}; \tag{A.1}$$

where $\vec{p}$, σ and $\vec{q}$ indicate respectively the electron momentum and spin and the phonon momentum. With $\overline{\sigma}$ we indicate the spin state opposite to that indicated by σ. This Hamiltonian describes a BCS superconductor, i.e. a fermionic system in the presence of a phonon-mediated coupling $V(\vec{q})$. It is made up of two terms: the kinetic energy and the attractive electron-electron effective interaction resulting from the electron-phonon scattering. Note that the interaction term does not conserve the particle number.
In the imaginary time representation, the correlation functions describing the propagators are defined as follows :

$$\begin{aligned}
\mathcal{G}(\vec{p}, \tau - \tau') &= -\left\langle T_\tau C_{\vec{p}\sigma}(\tau) C^{\dagger}_{\vec{p}\sigma}(\tau') \right\rangle \\
\mathcal{F}(\vec{p}, \tau - \tau') &= -\left\langle T_\tau C_{-\vec{p}\downarrow}(\tau) C_{\vec{p}\uparrow}(\tau') \right\rangle \\
\mathcal{F}^{\dagger}(\vec{p}, \tau - \tau') &= -\left\langle T_\tau C_{\vec{p}\uparrow}(\tau) C^{\dagger}_{\vec{p}\downarrow}(\tau') \right\rangle \\
\mathcal{G}^{\dagger}(\vec{p}, \tau - \tau') &= -\left\langle T_\tau C^{\dagger}_{\vec{p}\sigma}(\tau) C_{\vec{p}\sigma}(\tau') \right\rangle
\end{aligned} \tag{A.2}$$

where T_τ is the time-ordering operator. For the sake of simplicity, we write the explicit expression of the Green's function $\mathcal{G}$:

$$\mathcal{G}(\vec{p}, \tau - \tau') = -[\Theta(\tau - \tau') \left\langle C_{\vec{p}\sigma}(\tau) C^{\dagger}_{\vec{p}\sigma}(\tau') \right\rangle - \Theta(\tau' - \tau) \left\langle C^{\dagger}_{\vec{p}\sigma}(\tau') C_{\vec{p}\sigma}(\tau) \right\rangle], \tag{A.3}$$

where $\Theta(\tau - \tau')$ denotes the Heaviside step function

$$\Theta(\tau - \tau') = \begin{cases} 0 & \text{for } (\tau - \tau') < 0 \\ 1 & \text{for} (\tau - \tau') \geq 0, \end{cases} \tag{A.4}$$

By deriving with respect to the imaginary time τ, we have

$$\frac{\partial}{\partial\tau}\mathcal{G}(\vec{p},\tau-\tau') = -\delta(\tau-\tau')\left\langle C_{\vec{p}\sigma}(\tau)C^{\dagger}_{\vec{p}\sigma}(\tau') + C^{\dagger}_{\vec{p}\sigma}(\tau')C_{\vec{p}\sigma}(\tau)\right\rangle - \left\langle T_\tau\left[\frac{\partial}{\partial\tau}C_{\vec{p}\sigma}(\tau)\right]C^{\dagger}_{\vec{p}\sigma}(\tau')\right\rangle. \tag{A.5}$$

To calculate $\partial/\partial\tau C_{\vec{p}\sigma}(\tau)$ we use the Heisenberg equation

$$\frac{\partial}{\partial\tau}C_{\vec{p}\sigma}(\tau) = [H, C_{\vec{p}\sigma}(\tau)]. \tag{A.6}$$

Using the Hamiltonian in Eq. A.1, we obtain

$$\frac{\partial}{\partial\tau}C_{\vec{p}\sigma}(\tau) = -\xi_{\vec{p}}C_{\vec{p}\sigma}(\tau) - \sum_{\vec{q}\vec{p}'s'}V(\vec{q})C^{\dagger}_{\vec{p}'-\vec{q}s'}(\tau)C_{\vec{p}'s'}(\tau)C_{\vec{p}-\vec{q}\sigma}(\tau), \tag{A.7}$$

where s' is a spin variable. Inserting the last expression into Eq. A.5, we obtain

$$\left(-\frac{\partial}{\partial\tau} - \xi_{\vec{p}}\right)\mathcal{G}(\vec{p},\tau-\tau')+ \sum_{\vec{q}\vec{p}'s'}V(\vec{q})\left\langle T_\tau C^{\dagger}_{\vec{p}'-\vec{q}s'}(\tau)C_{\vec{p}'s'}(\tau)C_{\vec{p}-\vec{q}\sigma}(\tau)C^{\dagger}_{\vec{p}\sigma}(\tau')\right\rangle = \delta(\tau-\tau'). \tag{A.8}$$

Using the Wick theorem, the second term on the left hand side gives rise to all possible combinations $\langle CC^{\dagger}\rangle\langle CC^{\dagger}\rangle$ and $\langle CC\rangle\langle C^{\dagger}C^{\dagger}\rangle$. A possible simplification consists in neglecting the terms with $\vec{q}=0$, thus assuming that the long-wavelength phonons give no contribution to the potential ($V(\vec{q}=0)$).
The term which conserves the number of particle represents the exchange energy, thus being present even in the normal state,

$$-\left\langle T_\tau C^{\dagger}_{\vec{p}'-\vec{q}s}(\tau)C_{\vec{p}-\vec{q}\sigma}(\tau)\right\rangle\left\langle T_\tau C_{\vec{p}'s'}(\tau)C^{\dagger}_{\vec{p}\sigma}(\tau')\right\rangle. \tag{A.9}$$

If we explicitly perform the calculation, we find

$$-\left\langle T_\tau C^{\dagger}_{\vec{p}'-\vec{q}s'}(\tau)C_{\vec{p}-\vec{q}\sigma}(\tau)\right\rangle\left\langle T_\tau C_{\vec{p}'s'}(\tau)C^{\dagger}_{\vec{p}\sigma}(\tau')\right\rangle = \delta_{\vec{p},\vec{p}'}\delta_{s',\sigma}n_{\vec{p}-\vec{q}\sigma}\mathcal{G}(\vec{p},\tau-\tau'), \tag{A.10}$$

where $n_{\vec{p}\sigma}$ is the particle-number operator, defined as $n_{\vec{p}\sigma} = C^{\dagger}_{\vec{p}\sigma}C_{\vec{p}\sigma}$.
Other combinations do not conserve the particle number, hence they exist only in superconducting state and give ($\sigma = -s' = \uparrow$)

$$\left\langle T_\tau C_{\vec{p}'\downarrow}(\tau)C_{\vec{p}-\vec{q}\uparrow}(\tau)\right\rangle\left\langle T_\tau C^{\dagger}_{\vec{p}'-\vec{q}\uparrow}(\tau)C^{\dagger}_{\vec{p}\downarrow}(\tau')\right\rangle = -\delta_{\sigma,-s'}\delta_{\vec{p}',-\vec{p}+\vec{q}}\mathcal{F}(\vec{p}-\vec{q},0)\mathcal{F}^{\dagger}(\vec{p},\tau-\tau'), \tag{A.11}$$

The same result is obtained with the choice $\sigma = -s' = \downarrow$. It could be shown [3] that $\mathcal{F}$ and $\mathcal{F}^{\dagger}$ do not depend on the sign of their argument either momentum or τ.
Eq. A.8 becomes

$$\left(-\frac{\partial}{\partial\tau} - \xi_{\vec{p}}\right)\mathcal{G}(\vec{p},\tau-\tau')+ \tag{A.12}$$

$$\sum_{\vec{q}}V(\vec{q})[\mathcal{G}(\vec{p},\tau-\tau')n_{\vec{p}-\vec{q}} - \mathcal{F}(\vec{p}-\vec{q},0)\mathcal{F}^{\dagger}(\vec{p},\tau-\tau')] = \delta(\tau-\tau'). \tag{A.13}$$

The first term on the left hand side [3] can be rewritten as follows:

$$\sum_{\vec{q}} V(\vec{q})\mathcal{G}(\vec{p},\tau-\tau')n_{\vec{p}-\vec{q}\sigma} = \Sigma_x \mathcal{G}(\vec{p},\tau-\tau'); \tag{A.14}$$

that is the exchange self-energy of the electron due to the phonon induced interaction between electrons. It just renormalizes the chemical potential in $\xi_{\vec{p}}$, but its contribute is negligible for weak coupling and, thus, will be ignored.
Hence, the second term on the left hand side can be rewritten in terms of the following quantity

$$\Delta(\vec{p}) = -\sum_{\vec{q}} V(\vec{q})\mathcal{F}(\vec{p}-\vec{q},0). \tag{A.15}$$

that is the *gap function* or the BCS order parameter. Its relation with $\mathcal{F}$ implies a non vanishing value only in superconducting state.
Using Eq. A.15, Eq. A.12 can be rewritten in the form

$$\left(\left(-\frac{\partial}{\partial\tau}-\xi_{\vec{p}}\right)\mathcal{G}(\vec{p},\tau-\tau')\right) + \Delta(\vec{p})\mathcal{F}^\dagger(\vec{p},\tau-\tau') = \delta(\tau-\tau'). \tag{A.16}$$

Since Eq. A.16 two unknown terms: the normal $\mathcal{G}$ and the anomalous propagators $\mathcal{F}^\dagger$, we need to write the Equation-of-Motion for $\mathcal{F}^\dagger$:

$$\begin{aligned}\frac{\partial}{\partial\tau}\mathcal{F}^\dagger(\vec{p},\tau-\tau') &= -\frac{\partial}{\partial\tau}\left[\Theta(\tau-\tau')\left\langle C^\dagger_{\vec{p}\uparrow}(\tau)C^\dagger_{-\vec{p}\downarrow}(\tau')\right\rangle - \Theta(\tau'-\tau)\left\langle C^\dagger_{-\vec{p}\downarrow}(\tau')C^\dagger_{\vec{p}\uparrow}(\tau)\right\rangle\right] \\ &= -\delta(\tau-\tau')\left\langle C^\dagger_{\vec{p}\uparrow}, C^\dagger_{-\vec{p}\downarrow}\right\rangle + \left\langle T_\tau[\frac{\partial}{\partial\tau}C^\dagger_{\vec{p}\uparrow}(\tau)]C^\dagger_{-\vec{p}\downarrow}(\tau')\right\rangle \\ &= \left\langle T_\tau\left[\frac{\partial}{\partial\tau}C^\dagger_{\vec{p}\uparrow}(\tau)\right]C^\dagger_{-\vec{p}\downarrow}(\tau')\right\rangle.\end{aligned} \tag{A.17}$$

Here the term with $\delta(\tau-\tau')$ vanish due to the anticommutation relations. Again, using the Heisenberg equation we obtain

$$\frac{\partial}{\partial\tau}C^\dagger_{\vec{p}\sigma}(\tau) = [H, C^\dagger_{\vec{p}\sigma}(\tau)] = \xi_{\vec{p}}C^\dagger_{\vec{p}\sigma}(\tau) + \sum_{\vec{q}\vec{p}'s'} V(\vec{q})C^\dagger_{\vec{p}+\vec{q}\sigma}(\tau)C_{\vec{p}'+\vec{q}s'}(\tau)C_{\vec{p}'s'}(\tau), \tag{A.18}$$

which is not the Hermitian conjugate of $\partial C_{\vec{p}\sigma}(\tau)/\partial\tau$ since $[C_{\vec{p}\sigma}(\tau)]^\dagger$ is not the Hermitian conjugate of $C_{\vec{p}\sigma}(\tau)$.
Eq. A.17 becomes

$$\left(\left(-\frac{\partial}{\partial\tau}+\xi_{\vec{p}}\right)\mathcal{F}^\dagger(\vec{p},\tau-\tau')\right) + \sum_{\vec{q}\vec{p}'s} V(\vec{q})\left\langle T_\tau C^\dagger_{\vec{p}-\vec{q}\uparrow}(\tau)C^\dagger_{\vec{p}'+\vec{q}s'}(\tau)C_{\vec{p}'s'}(\tau)C^\dagger_{-\vec{p}\downarrow}(\tau')\right\rangle = 0. \tag{A.19}$$

Using the Wick theorem, the second term on the left hand side gives rise to all possible pair combinations, but the terms

$$\left\langle C^\dagger_{\vec{p}'+\vec{q}s'}(\tau)C_{\vec{p}'s'}(\tau)\right\rangle\left\langle C^\dagger_{\vec{p}-\vec{q}\uparrow}(\tau)C^\dagger_{-\vec{p}\downarrow}(\tau')\right\rangle = \delta_{\vec{q},0}n_{\vec{p}'s'}\mathcal{F}^\dagger(\vec{p},\tau-\tau'), \tag{A.20}$$

provides $\vec{q} = 0$ and thus will be neglected.
As well, the combination :

$$\langle C^{\dagger}_{\vec{p}'+\vec{q}s'}(\tau)C_{\vec{p}'s'}(\tau)\rangle \langle C^{\dagger}_{\vec{p}'+\vec{q}s'}(\tau)C^{\dagger}_{-\vec{p}\downarrow}(\tau')\rangle = -\delta_{s',\uparrow}\delta_{\vec{p}',\vec{p}-\vec{q}}n_{\vec{p}-\vec{q}}\mathcal{F}^{\dagger}(\vec{p},\tau-\tau'), \quad \text{(A.21)}$$

again gives the exchange self energy $\Sigma_x = \sum_{\vec{q}} V(\vec{q})n_{\vec{p}-\vec{q}}$, so will be ignored.
The only used combination is :

$$\langle C^{\dagger}_{\vec{p}-\vec{q}\uparrow}(\tau)C^{\dagger}_{\vec{p}'+\vec{q}s'}(\tau)\rangle \langle C_{\vec{p}'s'}(\tau)C^{\dagger}_{-\vec{p}\downarrow}(\tau')\rangle = \delta_{s',\downarrow}\delta_{\vec{p}',-\vec{p}}\Delta^{\dagger}(\vec{p})\mathcal{G}(-\vec{p},\tau-\tau'), \quad \text{(A.22)}$$

hence we have:

$$\left(\left(-\frac{\partial}{\partial\tau}+\xi_{\vec{p}}\right)\mathcal{F}^{\dagger}(\vec{p},\tau-\tau')+\Delta^{\dagger}(\vec{p})\mathcal{G}(\vec{p},\tau-\tau'\right)=0. \quad \text{(A.23)}$$

The Eqs. A.16-A.23 are the *Gor'kov equations* in the momentum space in the imaginary time representation.
In order to obtain the Eqs. A.16-A.23 in the Matsubara representation, we define the Fourier transforms of the correlation functions as follows:

$$\begin{aligned}\mathcal{G}(\vec{p},\tau) &= \frac{1}{\beta}\sum_{\omega_n} e^{-i\omega_n\tau}\mathcal{G}\left(\vec{p},\omega_n\right)\\ \mathcal{F}(\vec{p},\tau) &= \frac{1}{\beta}\sum_{\omega_n} e^{-i\omega_n\tau}\mathcal{F}\left(\vec{p},\omega_n\right)\\ \mathcal{F}^{\dagger}(\vec{p},\tau)&\frac{1}{\beta}\sum_{\omega_n} e^{-i\omega_n\tau}\mathcal{F}^{\dagger}\left(\vec{p},\omega_n\right).\end{aligned} \quad \text{(A.24)}$$

where $\beta = 1/k_BT$, with k_B Boltzmann constant. Using these transformations in Eqs. A.16-A.23 we obtain the Gor'kov equations in the Matsubara representation:

$$\left(i\omega_n-\xi_{\vec{p}}\right)\mathcal{G}\left(\vec{p},\omega_n\right)+\Delta(\vec{p})\mathcal{F}^{\dagger}\left(\vec{p},\omega_n\right)=1 \quad \text{(A.25)}$$

$$\left(i\omega_n+\xi_{\vec{p}}\right)\mathcal{F}^{\dagger}\left(\vec{p},\omega_n\right)-\Delta^{\dagger}(\vec{p})\mathcal{G}\left(\vec{p},\omega_n\right)=0. \quad \text{(A.26)}$$

In the same way we can obtain two equation for $\mathcal{F}$ and $\mathcal{G}^{\dagger}$:

$$\left(i\omega_n-\xi_{\vec{p}}\right)\mathcal{F}\left(\vec{p},\omega_n\right)+\Delta(\vec{p})\mathcal{G}^{\dagger}\left(\vec{p},\omega_n\right)=1 \quad \text{(A.27)}$$

$$-\left(i\omega_n+\xi_{\vec{p}}\right)\mathcal{G}^{\dagger}\left(\vec{p},\omega_n\right)+\Delta^{\dagger}(\vec{p})\mathcal{F}\left(\vec{p},\omega_n\right)=0. \quad \text{(A.28)}$$

We can generalize the Gor'kov equations considering a system with a generic Hamiltonian:

$$\mathcal{H}=\begin{bmatrix}H_N & \Delta\\ -\Delta^* & -H_N^*\end{bmatrix} \quad \text{(A.29)}$$

where H_N is the normal state Hamiltonian. Defining the matrix of the propagators:

$$\hat{G}\left(\omega_n\right)=\begin{bmatrix}\mathcal{G}\left(\omega_n\right) & \mathcal{F}\left(\omega_n\right)\\ -\mathcal{F}^*\left(\omega_n\right) & -\mathcal{G}^*\left(\omega_n\right)\end{bmatrix}; \quad \text{(A.30)}$$

we can rearrange the Gor'kov equations in a matricial form:

$$\left[i\omega_n\hat{1} - \begin{pmatrix} H_N & \Delta \\ -\Delta^* & -H_N^* \end{pmatrix}\right] \times \hat{G}\left(\omega_n\right) = \hat{1}, \tag{A.31}$$

where $\hat{1}$ is the unit matrix in Nambu space. These can be rewritten in the real space performing a Fourier transform thus finding:

$$\left[i\omega_n\hat{1} - \int d\vec{r}_1 \begin{pmatrix} H_N\left(\vec{r},\vec{r}_1\right) & \Delta\left(\vec{r},\vec{r}_1\right) \\ -\Delta^*\left(\vec{r},\vec{r}_1\right) & -H_N^*\left(\vec{r},\vec{r}_1\right) \end{pmatrix}\right] \times \hat{G}\left(\vec{r}_1,\vec{r}\,',\omega_n\right) = \hat{1}\delta\left(\vec{r}-\vec{r}\,'\right). \tag{A.32}$$

Appendix B

Green's function of a semi-infinite lead.

Green's functions of certain lattice systems may be obtained in analytical form rather than by matrix inversion, this is the case of semi-infinite lattices [150]. In the study of systems made up of two leads and one central device, e.g. the Josephson junctions, we may assume that the two electrodes as well described by semi-infinite lattices. In order to apply the RGF technique to resolve the Eq. 2.10 inside the barrier, and compute the barrier GF, we need to know the *surface Green's functions* of the superconducting leads. In our system, the barrier coincides with the ferromagnetic insulator with Rashba spin-orbit coupling, Fig. 2.1. Since we assume that the order parameter is uniform and that there is no disorder in the superconductors, we can "condense" all the semi-infinite two-dimensional superconducting leads in their edge stripes, thus calculating their surface GFs.

Here we will evaluate the surface Green's function of a semi-infinite normal lead. The extension of these calculations to the superconducting case is rather complicated and therefore we will only report the results of Ref.[135]. We start from the tight-binding Hamiltonian of a semi-infinite lead including nearest neighbor hopping. This lead extends infinitely to the right and ends at the site m_0, Fig. B.1. Let us denote

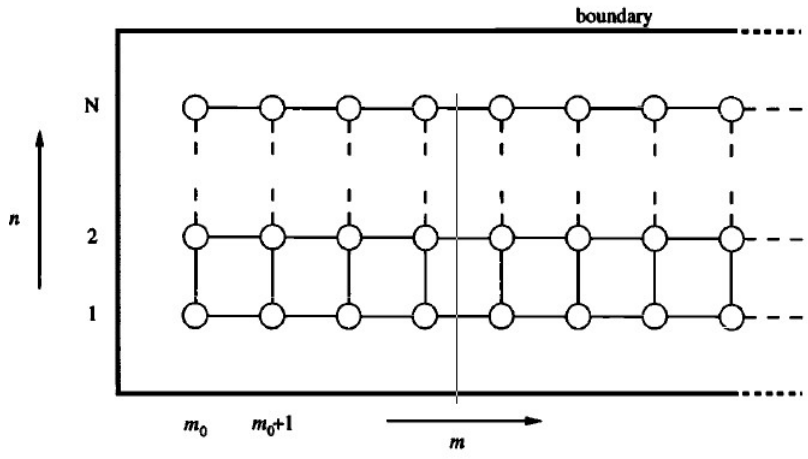

Figure B.1: Representative scheme of the semi-infinite lead, Ref.[150].

with x the longitudinal direction, parallel to transport, and with y the transverse one. The lead Hamiltonian as the following form:

$$H^{semi}(m_0) = \sum_{m=m_0}^{\infty}\sum_{n=1}^{N}[\varepsilon_{mn}c_{mn}^{\dagger}c_{mn} + t_x^{mn}c_{mn}^{\dagger}c_{m+1,n} + t_y^{mn}c_{mn}^{\dagger}c_{m,n+1} + \left(t_x^{m-1,n}\right)^* c_{mn}^{\dagger}c_{m-1,n} + \left(t_y^{m,n-1}\right)^* c_{mn}^{\dagger}c_{m,n-1}] \tag{B.1}$$

where m and n are respectively the indices of the lattice position in the longitudinal and transverse direction, t_x^{mn} (t_y^{mn}) is the hopping energy onto site (m,n) from its longitudinal x (transverse y) neighbor [150]. If we want to evaluate the exact Green's function of the lead from this tight-binding Hamiltonian, we have to ensure that we can recover the free-particle case from our results, in the continuum limit. In particular, we have to do two fundamental assumptions [150]. First, the on-site energy is set equal to the negative sum of the nearest-neighbor hopping energies,

$$\varepsilon_{mn} = -(t_x^{mn} + t_y^{mn} + \left(t_x^{m-1,n}\right)^* + \left(t_y^{m,n-1}\right)^*) \tag{B.2}$$

which yields the same zeros of energy in the undiscretized case as in the continuous case. Second we have to define the hopping energies as follows:

$$\begin{cases} t_x = \frac{-\hbar^2}{2m^*}\frac{1}{a_x^2} \\ \\ t_y = \frac{-\hbar^2}{2m^*}\frac{1}{a_y^2}, \end{cases} \tag{B.3}$$

where a_x (a_y) is the lattice constant in the x (y) direction.
From now on, we will consider the hopping energy to be uniform along each direction. Hence, we have $t_x^{mn} = t_x$ ($t_y^{mn} = t_y$). In this way, assuming uniform hopping parameters corresponds to consider an equally spaced grid in both directions.
Now, we start solving the time-independent Schrödinger equation to obtain eigenvalues and eigenstates of our system. For the Hamiltonian in Eq. B.1 the eigenvalue problem is :

$$H^{semi}\left|\Psi^{\mu\nu}\right\rangle = E^{\mu\nu}\left|\Psi^{\mu\nu}\right\rangle, \tag{B.4}$$

where μ and ν are respectively the longitudinal and transverse quantum numbers of the system (this distinction is due to the different hopping amplitudes along the two directions, $t_x \neq t_y$), $E^{\mu\nu}$ is the energy measured with respect to the bottom of the conduction band.
The eigenstates may be expanded as follows:

$$\left|\Psi^{\mu\nu}\right\rangle = \sum_{mn} u_{mn}^{\mu\nu}c_{mn}^{\dagger}\left|0\right\rangle \tag{B.5}$$

$$u_{mn}^{\mu\nu} = \left\langle 0\right| c_{mn}\left|\Psi^{\mu\nu}\right\rangle.$$

Substituting the first of the Eq. B.5 in the Eq. B.4, we find a set of coupled equations for the expansion coefficients $u_{mn}^{\mu\nu}$:

$$t_x^* u_{m-1,n}^{\mu\nu} + t_x u_{m+1,n}^{\mu\nu} + t_y^* u_{m,n-1}^{\mu\nu} + t_x u_{m,n+1}^{\mu\nu} = (E^{\mu\nu} - \varepsilon_{mn})\, u_{mn}^{\mu\nu}. \tag{B.6}$$

As a further simplification, we suppose that the eigenvalue problem has a separable solution. Hence, we can divide the dependence on the indices (m,n) and (μ,ν) in the expressions for the eigenvalue energies $E^{\mu\nu}$ and coefficients $u^{\mu\nu}_{mn}$.

$$u^{\mu\nu}_{mn} = \phi^{\mu}_{m} \cdot \chi^{\nu}_{n}, \qquad E^{\mu\nu} = E^{\mu} + E^{\nu}, \tag{B.7}$$

where ϕ^{μ}_{m} (χ^{ν}_{n}) represents the longitudinal (transverse) wave-function. Therefore, the Eq. B.6 splits into longitudinal and transverse parts:

$$\begin{aligned} t^{*}_{x}\phi^{\mu}_{m-1} + t_{x}\phi^{\mu}_{m+1} - \left(E^{\mu} - 2t_{x}\right)\phi^{\mu}_{m} &= 0 \\ t^{*}_{y}\chi^{\nu}_{n-1} + t_{y}\chi^{\nu}_{n+1} - \left(E^{\nu} - 2t_{y}\right)\chi^{\nu}_{n} &= 0. \end{aligned} \tag{B.8}$$

Now, we have to find a solution for ϕ^{μ}_{m} and χ^{ν}_{n}. We may therefore construct the solutions of the Eq. B.8 starting from well-known analytic solutions to the continuous problem. We choose functions that satisfy the hard-wall boundary conditions, i.e. the wave-functions must vanish at the left end $m = m_0 - 1$ and at the lateral edges of the lead $n = 0$, $n = N + 1$. Hence, we have:

- for the longitudinal wave-function ϕ^{μ}_{m}, the condition $\phi^{\mu}_{m_0-1} = 0$ yields

$$\phi^{\mu}_{m} = \sqrt{\frac{2}{\pi}} \cdot \sin\left(k^{\mu}_{x} \cdot a_{x}\left(m - m_0 + 1\right)\right), \tag{B.9}$$

  with k^{μ}_{x} as wave-vector in the longitudinal direction, and for the energy dispersion relation

$$E^{\mu} = -2t_{x} \cdot \left(1 - \cos\left(k^{\mu}_{x} \cdot a_{x}\right)\right); \tag{B.10}$$

- for the transverse wave-function χ^{ν}_{n}, the conditions $\chi^{\nu}_{0} = \chi^{\nu}_{N+1} = 0$ yield

$$\chi^{\nu}_{n} = \sqrt{\frac{2}{N+1}} \cdot \sin\left(\frac{\pi\nu n}{N+1}\right); \tag{B.11}$$

  with ν as discrete mode number of the transverse wave-function, $\nu = 1, \ldots, N$ and for the energy dispersion relation

$$E^{\nu} = -2t_{y} \cdot \left(1 - \cos\left(\frac{\pi\nu n}{N+1}\right)\right). \tag{B.12}$$

Therefore, the total energy dispersion relation has the form:

$$E^{\mu\nu} = -2\left(t_{x} + t_{y}\right) + 2t_{x}\cos\left(k^{\mu}_{x} \cdot a_{x}\right) + 2t_{y}\cos\left(\frac{\pi\nu n}{N+1}\right); \tag{B.13}$$

and the solutions of the time-independent Schrödinger equation are:

$$\left|\Psi^{\mu\nu}\right\rangle = \sum_{mn} \phi^{\mu}_{m}\chi^{\nu}_{n}c^{\dagger}_{mn}\left|0\right\rangle. \tag{B.14}$$

By definition [3, 149, 150], the Green's function of the system can be written as follows:

$$G\left(m,n,m',n';E\right) = G_{m,m'}\left(n,n'\right) = \sum_{\mu\nu} \frac{c^{\dagger}_{mn}\left|\Psi^{\mu\nu}\right\rangle\left\langle\Psi^{\mu\nu}\right|c_{m',n'}}{E - E^{\mu\nu} + i\eta}, \tag{B.15}$$

where η is an infinitesimal real positive quantity which is needed to preserve causality. Now we use the decomposition of $|\Psi^{\mu\nu}\rangle$ in Eq. B.14 inside the Eq. B.15, thus finding the expression :

$$G_{m,m'}(n,n') = \int_0^\pi d\mu \sum_{\nu=1}^{N} \frac{\phi_m^\mu \left(\phi_{m'}^\mu\right)^* \chi_n^\nu \left(\chi_{n'}^\nu\right)^*}{E - E^{\mu\nu} + i\eta}, \tag{B.16}$$

where we introduced the variable $\mu = k_x^\mu \cdot a_x$, as the product between the wave-vector and the lattice constant in the longitudinal direction. In principle, for each couple of transverse indices (n,n') we have an infinite-dimensional matrix (this comes from the fact that m goes from m_0 to ∞): the matrix of Green's functions. When we deal with a tight-binding model for our system, in the nearest-neighbor approximation, only adjacent transverse stripes of the system are connected with each others. Hence, when we consider the ensemble of two leads and one central device, only the edges of the leads influence the latter. Therefore, the unique Green's function we have to compute is that for $m = m' = m_0$, i.e. the *surface Green's function* of the lead:

$$G_{m,m'}(n,n') = \sum_{\nu=1}^{N} \chi_n^\nu \left(\chi_{n'}^\nu\right)^* \frac{2}{\pi} \int_0^\pi d\mu \frac{\sin^2(\mu = k_x^\mu \cdot a_x)}{E - (E^\mu + E^\nu) + i\eta}. \tag{B.17}$$

Using the Eq. B.13, we get for the integral:

$$\frac{2}{\pi} \int_0^\pi d\mu \frac{\sin^2(\mu)}{E + i\eta + 2(t_x + t_y) - 2t_x \cos(\mu) - 2t_y \cos\left(\frac{\pi\nu n}{N+1}\right)}.$$

It is useful to define the following parameters:

$$p = p(\nu) = E + i\eta + 2(t_x + t_y) - 2t_y \cos\left(\frac{\pi\nu n}{N+1}\right),$$
$$q = -2t_x,$$

so obtaining :

$$\frac{2}{\pi} \int_0^\pi d\mu \frac{\sin^2(\mu)}{p + q\cos\mu} = \frac{2p}{q^2}\left(1 - \sqrt{1 - \frac{q^2}{p^2}}\right) = \frac{2}{q}\left(\frac{p}{q} - i\sqrt{1 - \frac{p^2}{q^2}}\right).$$

The latter can be further simplified by introducing θ such that :

$$\exp(i\theta) = \cos\theta + i\sin\theta = \left(\frac{p}{q} - i\sqrt{1 - \frac{p^2}{q^2}}\right), \tag{B.18}$$
$$\theta = \arccos\left(\frac{p}{q}\right).$$

Hence, we find the final expression for the surface Green's function of the lead :

$$G_{m,m'}(n,n') = \sum_{\nu=1}^{N} \chi_n^\nu \left(\chi_{n'}^\nu\right)^* \frac{2}{q} \exp i\theta = \tag{B.19}$$
$$-\sum_{\nu=1}^{N} \frac{2}{N+1} \sin\left(\frac{\pi\nu n}{N+1}\right) \sin\left(\frac{\pi\nu n'}{N+1}\right) \frac{\exp(i\theta)}{2t_x}$$

with

$$\theta = -\frac{1}{2t_x}\left[i\arccos\left(-\frac{1}{2t_x}\left(E + i\eta + 2\left(t_x + t_y\right) - 2t_y\cos\left(\frac{\pi\nu n}{N+1}\right)\right)\right)\right]. \quad \text{(B.20)}$$

We can finally notice that the elements of the Green's functions' matrix depend on the transverse mode number ν. It is worth to notice that in these calculations we set the *hard-wall boundary conditions* in the y-direction [150]. Therefore, in this direction we obtain a quantized eigenvalues spectrum. At the end of our calculations, we get the GFs for every couple of sites (n, n') in the edge stripe of the leads [150].

Now we report the surface GF for the superconducting leads as in Ref.[135] applied to our junction scheme, that we report in Fig. B.2 for the sake of clarity. The barrier lies in the interval $1 \leq j \leq L$ and the superconducting leads lie in the intervals $j \leq 0$ and $j \geq L+1$. The left and right edge stripes are located, respectively, at $j = 0$ and $j = L+1$ and are described by the surface GFs $G_{0,0}$ and $G_{L+1,L+1}$ [135].

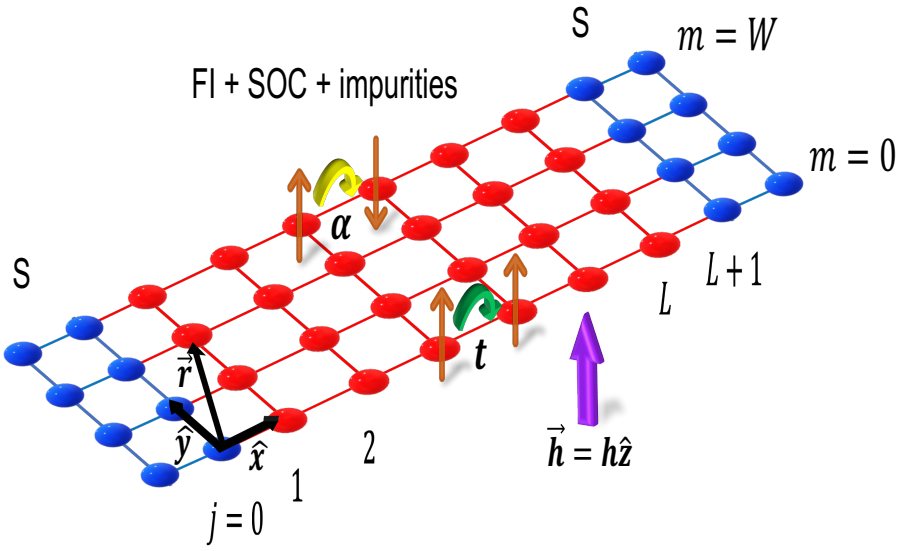

Figure B.2: $2D$-lattice model of the SFIS JJ including exchange field, spin-orbit coupling (SOC) and impurities in the barrier. The junction lies in the $x-y$ plane and it is represented by a lattice with $(L+2)$ and W sites along x and y directions, respectively. The influence of the S leads (blue sites) is condensed in the border stripes at $j = 0$ and $j = L+1$. The FI barrier (red sites) extends from $j = 1$ to $j = L$ along the transport direction, i.e. along x. The exchange field h (violet arrow) is parallel to the z axis, thus perpendicular to the JJ plane. The hopping t between nearest-neighbor sites is here represented by green arrows. The SOC α is depicted by the spin-flipping process highlighted by the yellow arrow.

Here, we will indicate with $G_{0,0,k,k'}$ ($G_{L+1,L+1,k,k'}$) the GF's matrix describing the particle propagation between the sites k and k' in the left (right) lead's edge stripe. For each couple of indices (k, k') we have a 2×2 matrix (in the Nambu space) [135] or a 4×4 matrix (in the Nambu-spin space).
We now start presenting the surface GFs of the S leads in the Nambu space [135]. Then we will generalize the result to Nambu-spin space. Therefore, the left and right surface GFs have the following structure in Nambu space, given in Ref.[135]:

$$G_{\omega_n}(0,0,k,k') = \sum_{l=1}^{W} \frac{e^{ip_l^+}}{t\,\Omega_n\,(W+1)} \sin(q_l k) \sin(q_l k')$$

$$\times \begin{matrix} & c_\uparrow & c_\downarrow^\dagger \\ c_\uparrow^\dagger & \Omega_1 & -i\,\Delta \\ c_\downarrow & -i\,\Delta & \Omega_2 \end{matrix}$$

$$- \sum_{l=1}^{W} \frac{e^{-ip_l^-}}{t\,\Omega_n\,(W+1)} \sin(q_l k) \sin(q_l k') \tag{B.21}$$

$$\times \begin{matrix} & c_\uparrow & c_\downarrow^\dagger \\ c_\uparrow^\dagger & \Omega_2 & -i\,\Delta \\ c_\downarrow & -i\,\Delta & \Omega_1 \end{matrix}$$

and

$$G_{\omega_n}(L+1,L+1,k,k') = \sum_{l=1}^{W} \frac{e^{ip_l^+}}{t\,\Omega_n\,(W+1)} \sin(q_l k) \sin(q_l k')$$

$$\times \begin{matrix} & c_\uparrow & c_\downarrow^\dagger \\ c_\uparrow^\dagger & \Omega_1 & -i\,\Delta\,e^{i\phi} \\ c_\downarrow & -i\,\Delta\,e^{-i\phi} & \Omega_2 \end{matrix}$$

$$- \sum_{l=1}^{W} \frac{e^{-ip_l^-}}{t\,\Omega_n\,(W+1)} \sin(q_l k) \sin(q_l k') \tag{B.22}$$

$$\times \begin{matrix} & c_\uparrow & c_\downarrow^\dagger \\ c_\uparrow^\dagger & \Omega_2 & -i\,\Delta\,e^{i\phi} \\ c_\downarrow & -i\,\Delta\,e^{-i\phi} & \Omega_1 \end{matrix}$$

where ϕ is the phase difference between the two superconductors and we have

$$\begin{aligned} \Omega_{1,2} &= \mp\Omega_n - \omega_n \\ \Omega_n &= \sqrt{\omega_n^2 + \Delta^2} \\ q_l &= \frac{l\pi}{W+1} \\ p_l^\pm &= \arccos\left[-\frac{1}{2t}\left(\mu + 2t\cos q_l \pm i\,\Omega_n\right)\right], \end{aligned} \tag{B.23}$$

with the conditions: $\Im(p^+) > 0$ and $\Im(p^-) < 0$ [135]. Note that q_l are the eigenvalues of the wavenumber labelling the eigenfunctions along the y-direction.

As next step, we have to generalize the matrices $\check{G}_{0,0,k,k'}$ ($\check{G}_{L+1,L+1,k,k'}$) in the Nambu-spin space. Here we use the notation $\check{G}$ to denote Green's function in the Nambu-spin space. Hence, we have:

$$\check{G}_{k,k'}(\omega_n,0,0) \longrightarrow \begin{array}{c} \\ c^\dagger_{k\uparrow} \\ c^\dagger_{k'\downarrow} \\ c_{k\uparrow} \\ c_{k'\downarrow} \end{array} \begin{array}{c} \begin{array}{cccc} c_{k\uparrow} & c_{k'\downarrow} & c^\dagger_{k\uparrow} & c^\dagger_{k'\downarrow} \end{array} \\ \begin{pmatrix} \Omega_1 & 0 & 0 & \Delta \\ 0 & -\Omega_2^* & -\Delta^* & 0 \\ 0 & -\Delta^* & -\Omega_1^* & 0 \\ \Delta & 0 & 0 & \Omega_2 \end{pmatrix} \end{array} \tag{B.24}$$

$$\check{G}_{k,k'}(\omega_n,L+1,L+1) \longrightarrow \begin{array}{c} \\ c^\dagger_{k\uparrow} \\ c^\dagger_{k'\downarrow} \\ c_{k\uparrow} \\ c_{k'\downarrow} \end{array} \begin{array}{c} \begin{array}{cccc} c_{k\uparrow} & c_{k'\downarrow} & c^\dagger_{k'\uparrow} & c^\dagger_{k'\downarrow} \end{array} \\ \begin{pmatrix} \Omega_1 & 0 & 0 & \Delta\, e^{i\,\phi} \\ 0 & -\Omega_2^* & -\Delta^*\, e^{i\,\phi} & 0 \\ 0 & -\Delta^*\, e^{-i\,\phi} & -\Omega_1^* & 0 \\ \Delta\, e^{-i\,\phi} & 0 & 0 & \Omega_2 \end{pmatrix} \end{array}. \tag{B.25}$$

Taking for example the left lead, each GF matrix with (k,k') fixed has the form in Fig. B.3. Thus we have $W \times W$ different matrix blocks $\check{G}_{0,0,k,k'}$ ($\check{G}_{L+1,L+1,k,k'}$) labelled by the couple of indices (k,k'). In order to reconstruct the stripe GF form as in Fig. 1.10 we have to rearrange them.
Let us consider the left S lead surface stripe with only two sites in the y-direction, $W = 2$. The indices (k,k') run from 1 to 2. In principle we have four different 4×4 matrices in the Nambu-spin space: $\check{G}_{1,1}(\omega_n,0,0)$, $\check{G}_{1,2}(\omega_n,0,0)$, $\check{G}_{2,1}(\omega_n,0,0)$, $\check{G}_{2,2}(\omega_n,0,0)$. Every block has the structure in Fig. B.3. We can reconstruct the whole matrix of the left surface GF by separating each block $\check{G}_{k,k'}(\omega_n,0,0)$ in its 2×2 component matrices $(G,F,-F^\dagger,-G^\dagger)$. Then we rearrange them in the following way, Fig. B.4. Doing the same for the right lead surface GF and generalizing this reasoning to W-sites stripes, we have the leads GFs ready to start the recursive algorithm of the RGF technique.

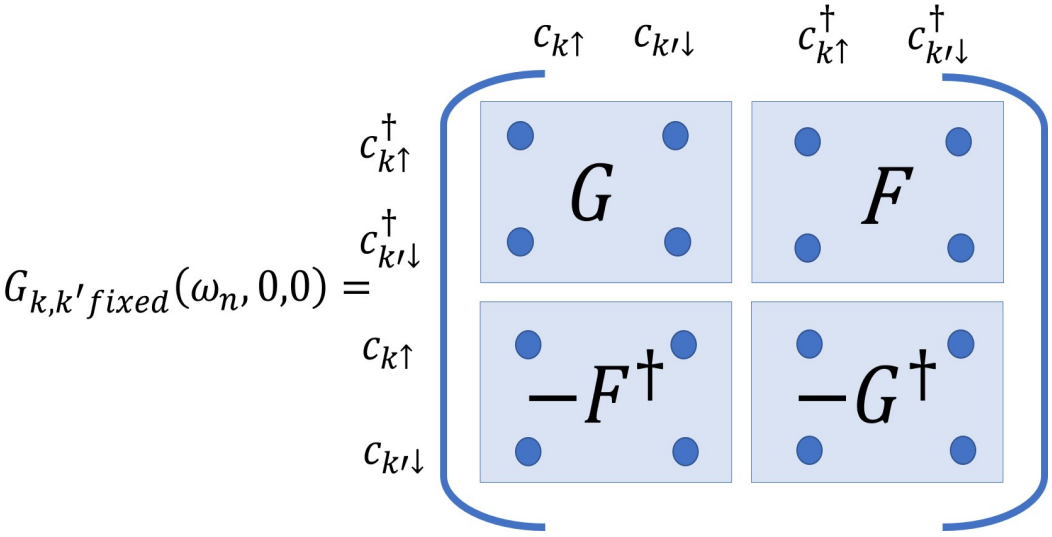

Figure B.3: Structure of the left Green's function matrix that describes the particle propagation between the sites k and k' (in Nambu-spin space).

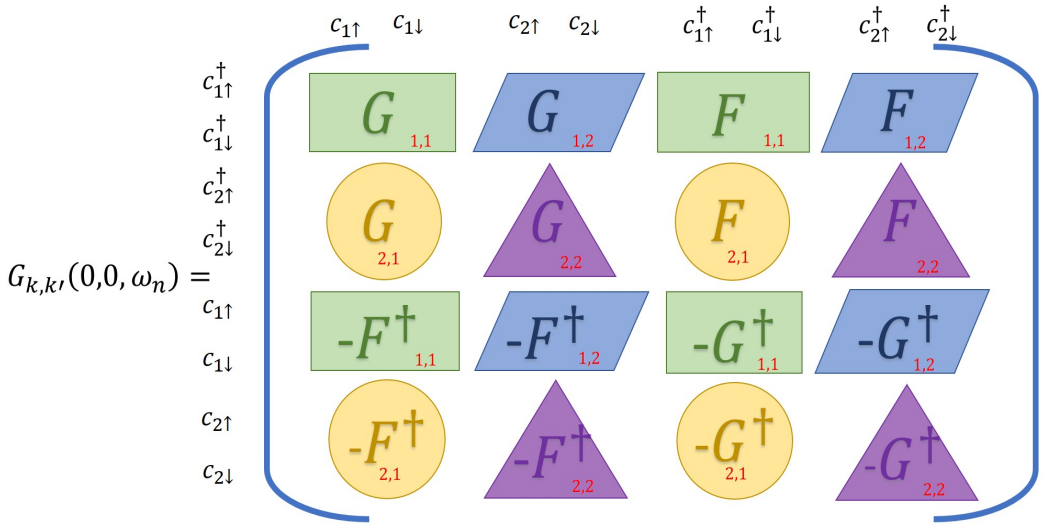

Figure B.4: Structure of the surface Green's function matrix for the left lead with two lattice sites along the y-direction (in Nambu-spin space).

Appendix C

From Andreev levels crossings to $J(\phi)$ jumps and current noise amplification

In this appendix, we illustrate the connection between the crossings of level pairs in Andreev Bound States (ABS) spectrum and the jumps discontinuities in the Josephson current. Moreover, we show that the abrupt change in sign of $J(\phi)$ leads to δ-like peaks in the current derivatives with respect to the dot energy and Zeeman field. These, in turn, provide an amplification of the current noise response to charge and magnetic, i.e. ε_d and h, fluctuations, as it can be predicted from Eq. 4.27. Let us consider, as an example, the ABS spectrum for the SQDS JJ in Fig. 4.3(c) (at $\varepsilon_d = 1$, $h = 1.3$, $\Gamma = 1$ and $\Delta = 0.01$) that we, here,report in Fig. C.1(a), for the sake of clarity. In this case, we indeed observe ABS crossings at $\pm\phi_0 \neq \pm\pi$ and energy $\varepsilon = 0$.

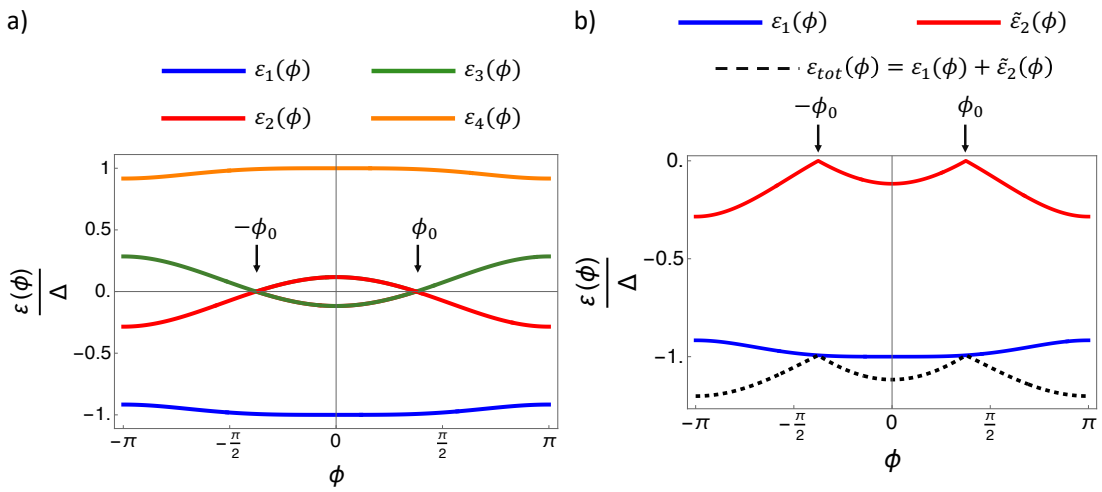

Figure C.1: Example of Andreev levels crossings at $\pm\phi_0 \neq \pm\pi$, for the SQDS JJ at $\varepsilon_d = 1$, $h = 1.3$, $\Gamma = 1$ and $\Delta = 0.01$ (a). Current carrying Andreev levels and the total energy state, defined as the sum of these two levels, that effectively carries current through the SQDS JJ (b).

If the Andreev levels $\{\varepsilon_n\}$ (with $n = 1, ..., 4$) together with the crossing phases $\pm\phi_0$ are functions of the system microscopical parameters $\{\lambda_i\} = \{\varepsilon_d, h, \Gamma, \Delta\}$, i.e. $\varepsilon_n = \varepsilon_n(\{\lambda_i\})$ and $\phi_0 = \phi_0(\{\lambda_i\})$, we clarify why jump-like discontinuities appear in

$J(\phi)$. Then we demonstrate that CPR jumps lead to δ-like divergences in the first current derivatives along $\{\lambda_i\}$, i.e. $\partial_{\lambda_i} J(\phi)$, in correspondence of the levels crossings.

Since the current is expressed in terms of the negative energy part of the Andreev spectrum we can define the current-carrying ABS level as follows

$$\varepsilon_{tot}(\phi) = \varepsilon_1(\phi) + \tilde{\varepsilon}_2(\phi) \tag{C.1}$$

where $\tilde{\varepsilon}_2(\phi)$ reads

$$\begin{aligned}\tilde{\varepsilon}_2(\phi) = \varepsilon_3(\phi)\left[\Theta(-\phi-\phi_0)+\Theta(\phi-\phi_0)\right]+\\ \varepsilon_2(\phi)\left[1-\Theta(-\phi-\phi_0)-\Theta(\phi-\phi_0)\right],\end{aligned} \tag{C.2}$$

and it is reported in Fig. C.1 (b).

Expression for $\tilde{\varepsilon}_2(\phi)$ can be simplified by noticing that the two crossing levels are particle-hole symmetric, thus, $\varepsilon_3(\phi) = -\varepsilon_2(\phi)$, leading to

$$\tilde{\varepsilon}_2(\phi) = \varepsilon_2(\phi)\left[1-2\Theta(-\phi-\phi_0)-2\Theta(\phi-\phi_0)\right]. \tag{C.3}$$

When computing the Andreev bound states contribution to the current, we have to perform the energy derivative along ϕ, according to the equation:

$$J(\phi) = \partial_\phi \varepsilon_{tot}(\phi), \tag{C.4}$$

that, using the expression in Eq. C.3, yields

$$\begin{aligned}J(\phi) =&\partial_\phi\varepsilon_2\left[1-2\Theta(-\phi-\phi_0)-2\Theta(\phi-\phi_0)\right]+\\ &+\partial_\phi\varepsilon_1+2\varepsilon_2\left[\delta(\phi+\phi_0)-\delta(\phi-\phi_0)\right].\end{aligned} \tag{C.5}$$

The first term in the right-hand side of Eq. C.5 provides the current with jumps at $\phi = \pm\phi_0$, while second term vanishes, since the δ functions are identically 0 except for the crossing points $\phi = \pm\phi_0$ where $\varepsilon_2(\phi = \pm\phi_0) = 0$. Therefore, the final expression for the CPR reads

$$J(\phi) = \partial_\phi\varepsilon_1 + \partial_\phi\varepsilon_2\left[1-2\Theta(-\phi-\phi_0)-2\Theta(\phi-\phi_0)\right]. \tag{C.6}$$

Starting from the CPR formula in Eq. C.6, we can easily demonstrate the presence of δ-like divergences in the current derivatives along system parameters $\{\lambda_i\}$ (e.g. h) by direct calculation. Performing the derivative along the system parameter λ_i, we get

$$\begin{aligned}\partial_{\lambda_i} J(\phi) = \partial_{\lambda_i}\partial_\phi\varepsilon_2\left[1-2\Theta(-\phi-\phi_0)-2\Theta(\phi-\phi_0)\right]+\\ +\partial_{\lambda_i}\partial_\phi\varepsilon_1+2\partial_\phi\varepsilon_2\partial_{\lambda_i}\phi_0\left[\delta(\phi+\phi_0)-\delta(\phi-\phi_0)\right],\end{aligned} \tag{C.7}$$

where we use that ϕ_0 is a function of $\{\lambda_i\}$ and consequently $\partial_{\lambda_i}\Theta(\pm\phi-\phi_0)$ yields

$$\partial_{\lambda_i}\Theta(\phi-\phi_0) = \partial_{\lambda_i}\phi_0(\{\lambda_i\})\,\delta(\phi-\phi_0). \tag{C.8}$$

In addition, the second term in the right-hand side of Eq. C.7 describing the δ divergences does not vanish unless $\partial_{\lambda_i}\phi_0$ does, i.e. unless ϕ_0 does not depend on the parameter λ_i. This demonstrates that, at $T = 0$, the current derivatives along the dot energy and Zeeman field exhibits δ-like divergences at the crossing points, $\phi = \pm\phi_0$, between two particle-hole symmetric Andreev levels. Divergent current derivatives, $\partial_{\varepsilon_d} J$ and $\partial_h J$, in turn suggest that the current noise response to charge and magnetic fluctuations may be amplified along the Zeeman field driven $0-\pi$ transitions.

Bibliography

[1] J. Bardeen, L. N. Cooper, and J. R. Schrieffer. "Theory of Superconductivity". In: *Phys. Rev.* 108 (5 1957), pp. 1175–1204. DOI: 10.1103/PhysRev.108.1175.

[2] Pierre Gilles De Gennes. *Superconductivity of Metals and Alloys*. Advanced book classics. Cambridge, MA: Perseus, 1999. DOI: https://cds.cern.ch/record/566105.

[3] Gerald D. Mahan. *Many-Particle Physics*. Boston, MA: Springer US, 2000. ISBN: 978-1-4757-5714-9. DOI: 10.1007/978-1-4757-5714-9_10.

[4] Alexandre Zagoskin. *Quantum Theory of Many-Body Systems*. 2nd ed. Springer Cham, 2014. ISBN: 978-3-319-07049-0. DOI: https://doi.org/10.1007/978-3-319-07049-0.

[5] Piers Coleman. *Introduction to Many-Body Physics*. Cambridge University Press, 2015. DOI: 10.1017/CBO9781139020916.

[6] Michael Tinkham. *Introduction to Superconductivity*. 2nd ed. Dover Publications, 2004. ISBN: 0486435032. DOI: http://www.worldcat.org/isbn/0486435032.

[7] A. Barone and G. Paternò. *Physics and applications of the Josephson effect*. Wiley, 1982. ISBN: 9780471014690. DOI: https://books.google.it/books?id=FrjvAAAAMAAJ.

[8] K. K. Likharev. *Dynamics of Josephson junctions and circuits*. GordonBreach, 1986. DOI: https://doi.org/10.1201/9781315141572.

[9] B.D. Josephson. "Possible new effects in superconductive tunnelling". In: *Physics Letters* 1.7 (1962), pp. 251–253. ISSN: 0031-9163. DOI: https://doi.org/10.1016/0031-9163(62)91369-0.

[10] F. Tafuri. *Fundamentals and Frontiers of the Josephson Effect*. Springer Series in Materials Science. Springer International Publishing, 2019. ISBN: 9783030207267. DOI: https://books.google.it/books?id=6gqwDwAAQBAJ.

[11] Vinay Ambegaokar and Alexis Baratoff. "Tunneling Between Superconductors". In: *Phys. Rev. Lett.* 10 (11 1963), pp. 486–489. DOI: 10.1103/PhysRevLett.10.486.

[12] Vinay Ambegaokar and Alexis Baratoff. "Tunneling Between Superconductors". In: *Phys. Rev. Lett.* 11 (2 1963), pp. 104–104. DOI: 10.1103/PhysRevLett.11.104.

[13] A. O. Caldeira and A. J. Leggett. "Quantum tunnelling in a dissipative system". English (US). In: *Annals of Physics* 149.2 (1983), pp. 374–456. ISSN: 0003-4916. DOI: 10.1016/0003-4916(83)90202-6.

[14] A.O. Caldeira and A.J. Leggett. "Path integral approach to quantum Brownian motion". In: *Physica A: Statistical Mechanics and its Applications* 121.3 (1983), pp. 587–616. ISSN: 0378-4371. DOI: https://doi.org/10.1016/0378-4371(83)90013-4.

[15] Lit-Deh Chang and Sudip Chakravarty. "Quantum decay in a dissipative system". In: *Phys. Rev. B* 29 (1 1984), pp. 130–137. DOI: 10.1103/PhysRevB.29.130.

[16] Michel H. Devoret et al. "Resonant Activation from the Zero-Voltage State of a Current-Biased Josephson Junction". In: *Phys. Rev. Lett.* 53 (13 1984), pp. 1260–1263. DOI: 10.1103/PhysRevLett.53.1260.

[17] Michel H. Devoret, John M. Martinis, and John Clarke. "Measurements of Macroscopic Quantum Tunneling out of the Zero-Voltage State of a Current-Biased Josephson Junction". In: *Phys. Rev. Lett.* 55 (18 1985), pp. 1908–1911. DOI: 10.1103/PhysRevLett.55.1908.

[18] S. Washburn et al. "Effects of Dissipation and Temperature on Macroscopic Quantum Tunneling". In: *Phys. Rev. Lett.* 54 (25 1985), pp. 2712–2715. DOI: 10.1103/PhysRevLett.54.2712.

[19] Andrew N. Cleland, John M. Martinis, and John Clarke. "Measurement of the effect of moderate dissipation on macroscopic quantum tunneling". In: *Phys. Rev. B* 37 (10 1988), pp. 5950–5953. DOI: 10.1103/PhysRevB.37.5950.

[20] John M. Martinis, Michel H. Devoret, and John Clarke. "Experimental tests for the quantum behavior of a macroscopic degree of freedom: The phase difference across a Josephson junction". In: *Phys. Rev. B* 35 (10 1987), pp. 4682–4698. DOI: 10.1103/PhysRevB.35.4682.

[21] Y. C. Chen, Matthew P. A. Fisher, and A. J. Leggett. "The return of a hysteretic Josephson junction to the zero voltage state: IV characteristic and quantum retrapping". In: *Journal of Applied Physics* 64.6 (1988), pp. 3119 –3142. DOI: 10.1063/1.341527.

[22] John Clarke et al. "Quantum Mechanics of a Macroscopic Variable: The Phase Difference of a Josephson Junction". In: *Science* 239.4843 (1988), pp. 992–997. DOI: 10.1126/science.239.4843.992. eprint: https://www.science.org/doi/pdf/10.1126/science.239.4843.992.

[23] Yuriy Makhlin, Gerd Schön, and Alexander Shnirman. "Josephson-junction qubits with controlled couplings". In: *Nature* 398.6725 (1999), pp. 305–307. DOI: 10.1038/18613.

[24] Yuriy Makhlin, Gerd Schön, and Alexander Shnirman. "Quantum-state engineering with Josephson-junction devices". In: *Rev. Mod. Phys.* 73 (2 2001), pp. 357–400. DOI: 10.1103/RevModPhys.73.357.

[25] Jens Koch et al. "Charge-insensitive qubit design derived from the Cooper pair box". In: *Phys. Rev. A* 76 (4 2007), p. 042319. DOI: 10.1103/PhysRevA.76.042319.

[26] M. H. Devoret and R. J. Schoelkopf. "Superconducting Circuits for Quantum Information: An Outlook". In: *Science* 339.6124 (2013), pp. 1169–1174. DOI: 10.1126/science.1231930. eprint: https://www.science.org/doi/pdf/10.1126/science.1231930.

[27] J. E. Mooij et al. "Josephson Persistent-Current Qubit". In: *Science* 285.5430 (1999), pp. 1036–1039. DOI: 10.1126/science.285.5430.1036. eprint: https://www.science.org/doi/pdf/10.1126/science.285.5430.1036.

[28] T. P. Orlando et al. "Superconducting persistent-current qubit". In: *Phys. Rev. B* 60 (22 1999), pp. 15398–15413. DOI: 10.1103/PhysRevB.60.15398.

[29] Caspar H. van der Wal et al. "Quantum Superposition of Macroscopic Persistent-Current States". In: *Science* 290.5492 (2000), pp. 773–777. DOI: 10.1126/science.290.5492.773. eprint: https://www.science.org/doi/pdf/10.1126/science.290.5492.773.

[30] I. Chiorescu et al. "Coherent Quantum Dynamics of a Superconducting Flux Qubit". In: *Science* 299.5614 (2003), pp. 1869–1871. DOI: 10.1126/science.1081045. eprint: https://www.science.org/doi/pdf/10.1126/science.1081045.

[31] I. Chiorescu et al. "Coherent dynamics of a flux qubit coupled to a harmonic oscillator". In: *Nature* 431.7005 (2004), pp. 159–162. DOI: 10.1038/nature02831.

[32] Michael A. Nielsen and Isaac L. Chuang. *Quantum Computation and Quantum Information*. Cambridge University Press, 2010. DOI: https://doi.org/10.1017/CBO9780511976667.

[33] A. O. Caldeira. *An Introduction to Macroscopic Quantum Phenomena and Quantum Dissipation*. Cambridge University Press, 2014. DOI: 10.1017/CBO9781139035439.

[34] A.D. Zaikin. "Quantum coherent effects in Josephson junctions and granular superconductors". In: *Physica B: Condensed Matter* 152.1 (1988), pp. 251–256. ISSN: 0921-4526. DOI: https://doi.org/10.1016/0921-4526(88)90097-X.

[35] Gerd Schön and A.D. Zaikin. "Quantum coherent effects, phase transitions, and the dissipative dynamics of ultra small tunnel junctions". In: *Physics Reports* 198.5 (1990), pp. 237–412. ISSN: 0370-1573. DOI: https://doi.org/10.1016/0370-1573(90)90156-V.

[36] Alexander Shnirman, Gerd Schön, and Ziv Hermon. "Quantum Manipulations of Small Josephson Junctions". In: *Phys. Rev. Lett.* 79 (12 1997), pp. 2371–2374. DOI: 10.1103/PhysRevLett.79.2371.

[37] V. Bouchiat et al. "Quantum coherence with a single Cooper pair". In: *Physica Scripta* 1998.T76 (1998), p. 165. DOI: 10.1238/Physica.Topical.076a00165.

[38] Y. Nakamura, C. D. Chen, and J. S. Tsai. "Spectroscopy of Energy-Level Splitting between Two Macroscopic Quantum States of Charge Coherently Superposed by Josephson Coupling". In: *Phys. Rev. Lett.* 79 (12 1997), pp. 2328–2331. DOI: 10.1103/PhysRevLett.79.2328.

[39] Y. Nakamura, Yu. A. Pashkin, and J. S. Tsai. "Coherent control of macroscopic quantum states in a single-Cooper-pair box". In: *Nature* 398.6730 (1999), pp. 786–788. DOI: 10.1038/19718.

[40] L.N. Bulaevskii, V.V. Kuzii, and Sobyanin A.A. "Superconducting system with weak coupling to the current in the ground state". In: *JETP Lett.* 25 (7 1977). DOI: https://www.osti.gov/biblio/7316063.

[41] AL Buzdin, LN Bulaevskil, and SV Panyukov. "Critical-current oscillations as a function of the exchange field and thickness of the ferromagnetic metal (F) in an SFS Josephson junction". In: *JETP lett* 35.4 (1982), pp. 178–180. DOI: http://jetpletters.ru/ps/1314/article_19853.pdf.

[42] AI Buzdin and M Yu Kupriyanov. "Josephson junction with a ferromagnetic layer". In: *Soviet Journal of Experimental and Theoretical Physics Letters* 53 (1991), p. 321. DOI: http://jetpletters.ru/ps/1151/article_17415.pdf.

[43] A. V. Andreev, A. I. Buzdin, and R. M. Osgood. "π phase in magnetic-layered superconductors". In: *Phys. Rev. B* 43 (13 1991), pp. 10124–10131. DOI: 10.1103/PhysRevB.43.10124.

[44] AI Buzdin, B Bujicic, and M Yu Kupriyanov. "Superconductor-ferromagnet structures". In: *Sov. Phys. JETP* 74.1 (1992), pp. 124–128. DOI: http://www.jetp.ras.ru/cgi-bin/dn/e_074_01_0124.pdf.

[45] V. V. Ryazanov et al. "Coupling of Two Superconductors through a Ferromagnet: Evidence for a π Junction". In: *Phys. Rev. Lett.* 86 (11 2001), pp. 2427–2430. DOI: 10.1103/PhysRevLett.86.2427.

[46] T. Kontos et al. "Josephson Junction through a Thin Ferromagnetic Layer: Negative Coupling". In: *Phys. Rev. Lett.* 89 (13 2002), p. 137007. DOI: 10.1103/PhysRevLett.89.137007.

[47] Y. Blum et al. "Oscillations of the Superconducting Critical Current in Nb-Cu-Ni-Cu-Nb Junctions". In: *Phys. Rev. Lett.* 89 (18 2002), p. 187004. DOI: 10.1103/PhysRevLett.89.187004.

[48] A. Buzdin. "π-junction realization due to tunneling through a thin ferromagnetic layer". In: *Journal of Experimental and Theoretical Physics Letters* 78 (9 2003), p. 583. DOI: 10.1134/1.1641489.

[49] S. M. Frolov et al. "Measurement of the current-phase relation of superconductor/ferromagnet/superconductor π Josephson junctions". In: *Phys. Rev. B* 70 (14 2004), p. 144505. DOI: 10.1103/PhysRevB.70.144505.

[50] A. A. Golubov, M. Yu. Kupriyanov, and E. Il'ichev. "The current-phase relation in Josephson junctions". In: *Rev. Mod. Phys.* 76 (2 2004), pp. 411–469. DOI: 10.1103/RevModPhys.76.411.

[51] A. I. Buzdin. "Proximity effects in superconductor-ferromagnet heterostructures". In: *Rev. Mod. Phys.* 77 (3 2005), pp. 935–976. DOI: 10.1103/RevModPhys.77.935.

[52] J. W. A. Robinson et al. "Critical Current Oscillations in Strong Ferromagnetic π Junctions". In: *Phys. Rev. Lett.* 97 (17 2006), p. 177003. DOI: 10.1103/PhysRevLett.97.177003.

[53] M. Weides et al. "High quality ferromagnetic 0 and π Josephson tunnel junctions". In: *Applied Physics Letters* 89.12 (Sept. 2006), p. 122511. ISSN: 0003-6951. DOI: 10.1063/1.2356104. eprint: https://pubs.aip.org/aip/apl/article-pdf/doi/10.1063/1.2356104/14360386/122511_1_online.pdf.

[54] E. Goldobin et al. "Josephson junctions with second harmonic in the current-phase relation: Properties of φ junctions". In: *Phys. Rev. B* 76 (22 2007), p. 224523. DOI: 10.1103/PhysRevB.76.224523.

[55] Francois Konschelle, Jérôme Cayssol, and Alexandre I. Buzdin. "Nonsinusoidal current-phase relation in strongly ferromagnetic and moderately disordered SFS junctions". In: *Phys. Rev. B* 78 (13 2008), p. 134505. DOI: 10.1103/PhysRevB.78.134505.

[56] A. K. Feofanov et al. "Implementation of superconductor/ferromagnet/ superconductor π-shifters in superconducting digital and quantum circuits". In: *Nature Physics* 6.8 (2010), pp. 593–597. DOI: 10.1038/nphys1700.

[57] F. S. Bergeret, A. F. Volkov, and K. B. Efetov. "Long-Range Proximity Effects in Superconductor-Ferromagnet Structures". In: *Phys. Rev. Lett.* 86 (18 2001), pp. 4096–4099. DOI: 10.1103/PhysRevLett.86.4096.

[58] F. S. Bergeret, A. F. Volkov, and K. B. Efetov. "Odd triplet superconductivity and related phenomena in superconductor-ferromagnet structures". In: *Rev. Mod. Phys.* 77 (4 2005), pp. 1321–1373. DOI: 10.1103/RevModPhys.77.1321.

[59] M. Eschrig et al. "Symmetries of Pairing Correlations in Superconductor-Ferromagnet Nanostructures". In: *Journal of Low Temperature Physics* 147.3-4 (2007), pp. 457–476. ISSN: 1573-7357. DOI: 10.1007/s10909-007-9329-6.

[60] Matthias Eschrig and Tomas Löfwander. "Triplet supercurrents in clean and disordered half-metallic ferromagnets". In: *Nature Physics* 4.2 (2008), pp. 138–143. DOI: 10.1038/nphys831.

[61] Tomas Löfwander, Roland Grein, and Matthias Eschrig. "Is CrO_2 Fully Spin Polarized? Analysis of Andreev Spectra and Excess Current". In: *Phys. Rev. Lett.* 105 (20 2010), p. 207001. DOI: 10.1103/PhysRevLett.105.207001.

[62] J. W. A. Robinson, J. D. S. Witt, and M. G. Blamire. "Controlled Injection of Spin-Triplet Supercurrents into a Strong Ferromagnet". In: *Science* 329.5987 (2010), pp. 59–61. ISSN: 0036-8075. DOI: 10.1126/science.1189246. eprint: https://science.sciencemag.org/content/329/5987/59.full.pdf.

[63] Trupti S. Khaire et al. "Observation of Spin-Triplet Superconductivity in Co-Based Josephson Junctions". In: *Phys. Rev. Lett.* 104 (13 2010), p. 137002. DOI: 10.1103/PhysRevLett.104.137002.

[64] D. Sprungmann et al. "Evidence for triplet superconductivity in Josephson junctions with barriers of the ferromagnetic Heusler alloy Cu_2MnAl". In: *Phys. Rev. B* 82 (6 2010), p. 060505. DOI: 10.1103/PhysRevB.82.060505.

[65] Matthias Eschrig. "Spin-polarized supercurrents for spintronics". In: *Physics Today* (1 2011), p. 43. DOI: 10.1063/1.3541944.

[66] Kartik Senapati, Mark G. Blamire, and Zoe H. Barber. "Spin-filter Josephson junctions". In: *Nature Materials* (2011), p. 849. DOI: 10.1038/nmat3116.

[67] F. Sebastian Bergeret, Alvise Verso, and Anatoly F. Volkov. "Spin-polarized Josephson and quasiparticle currents in superconducting spin-filter tunnel junctions". In: *Phys. Rev. B* 86 (6 2012), p. 060506. DOI: 10.1103/PhysRevB.86.060506.

[68] N. Banerjee, J. W. A. Robinson, and M. G. Blamire. "Reversible control of spin-polarized supercurrents in ferromagnetic Josephson junctions". In: *Nature Communications* 5.1 (2014), p. 4771. ISSN: 2041-1723. DOI: 10.1038/ncomms5771.

[69] Adrian Iovan, Taras Golod, and Vladimir M. Krasnov. "Controllable generation of a spin-triplet supercurrent in a Josephson spin valve". In: *Phys. Rev. B* 90 (13 2014), p. 134514. DOI: 10.1103/PhysRevB.90.134514.

[70] Jacob Linder and Jason W. A. Robinson. "Superconducting spintronics". In: *Nature Physics* 11 (2015), pp. 307–315. DOI: 10.1038/nphys3242.

[71] A. Singh et al. "Colossal Proximity Effect in a Superconducting Triplet Spin Valve Based on the Half-Metallic Ferromagnet CrO_2". In: *Phys. Rev. X* 5 (2 2015), p. 021019. DOI: 10.1103/PhysRevX.5.021019.

[72] Matthias Eschrig. "Spin-polarized supercurrents for spintronics: a review of current progress". In: *Reports on Progress in Physics* 78.10 (2015), p. 104501. DOI: 10.1088/0034-4885/78/10/104501.

[73] Taketoki Yamashita et al. "Proximity effect in a ferromagnetic semiconductor with spin-orbit interactions". In: *Phys. Rev. B* 100 (9 2019), p. 094501. DOI: 10.1103/PhysRevB.100.094501.

[74] Subhajit Pal and Colin Benjamin. "Quantized Josephson phase battery". In: *EPL (Europhysics Letters)* 126.5 (2019), p. 57002. DOI: 10.1209/0295-5075/126/57002.

[75] R. Caruso et al. "Tuning of Magnetic Activity in Spin-Filter Josephson Junctions Towards Spin-Triplet Transport". In: *Phys. Rev. Lett.* 122 (4 2019), p. 047002. DOI: 10.1103/PhysRevLett.122.047002.

[76] Roberta Satariano et al. "Inverse magnetic hysteresis of the Josephson supercurrent: Study of the magnetic properties of thin niobium/permalloy ($Fe_{20}Ni_{80}$) interfaces". In: *Phys. Rev. B* 103 (22 2021), p. 224521. DOI: 10.1103/PhysRevB.103.224521.

[77] Antonio Vettoliere et al. "High-Quality Ferromagnetic Josephson Junctions Based on Aluminum Electrodes". In: *Nanomaterials* 12.23 (2022). ISSN: 2079-4991. DOI: 10.3390/nano12234155.

[78] Halima Giovanna Ahmad et al. "Hybrid ferromagnetic transmon qubit: Circuit design, feasibility, and detection protocols for magnetic fluctuations". In: *Phys. Rev. B* 105 (21 2022), p. 214522. DOI: 10.1103/PhysRevB.105.214522.

[79] H. G. Ahmad et al. "Competition of Quasiparticles and Magnetization Noise in Hybrid Ferromagnetic Transmon Qubits". In: *IEEE Transactions on Applied Superconductivity* 33.5 (2023), pp. 1–6. DOI: 10.1109/TASC.2023.3243197.

[80] T. Yamashita et al. "Superconducting π Qubit with a Ferromagnetic Josephson Junction". In: *Phys. Rev. Lett.* 95 (9 2005), p. 097001. DOI: 10.1103/PhysRevLett.95.097001.

[81] T. Yamashita, Satoru Takahashi, and S. Maekawa. "Superconducting π qubit with three Josephson junctions". In: *Applied Physics Letters* 88 (Apr. 2006), pp. 132501 –132501. DOI: 10.1063/1.2189191.

[82] Gianni Blatter, Vadim B. Geshkenbein, and Lev B. Ioffe. "Design aspects of superconducting-phase quantum bits". In: *Phys. Rev. B* 63 (17 2001), p. 174511. DOI: 10.1103/PhysRevB.63.174511.

[83] Lev B. Ioffe et al. "Environmentally decoupled sds -wave Josephson junctions for quantum computing". In: *Nature* 398.6729 (1999), pp. 679 –681. ISSN: 1476-4687. DOI: 10.1038/19464.

[84] J. B. Majer, J. R. Butcher, and J. E. Mooij. "Simple phase bias for superconducting circuits". In: *Applied Physics Letters* 80.19 (2002), pp. 3638–3640. DOI: 10.1063/1.1478150. eprint: https://doi.org/10.1063/1.1478150.

[85] D. Balashov et al. "Passive Phase Shifter for Superconducting Josephson Circuits". In: *IEEE Transactions on Applied Superconductivity* 17.2 (2007), pp. 142–145. DOI: 10.1109/TASC.2007.897382.

[86] Taro Yamashita et al. "π phase shifter based on NbN-based ferromagnetic Josephson junction on a silicon substrate". In: *Scientific Reports* 10.1 (2020), p. 13687. DOI: 10.1038/s41598-020-70766-9.

[87] A. V. Ustinov and V. K. Kaplunenko. "Rapid single-flux quantum logic using π-shifters". In: *Journal of Applied Physics* 94.8 (2003), pp. 5405–5407. DOI: 10.1063/1.1604964.

[88] E. Goldobin et al. "Memory cell based on a φ Josephson junction". In: *Applied Physics Letters* 102.24 (2013), p. 242602. DOI: 10.1063/1.4811752. eprint: https://doi.org/10.1063/1.4811752.

[89] T. Kato, A. A. Golubov, and Y. Nakamura. "Decoherence in a superconducting flux qubit with a π-junction". In: *Phys. Rev. B* 76 (17 2007), p. 172502. DOI: 10.1103/PhysRevB.76.172502.

[90] M. Minutillo, R. Capecelatro, and P. Lucignano. "Realization of 0-π states in superconductor/ferromagnetic insulator/superconductor Josephson junctions: The role of spin-orbit interaction and lattice impurities". In: *Phys. Rev. B* 104 (18 2021), p. 184504. DOI: 10.1103/PhysRevB.104.184504.

[91] Halima Giovanna Ahmad et al. "Coexistence and tuning of spin-singlet and triplet transport in spin-filter Josephson junctions". In: *Communications Physics* 5.1 (2022), p. 2. DOI: 10.1038/s42005-021-00783-1.

[92] R. Capecelatro et al. "Andreev spin-noise detector". In: *Phys. Rev. B* 108 (10 2023), p. 104508. DOI: 10.1103/PhysRevB.108.104508.

[93] Shusaku Imajo et al. "Emergent anisotropy in the Fulde–Ferrell–Larkin–Ovchinnikov state". In: *Nature Communications* 13.1 (2022), p. 5590. DOI: 10.1038/s41467-022-33354-1.

[94] Peter Fulde and Richard A. Ferrell. "Superconductivity in a Strong Spin-Exchange Field". In: *Phys. Rev.* 135 (3A 1964), A550–A563. DOI: 10.1103/PhysRev.135.A550.

[95] A.I. Larkin and Y.N. Ovchinnikov. "Nonuniform state of superconductors". In: *Zh.Eksp.Teor.Fiz. 47 (1964) 1136-1146, Sov.Phys.JETP 20 (1965) 762* Vol: 47 (Sept. 1964). DOI: https://www.osti.gov/biblio/4653415.

[96] E. A. Demler, G. B. Arnold, and M. R. Beasley. "Superconducting proximity effects in magnetic metals". In: *Phys. Rev. B* 55 (22 1997), pp. 15174–15182. DOI: 10.1103/PhysRevB.55.15174.

[97] Roman Lutchyn, Leonid Glazman, and Anatoly Larkin. "Quasiparticle decay rate of Josephson charge qubit oscillations". In: *Phys. Rev. B* 72 (1 2005), p. 014517. DOI: 10.1103/PhysRevB.72.014517.

[98] G. Catelani et al. "Quasiparticle Relaxation of Superconducting Qubits in the Presence of Flux". In: *Phys. Rev. Lett.* 106 (7 2011), p. 077002. DOI: 10.1103/PhysRevLett.106.077002.

[99] G. Catelani et al. "Relaxation and frequency shifts induced by quasiparticles in superconducting qubits". In: *Phys. Rev. B* 84 (6 2011), p. 064517. DOI: 10.1103/PhysRevB.84.064517.

[100] G. Catelani et al. "Decoherence of superconducting qubits caused by quasiparticle tunneling". In: *Phys. Rev. B* 86 (18 2012), p. 184514. DOI: 10.1103/PhysRevB.86.184514.

[101] Xianchuang Pan et al. "Engineering superconducting qubits to reduce quasiparticles and charge noise". In: *Nature Communications* 13.1 (2022), p. 7196. DOI: 10.1038/s41467-022-34727-2.

[102] G Catelani and J P Pekola. "Using materials for quasiparticle engineering". In: *Materials for Quantum Technology* 2.1 (2022), p. 013001. DOI: 10.1088/2633-4356/ac4a75.

[103] Yukio Tanaka and Satoshi Kashiwaya. "Theory of Josephson effect in superconductor - ferromagnetic - insulator - superconductor junction". In: *Physica C: Superconductivity* 274.3 (1997), pp. 357–363. ISSN: 0921-4534. DOI: https://doi.org/10.1016/S0921-4534(97)80002-0.

[104] Shiro Kawabata et al. "Josephson π State in a Ferromagnetic Insulator". In: *Phys. Rev. Lett.* 104 (11 2010), p. 117002. DOI: 10.1103/PhysRevLett.104.117002.

[105] Shiro Kawabata and Yasuhiro Asano. "Theory of quantum transport in Josephson junctions with a ferromagnetic insulator". In: *Low Temperature Physics* 36.10 (2010), pp. 915–919. DOI: 10.1063/1.3515524. eprint: https://doi.org/10.1063/1.3515524.

[106] A. A. Bannykh et al. "Josephson tunnel junctions with a strong ferromagnetic interlayer". In: *Phys. Rev. B* 79 (5 2009), p. 054501. DOI: 10.1103/PhysRevB.79.054501.

[107] G. Wild et al. "Josephson coupling and Fiske dynamics in ferromagnetic tunnel junctions". In: *The European Physical Journal B* 78.4 (2010), pp. 509–523. ISSN: 1434-6036. DOI: 10.1140/epjb/e2010-10636-4.

[108] Avradeep Pal et al. "Pure second harmonic current-phase relation in spin-filter Josephson junctions". In: *Nature Communications* 5.1 (2014), p. 3340. DOI: 10.1038/ncomms4340.

[109] D. Massarotti et al. "Macroscopic quantum tunnelling in spin filter ferromagnetic Josephson junctions". In: *Nature Communications* (2015), p. 7376. DOI: 10.1038/ncomms8376.

[110] Shiro Kawabata et al. "Macroscopic quantum dynamics of π junctions with ferromagnetic insulators". In: *Phys. Rev. B* 74 (18 2006), p. 180502. DOI: 10.1103/PhysRevB.74.180502.

[111] A. S. Vasenko et al. "Current-voltage characteristics of tunnel Josephson junctions with a ferromagnetic interlayer". In: *Phys. Rev. B* 84 (2 2011), p. 024524. DOI: 10.1103/PhysRevB.84.024524.

[112] Timofei I. Larkin et al. "Ferromagnetic Josephson switching device with high characteristic voltage". In: *Applied Physics Letters* 100.22 (2012), p. 222601. DOI: 10.1063/1.4723576.

[113] D. Massarotti et al. "Electrodynamics of Josephson junctions containing strong ferromagnets". In: *Phys. Rev. B* 98 (14 2018), p. 144516. DOI: 10.1103/PhysRevB.98.144516.

[114] H.G. Ahmad et al. "Electrodynamics of Highly Spin-Polarized Tunnel Josephson Junctions". In: *Phys. Rev. Applied* 13 (1 2020), p. 014017. DOI: 10.1103/PhysRevApplied.13.014017.

[115] Halima Giovanna Ahmad et al. "Critical Current Suppression in Spin-Filter Josephson Junctions". In: *Journal of Superconductivity and Novel Magnetism* 33.10 (2020), pp. 3043–3049. DOI: 10.1007/s10948-020-05577-0.

[116] Caruso, Roberta et al. "Low temperature characterization of high efficiency spin-filter Josephson junctions". In: *EPJ Web Conf.* 233 (2020), p. 05007. DOI: 10.1051/epjconf/202023305007.

[117] Shiro Kawabata et al. "Theory of superconducting π-qubit with a ferromagnetic insulator". In: *Physica C: Superconductivity and its Applications* 437-438 (2006). Proceedings of the Fourth International Conference on Vortex Matter in Nanostructured Superconductors VORTEX IV, pp. 136–139. ISSN: 0921-4534. DOI: https://doi.org/10.1016/j.physc.2006.03.004.

[118] Dario Bercioux and Procolo Lucignano. "Quantum transport in Rashba spin-orbit materials: a review". In: *Reports on Progress in Physics* 78.10 (2015), p. 106001. DOI: 10.1088/0034-4885/78/10/106001.

[119] I. V. Krive et al. "Chiral symmetry breaking and the Josephson current in a ballistic superconductor - quantum wire - superconductor junction". In: *Low Temperature Physics* 30.5 (2004), pp. 398–404. DOI: 10.1063/1.1739160. eprint: https://doi.org/10.1063/1.1739160.

[120] A. A. Reynoso et al. "Anomalous Josephson Current in Junctions with Spin Polarizing Quantum Point Contacts". In: *Phys. Rev. Lett.* 101 (10 2008), p. 107001. DOI: 10.1103/PhysRevLett.101.107001.

[121] F. S. Bergeret and I. V. Tokatly. "Theory of diffusive ϕ_0 Josephson junctions in the presence of spin-orbit coupling". In: *Europhysics Letters* 110.5 (2015), p. 57005. DOI: 10.1209/0295-5075/110/57005.

[122] Tomohiro Yokoyama, Mikio Eto, and Yuli V. Nazarov. "Anomalous Josephson effect induced by spin-orbit interaction and Zeeman effect in semiconductor nanowires". In: *Phys. Rev. B* 89 (19 2014), p. 195407. DOI: 10.1103/PhysRevB.89.195407.

[123] A. Zazunov et al. "Anomalous Josephson Current through a Spin-Orbit Coupled Quantum Dot". In: *Phys. Rev. Lett.* 103 (14 2009), p. 147004. DOI: 10.1103/PhysRevLett.103.147004.

[124] Mohammad Alidoust and Klaus Halterman. "Long-range spin-triplet correlations and edge spin currents in diffusive spin-orbit coupled SNS hybrids with a single spin-active interface". In: *Journal of Physics: Condensed Matter* 27.23 (2015), p. 235301. DOI: 10.1088/0953-8984/27/23/235301.

[125] V. M. Edel'shtein. "Characteristics of the Cooper pairing in two-dimensional noncentrosymmetric electron systems". In: *Soviet Physics - JETP (English Translation)* 68.6 (1989), pp. 1244–1249. ISSN: 0038-5646. DOI: http://inis.iaea.org/search/search.aspx?orig_q=RN:22082571.

[126] N. Banerjee et al. "Controlling the superconducting transition by spin-orbit coupling". In: *Phys. Rev. B* 97 (18 2018), p. 184521. DOI: 10.1103/PhysRevB.97.184521.

[127] Kun-Rok Jeon et al. "Tunable Pure Spin Supercurrents and the Demonstration of Their Gateability in a Spin-Wave Device". In: *Phys. Rev. X* 10 (3 2020), p. 031020. DOI: 10.1103/PhysRevX.10.031020.

[128] M G Blamire and J W A Robinson. "The interface between superconductivity and magnetism: understanding and device prospects". In: *Journal of Physics: Condensed Matter* 26.45 (2014), p. 453201. DOI: 10.1088/0953-8984/26/45/453201.

[129] Avradeep Pal et al. "Spectroscopic evidence of odd frequency superconducting order". In: *Scientific Reports* 7.1 (2017), p. 40604. ISSN: 2045-2322. DOI: 10.1038/srep40604.

[130] Avradeep Pal and M. G. Blamire. "Large interfacial exchange fields in a thick superconducting film coupled to a spin-filter tunnel barrier". In: *Phys. Rev. B* 92 (18 2015), p. 180510. DOI: 10.1103/PhysRevB.92.180510.

[131] Yi Zhu et al. "Superconducting exchange coupling between ferromagnets". In: *Nature Materials* 16.2 (2017), pp. 195–199. ISSN: 1476-4660. DOI: 10.1038/nmat4753.

[132] Artem V. Galaktionov and Andrei D. Zaikin. "Fluctuations of the Josephson current and electron-electron interactions in superconducting weak links". In: *Phys. Rev. B* 82 (18 2010), p. 184520. DOI: 10.1103/PhysRevB.82.184520.

[133] M. Stern et al. "Flux Qubits with Long Coherence Times for Hybrid Quantum Circuits". In: *Phys. Rev. Lett.* 113 (12 2014), p. 123601. DOI: 10.1103/PhysRevLett.113.123601.

[134] T. Ando. "Quantum point contacts in magnetic fields". In: *Phys. Rev. B* 44 (15 1991), pp. 8017–8027. DOI: 10.1103/PhysRevB.44.8017.

[135] Akira Furusaki. "DC Josephson effect in dirty SNS junctions: Numerical study". In: *Physica B: Condensed Matter* 203.3 (1994), pp. 214 –218. ISSN: 0921-4526. DOI: https://doi.org/10.1016/0921-4526(94)90061-2.

[136] Yasuhiro Asano. "Numerical method for dc Josephson current between d-wave superconductors". In: *Phys. Rev. B* 63 (5 2001), p. 052512. DOI: 10.1103/PhysRevB.63.052512.

[137] Caio H. Lewenkopf and Eduardo R. Mucciolo. "The recursive Green's function method for graphene". In: *Journal of Computational Electronics* 12.2 (2013), pp. 203–231. DOI: 10.1007/s10825-013-0458-7.

[138] A. Buzdin. "Direct Coupling Between Magnetism and Superconducting Current in the Josephson φ_0 Junction". In: *Phys. Rev. Lett.* 101 (10 2008), p. 107005. DOI: 10.1103/PhysRevLett.101.107005.

[139] G Campagnano et al. "Spin–orbit coupling and anomalous Josephson effect in nanowires". In: *Journal of Physics: Condensed Matter* 27.20 (2015), p. 205301. DOI: 10.1088/0953-8984/27/20/205301.

[140] M. Minutillo et al. "Anomalous Josephson effect in S/SO/F/S heterostructures". In: *Phys. Rev. B* 98 (14 2018), p. 144510. DOI: 10.1103/PhysRevB.98.144510.

[141] Mohammad Alidoust, Chenghao Shen, and Igor Zutic. "Cubic spin-orbit coupling and anomalous Josephson effect in planar junctions". In: *Phys. Rev. B* 103 (6 2021), p. L060503. DOI: 10.1103/PhysRevB.103.L060503.

[142] Aldo Brunetti et al. "Anomalous Josephson current, incipient time-reversal symmetry breaking, and Majorana bound states in interacting multilevel dots". In: *Phys. Rev. B* 88 (14 2013), p. 144515. DOI: 10.1103/PhysRevB.88.144515.

[143] Fran çois Konschelle, Ilya V. Tokatly, and F. Sebastián Bergeret. "Theory of the spin-galvanic effect and the anomalous phase shift φ_0 in superconductors and Josephson junctions with intrinsic spin-orbit coupling". In: *Phys. Rev. B* 92 (12 2015), p. 125443. DOI: 10.1103/PhysRevB.92.125443.

[144] Konstantin N. Nesterov, Manuel Houzet, and Julia S. Meyer. "Anomalous Josephson effect in semiconducting nanowires as a signature of the topologically nontrivial phase". In: *Phys. Rev. B* 93 (17 2016), p. 174502. DOI: 10.1103/PhysRevB.93.174502.

[145] G. Eilenberger. "Transformation of Gorkov's equation for type II superconductors into transport-like equations". In: *Zeitschrift fur Physik* 214.2 (1968), pp. 195–213. DOI: 10.1007/BF01379803.

[146] Wolfgang Belzig et al. "Quasiclassical Green's function approach to mesoscopic superconductivity". In: *Superlattices and Microstructures* 25.5 (1999), pp. 1251–1288. ISSN: 0749-6036. DOI: https://doi.org/10.1006/spmi.1999.0710.

[147] C J Lambert and R Raimondi. "Phase-coherent transport in hybrid superconducting nanostructures". In: *Journal of Physics: Condensed Matter* 10.5 (1998), p. 901. DOI: 10.1088/0953-8984/10/5/003.

[148] Patrick A. Lee and Daniel S. Fisher. "Anderson Localization in Two Dimensions". In: *Phys. Rev. Lett.* 47 (12 1981), pp. 882–885. DOI: 10.1103/PhysRevLett.47.882.

[149] Supriyo Datta. *Electronic Transport in Mesoscopic Systems*. Cambridge Studies in Semiconductor Physics and Microelectronic Engineering. Cambridge University Press, 1995. DOI: 10.1017/CBO9780511805776.

[150] David K. Ferry, Stephen Goodnick, and Jonathan Bird. *Transport in Nanostructures*. English. Cambridge University Press, 2009. ISBN: 9780511840463. DOI: 10.1017/CBO9780511840463.

[151] Subhajit Pal and Colin Benjamin. "Yu-Shiba-Rusinov bound states induced by a spin flipper in the vicinity of a s-wave superconductor". In: *Scientific Reports* 8.1 (2018), p. 11949. DOI: 10.1038/s41598-018-30346-4.

[152] O. Vávra et al. "0 and π phase Josephson coupling through an insulating barrier with magnetic impurities". In: *Phys. Rev. B* 74 (2 2006), p. 020502. DOI: 10.1103/PhysRevB.74.020502.

[153] Jing-Chao Wang, Guo-Qiao Zha, and Shi-Ping Zhou. "$0-\pi$ transitions in mesoscopic Josephson junctions with magnetic impurity interlayers". In: *Physica C: Superconductivity* 483 (2012), pp. 79–81. ISSN: 0921-4534. DOI: https://doi.org/10.1016/j.physc.2012.07.010.

[154] Jacob Linder and Alexander V. Balatsky. "Odd-frequency superconductivity". In: *Rev. Mod. Phys.* 91 (4 2019), p. 045005. DOI: 10.1103/RevModPhys.91.045005.

[155] Johannes R. Eskilt et al. "Long-ranged triplet supercurrent in a single in-plane ferromagnet with spin-orbit coupled contacts to superconductors". In: *Phys. Rev. B* 100 (22 2019), p. 224519. DOI: 10.1103/PhysRevB.100.224519.

[156] Annica M. Black-Schaffer and Alexander V. Balatsky. "Odd-frequency superconducting pairing in topological insulators". In: *Phys. Rev. B* 86 (14 2012), p. 144506. DOI: 10.1103/PhysRevB.86.144506.

[157] Jorge Cayao and Annica M. Black-Schaffer. "Odd-frequency superconducting pairing in junctions with Rashba spin-orbit coupling". In: *Phys. Rev. B* 98 (7 2018), p. 075425. DOI: 10.1103/PhysRevB.98.075425.

[158] Jorge Cayao, Christopher Triola, and Annica M. Black-Schaffer. "Odd-frequency superconducting pairing in one-dimensional systems". In: *The European Physical Journal Special Topics* 229.4 (2020), pp. 545–575. DOI: https://doi.org/10.1140/epjst/e2019-900168-0.

[159] Johann Schmidt, Fariborz Parhizgar, and Annica M. Black-Schaffer. "Odd-frequency superconductivity and Meissner effect in the doped topological insulator Bi_2Se_3". In: *Phys. Rev. B* 101 (18 2020), p. 180512. DOI: 10.1103/PhysRevB.101.180512.

[160] Tomas Löthman et al. "Disorder-robust p-wave pairing with odd-frequency dependence in normal metal–conventional superconductor junctions". In: *Phys. Rev. B* 104 (9 2021), p. 094503. DOI: 10.1103/PhysRevB.104.094503.

[161] E. Vecino, A. Martín-Rodero, and A. Levy Yeyati. "Josephson current through a correlated quantum level: Andreev states and π junction behavior". In: *Phys. Rev. B* 68 (3 2003), p. 035105. DOI: 10.1103/PhysRevB.68.035105.

[162] C. Benjamin et al. "Controllable junction in a Josephson quantum-dot device with molecular spin". In: *Eur. Phys. J. B* (2007). DOI: 10.1140/epjb/e2007-00167-6.

[163] A. V. Rozhkov and Daniel P. Arovas. "Josephson Coupling through a Magnetic Impurity". In: *Phys. Rev. Lett.* 82 (13 1999), pp. 2788–2791. DOI: 10.1103/PhysRevLett.82.2788.

[164] A. Martín-Rodero and A. Levy Yeyati. "Josephson and Andreev transport through quantum dots". In: *Advances in Physics* 60.6 (2011), pp. 899–958. DOI: 10.1080/00018732.2011.624266. eprint: https://doi.org/10.1080/00018732.2011.624266.

[165] V Meden. "The Anderson-Josephson quantum dot: a theory perspective". In: *Journal of Physics: Condensed Matter* 31.16 (2019), p. 163001. DOI: 10.1088/1361-648X/aafd6a.

[166] Pasquale Marra, Alessandro Braggio, and Roberta Citro. "A zero-dimensional topologically nontrivial state in a superconducting quantum dot". In: *Beilstein Journal of Nanotechnology* 9 (2018), pp. 1705–1714. ISSN: 2190-4286. DOI: 10.3762/bjnano.9.162.

[167] C. W. J. Beenakker and H. van Houten. "Josephson current through a superconducting quantum point contact shorter than the coherence length". In: *Phys. Rev. Lett.* 66 (23 1991), pp. 3056–3059. DOI: 10.1103/PhysRevLett.66.3056.

[168] C. W. J. Beenakker. "Three "Universal" Mesoscopic Josephson Effects". In: *Transport Phenomena in Mesoscopic Systems*. Ed. by Hidetoshi Fukuyama and Tsuneya Ando. Berlin, Heidelberg: Springer Berlin Heidelberg, 1992, pp. 235–253. ISBN: 978-3-642-84818-6. DOI: https://doi.org/10.1007/978-3-642-84818-6_22.

[169] Gil-Ho Lee et al. "Ultimately short ballistic vertical graphene Josephson junctions". In: *Nature Communications* 6.1 (2015), p. 6181. DOI: 10.1038/ncomms7181.

[170] A. Zazunov et al. "Andreev Level Qubit". In: *Phys. Rev. Lett.* 90 (8 2003), p. 087003. DOI: 10.1103/PhysRevLett.90.087003.

[171] Pasquale Marra, Roberta Citro, and Alessandro Braggio. "Signatures of topological phase transitions in Josephson current-phase discontinuities". In: *Phys. Rev. B* 93 (22 2016), p. 220507. DOI: 10.1103/PhysRevB.93.220507.

[172] A. M. Whiticar et al. "Zeeman-driven parity transitions in an Andreev quantum dot". In: *Phys. Rev. B* 103 (24 2021), p. 245308. DOI: 10.1103/PhysRevB.103.245308.

[173] Mahn-Soo Choi et al. "Kondo effect and Josephson current through a quantum dot between two superconductors". In: *Phys. Rev. B* 70 (2 2004), p. 020502. DOI: 10.1103/PhysRevB.70.020502.

[174] F. S. Bergeret, A. Levy Yeyati, and A. Martín-Rodero. "Interplay between Josephson effect and magnetic interactions in double quantum dots". In: *Phys. Rev. B* 74 (13 2006), p. 132505. DOI: 10.1103/PhysRevB.74.132505.

[175] Minchul Lee, Thibaut Jonckheere, and Thierry Martin. "Josephson Effect through an Isotropic Magnetic Molecule". In: *Phys. Rev. Lett.* 101 (14 2008), p. 146804. DOI: 10.1103/PhysRevLett.101.146804.

[176] Tobias Meng, Serge Florens, and Pascal Simon. "Self-consistent description of Andreev bound states in Josephson quantum dot devices". In: *Phys. Rev. B* 79 (22 2009), p. 224521. DOI: 10.1103/PhysRevB.79.224521.

[177] Nils Wentzell et al. "Magnetoelectric spectroscopy of Andreev bound states in Josephson quantum dots". In: *Phys. Rev. B* 94 (8 2016), p. 085151. DOI: 10.1103/PhysRevB.94.085151.

[178] Sh. Kogan. *Electronic Noise and Fluctuations in Solids*. Cambridge University Press, 1996. DOI: 10.1017/CBO9780511551666.

[179] J.R. Taylor. *An Introduction to Error Analysis: The Study of Uncertainties in Physical Measurements*. ASMSU/Spartans.4.Spartans Textbook. University Science Books, 1997. ISBN: 9780935702422. DOI: https://books.google.it/books?id=ypNnQgAACAAJ.

[180] Francesco M. D. Pellegrino, Giuseppe Falci, and Elisabetta Paladino. "1/f critical current noise in short ballistic graphene Josephson junctions". In: *Communications Physics* 3.1 (2020), p. 6. DOI: 10.1038/s42005-019-0275-9.

[181] Francesco M. D. Pellegrino, Giuseppe Falci, and Elisabetta Paladino. "Low-frequency critical current noise in graphene Josephson junctions in the open-circuit gate voltage limit". In: *The European Physical Journal Special Topics* 230.4 (2021), pp. 821–825. DOI: 10.1140/epjs/s11734-021-00071-7.

[182] Francesco M. D. Pellegrino, Giuseppe Falci, and Elisabetta Paladino. *Second spectrum of charge carrier density fluctuations in graphene due to trapping/detrapping processes*. 2023. arXiv: 2305.07628 [cond-mat.mes-hall].

[183] Nikolai A Sinitsyn and Yuriy V Pershin. "The theory of spin noise spectroscopy: a review". In: *Reports on Progress in Physics* 79.10 (2016), p. 106501. DOI: 10.1088/0034-4885/79/10/106501.

[184] I. A. Merkulov, Al. L. Efros, and M. Rosen. "Electron spin relaxation by nuclei in semiconductor quantum dots". In: *Phys. Rev. B* 65 (20 2002), p. 205309. DOI: 10.1103/PhysRevB.65.205309.

[185] Eugene Aleksandrov Alexandrov and Valerii Zapasskii. "Magnetic resonance in the Faraday-rotation noise spectrum". In: *Sov. Phys. JETP* 54 (Jan. 1981). DOI: https://ui.adsabs.harvard.edu/abs/1981JETP...54...64A.

[186] M. Oestreich et al. "Spin Noise Spectroscopy in GaAs". In: *Phys. Rev. Lett.* 95 (21 2005), p. 216603. DOI: 10.1103/PhysRevLett.95.216603.

[187] S. A. Crooker et al. "Spin Noise of Electrons and Holes in Self-Assembled Quantum Dots". In: *Phys. Rev. Lett.* 104 (3 2010), p. 036601. DOI: 10.1103/PhysRevLett.104.036601.

[188] W. Reim et al. "Magnetic Equilibrium Noise in Spin-Glasses: $Eu_{0.4}Sr_{0.6}S$". In: *Phys. Rev. Lett.* 57 (7 1986), pp. 905–908. DOI: 10.1103/PhysRevLett.57.905.

[189] P. Svedlindh et al. "Equilibrium magnetic fluctuations of a short-range Ising spin glass". In: *Phys. Rev. B* 40 (10 1989), pp. 7162–7166. DOI: 10.1103/PhysRevB.40.7162.

[190] J. Magnusson, P. Nordblad, and P. Svedlindh. "Flux noise in $Bi_2Sr_2CaCu_2O_8$ displaying the paramagnetic Meissner effect: Evidence of spontaneous magnetic moments". In: *Phys. Rev. B* 57 (17 1998), pp. 10929–10935. DOI: 10.1103/PhysRevB.57.10929.

[191] L. I. Glazman and K. A. Matveev. "Resonant Josephson current through Kondo impurities in a tunnel barrier". In: *Soviet Journal of Experimental and Theoretical Physics Letters* 49 (1989), p. 659. DOI: https://ui.adsabs.harvard.edu/abs/1989JETPL..49..659G.

[192] C. W. J. Beenakker. "Universal limit of critical-current fluctuations in mesoscopic Josephson junctions". In: *Phys. Rev. Lett.* 67 (27 1991), pp. 3836–3839. DOI: 10.1103/PhysRevLett.67.3836.

[193] F. Siano and R. Egger. "Josephson Current through a Nanoscale Magnetic Quantum Dot". In: *Phys. Rev. Lett.* 93 (4 2004), p. 047002. DOI: 10.1103/PhysRevLett.93.047002.

[194] Silvano De Franceschi et al. "Hybrid superconductor–quantum dot devices". In: *Nature Nanotechnology* 5.10 (2010), pp. 703–711. DOI: 10.1038/nnano.2010.173.

[195] Jorden A. van Dam et al. "Supercurrent reversal in quantum dots". In: *Nature* 442.7103 (2006), pp. 667–670. DOI: 10.1038/nature05018.

[196] R. Delagrange et al. "0-π quantum transition in a carbon nanotube Josephson junction: Universal phase dependence and orbital degeneracy". In: *Phys. Rev. B* 93 (19 2016), p. 195437. DOI: 10.1103/PhysRevB.93.195437.

[197] Chung Ting Ke et al. "Ballistic superconductivity and tunable π-junctions in InSb quantum wells". In: *Nature Communications* 10.1 (2019), p. 3764. DOI: 10.1038/s41467-019-11742-4.

[198] Sujoy Karan et al. "Superconducting quantum interference at the atomic scale". In: *Nature Physics* 18.8 (2022), pp. 893–898. DOI: 10.1038/s41567-022-01644-6.

[199] Yunyan Yao et al. "Giant oscillatory Gilbert damping in superconductor/ferromagnet/superconductor junctions". In: *Science Advances* 7.48 (2021), eabh3686. DOI: 10.1126/sciadv.abh3686. eprint: https://www.science.org/doi/pdf/10.1126/sciadv.abh3686.

[200] G. E. Blonder, M. Tinkham, and T. M. Klapwijk. "Transition from metallic to tunneling regimes in superconducting microconstrictions: Excess current, charge imbalance, and supercurrent conversion". In: *Phys. Rev. B* 25 (7 1982), pp. 4515–4532. DOI: 10.1103/PhysRevB.25.4515.

[201] Akira Furusaki and Masaru Tsukada. "Current-carrying states in Josephson junctions". In: *Phys. Rev. B* 43 (13 1991), pp. 10164–10169. DOI: 10.1103/PhysRevB.43.10164.

[202] Akira Furusaki, Hideaki Takayanagi, and Masaru Tsukada. "Josephson effect of the superconducting quantum point contact". In: *Phys. Rev. B* 45 (18 1992), pp. 10563–10575. DOI: 10.1103/PhysRevB.45.10563.

[203] Gabriel Sellier et al. "π junction behavior and Andreev bound states in Kondo quantum dots with superconducting leads". In: *Phys. Rev. B* 72 (17 2005), p. 174502. DOI: 10.1103/PhysRevB.72.174502.

[204] Hermann Sellier et al. "Half-Integer Shapiro Steps at the $0-\pi$ Crossover of a Ferromagnetic Josephson Junction". In: *Phys. Rev. Lett.* 92 (25 2004), p. 257005. DOI: 10.1103/PhysRevLett.92.257005.

[205] E. A. de Andrada e Silva, G. C. La Rocca, and F. Bassani. "Spin-split subbands and magneto-oscillations in III-V asymmetric heterostructures". In: *Phys. Rev. B* 50 (12 1994), pp. 8523–8533. DOI: 10.1103/PhysRevB.50.8523.

[206] E. A. de Andrada e Silva, G. C. La Rocca, and F. Bassani. "Spin-orbit splitting of electronic states in semiconductor asymmetric quantum wells". In: *Phys. Rev. B* 55 (24 1997), pp. 16293–16299. DOI: 10.1103/PhysRevB.55.16293.

[207] LB Litinskii. "The band structure of hexagonal NbN". In: *Solid state communications* 71.4 (1989), pp. 299–305. DOI: https://doi.org/10.1016/0038-1098(89)91018-1.

[208] F. Leuenberger et al. "GdN thin films: Bulk and local electronic and magnetic properties". In: *Phys. Rev. B* 72 (1 2005), p. 014427. DOI: 10.1103/PhysRevB.72.014427.

[209] Lukas Eugen Marsoner Steinkasserer, Beate Paulus, and Nicola Gaston. "Hybrid density functional calculations of the surface electronic structure of GdN". In: *Phys. Rev. B* 91 (23 2015), p. 235148. DOI: 10.1103/PhysRevB.91.235148.

[210] Chun-gang Duan et al. "Strain Induced Half-Metal to Semiconductor Transition in GdN". In: *Phys. Rev. Lett.* 94 (23 2005), p. 237201. DOI: 10.1103/PhysRevLett.94.237201.

[211] P. Larson and Walter R. L. Lambrecht. "Electronic structure of Gd pnictides calculated within the $LSDA+U$ approach". In: *Phys. Rev. B* 74 (8 2006), p. 085108. DOI: 10.1103/PhysRevB.74.085108.

[212] P. Wachter and E. Kaldis. "Magnetic interaction and carrier concentration in GdN and $GdN_{1-x}O_x$". In: *Solid State Communications* 34.4 (1980), pp. 241–244. ISSN: 0038-1098. DOI: https://doi.org/10.1016/0038-1098(80)90401-9.

[213] Juan Pedro Cascales et al. "Switchable Josephson junction based on interfacial exchange field". In: *Applied Physics Letters* 114.2 (2019), p. 022601. DOI: 10.1063/1.5050382. eprint: https://doi.org/10.1063/1.5050382.

[214] A. Manchon et al. "New perspectives for Rashba spin-orbit coupling". In: *Nature Materials* 14.9 (2015), pp. 871–882. ISSN: 1476-4660. DOI: 10.1038/nmat4360.

[215] Yukio Tanaka et al. "Anomalous Josephson Effect between Even- and Odd-Frequency Superconductors". In: *Phys. Rev. Lett.* 99 (3 2007), p. 037005. DOI: 10.1103/PhysRevLett.99.037005.

[216] Bernard Dennis Cullity and Chad D Graham. *Introduction to magnetic materials*. John Wiley & Sons, 2011. DOI: https://onlinelibrary.wiley.com/doi/book/10.1002/9780470386323.

[217] Thomas E Baker, Adam Richie-Halford, and Andreas Bill. "Long range triplet Josephson current and 0-π transitions in tunable domain walls". In: *New Journal of Physics* 16.9 (2014), p. 093048. DOI: 10.1088/1367-2630/16/9/093048.

[218] Jun-Feng Liu, K. S. Chan, and J. Wang. "Tunable 0-π transition by spin precession in Josephson junctions". In: *Applied Physics Letters* 96.18 (2010), p. 182505. DOI: 10.1063/1.3425764. eprint: https://doi.org/10.1063/1.3425764.

[219] T. Maity et al. "Magnetoresistance of epitaxial GdN films". In: *Journal of Applied Physics* 128.21 (2020), p. 213901. DOI: 10.1063/5.0022950. eprint: https://doi.org/10.1063/5.0022950.

[220] Nina Fröhling, Frithjof B. Anders, and Mikhail Glazov. "Nuclear spin noise in the central spin model". In: *Phys. Rev. B* 97 (19 2018), p. 195311. DOI: 10.1103/PhysRevB.97.195311.

[221] E. Paladino et al. "1/f noise: Implications for solid-state quantum information". In: *Rev. Mod. Phys.* 86 (2 2014), pp. 361–418. DOI: 10.1103/RevModPhys.86.361.

[222] Alexander A. Balandin. "Low-frequency 1/f noise in graphene devices". In: *Nature Nanotechnology* 8.8 (2013), pp. 549–555. DOI: 10.1038/nnano.2013.144.

[223] Tobias Meng. *Andreev bound states in Josephson quantum dot devices*. 2009.

[224] E. A. Chekhovich et al. "Nuclear spin effects in semiconductor quantum dots". In: *Nature Materials* 12.6 (2013), pp. 494–504. DOI: 10.1038/nmat3652.

[225] C. Kittel. *Elementary Statistical Physics*. Dover Books on Physics Series. Dover Publications, 2004. ISBN: 9780486435145. DOI: https://books.google.it/books?id=5sd9SAoRjgQC.

[226] A. Krichevsky et al. "Spectrum and thermodynamic currents in one-dimensional Josephson elements". In: *Phys. Rev. B* 61 (5 2000), pp. 3723–3733. DOI: 10.1103/PhysRevB.61.3723.

[227] Craig E. Pryor and Michael E. Flatté. "Landé g Factors and Orbital Momentum Quenching in Semiconductor Quantum Dots". In: *Phys. Rev. Lett.* 96 (2 2006), p. 026804. DOI: 10.1103/PhysRevLett.96.026804.

[228] Craig E. Pryor and Michael E. Flatté. "Erratum: Landé g Factors and Orbital Momentum Quenching in Semiconductor Quantum Dots [Phys. Rev. Lett. 96, 026804 (2006)]". In: *Phys. Rev. Lett.* 99 (17 2007), p. 179901. DOI: 10.1103/PhysRevLett.99.179901.

[229] Weidong Sheng and A. Babinski. "Zero g factors and nonzero orbital momenta in self-assembled quantum dots". In: *Phys. Rev. B* 75 (3 2007), p. 033316. DOI: 10.1103/PhysRevB.75.033316.

[230] Peter Stano et al. "g-factor of electrons in gate-defined quantum dots in a strong in-plane magnetic field". In: *Phys. Rev. B* 98 (19 2018), p. 195314. DOI: 10.1103/PhysRevB.98.195314.

[231] Leon C. Camenzind et al. “Isotropic and Anisotropic g-Factor Corrections in GaAs Quantum Dots”. In: *Phys. Rev. Lett.* 127 (5 2021), p. 057701. DOI: 10.1103/PhysRevLett.127.057701.